Transport of Two-Phase Air-Water Flows in Radial Centrifugal Pumps

Dissertation
for the award of the degree

Doktoringenieur
(Dr.-Ing.)

by M.Sc. Michael Mansour
Date of birth: 12. February 1987
Place of birth: Cairo, Egypt

Approved by the Faculty of Process and System Engineering
of the Otto-von-Guericke-University of Magdeburg

Doctoral committee:

Prof. Dr.-Ing. Frank Beyrau	(Chairman)
Prof. Dr.-Ing. Dominique Thévenin	(Reviewer)
Prof. Dr.-Ing. Romuald Skoda	(Reviewer)
Dr.-Ing. Dirk Wenderott	(Reviewer)

Submitted on: 24.06.2019

Doctoral Colloquium on: 30.01.2020

To my God

Acknowledgments

Although the journey towards this degree was long and not always smooth, it was also very interesting with great experiences. First, I would like to give all honor and glory to my Lord Jesus Christ for offering me grace, ability, and opportunity to perform this research and complete my study. Without his blessings, this work would not have been done.

I really owe sincere thankfulness for the guidance, help, and support of my principal supervisor, Prof. Dominique Thévenin. I got to know during the journey that he is also a great teacher, a very kind friend, and he became a role model for me. Because of him, I could realize why a Ph.D. supervisor is called "Dokotorvater" in German. He has been always there, providing continuous guidance, and advice at all times. Without his guidance, this research would not have been accomplished. Many thanks! I would like to especially thank Dr. Bernd Wunderlich, who helped me with his excellent experience to perform the very first laboratory experiments. Special thanks go to Prof. Mohammed H. Mohammed from the Helwan University in Cairo, Egypt, for introducing and recommending me to Prof. Dominique Thévenin. I would like to thank Dr. Abouelmagd Abdelsamie for the very kind support he gave to me in my first days in Germany, and also the continuous help throughout my Ph.D. work. My special thanks go similarly to Dr. Katharina Zähringer for helping me with her deep experience in experimental issues. I would specifically like to thank Dr. Gábor Janiga for the support have give me in numerical simulations with his log-time experience. I also appreciate the support of all my colleagues at the Institute of Fluid Dynamics and Thermodynamics at the University of Magdeburg, Germany.

I would like to thank several people from my home university in Egypt for the scientific discussions and the academic assistance, including Prof. Mohammed Fatouh, Prof. M.F. Sedrak, and Dr. I. Elbadawy, Prof. Mohammed H. Ali and Prof. Rafea Abdel-Maksoud, and Prof. Khairy Elsayed. I would like to express my thanks as well to Prof. R. Skoda and his research group from Ruhr University in Bochum for the nice collaboration and the knowledge exchange in projects related to this thesis.

Additionally, I would like to express my earnest appreciation to the Egyptian government and Helwan University for nominating me for a two-year scholarship. I am very honored to be the recipient of this scholarship since they allowed me to travel and start my work in Germany. I would like also to acknowledge the financial support of the projects associated with this thesis by the Verband Deutscher Maschinen- und Anlagenbau e.V. (VDMA). I am also very honored to receive a scholarship from the "Katholischer Akademischer Ausländer-Dienst" (KAAD), which gave me great social support as a second family for me in Germany, and allowed me to travel around Germany and attend several amazing academic and cultural events during my Ph.D. period.

Special thanks to my all-time academic friend John Hennawy, who started the academic journey with me and was always there for me. I would, of course, like to show my gratitude to my parents, and my brother Pierre Mansour for their very kind support and persistent encouragement.

Magdeburg,
24.06.2019 Michael Mansour

Abstract

This dissertation aims at investigating gas-liquid transport by centrifugal pumps and the related performance degradation due to the gas accumulation in the impeller. Therefore, the focus is set to understand the interactions between the phases and the possible phase segregation. The investigations cover single and two-phase pumping performances, head degradation, performance hysteresis, two-phase flow regimes, flow pattern maps, flow instabilities and pump surging. The dissertation involves also the influence of employing closed or semi-open impellers, standard or increased tip clearance gaps, an inducer on pump performance and the two-phase flow regimes. For these purposes, two experimental test-rigs, manufactured from acrylic glass, were employed, i.e. 1) a horizontal diverging channel (static test-rig) and 2) a radial centrifugal pump (dynamic test-rig). The diverging channel was designed to investigate the process of gas accumulation that occurs similarly in the impeller, providing a first step toward understanding the flow behavior. The chapters and the main findings of the dissertation can be summarized as follows.

Chapter 1 gives a general introduction on two-phase flows and fundamentals of centrifugal pumps. Chapter 2 presents a review of the previous studies, where the main findings of the literature are summarized, highlighting several gaps and disagreements. This confirmed that the transport of gas-liquid flows is still not fully clear yet, particularly the gas accumulation process. Furthermore, detailed and accurate numerical simulations and flow modeling are still not possible, due to the lack of measurement data and/or boundary conditions. Bridging this gap, is also one of the main objectives of this dissertation, allowing accurate comparisons with CFD simulations and potential model developments. Chapter 3 presents the test-rigs details along with all measurement devices employed.

The results of the diverging channel are discussed in Chapter 4. The parameters leading to large gas accumulations were observed and discussed, revealing interesting insights. It was shown that the presence of large recirculation zones, visualized by Particle Image Velocimetry (PIV), can lead to gas bubble trapping and rapid accumulation. Even for very small gas volume fractions ($\varepsilon = 0.05\%$), a gas pocket was observed. Quantifying the gas accumulation size by shadowgraphy, it was found that the accumulated gas can be reduced by 1) avoiding large separations in the main liquid flow, 2) ensuring high enough turbulence levels and/or 3) choosing a stratified flow regime after the diverging part. It was also shown that the accumulated gas strongly affects pressure recovery; a significant decay in pressure recovery is observed when more gas is accumulated. Furthermore, sample boundary conditions for the inlet velocity and the bubble size distributions (BSDs) are measured by Laser Doppler Anemometry (LDA) and shadowgraphy, respectively.

Chapter 5 discusses the experimental results of the centrifugal pump. Comparing a closed and a similar semi-open impeller, it was shown that the single-phase performance of the semi-open impeller is slightly lower, due to the leakage flow. The difference is considerably larger when the tip clearance gap of the semi-open impeller is increased. When an inducer is installed, only insignificant changes could be seen in the single-phase performance. For two-phase flow, the semi-open impeller with a standard gap can generally resist gas accumulations up to $\varepsilon = 3\%$, showing better performance than that of the closed impeller. However, the trend is reversed for ε between 4 % and 6 %, where the accumulation of huge pockets starts in the semi-open impeller. Increasing the semi-open impeller tip clearance gap leads to increased leakage flow, enhancing the gas accumulation resistance. This retards the sudden performance drop and provides more robust two-phase performance up to $\varepsilon = 7\%$. Further, installing the inducer with the semi-open impeller resulted positively in improved performance, particularly for part-load flow conditions (up to $\varepsilon = 7\%$).

Interestingly, the pump exhibited substantially different two-phase pumping performances (hysteresis) for exactly the "same" flow conditions, depending on the history of setting the desired flow parameters. The semi-open impeller with standard gap involved strong hysteresis, especially when the air is reduced from an originally high flow rate. Increasing the tip clearance gap was found able to eliminate the performance hysteresis while installing the inducer could strongly reduced it. No significant hysteresis effects could be observed in the closed impeller. It was also found that the semi-open impeller involves generally lower instabilities and more limited surging conditions compared to the closed impeller. When the inducer is installed, the flow instabilities and the surging region could be reduced.

The two-phase flow patterns were recorded by a high-speed camera and associated along with the undesirable phenomena (breakdown, surging, cavitation. . .) directly to the pump performance curves. The resulting maps confirm the higher gas accumulation resistance of the semi-open impeller, which positively increases by increasing the tip clearance gap. The inducer has only a slight influence on the flow regime map. For $\varepsilon \geq 8\%$, a segregated flow regime occurs in the closed impeller, which was never found in the semi-open impeller. In this range, neither increasing the gap nor installing the inducer could significantly improve the performance due to the occurrence of gas-locking.

A video library including time-resolved and cyclic recordings was generated in this work. The videos involve recording for the flow regimes of 115 various two-phase flow conditions. Furthermore, selected two-phase flow cases were optically analyzed by time-averaging to obtain the gas accumulation size. The time-averaged images are very useful to be compared with CFD simulations for validation. Using shadowgraphy measurements, the BSDs were also measured, which can be implemented for some two-phase flow models. Chapter 6 presents results of relevant CFD simulations to give more details about the flow behaviour in the channel, across the inducer, and in the pump. Some important flow features could be justified numerically. Additionally, the limitations of several common numerical models are discussed. Finally, conclusions and all findings of the dissertation are summarized in Chapter 7, together with recommendations for possible future work.

Zusammenfassung

Ziel dieser Arbeit ist es, den Gas-Flüssigkeitstransport durch Kreiselpumpen und den damit verbundenen Leistungsabfall durch die Gasansammlung innerhalb des Laufrades zu untersuchen. Hierbei liegt der Schwerpunkt auf dem Verständnis der Wechselwirkungen zwischen den Phasen und der möglichen Phasentrennung. Die Untersuchungen umfassen ein- und zweiphasige Pumpleistungen, Förderhöhenabbau, Leistungshysterese, zweiphasige Strömungsregime, Strömungsmusterkarten, Strömungsinstabilitäten und „Surging". Zudem beinhaltet diese Dissertation die Betrachtung des Einflusses durch den Einsatz von geschlossenen oder halboffenen Laufrädern, Standard- oder vergrößerten Spaltweiten, eines Vorsatzläufers auf die Pumpenleistung sowie die zweiphasigen Pumpleistungen. Zu diesem Zweck wurden zwei aus Acrylglas gefertigte Versuchsstände eingesetzt, wobei es sich 1. um einen horizontal divergierenden Kanal (statischer Prüfstand) und 2. um eine Radialkreiselpumpe (dynamischer Prüfstand) handelt. Der divergierende Kanal wurde entwickelt, um den innerhalb des Laufrades ähnlich ablaufenden Prozess der Gasansammlung zu untersuchen und dient somit einem ersten Schritt zum Verständnis des Strömungsverhaltens. Die Kapitel sowie die wichtigsten Ergebnisse der Dissertation lassen sich wie folgt zusammenfassen.

Das Kapitel 1 gibt eine allgemeine Einführung in die Zweiphasenströmungen und die Grundlagen von Kreiselpumpen. Kapitel 2 präsentiert einen Überblick über die bisherigen Studien, in denen die wichtigsten Ergebnisse der Literatur zusammengefasst sind, wobei mehrere Lücken und Meinungsverschiedenheiten hervorgehoben werden. Hierdurch wurde bestätigt, dass der Transport von Gas-Flüssigkeitsströmen, insbesondere der Prozess der Gasakkumulation, noch nicht vollständig geklärt ist. Darüber hinaus sind detaillierte und genaue numerische Simulationen und Strömungsmodellierungen aufgrund fehlender Messdaten und/oder Randbedingungen noch nicht möglich. Somit bildet die Überwindung dieser Lücke eines der Hauptziele dieser Dissertation, indem sie einen genauen Vergleich mit CFD-Simulationen und möglichen Modellentwicklungen schafft. Im Kapitel 3 werden die Details der Prüfstände sowie alle verwendeten Messgeräte vorgestellt.

Die Ergebnisse des divergierenden Kanals werden im Kapitel 4 diskutiert. Die Beobachtung und Diskussion, der zu großen Gasansammlung führenden Parameter, resultierten hierbei in interessanten Erkenntnissen. Es wurde gezeigt, dass das Vorhandensein großer Rezirkulationszonen, visualisiert durch die Particle Image Velocimetry (PIV), zu Gasblaseneinschlüssen und schneller Akkumulation führen kann. Selbst bei sehr kleinen Gasvolumenanteilen ($\varepsilon = 0,05\%$) wurde eine Gastasche beobachtet. Bei der Quantifizierung der Gasakkumulationsgröße, mit Hilfe des Schattenverfahrens, wurde festgestellt, dass das angesammelte Gas reduziert werden kann, indem 1. große Trennungen im Hauptflüssigkeitsstrom

vermieden werden, 2. ausreichend hohe Turbulenzen gewährleistet werden und/oder 3. ein geschichtetes Strömungssystem nach dem divergierenden Teil gewählt wird. Es wurde auch gezeigt, dass das akkumulierte Gas die Druckrückgewinnung stark beeinflusst; wird mehr Gas akkumuliert, kann ein signifikanter Abfall der Druckrückgewinnung beobachtet werden. Darüber hinaus werden die Proberandbedingungen für die Einströmgeschwindigkeit und die Blasengrößenverteilung (BSDs) mittels Laser-Doppler-Anemometry (LDA) bzw. dem Schattenverfahren gemessen.

Kapitel 5 diskutiert die experimentellen Ergebnisse der Kreiselpumpe. Vergleicht man ein geschlossenes und ein ähnliches halboffenes Laufrad, so zeigte sich, dass die Leistung bei einphasiger Strömung des halboffenen Laufrades aufgrund des Leckstroms etwas geringer ist. Die Differenz ist wesentlich größer, wenn die Spaltweite des halboffenen Laufrades vergrößert wird. Bei der Installation eines Vorsatzläufers waren nur geringfügige Änderungen in der Leistung bei einphasiger Strömung zu erkennen. Bei zweiphasiger Strömung kann das halboffene Laufrad mit einem Standardspalt im Allgemeinen Gasansammlungen bis zu $\varepsilon = 3\%$ widerstehen und eine bessere Leistung als das geschlossene Laufrad aufweisen. Allerdings ist der Trend bei ε zwischen 4 % und 6 % umgekehrt, wo im halboffenen Laufrad die Ansammlung riesiger Taschen beginnt. Die Erhöhung der Spaltweite des halboffenen Laufrades führt zu einem erhöhten Leckstrom und steigert den Gasakkumulationswiderstand. Dies verzögert den plötzlichen Leistungsabfall und bietet eine robustere Zweiphasenleistung bis zu $\varepsilon = 7\%$. Darüber hinaus führte die Installation des Vorsatzläufers mit dem halboffenen Laufrad zu einer positiven Leistungssteigerung, insbesondere bei Teillastströmungen (bis zu $\varepsilon = 7\%$).

Interessanterweise zeigte die Pumpe wesentliche Unterschiede in den zweiphasigen Pumpleistungen (Hysterese) für genau die gleichen Strömungsbedingungen, abhängig von der Reihenfolge der Einstellung der gewünschten Strömungsparameter. Das halboffene Laufrad mit Standardspalt stand in Verbindung mit einer starken Hysterese, insbesondere wenn die Luft von einem ursprünglich hohen Volumenstrom reduziert wurde. Eine Vergrößerung der Spaltweite konnte die Leistungshysterese eliminieren, während die Installation des Vorsatzläufers diese stark reduzieren konnte. Im geschlossenen Laufrad konnten keine signifikanten Hysterese-Effekte beobachtet werden. Es wurde auch festgestellt, dass das halboffene Laufrad im Allgemeinen geringere Instabilitäten und begrenztere Bedingungen von Surging aufweist als das geschlossene Laufrad. Wenn der Vorsatzläufer installiert ist, können die Strömungsinstabilitäten und der Bereich von Surging reduziert werden.

Die zweiphasigen Strömungsmuster wurden von einer Hochgeschwindigkeitskamera aufgenommen und zusammen mit den unerwünschten Phänomenen (Pumpenausfall, Surging, Kavitation) direkt mit den Pumpenleistungskurven verknüpft. Die daraus resultierenden Karten bestätigen den höheren Gasakkumulationswiderstand des halboffenen Laufrades, der mit zunehmender Spaltweite positiv zunimmt. Der Vorsatzläufer hat nur einen geringen Einfluss auf die Strömungskarte. Für $\varepsilon \geq 8\%$ tritt ein getrenntes Strömungssystem im geschlossenen Laufrad auf, das nie im halboffenen Laufrad gefunden wurde. In diesem Bereich konnte weder eine Vergrößerung des Spaltes noch die Installation des Vorsatzläufers die Leistung durch das Auftreten einer „Gassperre“ signifikant verbessern.

In dieser Arbeit wurde eine Videothek mit zeitaufgelösten und zyklischen Aufnahmen erstellt. Die Videos beinhalten die Aufzeichnungen der Strömungsregime von 115 verschiedenen zweiphasigen Strömungsverhältnissen. Zur Ermittlung der Gasakkumulationsgröße wurden darüber hinaus ausgewählte Zweiphasenströmungsfälle optisch durch Zeitmittelung analysiert. Die zeitgemittelten Bilder sind hierbei für die Validierung mit den CFD-Simulationen sehr nützlich. Mit Hilfe des Schattenmessverfahrens wurden auch die BSDs gemessen, welche für einige Zweiphasenströmungsmodelle implementiert werden können.

Kapitel 6 stellt die Ergebnisse relevanter CFD-Simulationen vor, um mehr Details über das Strömungsverhalten im Kanal, innerhalb des Vorsatzläufers und in der Pumpe zu erhalten. Einige wichtige Strömungsmerkmale konnten numerisch begründet werden. Zusätzlich werden die Grenzen mehrerer gängiger numerischer Modelle diskutiert. Schließlich werden die Schlussfolgerungen und alle Ergebnisse der Dissertation sowie Empfehlungen für mögliche zukünftige Arbeiten in Kapitel 7 zusammengefasst.

Contents

List of Tables

List of Figures

Nomenclature

Roman Letters

Symbol	Description	Units
$A_{channel}$	Impeller channel area	[m^2]
A_D	Cross-sectional area at pump discharge	[m^2]
A_f	Numerical grid face area	[m^2]
A_{gas}	Gas accumulation area	[m^2]
A_S	Cross-sectional area at pump suction	[m^2]
B	Laser beam spacing	[m]
b_1	Blade inlet width	[m]
b_2	Blade outlet width	[m]
c	Volume fraction of air in a local grid face	
C_h	Chord length at inducer blade hub	[m]
C_t	Chord length at inducer blade tip	[m]
$\bar{c}$	Surface-averaged volume fraction of air	
b_i	Inducer blade height	[m]
D_1	Impeller inlet diameter	[m]
D_2	Impeller outlet diameter	[m]
D_D	Diameter of discharge pipe	[m]
D_h	Hub diameter	[m]
D_S	Diameter of suction pipe	[m]
D_t	Inducer blade tip diameter	[m]
d_B	Bubble diameter in monodisperse model	[m]
d_{fringe}	Fringe spacing of laser beams intersection	[m]
d_{hd}	Downstream hydraulic diameter	[m]
d_{hu}	Upstream hydraulic diameter	[m]
$d\dot{m}_a$	Uncertainty of air mass flow rate	[kg/s]
dn	Uncertainty of rotational speed	[min^{-1}]
dP_{Sh}	Uncertainty of shaft power	[kW]
dp_S	Uncertainty of suction pressure	[Pa]
dQ_w	Uncertainty of water volume flow rate	[m^3/s]
dT	Uncertainty of flow temperature	[K]
E	Blade thickness	[m]
g	Gravitational acceleration	[m/s^2]

H	Pump head	[m]
H_{opt}	Optimal pump head	[m]
h	Specific enthalpy of the fluid	[J/kg]
I	Light intensity	[cd]
k	Turbulence kinetic Energy	[m^2/s^2]
L	Length of simulation domain of the inducer	[m]
L_1	upstream straight pipe length	[m]
L_2	downstream straight pipe length	[m]
L_f	Focal length of the LDA system lens	[m]
L_p	Thickness of acrylic glass	[m]
M_c	Mixing coefficient	
$\dot{m}$	Mass flow rate of the fluid	[kg/s]
$\dot{m}_a$	Air mass flow rate	[kg/s]
$\dot{m}_w$	Water mass flow rate	[kg/s]
$\dot{m}_t$	Total mass flow rate ($\dot{m}_a$+$\dot{m}_w$)	[kg/s]
n	Rotational speed	[min^{-1}]
n_q	Specific speed	[min^{-1}]
P_h	Pitch at inducer blade hub	[m]
P_P	Pump useful power	[kW]
P_{Sh}	Shaft power	[kW]
P_t	Pitch at inducer blade tip	[m]
P_{max}	Maximum shaft power	[kW]
$P_{Sh\ opt}$	Shaft power at optimal conditions	[kW]
p	Local pressure	[mbar]
p_2	Reference pressure (at sensor 2) in the diverging channel investigations	[mbar]
p_a	Air static pressure	[Pa]
p_D	Discharge static pressure	[Pa]
p_{in}	Inlet pressure in the inducer investigations	[Pa]
p_{out}	outlet pressure in the inducer investigations	[Pa]
p_S	Suction static pressure	[Pa]
p_{s1}	Pressure at sensor 1 in the inducer investigations	[Pa]
p_{s2}	Pressure at sensor 2 in the inducer investigations	[Pa]
p_v	Vapor pressure	[Pa]
p_w	Water static pressure	[Pa]
Q	Volume flow rate of the fluid	[m^3/s]
$\dot{Q}$	Rate of heat transfer across the system	[W]
Q_a	Air volume flow rate	[m^3/s]
Q_{opt}	Optimal (nominal) flow rate	[m^3/s]
Q_w	Water volume flow rate	[m^3/s]
Q_t	Total volume flow rate (Q_a+Q_w)	[m^3/s]
qG	Linearity limit of measurement accuracy	[%]
R	Gas constant of air	[J/kg K]

S	Tip clearance gap	[m]
S_i	Inducer tip clearance gap	[m]
S_u	Surface uniformity	
T	Flow temperature	[K]
Tu_x	Fluctuating velocity component in x-direction	[m/s]
Tu_y	Fluctuating velocity component in y-direction	[m/s]
t_h	Inducer hub blade thickness	[°]
t_t	Inducer tip blade thickness	[°]
u	Specific internal energy of the fluid	[J/kg]
u_a	Superficial air velocity	[m/s]
u_w	Superficial water velocity	[m/s]
$\vec{V}$	Velocity vector	[m/s]
V_D	Discharge pipe superficial flow velocity	[m/s]
V_S	Suction pipe superficial flow velocity	[m/s]
V_a	Inlet air velocity in the simulations	[m/s]
V_w	Inlet water velocity in the simulations	[m/s]
v_x	Flow velocity in x-direction (axial direction)	[m/s]
v_y	Flow velocity in y-direction	[m/s]
$\dot{W}$	Useful work	[W]
$\dot{W}_{diss}$	Dissipation work	[W]
$\dot{W}_t$	Total work given to the system	[W]
$\vec{X}$	Position vector	[m]
x	Axial distance	[m]
x_w	Location of the LDA measurement volume after refraction through acrylic glass	[m]
x_p	Actual location of the LDA measurement volume after refraction through acrylic glass and water	[m]
y	Vertical distance	[m]
z_D	Delivery elevation	[m]
z_S	Suction elevation	[m]

Greek Letters

Symbol	Description	Units
β_1	Blade inlet angle	[°]
β_2	Blade outlet angle	[°]
Δp	Pump static pressure difference (p_D-p_S)	[Pa]
Δt	Time between the two laser pulses of PIV	[s]
$\Delta\vec{X}$	Displacement vector	[m]
Δx	Horizontal grid spacing for LDA velocity measurements	[Pa]
Δy	Vertical grid spacing for LDA velocity measurements	[Pa]

ε	Inlet gas volume fraction	[%]
ϵ	Turbulence dissipation rate	[m^2/s^3]
η	Pump efficiency	[%]
η_{opt}	Optimal (maximum) pump efficiency	[%]
θ_1	Incident angle of laser beam	[°]
θ_2	Angle of laser beam refraction at the interface between air and acrylic glass	[°]
θ_3	Angle of laser beam refraction at the interface between acrylic glass and water	[°]
θ_h	Inducer hub blade angle	[°]
θ_t	Inducer tip blade angle	[°]
$\dot{\mu}$	Gas mass fraction	[%]
μ_a	Dynamic viscosity of gas	[Pa s]
μ_w	Dynamic viscosity of liquid	[Pa s]
ν	Phase velocity of light in a medium	[m/s]
ρ	Fluid density	[kg/m^3]
ρ_a	Air density	[kg/m^3]
ρ_w	Water density	[kg/m^3]
σ_a	Inducer area solidity	
σ_h	Inducer hub solidity	
σ_t	Inducer tip solidity	
τ	Shaft torque	[N m]
φ	Inducer sweep angle	[N m]
ω	Angular speed	[rad/s]
Υ	Specific delivery work	[m^2/s^2]
Υ_{opt}	Optimal specific delivery work	[m^2/s^2]
Υ_{max}	Maximum specific delivery work	[m^2/s^2]
$d\Delta p$	Uncertainty of pump static pressure difference	[Pa]
$d\tau$	Uncertainty of shaft torque	[N m]
$d\varepsilon$	Uncertainty of inlet gas volume fraction	[%]
$d\eta$	Uncertainty of pump efficiency	[%]
$d\Upsilon$	Uncertainty of pump specific delivery work	[m^2/s^2]

Non-dimensional Numbers

Symbol	Description
n_r	Refractive index of a medium
n_{r1}	Refractive index of air
n_{r2}	Refractive index of acrylic glass
n_{r3}	Refractive index of water
Re_a	Superficial air Reynolds number
Re_w	Superficial water Reynolds number

y+	Dimensionless wall distance
δ	Diameter number (for Cordier diagram)
π	Archimedes' constant (3.14159)
σ	Speed number (for Cordier diagram)

Operators

Symbol	Description
$\boldsymbol{\nabla}$	Differential operator

Subscripts

Symbol	Description
0	Refers to hub dimensions
1	Refers to inlet
2	Refers to outlet
a	Refers to the air phase
D	Refers to discharge
hd	Refers to downstream hydraulic diameter
hu	Refers to upstream hydraulic diameter
i	Refers to dimensions of inducer
opt	Refers to optimal conditions of the pump (conditions at maximum efficiency)
max	Refers to maximum values
S	Refers to suction
Sh	Refers to shaft (power)
t	Refers to total parameters
x	Refers to properties in x-direction
y	Refers to properties in x-direction
w	Refers to the water phase

Abbreviations

Acronym	Description
% FS	Percentage of full scale (a method used to quantify the accuracy of measurement devices)
% RD	Percentage of reading (a method used to quantify the accuracy of measurement devices)
BEP	Best (maximum) efficiency point of the pump characteristic curve

BSD	Bubble size distribution
CFD	Computational fluid dynamics
GVF	Gas volume fraction
HireCT	High–resolution gamma–ray computed tomography
LED	Light-emitting diodes
LDA	Laser Doppler Anemometry
MRF	Moving reference frame
NPSH	Net positive suction head [m]
$NPSH_{available}$	Net positive suction head available [m]
$NPSH_{required}$	Net positive suction head required [m]
PIV	Particle Image Velocimetry
RANS	Reynolds-averaged Navier-Stokes equations
RSM	Reynolds-stress turbulence model
SST	Shear stress transport
TCF	Taylor–Couette flow
VOF	Volume of fluid model

Chapter 1

Introduction

1.1 Multiphase flows

The term multiphase flow is used to refer to the flow of mixture consisting of more than one phase or component. Here, the word phase stands for the thermodynamic state of the matter which can be a gas, a liquid or a solid. Some examples of multiphase flows are gases (bubbles) in a liquid, liquid (droplets) in gases, or solid particles in a gas or a liquid. In several multiphase flows, one phase is usually continuous, representing the primary phase, while the other phases are dispersed within the continuous (main) phase, representing the secondary phases. A multiphase flow can also be either a single-component flow, such as steam-water mixture, or a two-component flow such as air-water mixture. Considering the flow nature and/or the different engineering and industrial applications, various classifications of multiphase flows are available in the literature [1, 2]. However, multiphase flows can be classified generally into five main categories as listed below and schematically illustrated in Figure 1.1:

- Gas-liquid flows
  Bubble columns, boiling, floatation, aeration of liquids.

- Liquid-liquid flows
  liquid-liquid extraction, liquid-liquid mixing.

- Liquid-solid flows
  Particle dispersion in stirred tanks, crystallization systems, hydro-cyclones.

- Gas-solid flows
  Fluidized beds, pneumatic conveying, cyclones, pulverized fuel combustion.

- Three-phase flows
  Oil-water-gas (liquid-liquid-gas) mixtures in oil production, gas-liquid-solid reactors and bubble columns.

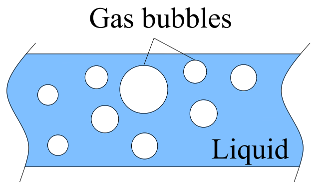

(a) Gas-liquid flows

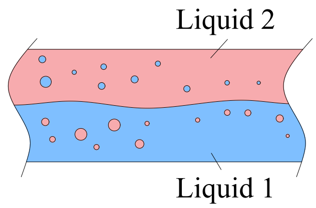

(b) Liquid-liquid flows

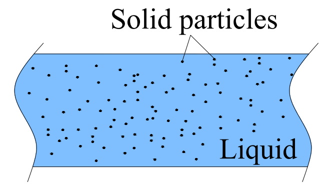

(c) Liquid-solid flows

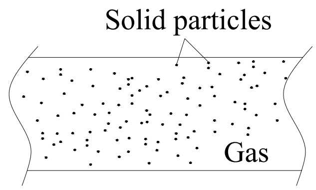

(d) Gas-solid flows

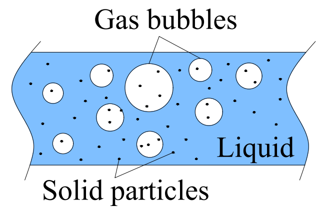

(e) Three-phase flows

Figure 1.1: Different categories of multiphase flows.

In the present study, the considered type of multiphase flows is namely two-phase, two-component, gas-liquid flows. Therefore, the following sections concentrate mainly on the basic features of the transport of such kind of two-phase (air-liquid) mixtures.

1.2 General characteristics of gas-liquid two-phase flows

Regarding the patterns of gas-liquid two-phase flows, numerous classifications have been created by different researchers based on the considered application and/or on flow orientation, i.e. vertical or horizontal. However, the gas-liquid two-phase flows can be usually divided into three main groups based on the flow regimes as classified in [1]. Nevertheless, each regime has again different sub-patterns as can be found in the literature [3–5]. The three main regimes and some sub-regimes are illustrated in Figure 1.2 and described as follows:

- Dispersed flows

  These are flows in which one phase consists of discrete elements, such as dispersed bubbles in a main liquid stream. The discrete elements are not connected (secondary phase), while the other phase is continuous and usually called the carrier phase (primary phase). Two examples (bubbly and droplet flows) are illustrated in Figure 1.2a.

- Transitional flows

  When the volume fraction of the dispersed phase is big enough, agglomeration starts, forming bigger slugs or pockets. Normally, the two phases are characterized by complex interaction mechanisms. Examples of these flows are shown in Figure 1.2b.

- Separated flows

  In a separated flow, the two phases are separated by a line of contact (the phases interface). A stratified flow is one kind of such flows, in which the two phases move in different adjacent layers. An annular flow is another example of separated flows with a liquid layer on the pipe wall and a gaseous core as presented in Figure 1.2c.

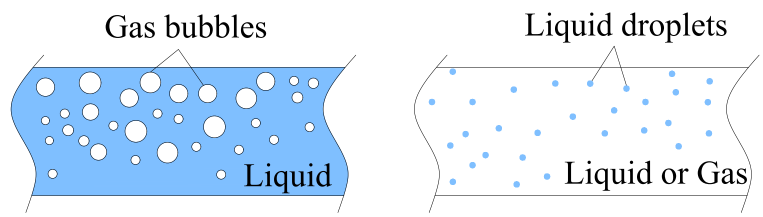

Bubbly Droplet

(a) Dispersed flows

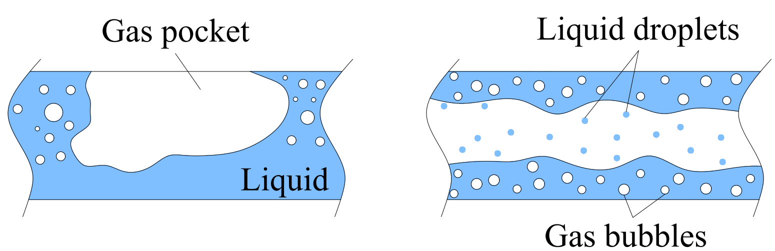

Pocket (slug) Bubbly droplet annular

(b) Transitional flows

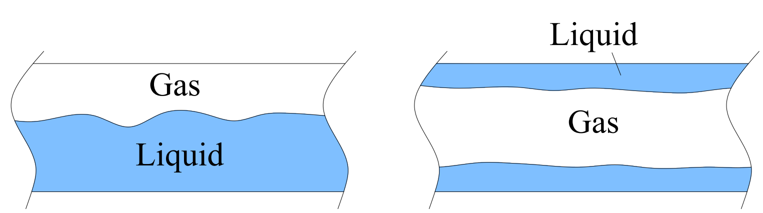

Stratified (segregated) Annular

(c) Separated flows

Figure 1.2: Different regimes of two-phase flows.

1.3 Challenges of gas-liquid two-phase flows

Because it is widely found in numerous engineering and industrial applications, this kind of multiphase flows is possibly the most significant. However, investigating such flows always involve several challenges. For instance, the estimation of the mixture properties is highly complex, depending on many flow parameters. Besides, the presence of flow slip due to the difference in velocities of each phase introduces increased difficulties in the flow calculations. Additionally, the local forces acting on the gas phase, such as the buoyancy and drag forces lead to large variations in space regarding flow patterns and properties. General averaging of the trends or properties cannot be applied. Furthermore, two-phase flows are obviously difficult for all flow meters, depending on the fraction of each phase, which might be variable in space and time. For these reasons, the investigations of gas-liquid two-phase flows are quite challenging experimentally as well as numerically.

1.4 Scientific and practical importance of two-phase transport

Two-phase flows involving gas bubbles and pockets in a main liquid phase are found in a broad diversity of environmental and industrial applications, very often pertaining to energy. For instance, they appear in the tubes of solar collectors, in chemical reactors, oil wells, membrane processes, refrigeration and heat exchangers [6–8]. Likewise, such multiphase flows are ubiquitous in energy storage systems [9]. Thus, the optimal design and performance of such systems require a detailed understanding of the two-phase flow behaviour, since it is observed to be completely different from the single-phase case even at quite low gas loading. The intricacy of such type of flows poses a major challenge due to the need to resolve the coupled interaction of the liquid and gas phases. Increasingly, simulations relying on Computational Fluid Dynamics (CFD) are considered to design and optimize corresponding installations. However, such investigations are only meaningful if they rely on thoroughly validated sub-models and numerical procedures.

Due to their simplicity, compact design and extreme flexibility, centrifugal pumps are used very commonly in many domestic and industrial applications. They can be operated at high speed and can be easily adjusted to fit the demand with minimal maintenance. Additionally, centrifugal pumps are often preferable over positive displacement pumps because of their steady delivery with no or low pulsation.

The transport of two-phase gas-liquid mixtures through centrifugal pumps appear similarly in a wide diversity of engineering and industrial applications. For instance, pumping two-phase flows is necessary for petroleum and natural gas transportation [10, 11], production of crude oil, medical treatment, paper industry, waste water treatment, geothermal power plants [12] and the cooling systems of nuclear power plants [13, 14].

Centrifugal pumps were traditionally developed for the transport of pure liquids, showing excellent properties for this purpose. However, the performance, efficiency, and most of the flow parameters significantly drop, when the pump is operated under two-phase flow conditions. A remarkable drop in pump parameters can be seen even at very low gas volume fractions (GVF lower than 1%). At high gas volume fractions, the gas tends to rapidly accumulate in the impeller passages, hindering the ability of the pump to transfer energy to the mixture, which is known as "gas-locking" [10, 15]. Even worse, a complete breakdown of the pump performance can occur [14, 16–18], usually for part-load conditions, where the flow completely stops.

Therefore, detailed experimental characterizations of relevant configurations are absolutely necessary. Unfortunately, only a few configurations of interest have been studied in the past with high-quality, non-intrusive experimental techniques. Often, important details concerning process parameters or boundary conditions are missing, preventing meaningful comparisons with CFD.

1.5 Key definitions

In this section, important definitions and general terminology of centrifugal pumps, that are re-called and used later, are given. For instance, definitions concerning fundamental parameters, characteristic curves, operating zones, and pump classification are briefly discussed.

1.5.1 Pump performance parameters

The performance of pumps is characterized by some fundamental parameters, which are:

- The volume flow rate of the fluid through the pump Q also called the pump capacity or discharge.

- The specific delivery work Υ of the pump, defined as the useful energy delivered by the pump to the transferred medium per unit of mass. The specific delivery work is commonly replaced by the pump head H, simply representing the total change of Bernoulli's head across the pump where:

$$H = \frac{\Upsilon}{g} \tag{1.1}$$

  assuming a pump that causes a change of Bernoulli's head between the suction and delivery lines as shown in Figure 1.3. In this sketch, p_S and p_D are the suction and discharge pressures, V_S and V_D are the suction and discharge velocities, D_S and D_D are the suction and discharge pipe diameters, and z_S and z_D are the suction and discharge elevations, respectively. Considering a fluid with a density ρ, the pump head can be calculated by:

$$H = \frac{p_D - p_S}{\rho g} + \frac{{V_D}^2 - {V_S}^2}{2g} + (z_D - z_S) \tag{1.2}$$

- The power consumed by the pump shaft P_{Sh}, also called the brake horsepower. The shaft power can be obtained from the shaft rotational speed ω (rad/s) and the shaft torque τ, where:

$$P_{Sh} = \tau\omega \tag{1.3}$$

and

$$\omega = \frac{2\pi n}{60} \tag{1.4}$$

where n is the rotational speed of the pump in revolution per minute (rpm).

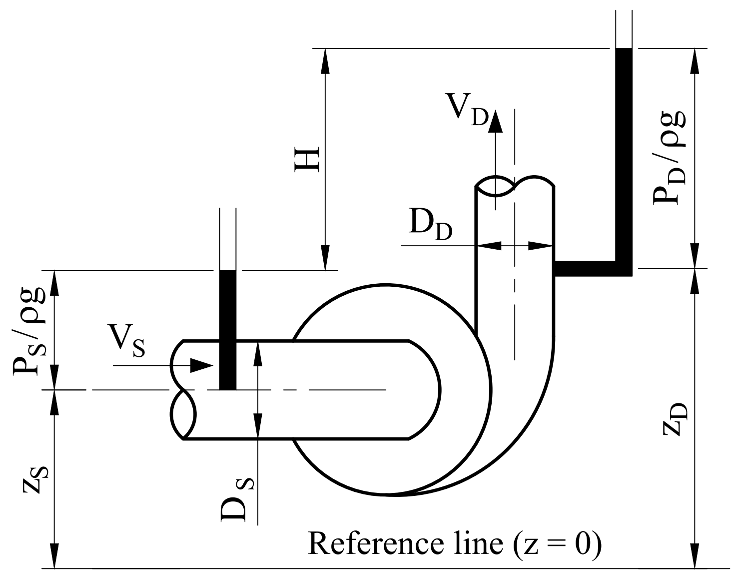

Figure 1.3: Schematic sketch for the energy change between the suction and delivery lines of a pump.

- The efficiency of the pump η, defined as the ratio between the useful power of the pump P_P to the power consumed by the pump shaft P_{Sh}. The useful power of the pump represents the total transferred power from the pump to the conveyed medium and can be calculated by using the mass flow rate $\dot{m}$ and the specific head of the pump Υ, so that:

$$P_P = \dot{m}\Upsilon \tag{1.5}$$

and

$$\eta = \frac{P_P}{P_{Sh}} \tag{1.6}$$

1.5.2 Pump characteristic curves

The curves of pump parameters as a function of the volume flow rate are called the pump characteristic (performance) curves. Figure 1.4 shows examples of the main characteristic curves of a pump at a constant rotational speed. Usually, the head-flow rate $H-Q$, efficiency-flow rate $\eta-Q$, and the shaft power-flow rate $P_{Sh}-Q$ curves are the most important curves to characterize the pump. The point where the efficiency curve reaches its maximum values is usually called the best efficiency point (BEP) or optimal point of the pump. The pump parameters at this point are called the optimal or rated conditions (Q_{opt}, H_{opt}, and $P_{Sh\ opt}$). The different operating zones are also displayed in Figure 1.4, such as part-load, overload, cavitation zone. When the pump is operated at flow rates being lower or higher than the rated flow rate of the pump, the operation is called part-load or overload operation, respectively, as indicated in Figure 1.4.

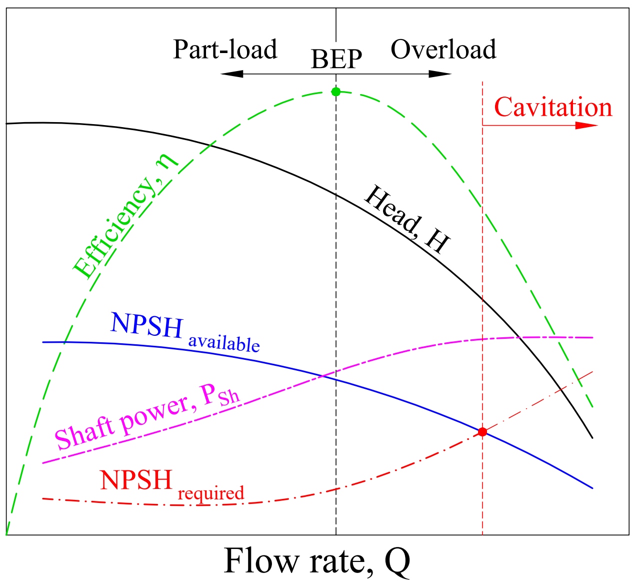

Figure 1.4: Pump characteristic curves as a function of flow rate.

If the local pressure in the pump falls below the vapor pressure (p_v) of the transported liquid, the liquid evaporates forming “cavitation” bubbles. These bubbles move through the pump to higher pressure regions, where they collapse (implode) rapidly. This phenomenon is called “pump cavitation”, which is strongly undesired and should be necessarily avoided since it causes excess noise, strong system vibration, reduced pump efficiency, and severe damage to the impeller surface (blades). A repeated implosion of cavitation bubble near the blades results in increased erosion and can lead in the worst case to complete blade failure. Cavitation mostly occurs at very high flow rates (overload operation) as shown in Figure 1.4, where the local pressure drops to the vapor pressure due to excess velocities.

A pump parameter called net positive suction head (NPSH) is typically used to examine the pump cavitation. The NPSH is defined as the difference between the suction stagnation pressure head of the pump and the vapor pressure head of the liquid, where

$$NPSH = \left(\frac{p_S}{\rho g} + \frac{{V_S}^2}{2g}\right) - \frac{p_v}{\rho g} \tag{1.7}$$

Pumps can be examined for cavitation by a common test, where the inlet pressure of the pump is gradually decreased at a constant flow rate and flow temperature until cavitation starts anywhere inside the pump. The NPSH is then calculated at these conditions and the whole process is repeated at different flow rates, then the curve of the required net positive suction head ($\text{NPSH}_{\text{required}}$) to avoid cavitation is obtained as shown in Figure 1.4. After installing the pump in the system, the available (actual) net positive suction head ($\text{NPSH}_{\text{available}}$) can be calculated at the pump inlet, which must be greater than the $\text{NPSH}_{\text{required}}$ to avoid cavitation. As shown in Figure 1.4, the value of NPSH decreases with the increase of flow rate, since the suction stagnation pressure decreases with flow rate due to the increased losses of the piping system. Pump cavitation starts when $\text{NPSH}_{\text{available}}$ goes lower than the $\text{NPSH}_{\text{required}}$ after the intersection point as represented in Figure 1.4.

1.5.3 Pump specific speed

Centrifugal pumps can be generally classified into three main categories; having either a radial, mixed or axial impeller. These three types are categorized based on the value of the specific speed (n_q) of the pump impeller. The specific speed can be defined as:

$$n_q = \frac{n\sqrt{Q}}{H^{3/4}} \tag{1.8}$$

where n is the rotational speed of the pump, Q in is the volume flow rate m^3/s and H is the pump head in m. The specific speed of a pump is defined as the speed of a geometrically similar ideal pump which produces a unit volume flow rate and a unit head. The value of the specific speed is typically used to determine the shape (geometry) of the pump impeller. This is illustrated in Figure 1.5, which shows the exemplary impeller shapes based on the specific speed value. In this work, a low-specific-speed radial centrifugal pump was considered with a value of $n_q \approx 21\ \text{min}^{-1}$, as will be discussed in details in Chapter 3.

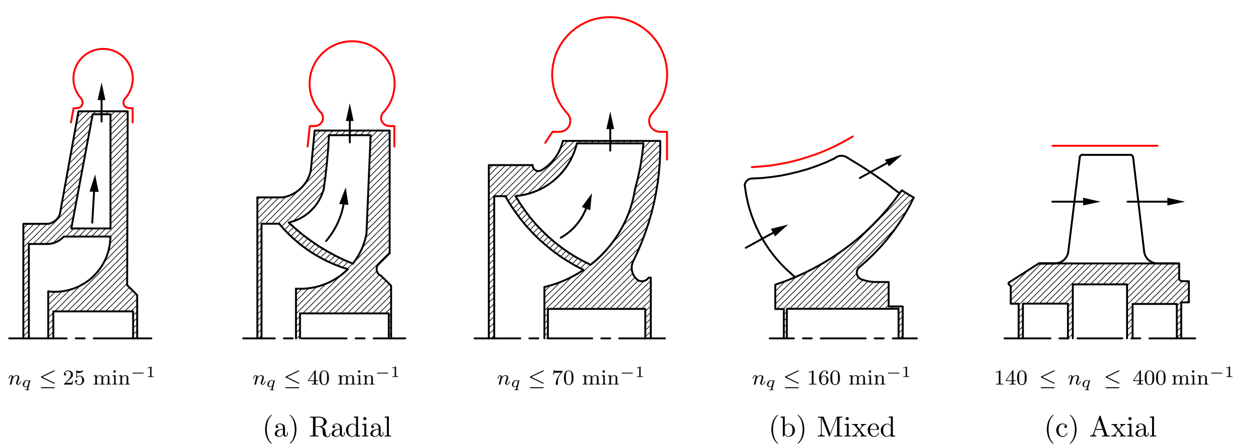

Figure 1.5: Pump impeller shapes as a function of the specific speed.

1.6 Scope and objectives of the dissertation

The scope of this dissertation is set mainly on the transport of two-phase mixtures, considering two-component gas-liquid (air-water) flow. The complex interactions between the gas and liquid phases and the possible phase segregation (gas accumulation) have been studied in a centrifugal pump of a radial type under different operational and flow conditions. Additionally, the transport of the air-water mixture has been investigated in a specially-designed horizontal, diverging channel, simulating the process of gas accumulation that occurs in the impeller channels. Since the flow in such a simple canonical configuration does not involve any rotating part, the investigated channel flow allows a far more accurate and complete experimental characterization. Therefore, this provides a first step toward understanding the complex flow patterns occurring inside centrifugal pumps transporting gas-liquid mixtures.

Accordingly, two experimental test-rigs have been employed in the present work; 1) a horizontal diverging channel (static test-rig) and 2) a radial centrifugal pump (dynamic test-rig). The details of both experimental test-rigs are given in Chapter 3. The main objectives of the work can be summarized as follows

1. Investigating the transport of two-phase flows in a centrifugal pump and analyzing the corresponding pump performance, considering the influence of the following operating conditions, which have been hardly considered in the literature:

    - Effect of changing the impeller design (closed vs. semi-open impellers);
    - Effect of varying the tip clearance gap of the semi-open impeller;
    - Effect of installing an upstream axial inducer.

    As a result, the conditions corresponding to the efficient transport of two-phase flows by centrifugal pumps are investigated and discussed in detail. Accordingly, the results are very useful to select the appropriate impeller design and pump settings based on the considered operating flow conditions.

2. Improving the general understanding of the interaction between the two phases, the phase separation, and the process of gas accumulation, which is very likely to occur in the impeller passages of centrifugal pumps and is responsible for the steep performance degradation. Therefore, the gas-liquid flow patterns are recorded by a high-speed camera, and regime maps are generated for all the considered flow conditions, associating the system performance with the two-phase regime.

3. Furthermore, the process of gas accumulation is investigated in detail in the diverging channel to provide the basic characteristics and behavior of such big cavities, discussing the parameters leading to large gas accumulations.

4. Developing a freely accessible, detailed experimental database for an air-water flow in a simple divergent channel and a radial centrifugal pump, covering wide ranges of operational and flow conditions.

5. Providing all details about the measured flow and boundary conditions, which allows meaningful and accurate comparisons with CFD simulations, opening the door for proper validation and further development of two-phase models.

6. Performing some CFD simulations to understand additional details about the flow behavior and to check the accuracy of different numerical models, giving discussions about the limitations of studying such complex flows by numerical simulations.

After giving a general introduction on two-phase flows and some fundamentals of centrifugal pumps here in Chapter 1, Chapter 2 presents a thorough review of the previous studies concerning the transport of two-phase flows. The literature review 1) covers relevant studies for two-phase flows in channels, and 2) focuses on the main findings of the previous investigations regarding gas-liquid two-phase transport in centrifugal pumps, considering all important parameters and highlighting gaps and disagreements in the literature.

The details of the two experimental test-rigs and all measurement instruments employed in the present work are explained in Chapter 3. The experimental set-ups of all the measured parameters are also illustrated in this chapter, including for example the Particle Image Velocimetry (PIV), the Laser Doppler Anemometry (LDA) and the shadowgraphy systems.

The results of the diverging channel test-rig are shown and discussed in Chapter 4. Different single and two-phase flow conditions are considered, explaining important reasons for the gas accumulation phenomenon. Additionally, sample boundary conditions data for the inlet velocity and the bubble size distributions (BSDs) are measured and given.

Chapter 5 discusses the experimental results of the pump test-rig. The effect of different flow parameters and experimental procedures on the pump performance under two-phase flow are investigated. For example, the chapter shows the effect of changing the impeller type (i.e. closed or semi-open impellers), increasing the tip clearance gap and installing an upstream inducer on the two-phase flow behavior in the pump and the corresponding performance. Further, the two-phase flow regimes recorded by a high-speed camera are also shown and discussed in details. Finally, in Chapter 6, relevant CFD simulations for the diverging channel flow are presented. In addition, some important findings concerning the effect of the upstream inducer and the tip clearance gap are also studied and justified by numerical simulations in this chapter. Several limitations of using numerical simulations to predict such highly complex two-phase flows are identified.

Conclusions and all findings of the dissertation are summarized in Chapter 7, together with recommendations for future work. The dissertation involves also 6 appendices, providing all supplementary information. Appendix A presents an overview of the PIV system. Similarly, Appendix B explains the working principle of the LDA system and the refraction calibration. Appendix C shows the error propagation and uncertainty analysis of the experiments. Appendix D describes a MATLAB code used to analyze the two-phase images and quantify the gas accumulation size in the diverging channel. Sample inlet velocity boundary conditions are given in Appendix E. Appendix F explains the derivation of the specific delivery work of the pump under two-phase flow. A short introduction about the turbulence models used in Chapter 6 is given in Appendix G. Lastly, some numerical results of the pump obtained in a companion study at Bochum University are presented and discussed in Appendix H, highlighting the importance of the experimental data presented in this thesis.

Chapter 2

Literature Review

2.1 Introduction

In this chapter, a detailed literature review is given, considering most relevant previous studies to the considered systems (diverging channel and centrifugal pump). Additionally, important characteristics and comprehensive information about the transport of gas-liquid mixtures by centrifugal pumps are analyzed and discussed. Finally, the open issues discussed in previous studies are summarized, leading to motivations and aims of the present work.

2.2 Transport of two-phase flows in diverging channels

Due to the complexity of measurements in rotating machines, several experimental and theoretical studies have considered two-phase flows in simplified configurations, as will be done as well in this study. Most of these investigations considered simple, horizontal, rectangular flow channels, concentrating on flow regime classifications or investigating frictional effects as a function of the flow parameters [8, 19–21]. As a next step, flows involving channels with a variable cross-section, starting with sudden expansion or sudden contraction, have been studied for the same purpose [8, 22–24]. However, variable-area channels having gradual expansions have hardly been considered in the literature.

In a recent study, the annular flow of an air-water mixture through a diverging, vertical circular pipe was studied to investigate the expansion pressure loss [25]. In this study, the focus was limited only on the annular two-phase flow regime. Another study considered the pressure drop for a two-phase flow in a horizontal, converging or diverging rectangular channel, but specifically at micro-scale [26]. Important conclusions of this study are that 1) the superficial gas velocity decreases due to the deceleration effect in the diverging microchannel; 2) collision and coalescence between bubbles play a very important role to explain the resulting flow features. Nevertheless, large accumulations or stationary large gas pockets, as shown later in the present work, have not been observed.

2.3 Transport of two-phase flows in centrifugal pumps

2.3.1 Loss of pumping efficiency

As already mentioned in Chapter 1, transporting gas-liquid mixtures by centrifugal pumps is still a complex job, due to the high tendency of the gas phase to separate and accumulate within the impeller. In this case, the pump works very inefficiently due to gas-locking [10, 15], and in some cases the pump loses completely its function (breakdown) [14, 16–18].

2.3.2 Pump surging and flow instabilities

The presence of large gas pockets not only is responsible for the dramatic deterioration of the head and flow but also can lead, at some specific conditions, to severe flow instabilities and system vibrations. Under these conditions, continuous formation and discharging of huge gas pockets occur. This phenomenon is known as pump "surging", which corresponds to two different operational points, resulting in strong fluctuation of the pump performance between two distinct points [27–29]. The two-phase flow pattern in the impeller is strongly unsteady in this condition, where the gas pockets are characterized by considerable size change, large oscillations, and alternating appearing and disappearing behaviour [30, 31]. The oscillating pump performance leads to high fluctuations in all relevant pump parameters (flow rate, pressure, efficiency).

2.3.3 Gas handling ability of centrifugal pumps

Generally, any level of entrained gas affects the pump performance. For low gas volume fractions (lower than 3%), the effect is more pronounced at part-load and overload operating conditions than near nominal conditions [32–35]. Also, levels of air slightly above 1% can negatively increase the $\mathrm{NPSH}_{\mathrm{required}}$ [36]. At nominal conditions, the pumping pressure and the flow rate of many single-stage radial centrifugal pump impellers drastically drop for gas volume fractions between 4% and 6% [34, 37]. In many cases, centrifugal pumps will totally stop (breakdown) at about 7%–10% gas volume fraction [14, 33, 34, 37–39].

2.3.4 Influence of flow parameters

The effects of several flow parameters have been already reported in the literature, providing interesting details about the problem. Increasing the rotational speed was often found to be positive concerning the two-phase pumping capability. Higher rotational speeds result in higher turbulence and more homogeneous mixtures, disrupting the gas accumulation, increasing redispersion of gas and allowing the pump to transport more gas [29, 31, 33, 40].

In the study of Cirilo [39], a radial pump impeller (low specific speed) was compared to a mixed one (moderate specific speed). It was shown that the mixed impeller could transport air-water mixtures with air content up to 30%, while the radial one was able to pump air content only lower than 10%. Similarly, by increasing now the specific speed of a radial impeller, the two-phase performance was improved in [40]. On the contrary to these two studies, the increase of specific speed was found to have a negative effect on two-phase pumping performance in [31]. The reason is that the specific speed combines the influence of different parameters, i.e., rotational speed and impeller geometry (shape). As mentioned above, a higher rotational speed (thus a higher specific speed, keeping all other parameters constant) improves the two-phase performance. Assuming now a constant rotational speed and flow rate, a larger impeller diameter (longer blade length) results in a higher pump head, which decreases the specific speed. In this case, the blade loading is also reduced, which is beneficial, together with the additional space available for the flow to reattach after a local gas accumulation [31, 41].

Some studies showed that a higher liquid viscosity results in reduced turbulence levels, leading to more gas accumulation and faster performance deterioration [42–45]. However, in other studies considering oil/gas mixtures, the increase of oil viscosity caused an improvement of the two-phase performance, particularly in overload operation. This is due to the increased drag exerted on the bubbles, which delayed phase separation [31].

Increasing the suction pressure was found to have a positive effect on the pumping performance; a lower gas volume expansion occurs in the pump, improving gas handling capability [38, 46–48]. Further, a recent experimental study [49] showed that the air-water pumping performance can be significantly improved by a surfactant injection. The injected surfactants (isopropanol IPA) could change the interfacial properties of the working fluid. Accordingly, the pump could handle higher gas content with only moderate performance degradation; the sudden drop in the performance could be eliminated.

2.3.5 Two-phase flow patterns in centrifugal pumps

Although it was found to be directly related to the pumping performance, only a few experimental studies have investigated the flow details inside the impeller passages [12, 14, 15, 50–53]. The two-phase flow regimes were mostly identified by making a transparent window in the pump body or using a transparent pump casing. Additionally, some recent studies employed a new non-intrusive technique to identify the gas-liquid distribution in an industrial pump impeller [54, 55]. This new technique is called high-resolution gamma-ray computed tomography (HireCT), which can be applied to non-transparent pumps, but appears to be quite complex.

Visualization studies showed that the degradation of pump performance is caused mainly by the formation of gas pockets on the blades, often near the impeller inlet [15, 29, 51, 56]. In an early visualization study, Murakami and Minemura [57] showed firstly that the pump performance discontinuities correspond to changes in the two-phase flow patterns inside the impeller when the gas amount is increased. It was found in [58] that the pump breakdown occurs when the accumulated gas reaches the impeller outer diameter. Several two-phase flow patterns were observed in the literature, such as:

- Bubble, agglomerated bubble, gas pocket, and segregated flow in [29].
- Bubble, slug, and pocket flows in [58]
- Bubble, unstable pocket, stable pocket, segregated flow in [48]
- Isolated bubbles, bubble, gas pocket, and segregated flow in [53].

Figure 2.1 shows sample images and schematic sketches for the different flow regimes observed in the impeller passages of the centrifugal pump studied recently in [29].

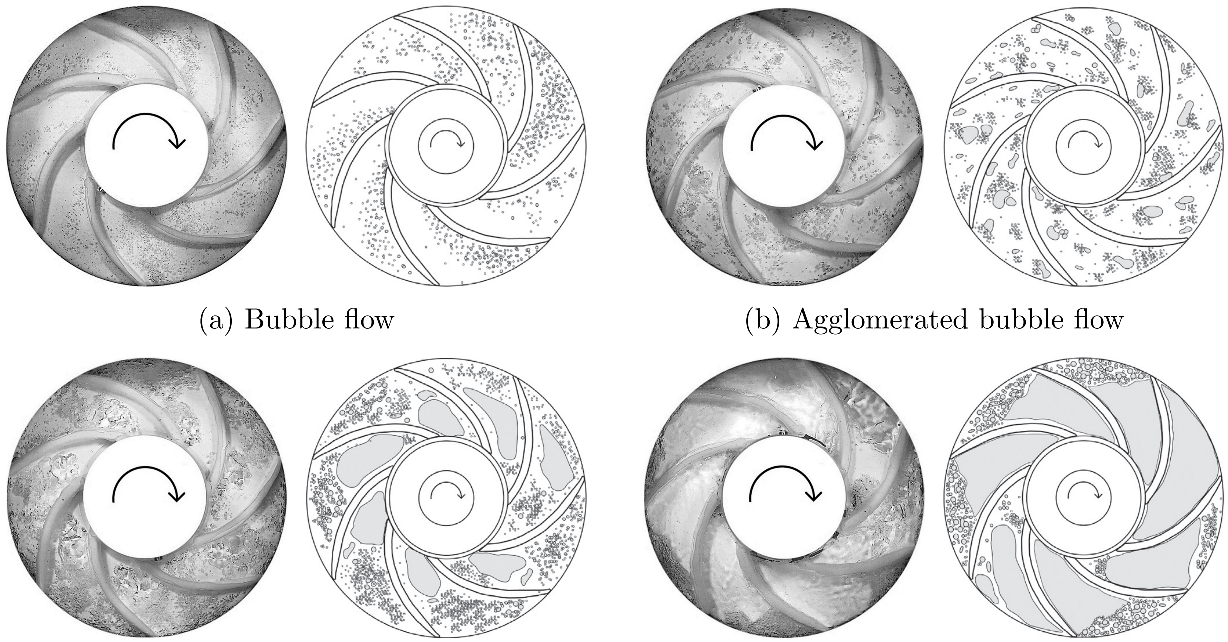

(a) Bubble flow (b) Agglomerated bubble flow

(c) Gas pocket flow (d) Segregated flow

Figure 2.1: Different gas-liquid two-phase flow patterns observed in centrifugal pumps impellers in [29].

Controversial discussions exist in the literature regarding the location of the first gas accumulation. Sometimes the onset was observed on the blade suction side [14, 51, 52]. Poullikkas (2003) [14] showed that the gas starts accumulating on the blade suction side, and near the impeller back plate. Figure 2.2 describes the three stages of gas accumulation in the impeller as observed in [14] by high-speed video recordings when the gas content is gradually increased. This behaviour might be related to the considered steam-water two-phase mixture. Nevertheless, a similar behaviour was observed for air-water mixtures in [51], where the formation of large gas pockets started from the blade suction side, near the impeller inlet. Figure 2.3 shows the development of the two-phase flow structure inside the impeller channels observed in [51] when the gas volume fraction (GVF) is gradually increased.

However, the first gas accumulation was found differently near or on the blade pressure side in other studies [10, 15, 53, 57, 59]. The two-phase flow regimes and the gradual accumulation of gas detected in [15] are shown in Figure 2.4. Here, the gas pockets stand firstly on the pressure side. Therefore, further investigations are required; there is still no commonly accepted explanation for the observations. The observed differences partly result from the different 1) impeller geometries (closed, semi-open, or open impeller), 2) flow conditions (part-load, nominal, or overload), and 3) mixture components (air/water or steam/water), used in the studies. Furthermore, not only very few flow regimes maps were generated in the literature [27, 29, 48, 60], but also the maps were often not directly associated with the performance curves of the pump. This is one of the objectives of the present work.

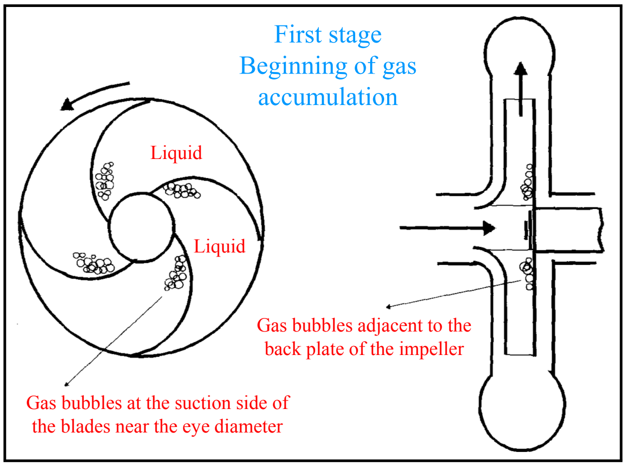

(a) Low gas content

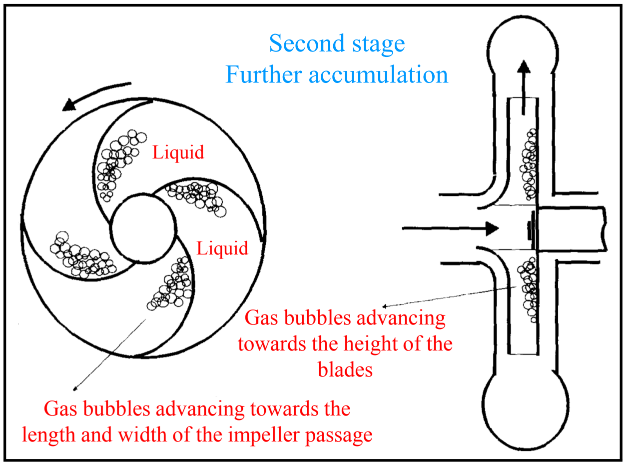

(b) Medium gas content

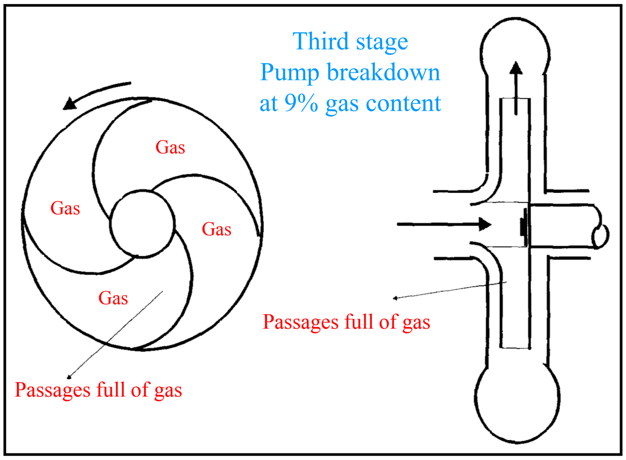

(c) High gas content

Figure 2.2: Stages of gas accumulation as observed in [14].

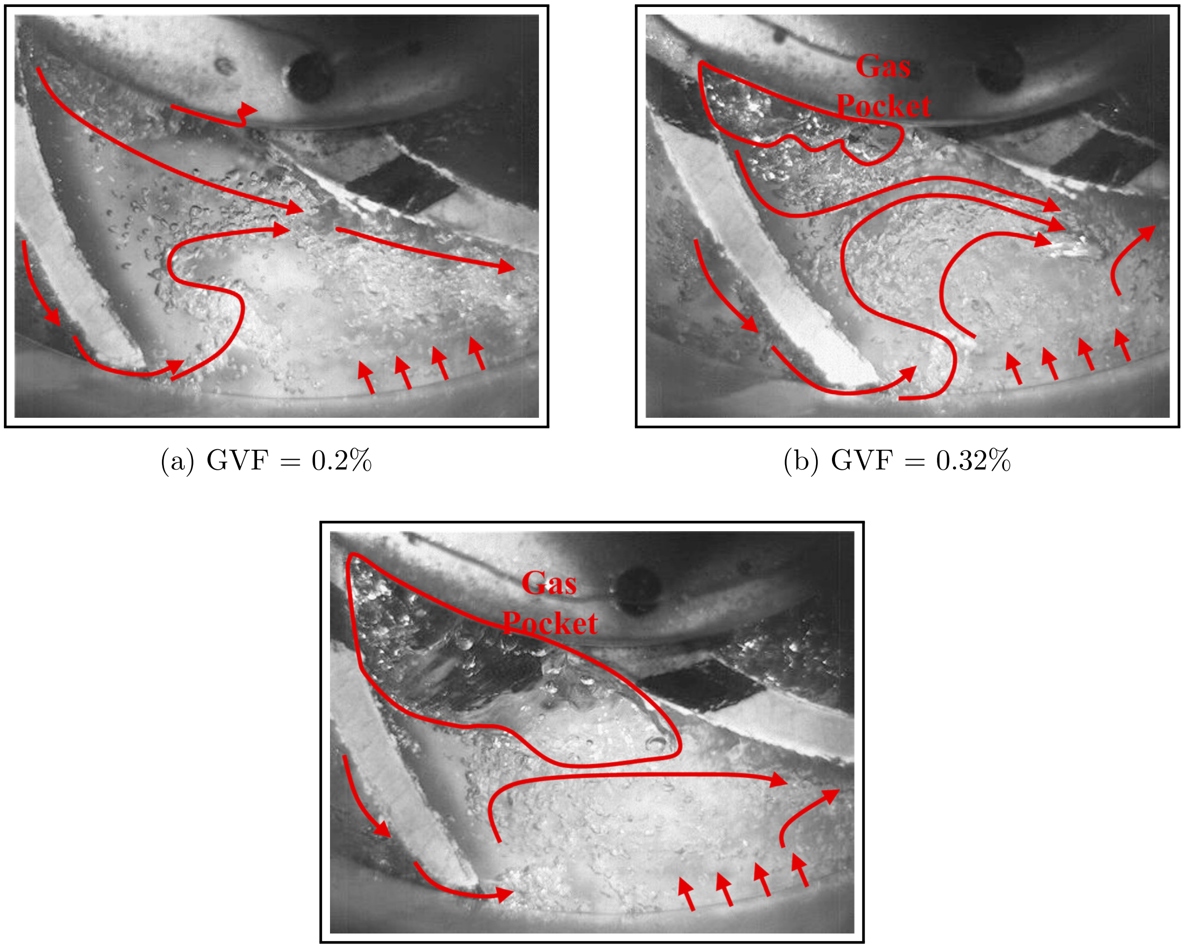

(a) GVF = 0.2%

(b) GVF = 0.32%

(c) GVF = 0.45%

Figure 2.3: High-speed video observations for the flow structure inside the impeller channel from [51].

2.3.6 Influence of the impeller geometry

Considering five different closed impellers, Sato et al. [59] observed that the accumulation starts on the blade suction surface for high-incidence-angle impellers and on the blade pressure surface for low-incidence-angle impellers. Normally, large gas accumulations in two-phase flows are directly connected to the location of large circulation (separation) zones in single-phase flow. Flow separation creates a perfect room for the gas phase to be trapped and accumulate, due to the very low pressure available and zero velocities near the circulation core. Therefore, the observations of Sato et al. [59] can be easily explained here since flow separation occurs on the suction side for high-incidence-angle blades, and on the pressure side for low-incidence-angle blades as schematically explained in Figure 2.5. Nevertheless, the location of the inception of bubble accumulation also depends strongly on the resulting force acting on the bubbles inside the impeller, as a combination of pressure, centrifugal, Coriolis, and drag forces.

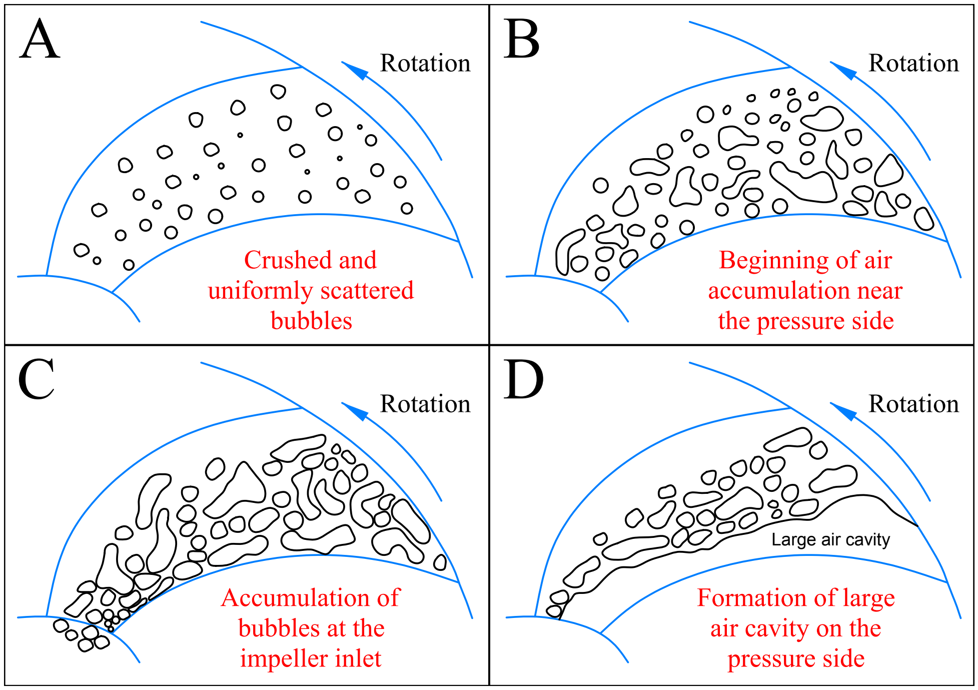

Figure 2.4: Gas accumulation and two-phase flow regimes in the radial pump impeller passages as detected in [15].

The effect of the number of blades was studied by Murakami and Minemura [61], considering semi-open impellers with 3, 5 and 7 blades. Due to an insufficient number of blades, the single-phase performance of the three-blade impeller was much lower than the other ones. However, the use of only 3 blades could slightly improve the two-phase performance for low gas contents. No significant difference was found between the five and seven-blade impellers so that a number of blades between 5 to 7 blades appears to be suitable for both single and two-phase transport. Later, Cappellino et al. [38] compared the performance of two-blade and five-blade semi-open impellers, showing that with an increased tip clearance gap, the two-blade impeller can keep its performance for higher gas levels.

2.3.7 Influence of the tip clearance gap

Semi-open impellers show usually a higher resistance to gas accumulation and better gas handling capability [38, 62–64]. The leakage (secondary) flow occurring across the blades in the tip clearance gap disturbs the accumulated gas, providing better mixing of the phases. Therefore, large gas pockets can only appear at higher gas volume fractions, and the degradation of pump performance is delayed. Semi-open impellers with standard tip clearance gaps (0.4-0.5 mm) show very good two-phase characteristics up to a gas volume fractions around 4% before a sharp reduction occurs afterward. Increasing the tip clearance gap already causes a performance drop for single-phase flow and low-gas-contents mixtures (1%-3%). However, a bigger gap offers increased turbulence and higher resistance against gas accumulation, which can be very favourable if high gas loading flows are considered [38, 65].

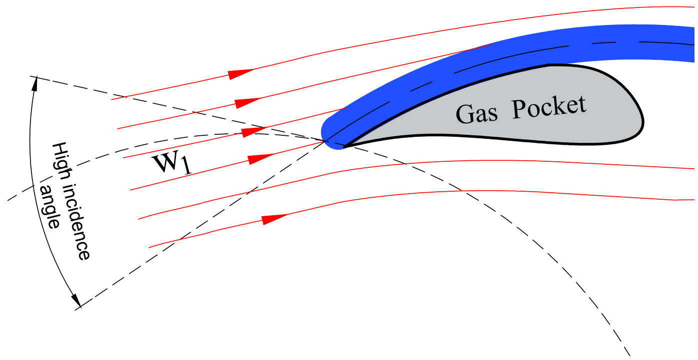

(a) Low-incidence-angle impeller

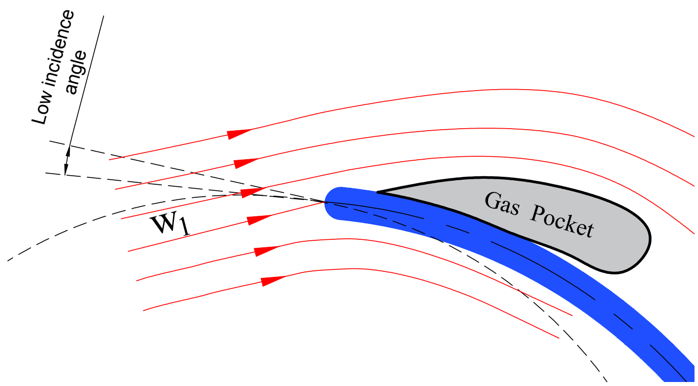

(b) high-incidence-angle impeller

Figure 2.5: Schematic explanation for location of gas accumulation according to the impeller incidence angle.

2.3.8 Influence of upstream inducers

Inducers are axial impellers that can be installed upstream of the main pump impeller. They are designed usually with two to four helical blades to produce low inlet solidity [41]. Inducers are often used to improve the suction conditions for the main impeller, and thus the cavitation characteristics of a centrifugal pump. They are typically installed for high flow pumps to reduce the net positive suction head required [35, 41]. Additionally, inducers were found to have a positive influence on the transport of two-phase flows by centrifugal pumps, particularly in part-load [38]. However, the physical mechanisms explaining the effect of inducers on two-phase pumping performance are still not completely clear. Inducers will simultaneously impact other important features, like pump surging, flow instabilities, and flow regimes. Filling this gap is also one of the objectives of the present work.

2.3.9 Modeling of two-phase flow in centrifugal pumps

Empirical models

Based on experimental data, several attempts were done in the literature to develop suitable empirical correlations to calculate centrifugal pumps performance when transporting gas-liquid two-phase flows. For example, Turpin et al. [47] developed an empirical model to predict the head-capacity curve for an electrical submersible centrifugal pump as a function of the gas-liquid flow rates ratio, single phase pump head, and the intake pressure. A similar correlation for two-phase pumping head was developed in [66] but for a mixed-type centrifugal pump, covering only the bubbly flow regime. Additionally, Duran and Prado [67] developed an empirical model for slightly extended application range, including bubbly and elongated bubble flow regimes. Nevertheless, these empirical models were always generated for a specific pump geometry and can only be used within a restricted range of conditions. Additionally, information about the local gas volume fraction is sometimes required for good prediction of the pump performance [67], limiting the practical use of these models.

Mechanistic models

Several studies focused on developing mechanistic models based on a one-dimensional control volume method [68–74]. However, predictions from such models are likewise limited within specific ranges of conditions and involve large relative errors, as large as 20% [72] and 30% [69]. Recent studies [28, 75, 76] have presented mechanistic models leading to improved predictions for the two-phase pump performance, but are still only valid for specific and/or narrow flow conditions.

In the recent work of Zhu et al. 2017 [28], predictions for the critical gas volume fraction for surging initiation are compared among different correlations available in the literature [27, 39, 47, 77, 78]. The comparison revealed strong deviations between different models, considering exactly the same flow conditions and rotational speed in the calculations. The comparison is shown in Figure 2.6, where the vertical axis represents critical gas volume fraction, and the horizontal axis represents the volume flow rate.

Numerical CFD models

Numerical CFD modeling is a very useful tool to provide detailed information about the internal flow structures and local flow parameters everywhere in the solution domain. However, care must be taken while building the numerical set-up, due to the limitations and/or the restricted applicability of CFD models. Special considerations should also be given to the selection of grid resolution, turbulence models, multiphase models, boundary and initial conditions. Furthermore, numerical simulations of turbo-machinery have their additional difficulties, such as the highly complex geometry and the need for employing an extra meshing technique to consider the impeller rotation (sliding mesh [79, 80] or overset mesh [81, 82]).

For single-phase flows, the CFD simulations of centrifugal pump could show, within specific ranges, good agreement with experimental data [80, 83–89], involving deviations usually

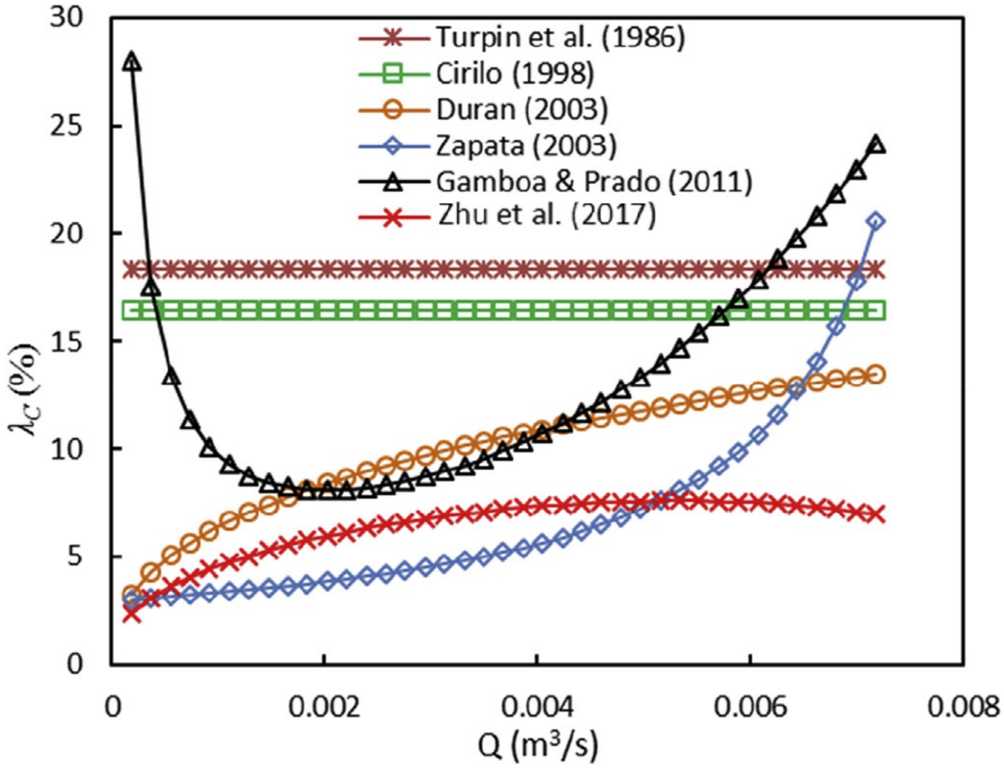

Figure 2.6: Comparison of predictions of surging initiation from different models from [28].

limited to 5 to 20% [10, 90]. Considering now CFD simulations of two-phase flows in centrifugal pumps, new requirements are needed for the solution. Firstly, a new set of conservation equations are normally solved for the second phase. Secondly, the phase interactions between the two phases need to be modeled by additional equations. For instance, extra models are essential to account for the interfacial momentum and all forces (i.e. drag, lift, and virtual mass forces) between the phases [91–94]. It is also very difficult to predict the sudden pump breakdown by CFD simulations [33].

Generally, the available two-phase CFD models for centrifugal pumps require several non-realistic assumptions and immoderate simplifications, and thus often provide poor predictions for the complex flow behaviour in centrifugal pumps [10, 95, 96]. Additionally, these strong simplifying assumptions constrain the validity range of most modeling approaches. Among usual assumptions employed in two-phase models, clearly not suitable for most practical applications, are: 1) considering the gas bubbles as perfect spheres; 2) employing a single, constant diameter for all gas bubbles; 3) ignoring gas density change; and 4) ignoring coalescence and break-up of bubbles [10, 97]. Currently, predictive CFD studies of two-phase flow transport in centrifugal pumps are still beyond reach. This is due, of course, to the complexity of the underlying physics; but also to missing reference experimental data suitable for a direct comparison with CFD, hindering model development and validation. Bridging this gap is one central objective of the current study.

2.4 Motivation and aims of the present study

Summarizing the existing literature, it can be concluded that the transport of gas/liquid flows is still poorly understood, in spite of many interesting studies concerning this highly relevant process for practical applications. Even for a simplified canonical configuration, like diverging channels, the process of gas accumulation and the connection between bubble dynamics, pressure and velocity fields are not fully clear yet. Additionally, most of the previous studies considered only constant opening angle (straight diffuser) for the diverging part [25, 26, 98–102]; in that case, the formation of large gas cavities or gas pockets are not likely to occur. Shedding further light on this issue, thanks to a comprehensive experimental study, is one objective of the present investigations.

Similarly, several disagreements exist in previous studies for the flow behaviour and the influence of different parameters regarding the two-phase flow transport in centrifugal pumps. The phase interaction in the impeller passages and the mechanism responsible for the loss of efficiency have not been clearly explained. Only very few general conclusions for the flow behaviour can be found in the literature. Further, the few formerly generated two-phase flow maps were often not associated with the pump performance curves, which would be very useful to define regions of efficient or critical operation of the pump. Additionally, detailed flow modeling and CFD simulations are still not possible, due to the lack of measurement data and/or boundary conditions. Accordingly, the present investigations should provide further explanations and a detailed experimental database for the transport of gas-liquid two-phase flows in centrifugal pumps.

In the present work, experiments have been done employing two test-rigs to investigate the transport of air-water mixtures, as briefly explained below. The test-sections have been manufactured completely from acrylic glass, providing full optical accessibility for the measurements. Further, some CFD simulations have been done to obtain additional details about the flow and to discuss the accuracy of common numerical models.

2.4.1 Diverging channel: Static test-rig

In these first experiments, the different parameters leading to large gas accumulation and phase segregation have been observed and discussed in a diverging rectangular channel. This simplified configuration is suitable for direct comparisons with CFD but is also directly related to the more complex phenomena occurring into the impeller passages while pumping two-phase, gas-liquid mixtures. The results from these experiments, which are presented in Chapter 4, will help as well to examine available two-phase models and improve them further.

2.4.2 Centrifugal pump: Dynamic test-rig

In the centrifugal pump test-rig, the transport of two-phase flows and the performances of a closed impeller and of a geometrically similar semi-open impeller have been compared. Additionally, the possible performance improvements for a similar semi-open impeller with a standard tip clearance gap have been systematically investigated, by either increasing the gap or adding an upstream inducer. The study involves comparisons of single-phase and two-phase pumping performances, head degradation behaviour, performance hysteresis, two-phase flow regimes, flow instabilities and pump surging.

The performance hysteresis is defined here as the dependence of the pump performance on the procedure (history) employed for setting the desired conditions, i.e. air and water flow rates. This phenomenon appears in different flow applications; for example in Taylor–Couette flow (TCF), where the shape and number of vortices depend strongly on the starting acceleration or the way the flow is started [103]. Similarly, in centrifugal pumps, when reducing the air flow rate from an originally high value, or conversely starting from zero and increasing the air flow rate, large differences in the performance can occur for formally identical operating points. This is due to the prior accumulation of large air pockets, which can still persist along the blades for some flow conditions, even after reducing the air flow rate to values, where smaller or no pockets at all should exist [32].

Gas volume fractions from zero up to a maximum of 15% have been considered. Two tip clearance gaps have been studied, i.e. a standard value and a doubly-increased gap. Three different experimental procedures have been applied to set the desired flow conditions, in order to check possible performance hysteresis.

Furthermore, by using high-speed recording, the phase interaction in the impeller has been systematically observed and flow regime maps have been measured in combination with the pump performance curves for all the considered conditions. In this manner, it becomes possible to associate the pumping behavior with the two-phase flow regime in the impeller. Accordingly, the connection between the two-phase regime found in the impeller and the resulting pump performance can be explained. The present analysis and comparisons are also very helpful to choose optimal impeller settings as a function of the desired operating flow conditions. Similarly, these experimental results are very useful to develop and validate suitable numerical procedures in computational fluid dynamics studies. All results of the centrifugal pump test-rig are presented in Chapter 5.

2.4.3 CFD simulations

Further, in the last part of the thesis (Chapter 6), some CFD simulations have been done to provide further details about the flow, explaining and complementing the experimental observations. Additionally, the numerical accuracy of different and common CFD models have been discussed. In total, three different simulation groups have been considered, covering the diverging flow channel, the flow across the inducer, and the whole pump setup, delivering some interesting information. In Chapter 3, all the details of the two employed experimental test-rigs are given.

Chapter 3

Experimental methodology

This chapter shows the details of the employed experimental test-rigs. The experimental techniques, methods, and measuring devices are also described.

3.1 Diverging channel: Static test-rig

3.1.1 Test-rig details

The experimental set-up of the diverging channel, shown in Figure 3.1, was constructed using transparent acrylic glass to allow high-quality flow visualization and accessibility for all optical measurements. The experiments involving air-water mixtures are performed at a controlled temperature of 291 ± 2 K. Water is circulated through the test section by using a submersible pump (Model: Ama-drainer A 422 ND/35) with a rated flow and head of 25 m^3/h and 10 m, respectively, from a water tank with a total capacity of 6.0 m^3. Air is supplied from a compressed air network via a mixing joint to the channel as shown in Figure 3.1. The air is injected into the mixing joint through 21 small holes of 1.0 mm diameter distributed peripherally in the mixing joint.

The flow rates of water and air are controlled separately through control valves and are measured individually before mixing. An electromagnetic flow meter (Model: Endress+Hauser Promag 30), which has an accuracy of ± 0.5% RD, is used to measure the water volume flow rate; whereas, two rotameters (Model: RGC1269 and RGC1263 from Yokogawa) are employed to measure the air flow with a relative measuring accuracy of 2.5% and a linearity limit of qG = 50%. Currently, the accuracy of variable-area flow meters is specified by the "qG" parameter, rather than by accuracy classes. qG is a linearity limit value in % of full scale, indicating constant relative error above this limit. For example, a Rotameter having an accuracy of 2.5% with a linearity limit of qG = 50% means that the relative error is always equal to 2.5% of the measured value, for any reading above 50% of the rotameter capacity. The error is usually higher near the lower reading of the rotameter scale.

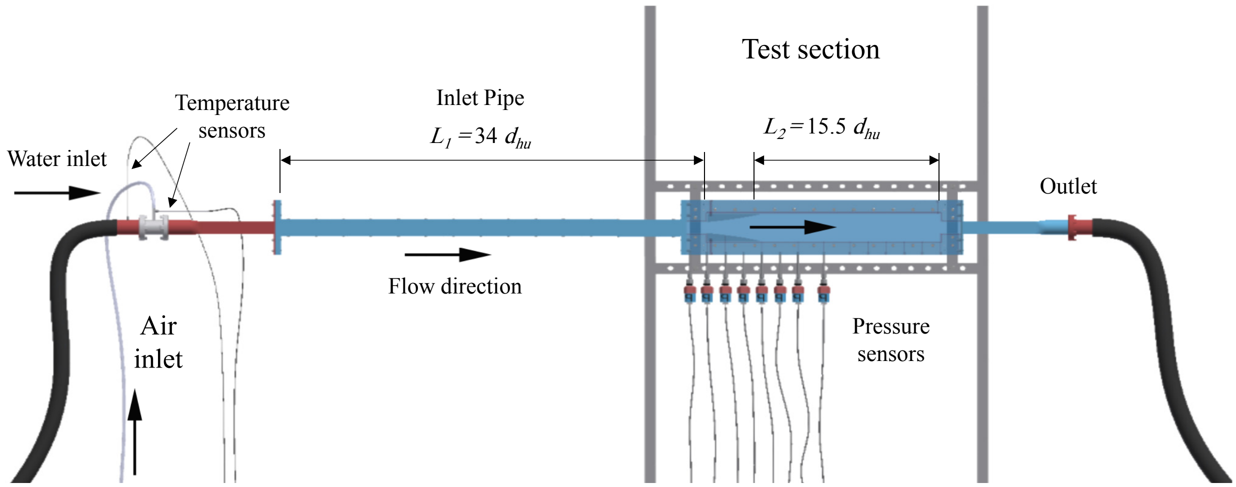

(a) Details of the test section.

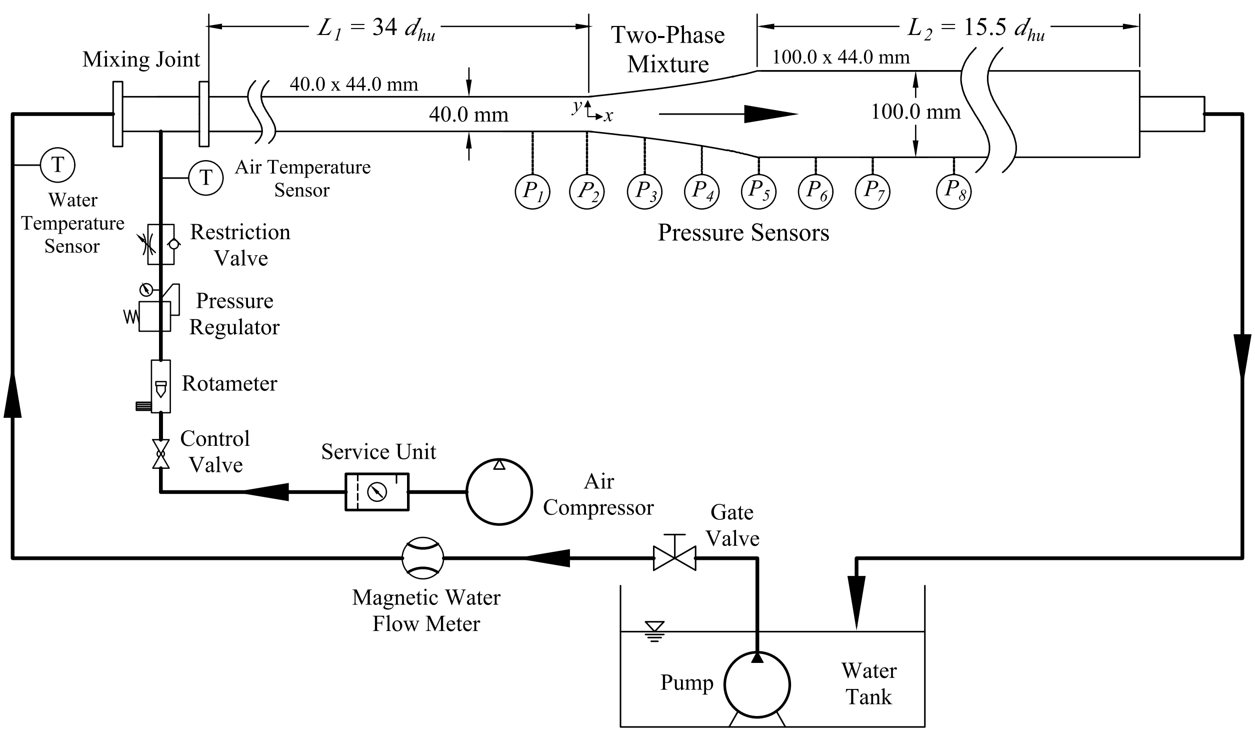

(b) Complete schematic sketch of the set-up.

Figure 3.1: Details of the diverging channel experimental set-up.

Table 3.1: Specifications and uncertainties of measurement devices of the static test-rig.

Device	Model	Uncertainty
Water volume flow meter	Endress+Hauser Promag 30F	± 0.5% RD
Air flow rotameters	Yokogawa RGC1269 and RGC1263	± 2.5% RD with qG = 50%
Pressure sensors	Cerabar T PMC131 ($-1 : +1$ bar)	± 0.5% RD
Temperature sensors	Pt100 Sensor Probe, Class B	± 0.3 K (max. absolute error)

The temperature of each phase is measured separately before the mixing joint by two identical temperature sensors (Model: Pt100 Industrial Sensor Probe, Class B). The inlet air-line is equipped with a service unit, a control valve, a pressure regulator and a restriction valve to attain precise control of the injected air. To follow the pressure variation along the axial direction of the channel, 8 pressure sensors are installed at different axial locations. The model of the pressure sensors is Cerabar T PMC131, which has a measuring range of -1.0:1.0 bar and an accuracy of 0.5% of the nominal value. The specifications and uncertainties of the measurement instruments of the diverging channel test-rig are listed in Table 3.1.

The flow channel has an upstream rectangular cross-section of 40 x 44 mm and a downstream rectangular cross-section of 100 x 44 mm, leading to a ratio of 1.45 for the hydraulic diameters. Based on the present flow channel dimensions, the upstream and downstream hydraulic diameters are $d_{hu} = 42$ mm and $d_{hd} = 61$ mm, respectively. The diffuser is designed with an increasing opening angle in the flow direction. In this way, it is possible to observe flow separation and large recirculation zones, leading to bubble trapping and large gas pockets. The diffuser has an initial half-included angle of 6° with an upper contour corresponding to the function $x = 13.5y - y^2/10 - 230$ (x: axial direction, y: vertical direction, and the origin is at the center of the diffuser inlet as indicated in Figure 3.1b), following which the half-included angle is progressively increased up to 16°.

The channel is mounted in a horizontal position. In this manner, the impact of the Coriolis force acting in radial pumps as a lateral force on the flow within the impeller passages can be, to some extent, mimicked here by gravity. This would not be the case for a vertical orientation. A long inlet pipe was installed before the diverging channel in order to ensure fully-developed flow conditions. Note that this feature proved to be of high importance; preliminary studies involving a shorter inlet pipe have led to completely different observations regarding gas accumulation in the diffuser, as discussed later in Section 4.2.1. The lengths of the straight inlet and outlet parts before and after the diverging part are kept constant at $L_1 = 34d_{hu}$ and $L_2 = 15.5d_{hu}$, respectively.

3.1.2 Particle Image Velocimetry (PIV) measurements

The velocity field for single-phase flows of water has been measured at the middle vertical plane of the channel by using a Particle Image Velocimetry (PIV) system, as shown in Figure 3.2. An overview of the main components and the working principle of the PIV is given in Appendix A. An Imager pro HS 4M CCD camera with a resolution of 2016 x 2016 pixels has been used to acquire the flow images. To illuminate the particles, a high-speed Nd:YLF laser (Litron) with a wavelength of 527 nm and an energy of 4.45 mJ/pulse has been employed.

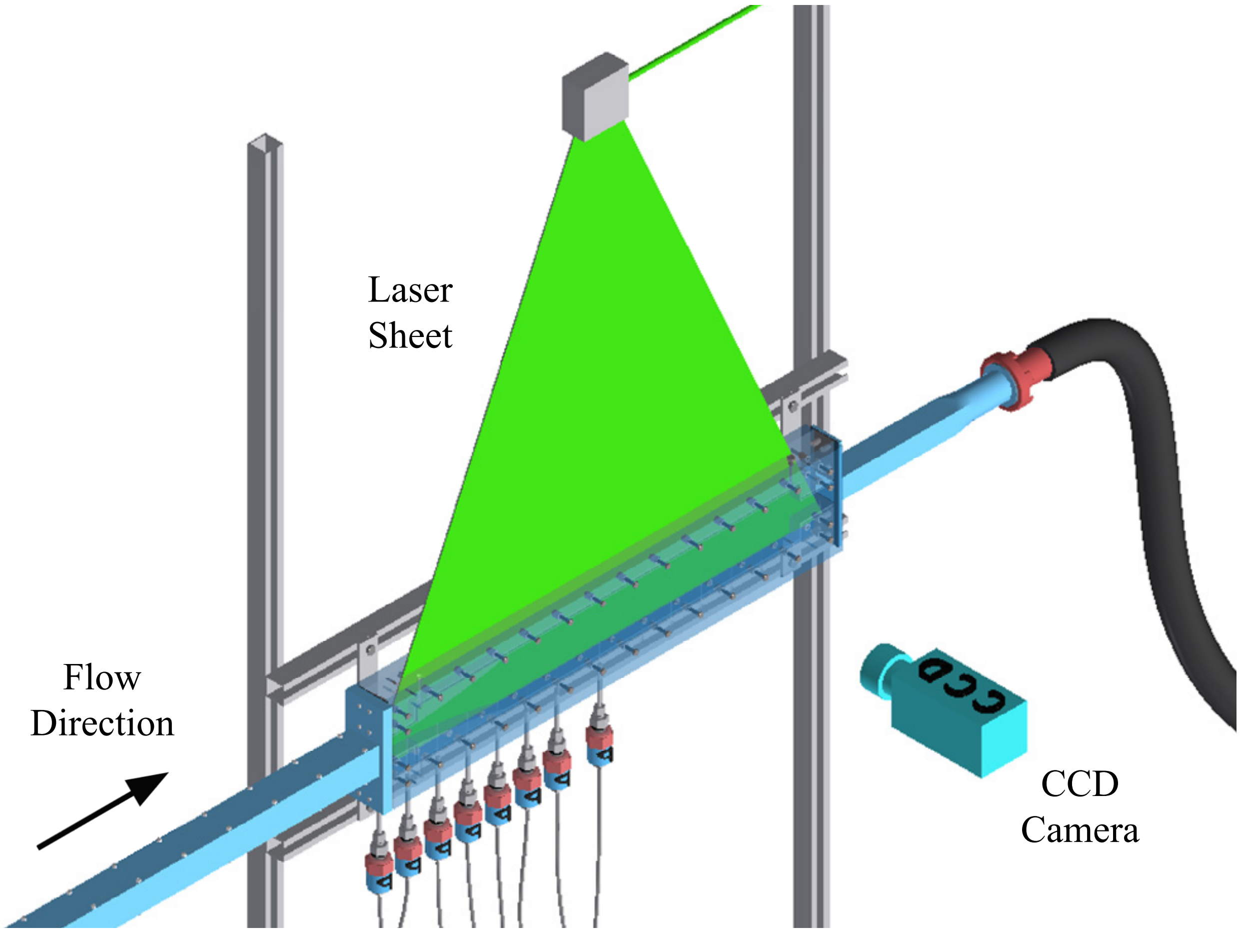

Figure 3.2: Illustration of the PIV measurements.

3.1.3 Gas accumulation measurement by shadowgraphy

To investigate gas accumulations due to flow separation in two-phase flows, shadowgraphy images have been obtained using the same high-speed camera as employed for the PIV measurements. The background of the test section has been illuminated by two continuous tungsten lamps (Model: COOLH dedocool, 24V/250W), as shown in Figure 3.3. In this way, the interface between the water and air appears dark and the accumulated gas could be clearly observed.

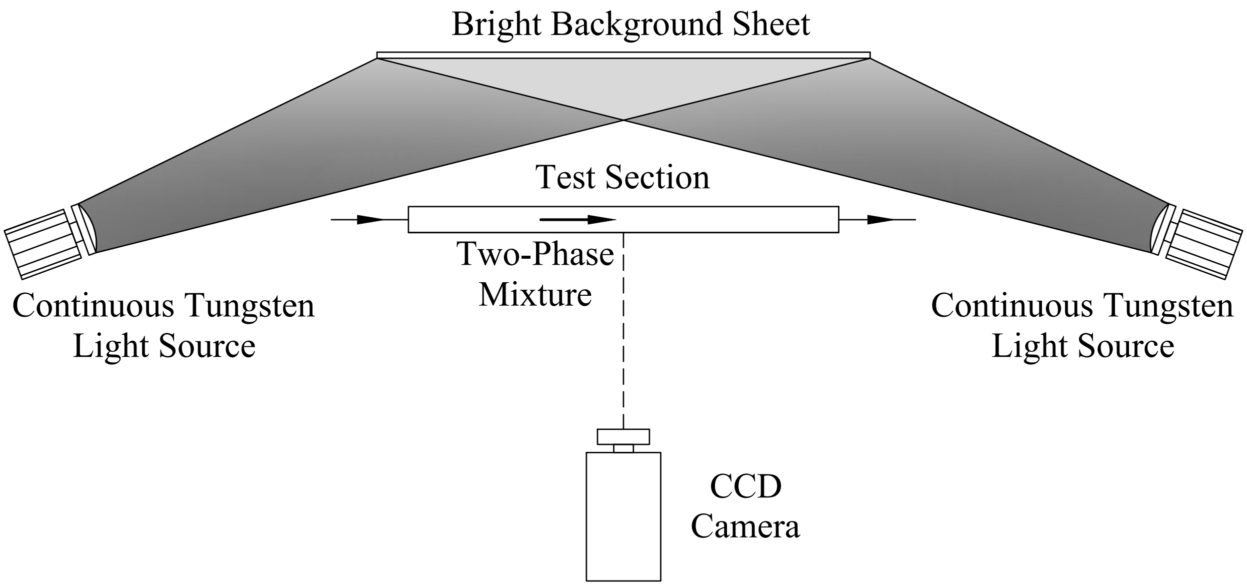

Figure 3.3: Shadowgraphy set-up for recording the gas accumulation.

3.1.4 Boundary conditions measurements

Inlet velocity measurements by Laser Doppler Anemometry (LDA)

Furthermore, to simplify future numerical simulations, the inlet boundary conditions, i.e. flow velocities, have been recorded at the section where the diverging part starts, as shown in Figure 3.4a. The velocity has been measured by using a Laser Doppler Anemometry (LDA) system, for a grid of 99 points as shown in Figure 3.4c. A brief overview of the working principle of the Laser Doppler Anemometry (LDA) system is given in Appendix B. The actual location of each measurement point of the LDA has been obtained after accounting for the refraction of the laser beams through the acrylic glass and water. This calculation and details about the index of refraction are also elaborated in Appendix B. As tracer particles for PIV and LDA measurements, VESTOSINT 1164 white nylon particles, with a mean diameter of 50 µm and a density of approximately 1060 kg/m^3 have been used.

Bubble size distribution measurement by shadowgraphy

Additionally, the bubble size distributions (BSD) have been determined by using shadowgraphy measurements considering a small sample window, at the beginning of the diverging part of the channel. The shadowgraphy set-up and the considered window are illustrated in Figure 3.4a and 3.4b, respectively. As shown, a background LED (light-emitting diodes) light source has been used to make the bubble boundaries clearly observable. Similarly, the bubble size distribution is significant for the force calculations in many models, such as the drag force. Therefore, the BSD data are helpful for validating and developing two-phase models.

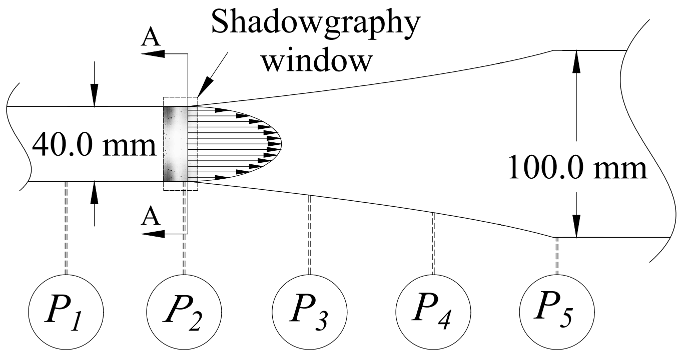

(a) Location of measurements of the boundary conditions.

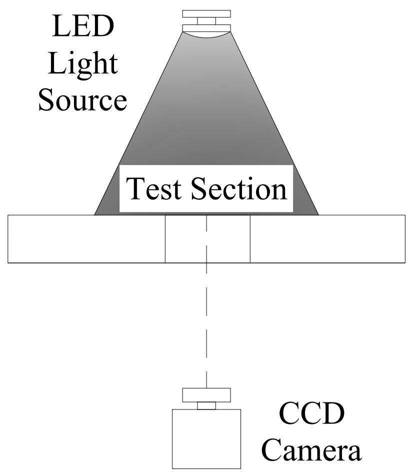

(b) Shadowgraphy set-up for BSD measurements in the diverging channel.

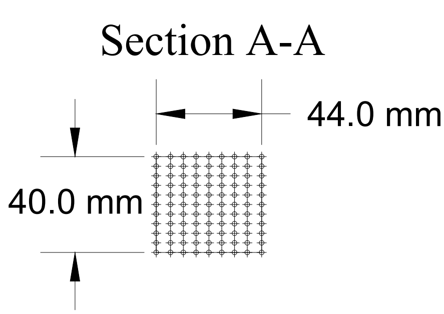

(c) Grid points for the inlet velocity measurements in the cross-section.

Figure 3.4: Illustration of measurements of the boundary conditions.

3.2 Centrifugal pump: Dynamic test-rig

Figure 3.5 shows the details of the pump employed in the present work. As shown in Figure 3.5b, the whole pump casing and part of the suction pipe were made of transparent acrylic glass to allow high-quality visualization of the flow behavior and regimes. To maximal optical accessibility, the impellers were designed with 6 non-twisted blades as shown in Figure 3.5a. The locations where the flow regimes and bubble size distributions have been recorded and analyzed are also shown by dashed lines. Four LED lamps have been installed peripherally around the pump to illuminate the flow for recording the flow regimes.

3.2.1 Impeller details

The two impellers are geometrically identical as shown in Figure 3.6a and 3.6b. When the semi-open impeller is used, a front shroud, exactly similar to that glued on the blades of the closed impeller, is fixed on the pump body, to provide similar flow passages in each case. The tip clearance gap of the semi-open impeller can be changed by adjusting shaft rings placed behind the impeller as shown in Figure 3.6b. A rotational speed of 650 min^{-1} has been kept for all experiments, to avoid cavitation and strong system vibrations that occurred at higher rotational speeds, which could destroy the acrylic components. The corresponding specific speed value is approximately $n_q = 21\ \text{min}^{-1}$, calculated by Equation 1.8.

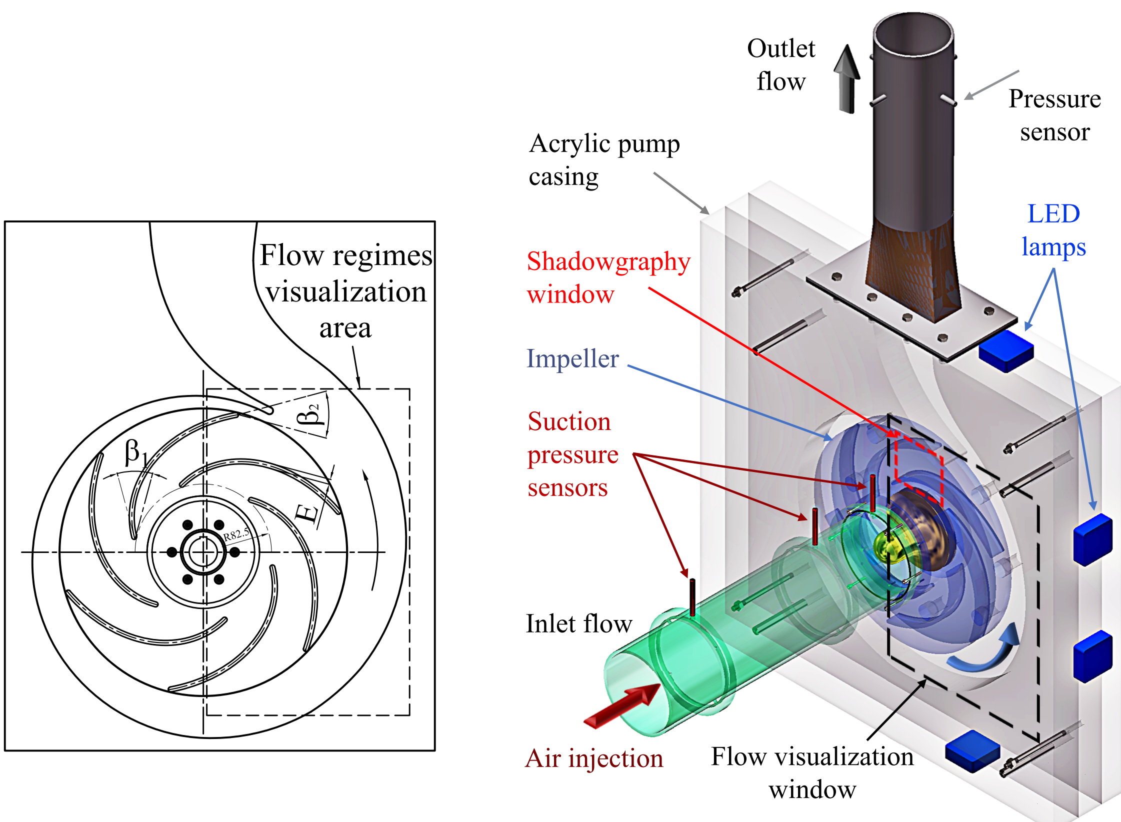

(a) Pump front view

(b) Pump casing

Figure 3.5: Pump details.

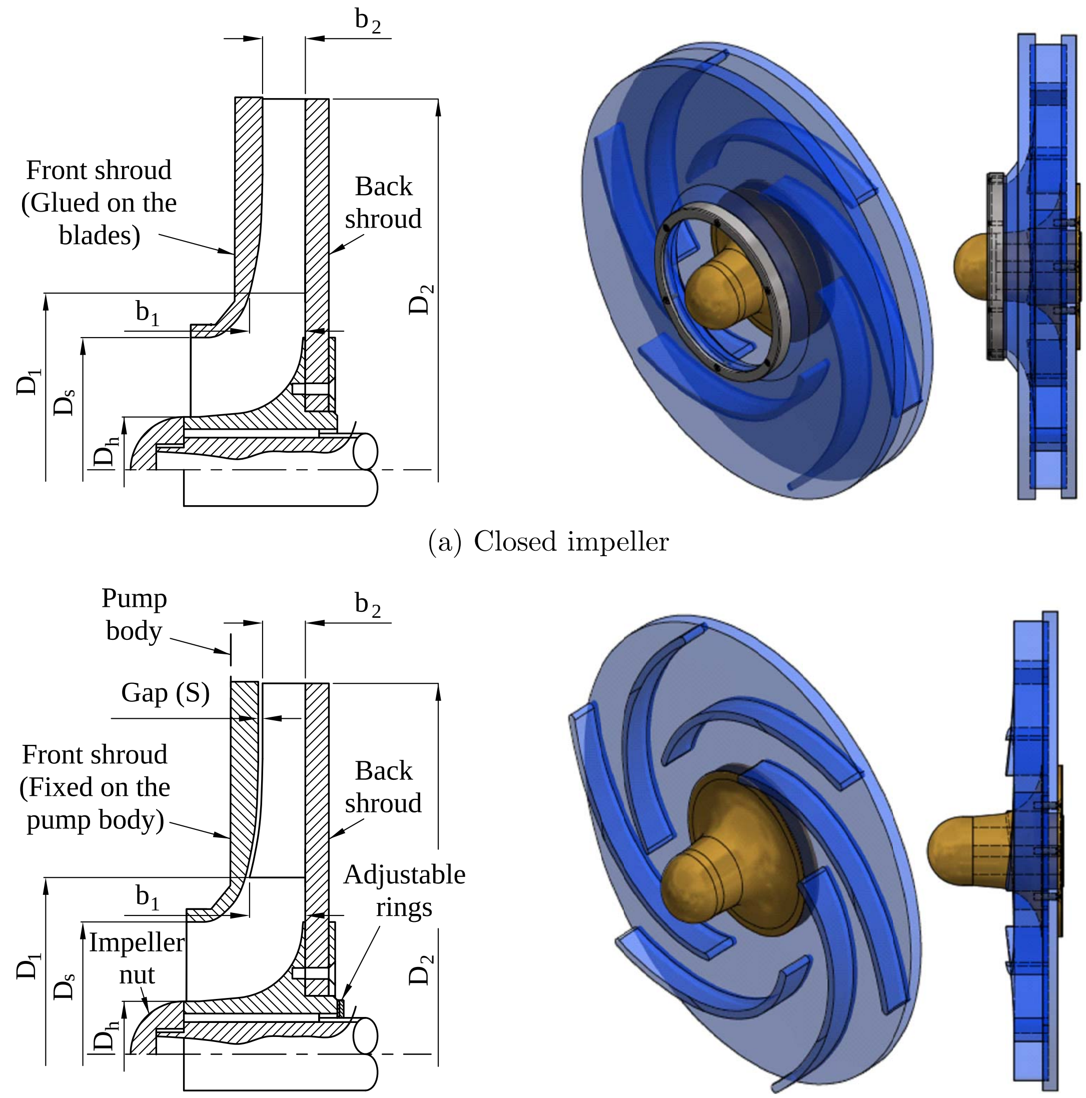

(a) Closed impeller

(b) Semi-open impeller

Figure 3.6: Geometrical details of the impellers.

3.2.2 Inducer details

The geometrical details of the inducer used with the semi-open impeller are shown in Figure 3.7. All important geometrical specifications of the employed inducer are given in Figure 3.7 and Table 3.2. In Figure 3.7, a 3D view of inducer, two sectional views and two developed views of the linear cascade are presented, showing all geometrical specifications of the inducer. Corresponding values of each geometrical parameters are listed in Table 3.2. Some parameters are given as a function of the suction pipe diameter (D_s). The three-bladed inducer can be easily installed ahead of the impeller by replacing the impeller nut as shown in Figure 3.8. The inducer has a high efficiency within the flow range of $Q/Q_{opt} = 0.6 - 0.8$, where Q_{opt} is the best efficiency flow of the impeller.

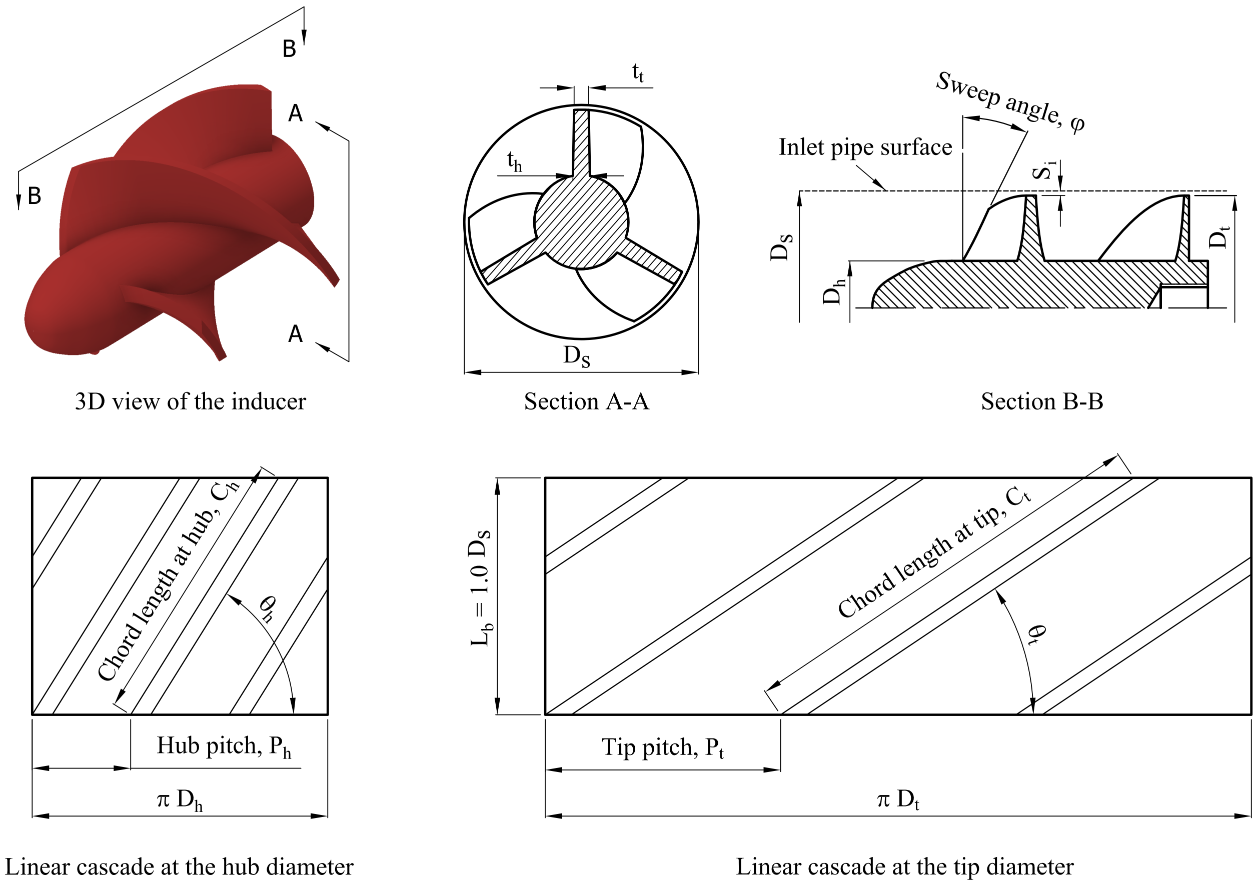

Figure 3.7: Inducer geometrical details.

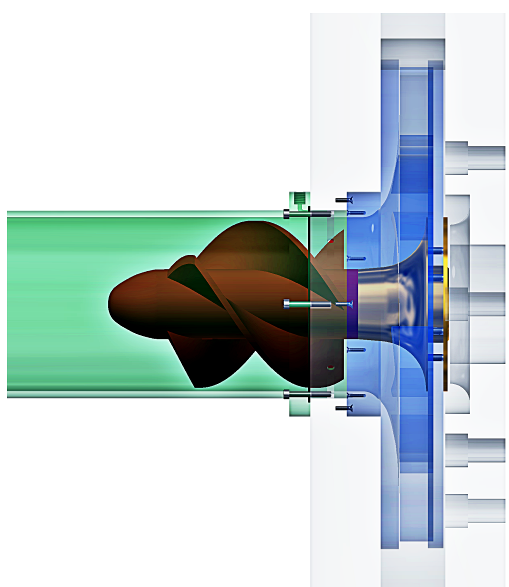

Figure 3.8: Installation of the inducer ahead of the pump impeller.

Table 3.2: Impeller geometrical dimensions.

Parameter	Symbol	Value
Impeller outer to inlet diameter ratio	D_2/D_1	2.1
Blade thickness	E	6 mm
Blade inlet angle	β_1	24°
Blade outlet angle	β_2	24°
Inducer hub to tip diameter ratio	D_h/D_t	41.85 %
Inducer hub solidity	$\sigma_h = C_h/P_h$	2.836
Inducer tip solidity	$\sigma_t = C_t/P_t$	1.807
Inducer area solidity	σ_a	23.326 %
Inducer hub blade angle	θ_h	34°
Inducer tip blade angle	θ_t	58°
Inducer sweep angle	φ	29.4°
Inducer hub blade thickness	t_h/D_s	7.26 %
Inducer tip blade thickness	t_t/D_s	6.22 %
Inducer blade axial length	L_b/D_s	1.0
Standard tip clearance gap to blade outlet width	S/b_2	2.5%
Increased tip clearance gap to blade outlet width	S/b_2	5%
Inducer tip clearance gap to blade outlet width	S_i/b_2	12.5% mm

3.2.3 Test-rig details

Figure 3.9 shows a detailed schematic sketch for the experimental test-rig. A water tank with a total internal capacity of 6.3 m^3 is employed to provide a closed-loop pump operation. The tank has an air-release pipe at the top to allow the air phase to go out of the tank. The returning mixture is injected over the water free surface in the tank, which is 3 m high above the suction-line, ensuring no air carry-under. Additionally, the pure water flow can be extra checked through a transparent part of the suction line, directly before the pump inlet as shown in Figure 3.5b. For maintenance purposes, a gate valve is installed on the suction line just after the water tank. This valve is always set fully-open during the measurements. The water flow rate is measured separately by an electro-magnetic flow-meter (Model: Endress+Hauser Promag 30F, with an accuracy of ±0.5% RD). A motorized gate valve is installed on the discharge line to precisely control the desired water flow rate.

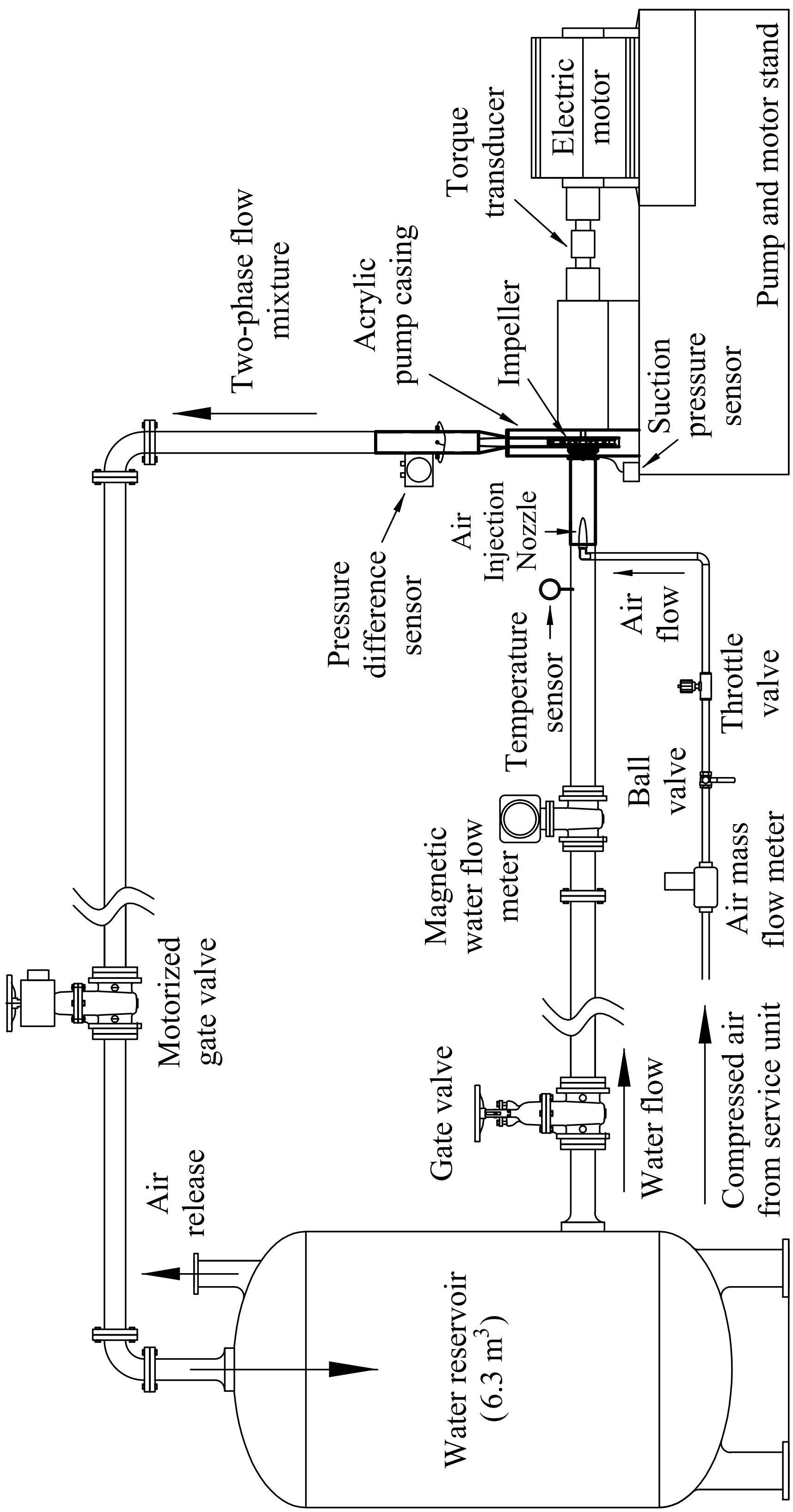

Figure 3.9: Schematic sketch of the experimental set-up.

The air phase is supplied from a service unit to the air-line, which is equipped with a mass flow-meter (Model: Bronkhorst F-113AC-HD-55-V, with an accuracy of ±0.5% RD plus ±0.1% FS). Additionally, an on/off ball valve and a throttle (restriction) valve are installed on the air-line to attain accurate control of the inlet air flow rate. The air is injected in the suction line of the pump through a gas distribution nozzle made of pure borosilicate glass. The static pressure difference across the pump is measured by a differential pressure sensor (Model: Deltabar M PMD55, with a measuring range of $-3:+3$ bar and a reference accuracy of 0.1%). Additionally, the suction pressure is measured explicitly by an absolute pressure sensor (Model: Sensotec Z, with an accuracy of ±0.25% FS) to calculate the air volume flow rate and the air volume fraction at the pump inlet. The temperature of the flow is measured close to the air injection point by a temperature sensor (Model: Pt100 Industrial Sensor Probe, Class B, with a maximum absolute error of ±0.3 K). The pump is driven through a variable-speed electric motor (5.7 kW, max. rpm = 3000). The rotational speed is measured by an analog tachometer and set through a frequency controller. To obtain the shaft power and the pump efficiency, a torque transducer (Model: HBM T1, with an accuracy of ±0.4% FS) is installed on the motor shaft. The model specifications and the uncertainties of the measurement instruments of the centrifugal pump test-rig are listed in Table 3.3. For the pump measurements, uncertainty analysis has been done using the method of sequential perturbation described by Moffat [104], and is shown in Appendix C.

Table 3.3: Specifications and uncertainties of measurement devices of the pump test-rig.

Device	Model	Uncertainty
Water volume flow meter	Endress+Hauser Promag 30F	± 0.5% RD
Air mass flow meter	Bronkhorst F-113AC-HD-55-V	±0.5% RD plus ± 0.1% FS
Differential pressure sensor	Deltabar M PMD55 ($-3:+3$ bar)	± 0.1% FS
Suction pressure sensor	Sensotec Z	± 0.25% FS
Suction temperature sensor	Pt100 Sensor Probe, Class B	± 0.3 K (max. absolute error)
Torque transducer	HBM T1	± 0.4% FS
Analog tachometer	TDP 0.2 LT - 4	± 1% RD

3.2.4 Bubble size distribution measured by shadowgraphy

The bubble size distributions in the pump have been also determined by using shadowgraphy measurements as presented in Figure 3.10a. The LED light source has been installed behind the pump opposite to the camera. In this way, the interface between the water phase and the air bubbles appears dark, so that bubble size can be clearly determined. The shadowgraphy images have been obtained by using the same high-speed camera as employed for the flow regimes measurements. A specific window in the impeller channels has been selected and considered as a representative area for the BSD. The location of the window, where the bubbles have been observed is shown in Figure 3.10b. The bubbles moving through the area marked by the red border in Figure 3.10b have been then masked and analyzed.

In the next chapter, the results of the measurements using the diverging channel (Section 3.1) are described in detail.

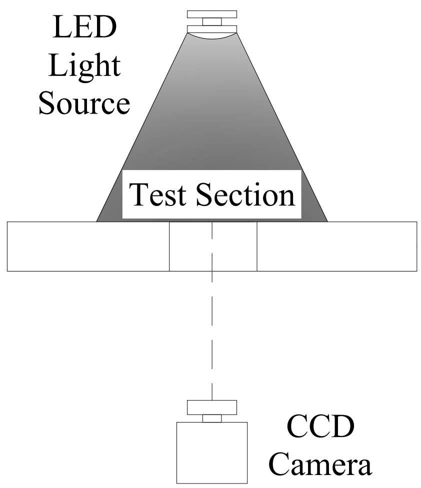

(a) Shadowgraphy set-up.

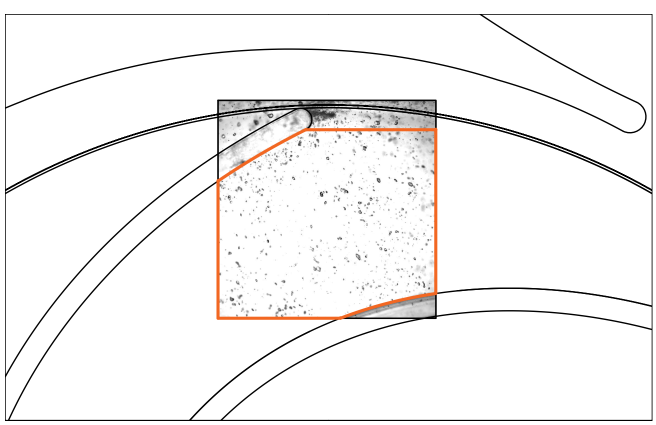

(b) Shadowgraphy window.

Figure 3.10: Explanation of the shadowgraphy measurements for the bubble size distribution in the pump test-rig.

Chapter 4

Diverging channel experiments: Results and discussions

4.1 Introduction

As discussed in the abstract section and Chapter 1, one of the main objectives of this dissertation is to investigate the phenomenon of gas accumulation in two-phase flows and to develop a freely accessible, detailed experimental database, which can be directly used to validate CFD models. In this chapter, the experimental results of the diverging channel (static) test-rig, are described in detail. The chapter begins with some preliminary experiments, discussing the effect of the inlet pipe on the flow behaviour in the channel, followed by final experiments done after modifying the test-rig. Then, different cases of two-phase flow experiments are considered, discussing in details the physical mechanisms leading to the gas accumulation in the flow. Additionally, the inlet boundary conditions of sample cases are given in the last section of the chapter. Part of this chapter is based on a publication in Experimental Thermal and Fluid Science [105].

4.2 Single-phase velocity measurements

4.2.1 Preliminary experiments

In the preliminary experiments, a short inlet pipe (500 mm) was installed before the diverging section of the flow channel. The single-phase velocity field was measured by the Laser Doppler Anemometry (LDA) system. Using automatic traversing, the vertical and horizontal velocity components were measured on a grid of 2827 points at the middle plane of the channel, as shown in Figure 4.1. The horizontal and the vertical grid spacing are $\Delta x = 5$ mm and $\Delta y = 3$ mm, respectively. The initial test was done at $\mathrm{Re}_w = 78,330$, defined as:

$$\mathrm{Re}_w = \frac{\rho_w \; u_w \; d_{hu}}{\mu_w} \tag{4.1}$$

where ρ_w is the water density, u_w is the average water velocity in the inlet pipe, and μ_w is the water dynamic viscosity. The resulting velocity field and the corresponding velocity fluctuations are shown in Figure 4.2

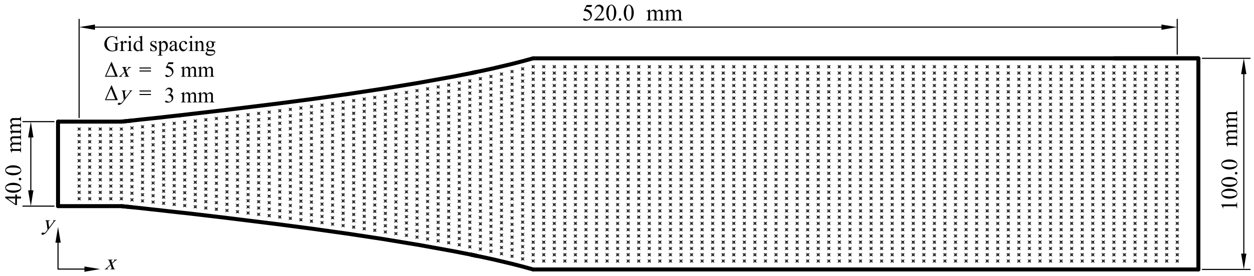

Figure 4.1: Grid points of the preliminary LDA experiments.

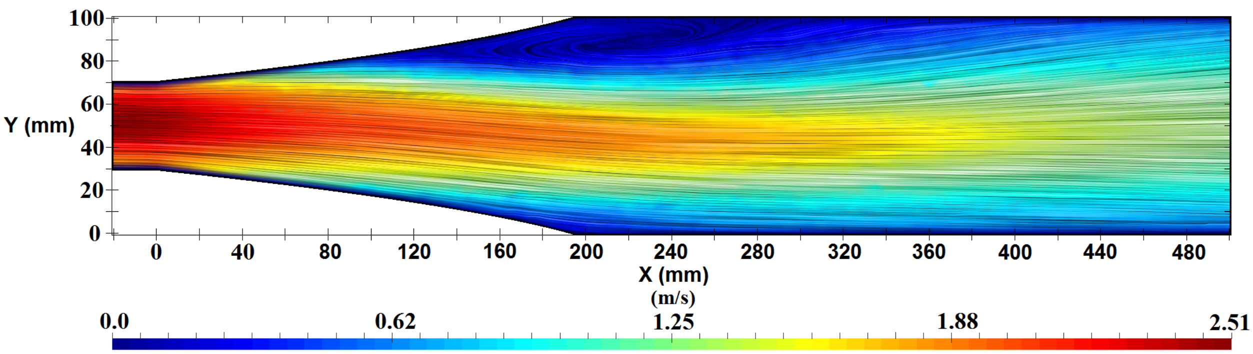

(a) Velocity field with short inlet pipe

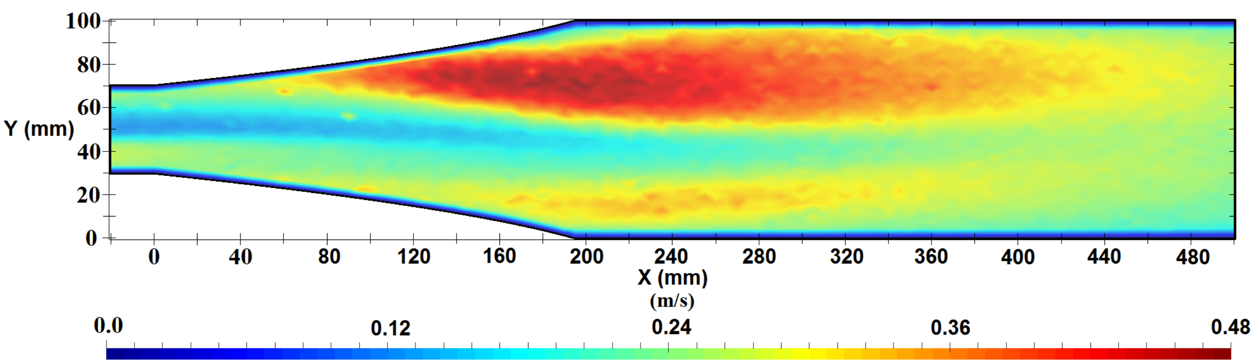

(b) Velocity fluctuations with short inlet pipe

Figure 4.2: Preliminary LDA velocity measurements at Re_w = 78,330, showing (a) average velocity field, (b) the corresponding velocity fluctuations.

As shown in Figure 4.2 the initial velocity measurements done with the short inlet pipe exhibits a large separation on the upper side of the diffuser. Further, when the water pump is restarted, the separation zone can alternatively appear on the upper or the lower side of the diffuser. This effect occurred due to the insufficient length of the inlet pipe before the diverging part of the channel. In this case, the gas accumulation behaviour in the subsequent two-phase flow experiments was found to be strongly unstable and very dependent on the location of the flow separation. Therefore, a very long inlet pipe (34 d_{hu}) was later manufactured and installed before the test section in order to ensure fully-developed flow conditions before the test section [106, 107]. Accordingly, the influence of the inlet on the flow behaviour in the diffuser could be eliminated, as discussed in the following section.

4.2.2 Improved experiments

After installing the long inlet pipe, it was found that the flow behaviour in the diffuser does not change, when the system is restarted, showing always two separation zones with comparable sizes on the upper and lower sides of the diffuser. Additionally, the gas accumulation behaviour was found to be stable in the corresponding two-phase flow experiments, as discussed later in Section 4.3.

Now, the velocity field for single-phase flow of water was measured again at the middle vertical plane of the channel by using the Particle Image Velocimetry (PIV) system. Five different Reynolds numbers were considered for the single-phase flow experiments in the range of Re_w = 50,130:87,730. Similar values of water Reynolds number were used later for the water phase in the two-phase flow measurements. This range of Re_w was found to be suitable for investigating gas accumulation in the test-rig.

Figure 4.3 shows two arbitrarily selected instantaneous velocity fields, the time-averaged velocity field, and the associated velocity fluctuations at Re_w= 68,930. As seen from the instantaneous fields, the flow is highly turbulent and flow separation occurs, creating two large recirculation zones on both sides of the divergent part. Along the channel horizontal axis, a highly fluctuating turbulent jet can be seen, starting between the two recirculation zones.

The average velocity field and the velocity fluctuation magnitude shown in Figure 4.3c and 4.3d, respectively, were obtained by using systematically 5000 instantaneous velocity fields recorded with a frequency of 1000 Hz. Tests have shown that this procedure is sufficient to get converged results for the considered range of water Reynolds number. As shown in Figure 4.3c, the average velocity field shows smooth and nearly symmetric streamlines; however, it must be kept in mind that this flow is very unstable and that the average flow appearing in Figure 4.3c is not a real, instantaneous solution. As expected, the maximum velocity fluctuations occur close to the boundaries of the recirculation zones, as presented in Figure 4.3d.

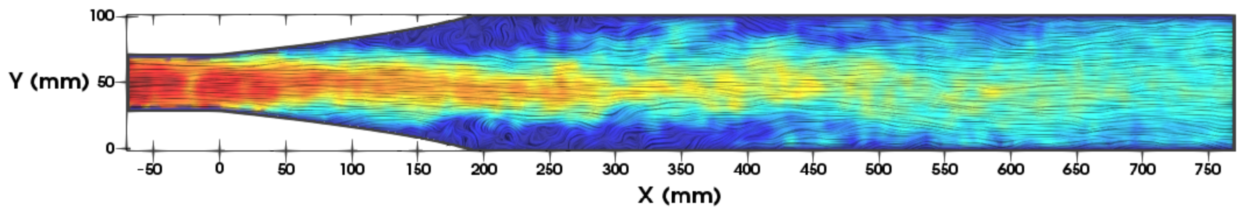

(a) Instantaneous velocity field (sample 1)

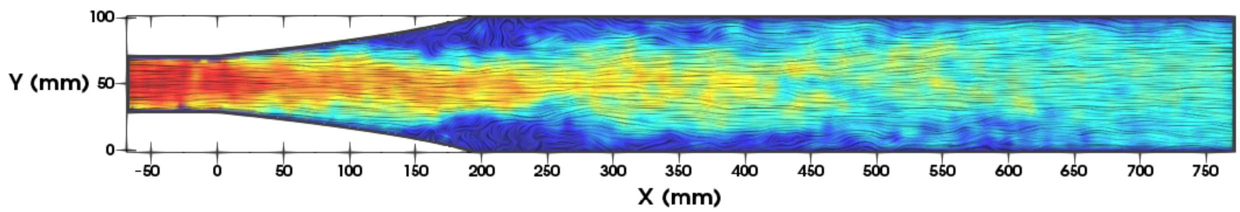

(b) Instantaneous velocity field (sample 2)

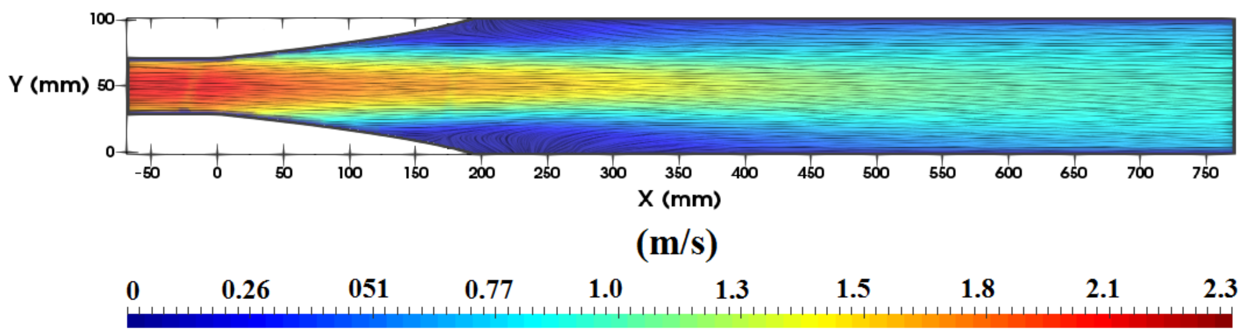

(c) Average velocity field

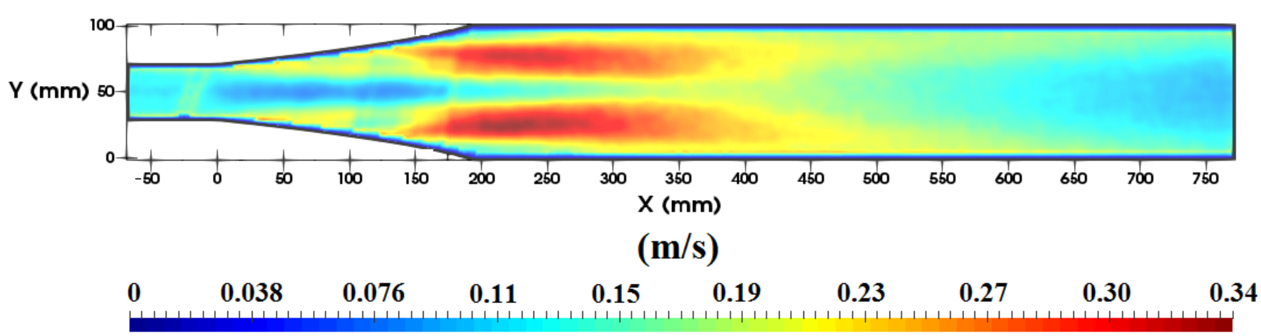

(d) Velocity fluctuations

Figure 4.3: Velocity measurements at $\mathrm{Re}_w = 68{,}930$, showing (a) and (b) two different instantaneous velocity fields, (c) the time-averaged velocity field and (d) the velocity fluctuations.

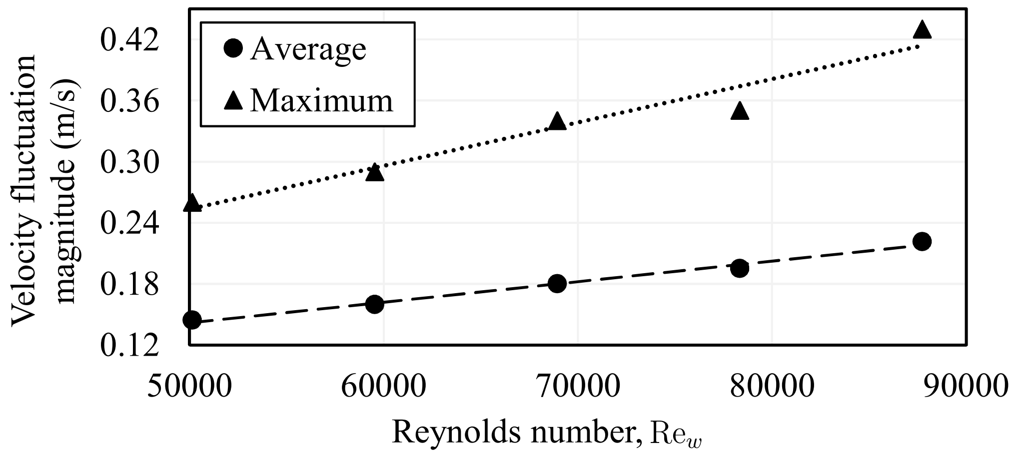

Figure 4.4: Velocity fluctuation as a function of water Reynolds number.

The overall shape of the single-phase velocity field stays qualitatively similar to the fields shown in Figure 4.3 for the whole range of Reynolds numbers. Nevertheless, the size of the recirculation zones, as well as the velocity fluctuations, increase monotonically when increasing the Reynolds number, as shown in Figure 4.4.

4.3 High-speed shadowgraphy recording of two-phase flow

Table 4.1 shows the details of the 25 different experimental two-phase flow cases considered in the investigations, where Q_w, Q_a, Re_w, Re_a, and ε represent the water flow rate, the air flow rate, the superficial water Reynolds number, the superficial air Reynolds number, and the gas volume fraction, respectively, with,

$$\mathrm{Re}_a = \frac{\rho_a \; u_a \; d_{hu}}{\mu_a} \tag{4.2}$$

$$\varepsilon = \frac{Q_a}{Q_a \; + \; Q_w} \tag{4.3}$$

In these equations ρ_a is the air density, u_a is the superficial air velocity in the inlet pipe, μ_a is the air dynamic viscosity. Here, Q_w, Q_a, ε, and all the fluid properties are defined based on the flow conditions at the beginning of the inlet pipe. As shown in Table 4.1, the lowest gas volume fraction considered is 0.05% (Case 21), while, the highest value is 0.527% (Case 5).

Table 4.1: Details of the experimental two-phase flow cases considered.

Case#	Q_w (m^3/h)	Q_a (L/h)	Re_w	Re_a	ε (%)
1	8	7.07	50,130	3.10	0.088
2	8	14.14	50,130	6.17	0.176
3	8	21.21	50,130	9.25	0.264
4	8	28.28	50,130	12.34	0.352
5	8	42.42	50,130	18.51	0.527
6	9.5	7.07	59,530	3.10	0.074
7	9.5	14.14	59,530	6.17	0.148
8	9.5	21.21	59,530	9.25	0.223
9	9.5	28.28	59,530	12.34	0.297
10	9.5	42.42	59,530	18.51	0.444
11	11	7.07	68,930	3.10	0.064
12	11	14.14	68,930	6.17	0.128
13	11	21.21	68,930	9.25	0.192
14	11	28.28	68,930	12.34	0.256
15	11	42.42	68,930	18.51	0.384
16	12.5	7.07	78,330	3.10	0.056
17	12.5	14.14	78,330	6.17	0.113
18	12.5	21.21	78,330	9.25	0.169
19	12.5	28.28	78,330	12.34	0.225
20	12.5	42.42	78,330	18.51	0.338
21	14	7.07	87,730	3.10	0.050
22	14	14.14	87,730	6.17	0.101
23	14	21.21	87,730	9.25	0.151
24	14	28.28	87,730	12.34	0.201
25	14	42.42	87,730	18.51	0.302

Figures 4.5, 4.6, 4.7, 4.8, and 4.9 display sample instantaneous images for the accumulated gas for different flow conditions. High-speed videos have been also recorded for all cases, and are available in the supplementary material of the thesis. Due to the flow separation, a low-pressure recirculation zone is created, particularly at the upper side of the channel, which sucks and confines the gas bubbles. Even for very small air flows, a large cavity can accumulate at the top of the channel due to the rapid bubble trapping, see for example Case 1 in Figure 4.5. For high gas contents, i.e., $\mathrm{Re}_a = 18.51$, the accumulated gas pocket grows rapidly and fills up the whole visible length of the channel (see Cases 10, 15, and 20 in Figures 4.6, 4.7, 4.8, respectively).

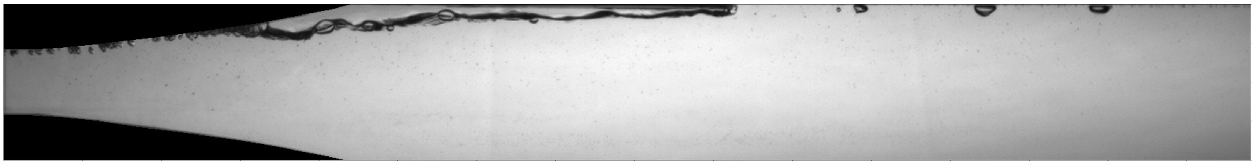

Case 1: Re_w= 50,130, Re_a = 3.1

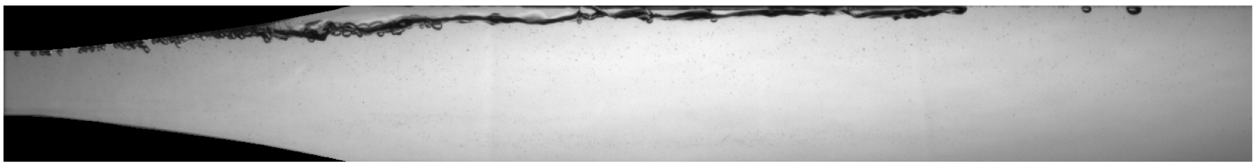

Case 2: Re_w= 50,130, Re_a = 6.17

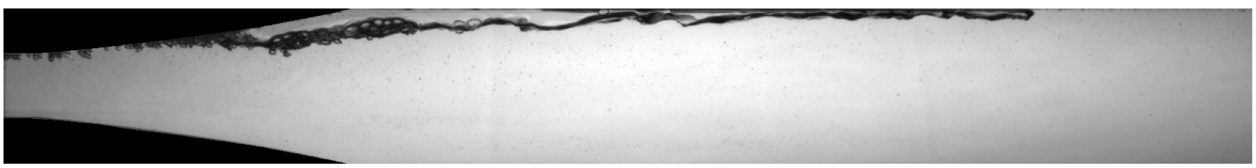

Case 3: Re_w= 50,130, Re_a = 9.25

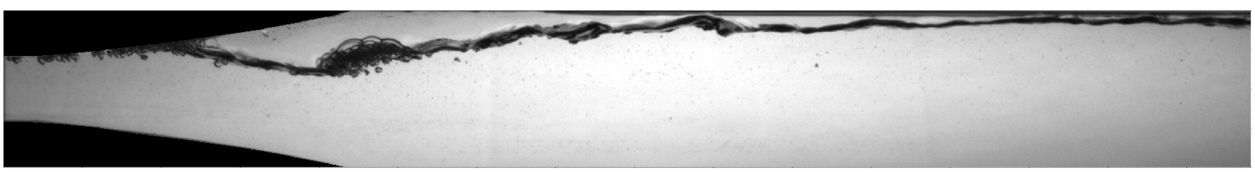

Case 4: Re_w= 50,130, Re_a = 12.34

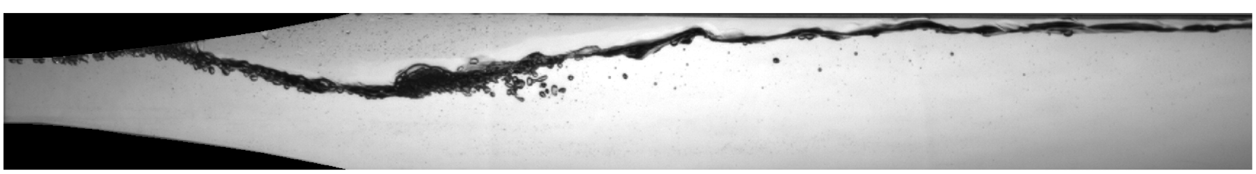

Case 5: Re_w= 50,130, Re_a = 18.51

Figure 4.5: Sample instantaneous images from shadowgraphy recording of the accumulated gas for Re_w= 50130 and different values of Re_a.

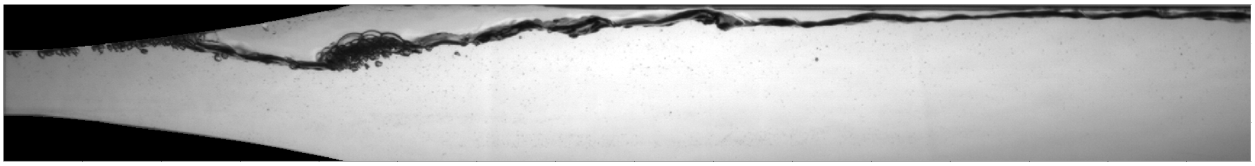

Case 6: Re_w= 59,530, Re_a = 3.1

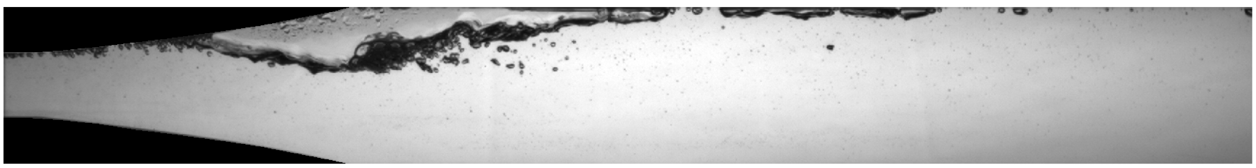

Case 7: Re_w= 59,530, Re_a = 6.17

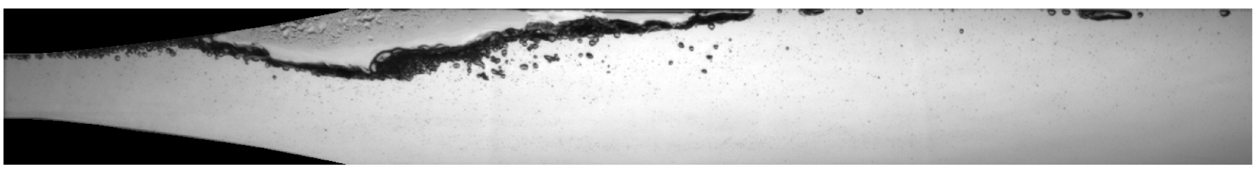

Case 8: Re_w= 59,530, Re_a = 9.25

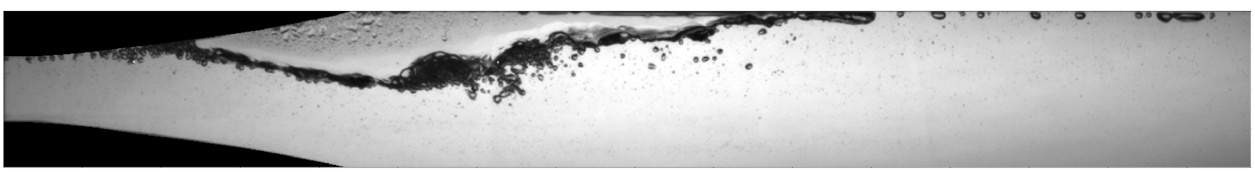

Case 9: Re_w= 59,530, Re_a = 12.34

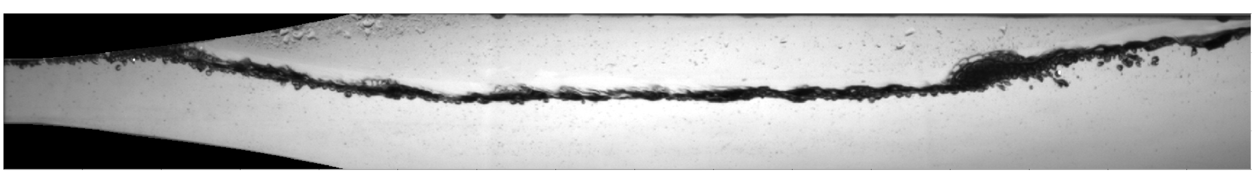

Case 10: Re_w= 59,530, Re_a = 18.51

Figure 4.6: Sample instantaneous images from shadowgraphy recording of the accumulated gas for Re_w= 59530 and different values of Re_a.

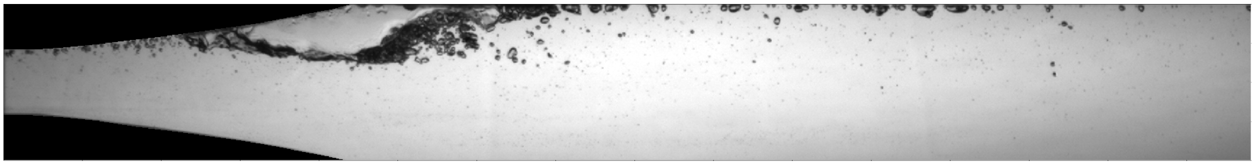

Case 11: Re_w= 68,930, Re_a = 3.1

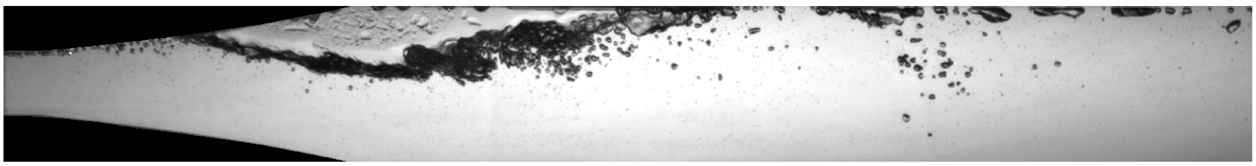

Case 12: Re_w= 68,930, Re_a = 6.17

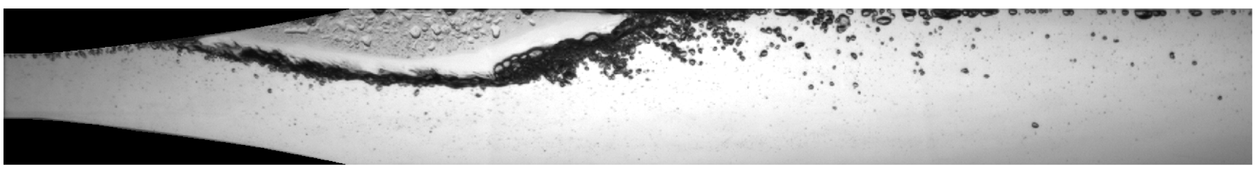

Case 13: Re_w= 68,930, Re_a = 9.25

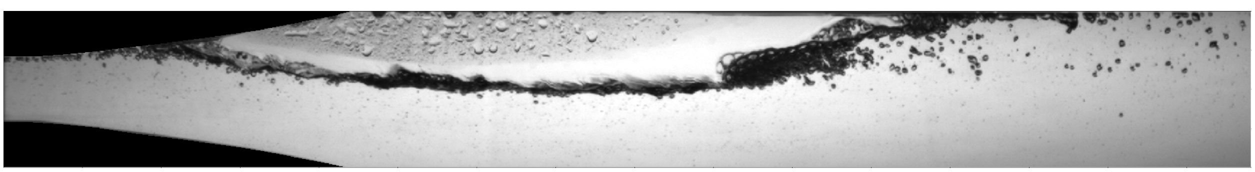

Case 14: Re_w= 68,930, Re_a = 12.34

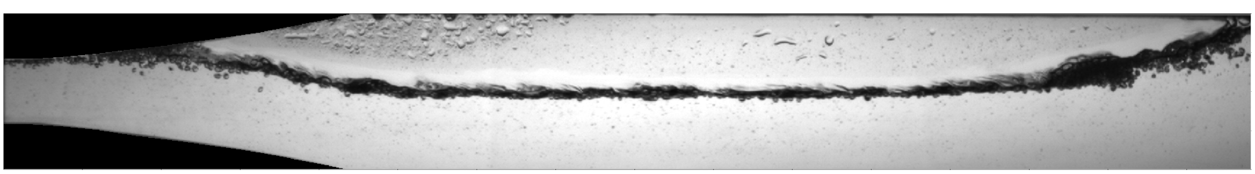

Case 15: Re_w= 68,930, Re_a = 18.51

Figure 4.7: Sample instantaneous images from shadowgraphy recording of the accumulated gas for Re_w= 68930 and different values of Re_a.

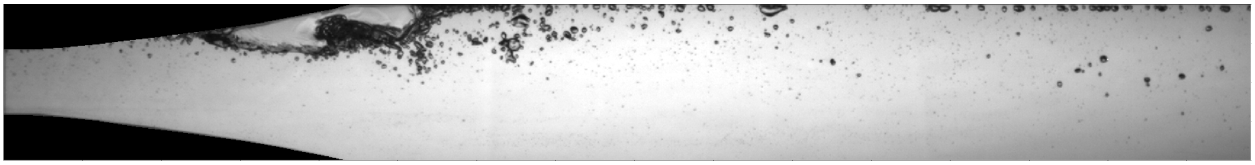

Case 16: Re_w= 78330, Re_a = 3.1

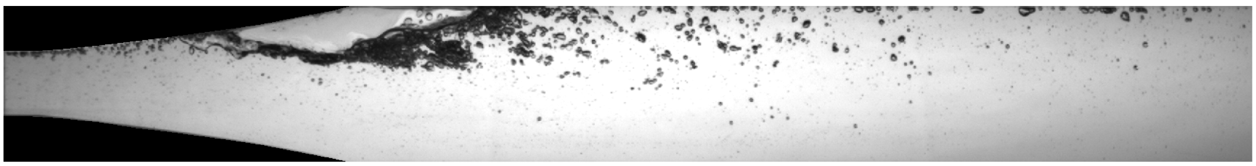

Case 17: Re_w= 78,330, Re_a = 6.17

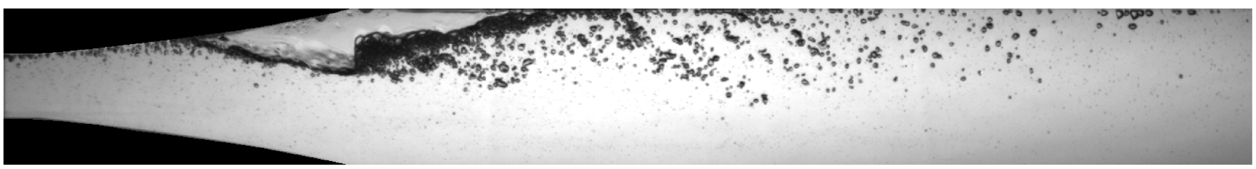

Case 18: Re_w= 78,330, Re_a = 9.25

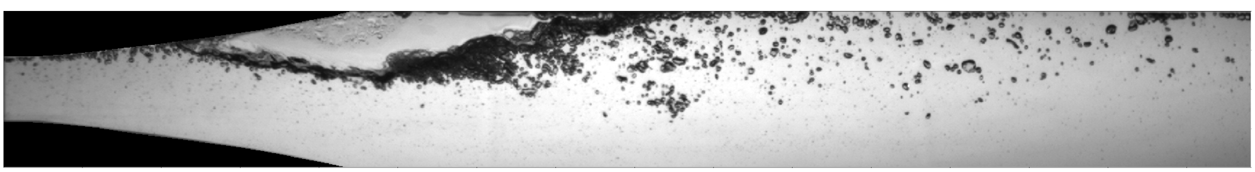

Case 19: Re_w= 78,330, Re_a = 12.34

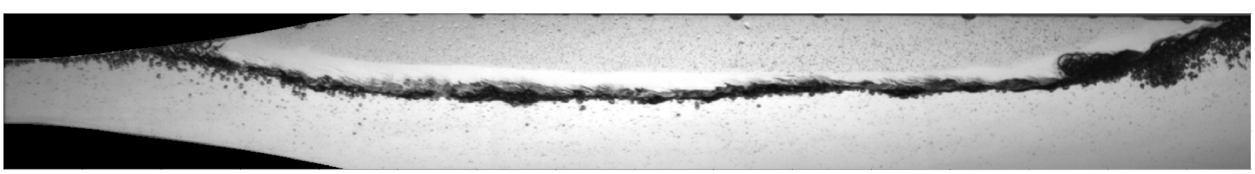

Case 20: Re_w= 78,330, Re_a = 18.51

Figure 4.8: Sample instantaneous images from shadowgraphy recording of the accumulated gas for Re_w= 78330 and different values of Re_a.

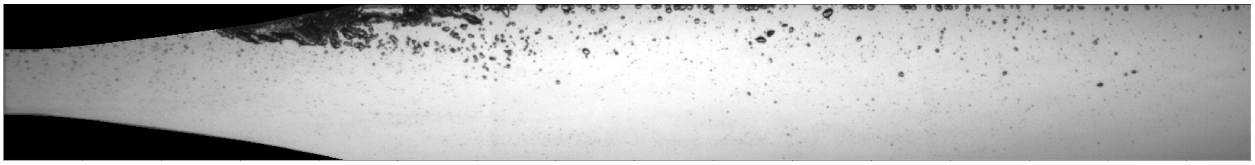

Case 21: Re_w= 87,730, Re_a = 3.1

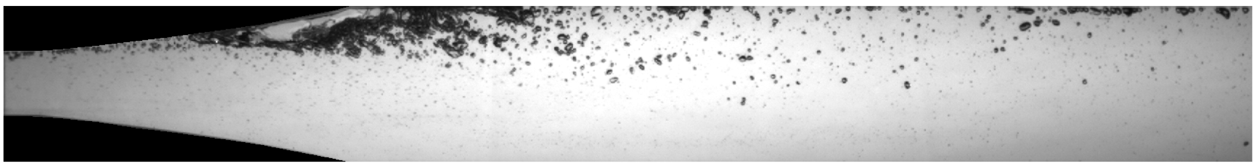

Case 22: Re_w= 87,730, Re_a = 6.17

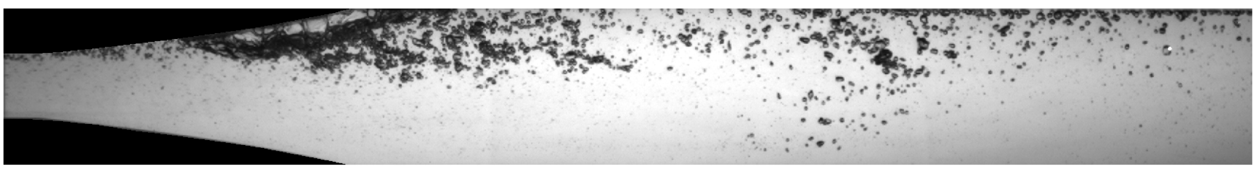

Case 23: Re_w= 87,730, Re_a = 9.25

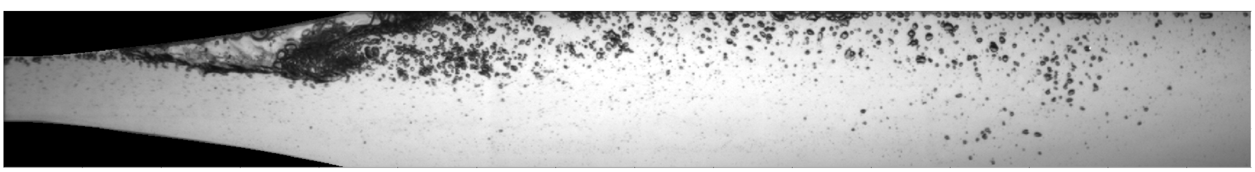

Case 24: Re_w= 87,730, Re_a = 12.34

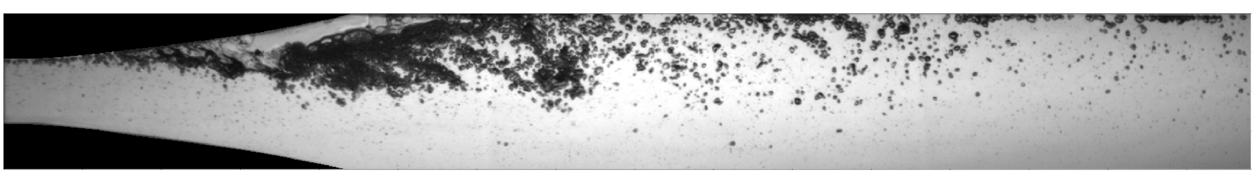

Case 25: Re_w= 87,730, Re_a = 18.51

Figure 4.9: Sample instantaneous images from shadowgraphy recording of the accumulated gas for Re_w= 87730 and different values of Re_a.

In order to quantify the size of the accumulated gas pocket, 1000 images were recorded with a frequency of 50 Hz for each flow case. Afterwards, an averaged image was deduced from those 1000 images, as shown by selected examples in Figure 4.10. This number was finally retained by first checking the results obtained for an increasing number of acquired images, until a clear and converged water-air interface could be seen on the averaged picture. Here, a lower recording frequency was used in order to increase the recording time, as some cavity boundaries were found to be very unstable, particularly for high Reynolds numbers.

The averaged (grayscale) images were then binarized, by setting an intensity threshold based on the brightness spectrum of the images. A value of $I = 710$ cd for the light intensity threshold was found to be suitable to generate clear black-and-white images (meaning that all pixels with $I \geq 710$ cd were changed to white and all pixels with $I < 710$ cd were changed to black). Similarly, selected examples for binarized images, which were used eventually to quantify the accumulated gas size, are shown in Figure 4.11. As shown from the different images, the size and the shape of the accumulated gas strongly depend on the superficial Reynolds number of both phases.

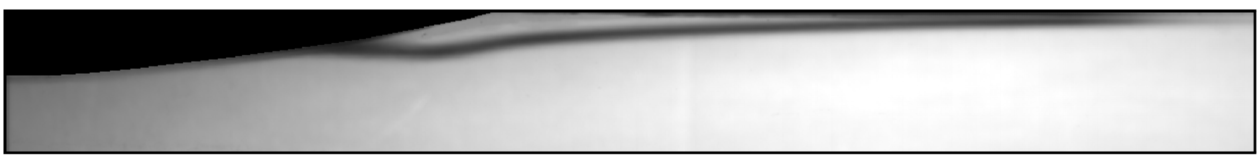

(a) Case 1

(b) Case 2

(c) Case 11

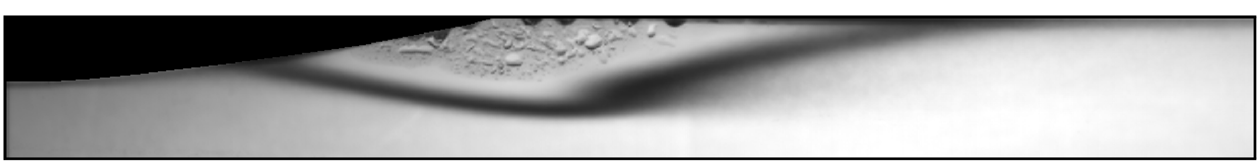

(d) Case 12

Figure 4.10: Processed images for quantifying gas accumulation: Averaged images.

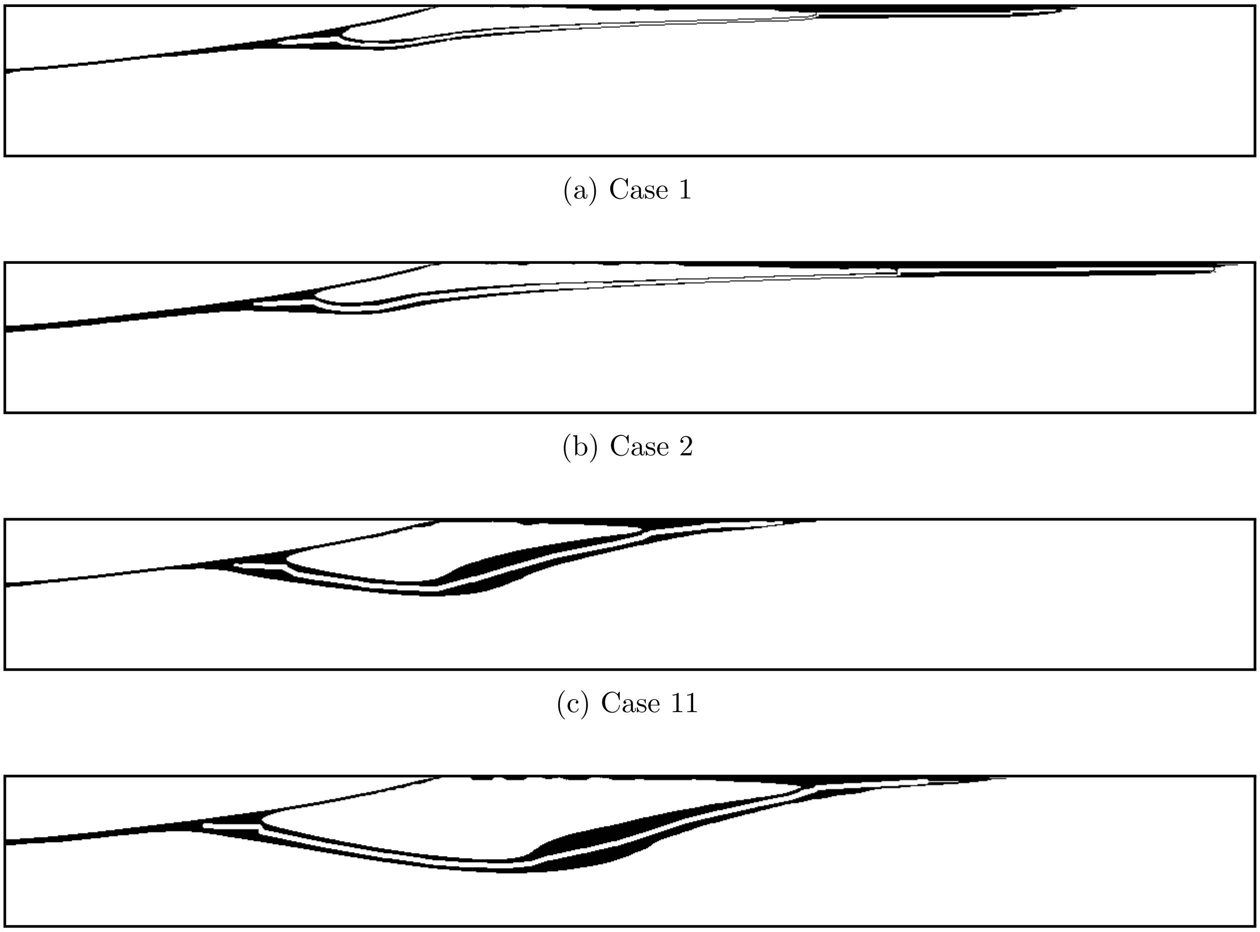

(a) Case 1

(b) Case 2

(c) Case 11

(d) Case 12

Figure 4.11: Processed images for quantifying gas accumulation: Binarized images.

The boundaries of the cavity were defined as the middle line of the water-air interface by using a MATLAB script, which is described in details in Appendix D. The black pixels of the water-air interface, in the binarized images (Figure 4.11), were scanned by the script, and then the middle line was identified. The middle lines calculated by the script are shown as well on the binarized images in Figure 4.11 by thin white lines. In some flow cases, a stratified flow regime was observed, where a thin layer of air is visible throughout the whole length of the observation window (see for instance Case 4 in Figure 4.5). In this case, the end of the gas cavity was defined as the location where the stratified air layer starts showing a constant thickness.

4.4 Size of accumulated gas

Figure 4.12 demonstrates the relation between the accumulated gas size and the superficial air Reynolds number for different superficial water Reynolds numbers. The cavity size is represented as the gas void fraction of the accumulated air in the channel. The gas void fraction is obtained by dividing the cavity volume by the total volume of the channel, calculated from the inlet plane of the diverging section, and assuming a two-dimensional flow structure.

In the whole range of superficial water Reynolds numbers, the higher the superficial air Reynolds number, the larger the accumulated gas pocket becomes. At $\mathrm{Re}_a = 18.51$, an abrupt change in the gas pocket size occurred for $\mathrm{Re}_w = 59,530$, $\mathrm{Re}_w = 68,930$ and $\mathrm{Re}_w = 78,330$. However, this sudden increase in the cavity size did not occur for the highest and lowest superficial water Reynolds numbers ($\mathrm{Re}_w = 50,130$ and $\mathrm{Re}_w = 87,730$), where the increase in cavity size was more gradual. The reason that prevented this transition behavior for $\mathrm{Re}_w = 50,130$ is that the flow was very slow and a stratified air flow formed at the top of the channel. Therefore, the gas was not completely trapped within the cavity, being able to escape through the connected stratified flow. For $\mathrm{Re}_w = 87,730$, the turbulence level was very high, leading to the formation of many bubbles by break-up at the end of the gas pocket (see Cases 24 and 25 in Figure 4.9), preventing its rapid growth.

The cavity size is presented as a function of the superficial water Reynolds number for different values of Re_a in Figure 4.13. As already shown before, the increase in Re_a always leads to an increase in cavity size. However, by increasing Re_w, the cavity size first increases up to a certain limit, before decreasing again. In the first range of the curves (up to $\mathrm{Re}_w = 68,930$), increasing the superficial water Reynolds number leads to a larger recirculation zone, which creates a bigger space for the gas to be accumulated; no gas stratification is observed along the upper wall. On the other hand, a further increase in the superficial water

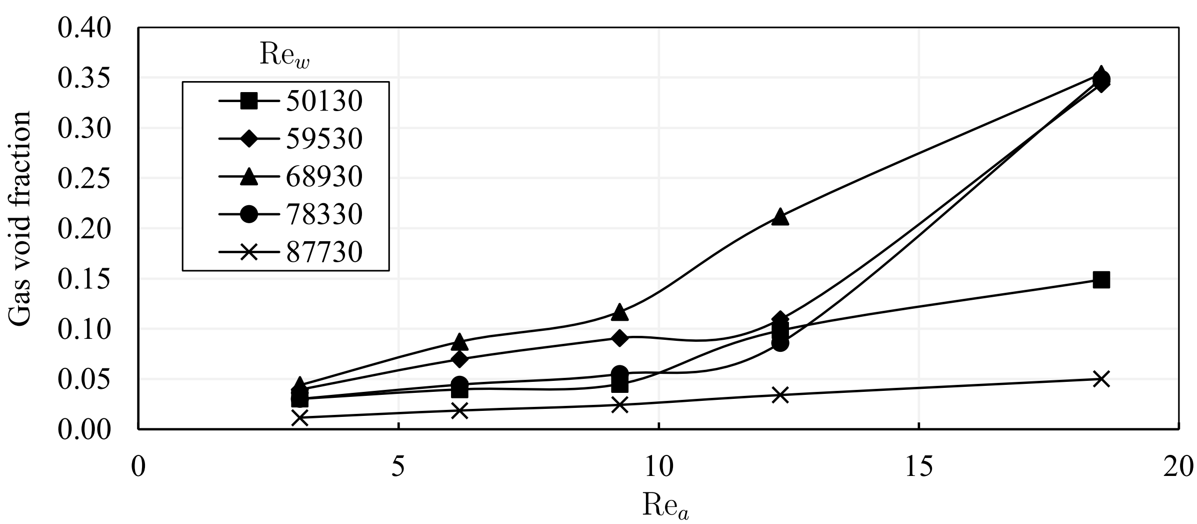

Figure 4.12: Accumulated gas size as a function of the superficial air Reynolds number for different superficial water Reynolds numbers.

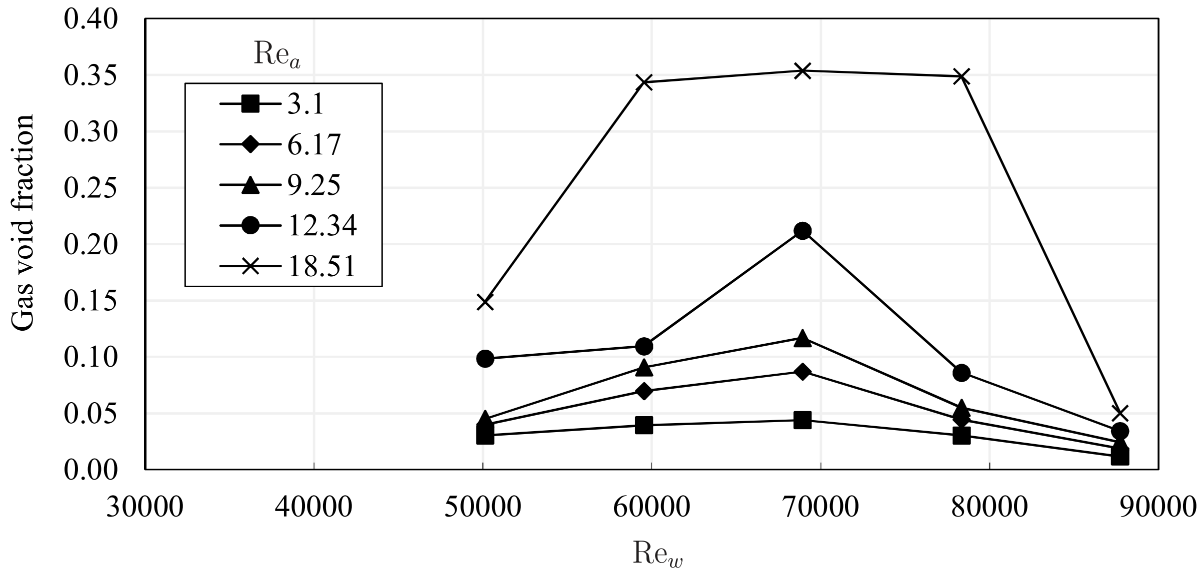

Figure 4.13: Accumulated gas size as a function of the superficial water Reynolds number for different superficial air Reynolds numbers.

Reynolds number leads to a high level of turbulence; many bubbles are formed by break-up at the end of the gas cavity, preventing gas accumulation.

4.5 Pressure measurements

In this section, the effect of the accumulated gas on the pressure recovery in the diffuser is discussed. The pressure is measured at 8 different axial locations along the streamwise direction in the channel (see again Figure 3.1). Since the flow is highly turbulent, the pressure is continuously monitored at each point during 15 minutes with a frequency of 8 Hz; then, the average value of five repeated measurements is deduced, and shown in what follows.

Pressure sensor number 2, which is located just at the beginning of the diffuser (i.e., at $x = 0$), was always taken as a reference; all pressure values are given by the difference to this reference value. Figures 4.14a and 4.14b show the corresponding pressure variation along the channel for $\mathrm{Re}_w = 68,930$ and $\mathrm{Re}_w = 87,730$, respectively.

It is observed that increasing the air Reynolds number causes a significant decay in the pressure recovery within the diffuser. The effect of the accumulated gas on pressure is much more pronounced in Figure 4.14a, since larger cavities are observed under such conditions compared to those corresponding to Figure 4.14b. The large gas pocket starts around $x/d_{hu} = 5$. A higher deterioration of the pressure recovery is observed after this position, particularly in Figure 4.14a.

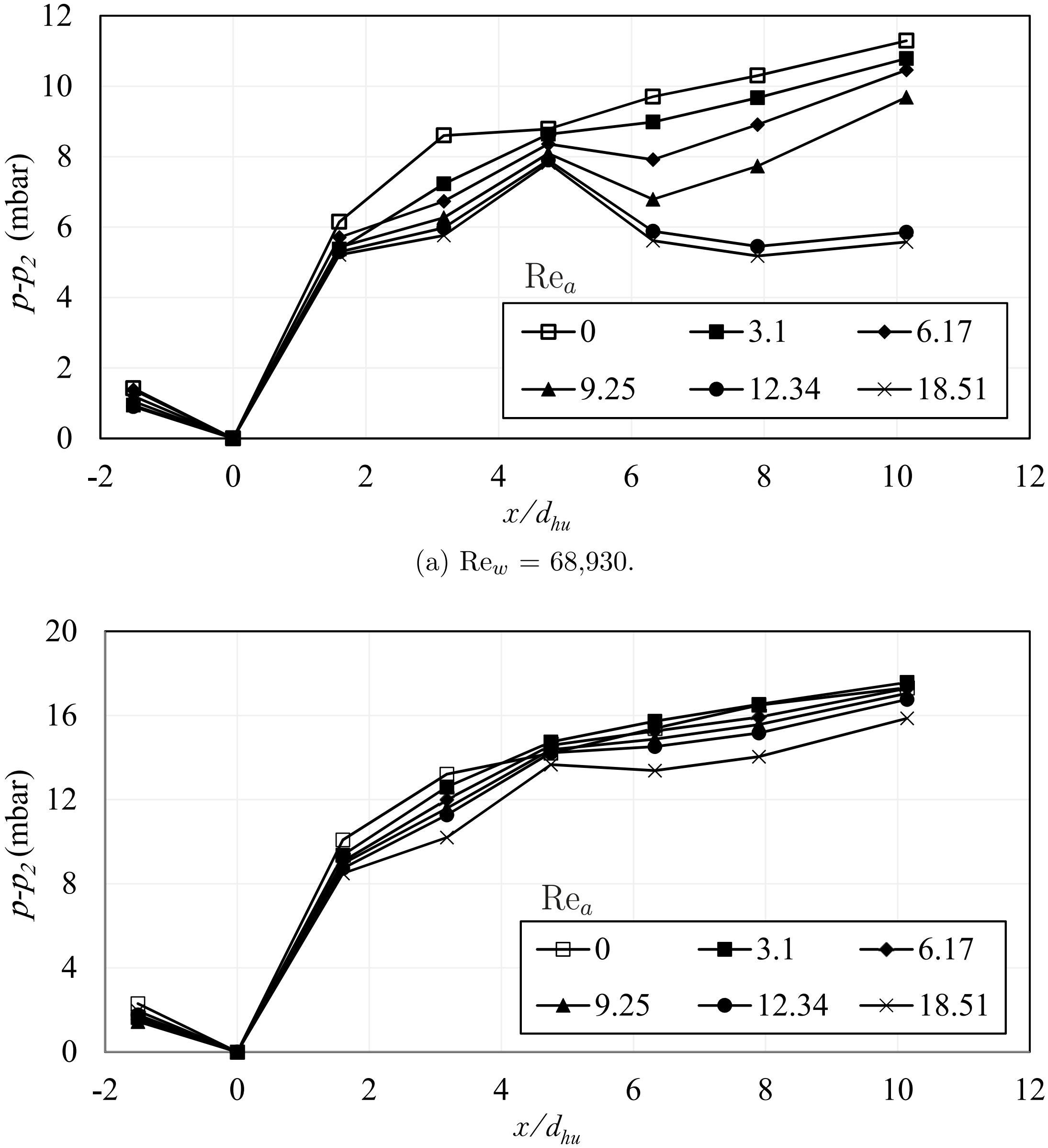

(a) Re_w = 68,930.

(b) Re_w = 87,730.

Figure 4.14: Evolution of the pressure within the diffuser in the streamwise direction as a function of the water Reynolds number for different air Reynolds numbers. Pressure sensor number 2, which is located just at the beginning of the diffuser (i.e., at x=0), is always taken as a reference.

4.6 Boundary conditions measurements

4.6.1 Inlet velocity measurements

The inlet velocity for single-phase flow and sample two-phase flow cases were measured by using the Laser Doppler Anemometry (LDA) system at the beginning of the diverging part. The velocity was measured on the grid of points shown in Figure 3.4c. These data could be very helpful to reduce the efforts and cost of future numerical work, simulating smaller domains. Figure 4.15 shows the typical shape of the measured velocity profile for three sample cases of the single-phase flow.

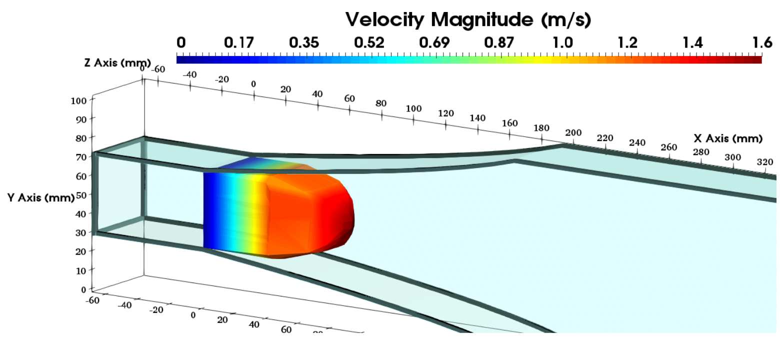

(a) Re_w = 50,130.

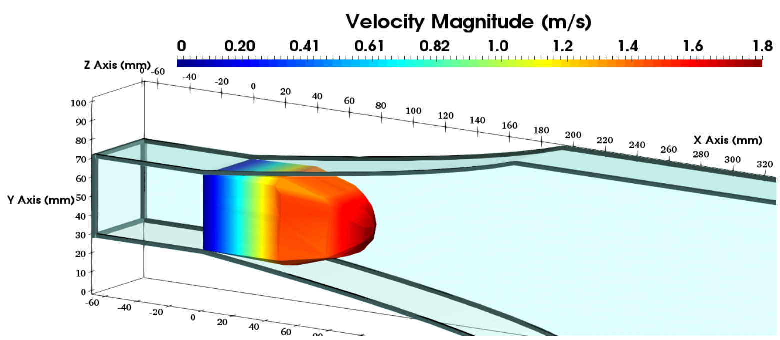

(b) Re_w = 59,530.

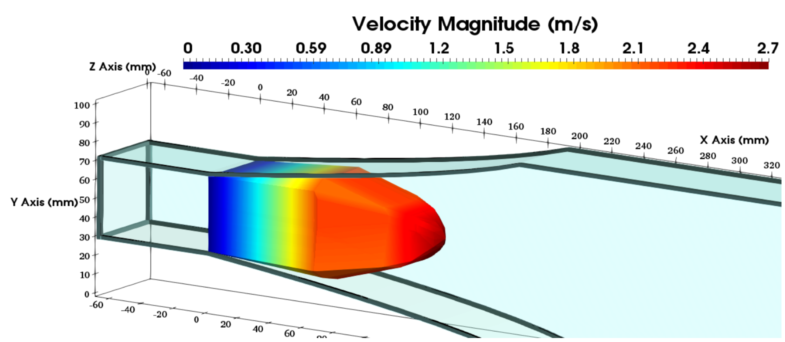

(c) Re_w = 87,730.

Figure 4.15: Inlet velocity profiles for single-phase flow measured by LDA.

Figure 4.16 compares the velocity profile at the middle vertical line of the diffuser inlet for sample two-phase flow cases. Only slight changes in the velocity profile can be seen when the air Reynolds number is varied. Sample data tables of the measured boundary conditions are given in Appendix E. Additionally, all measurement data and boundary conditions obtained during this work are available in the supplementary material of the thesis.

4.6.2 Bubble size distribution measurements

For sample cases of two-phase flows, the bubble size distributions (BSD) have been determined by using shadowgraphy measurements. A small sample window has been considered, at the beginning of the diverging part of the channel. The shadowgraphy set-up and the considered window are illustrated in Chapter 3 in Figure 3.4a and 3.4b, respectively. Information about the bubble size distribution is helpful for examining and validating two-phase models, since the force calculations in many models depend strongly on the size of the bubbles, for example, the drag force. Additionally, the BSD can be used as an inlet boundary condition in future numerical simulations. The inlet bubble sizes depend on different parameters, including:

- The size and number of holes, through which the gas is injected in the mixing joint. As already described in Section 3.1.1, the gas is injected here through 21 small holes of 1 mm diameter distributed peripherally in the mixing joint.
- The air Reynolds number, which changes the speed of injection in the mixing joint.
- The length of the inlet pipe, which affects the residence time in the inlet pipe, before the inlet section. A higher residence time allows the bubble to rise up in the pipe and interact with each other by coalescence, forming bigger bubbles at the inlet section.
- The water Reynolds number and the corresponding turbulence intensity. A higher water Reynolds number reduces the residence time and increases the turbulence intensity, which increases the bubble break-up.
- The static pressure in the mixing joint, which decreases with the increase of the water Reynolds number. Therefore, a higher water Reynolds number can increase the bubble size, due to the lower pressure available in the mixing joint.

Figure 4.17 shows the measured BSD for sample cases of two-phase flows. Despite the various parameter affecting the bubble sizes, among different cases considered, there are only slight changes in the inlet bubble distributions. Therefore, the median diameter of most distributions is around 0.3 mm. Additionally, the standard deviation of most BSDs is limited between 0.3 and 0.5 mm. Figure 4.18 compares the median diameter of BSD for all the considered cases. As shown, the median diameter of most BSD is restricted between 0.2 and 0.4 mm.

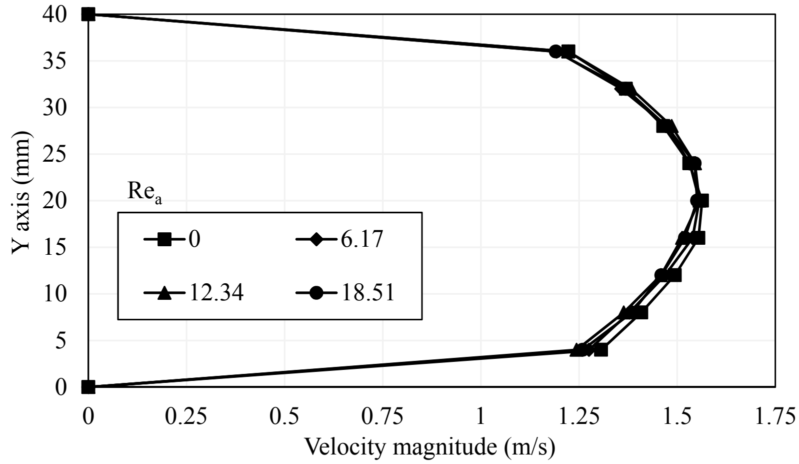

(a) Re$_w$ = 50,130.

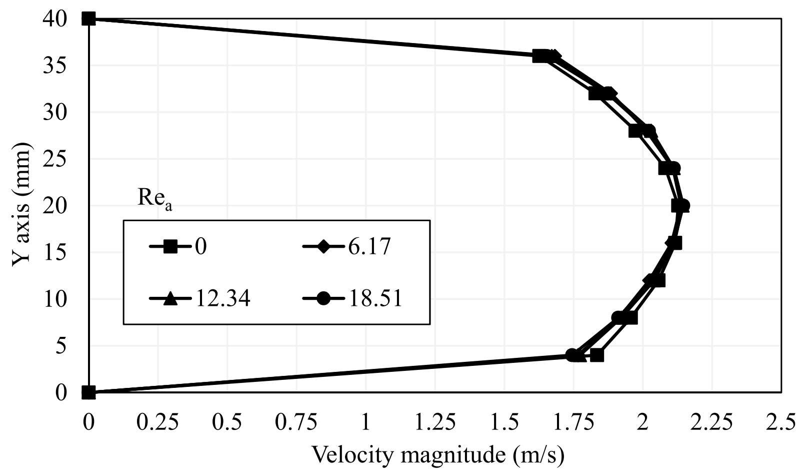

(b) Re$_w$ = 68,930.

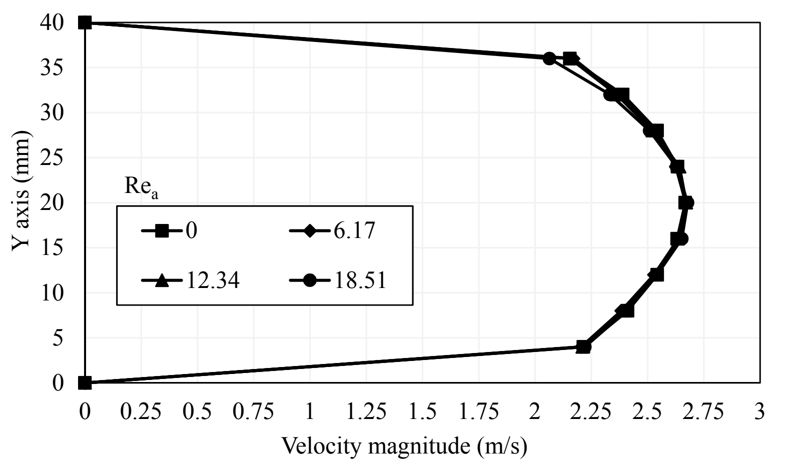

(c) Re$_w$ = 87,730.

Figure 4.16: Velocity profiles at the middle vertical line of the diffuser inlet measured by LDA.

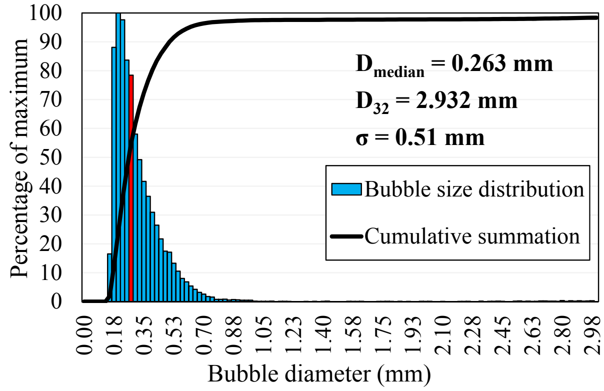

(a) Case 2: Re_w= 50,130, Re_a = 6.17

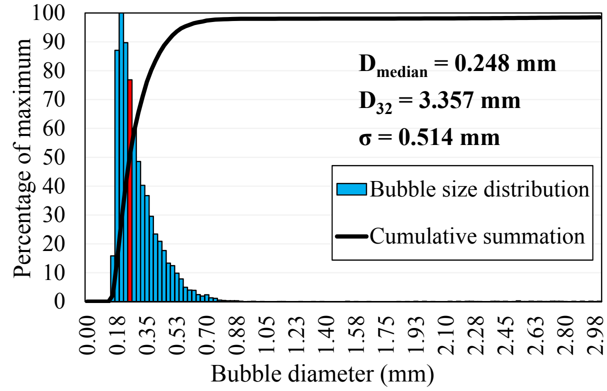

(b) Case 4: Re_w= 50,130, Re_a = 12.34

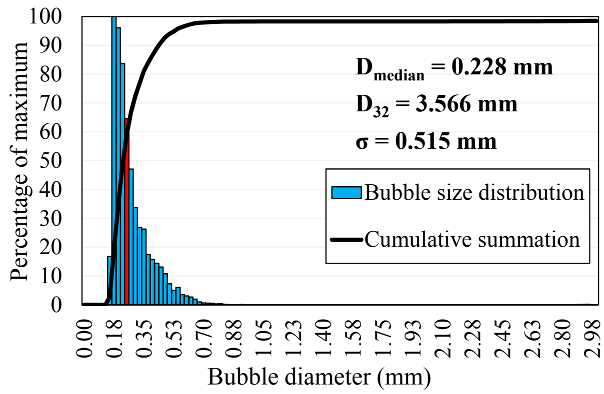

(c) Case 5: Re_w= 50,130, Re_a = 18.51

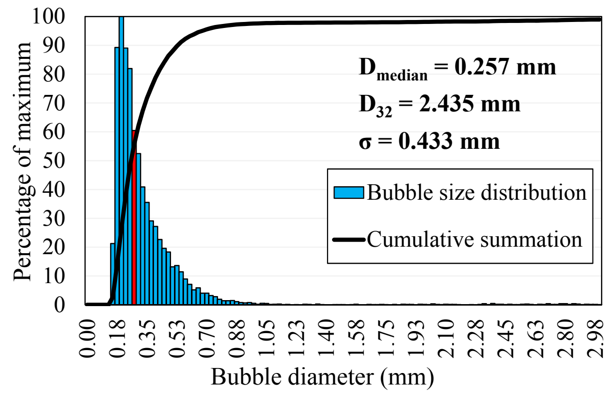

(d) Case 7: Re_w= 59530, Re_a = 6.17

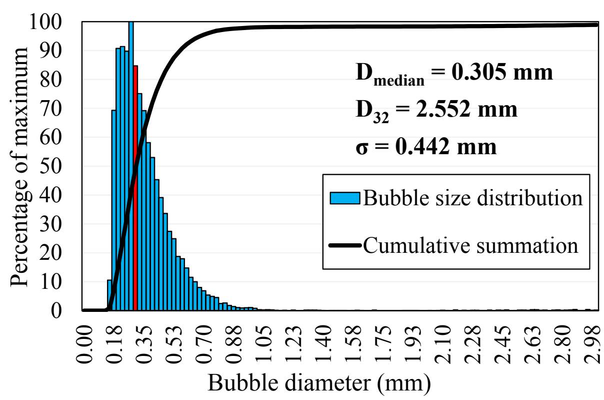

(e) Case 9: Re_w= 59530, Re_a = 12.34

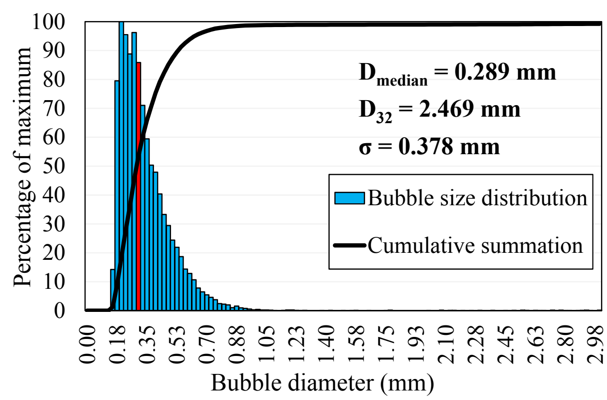

(f) Case 10: Re_w= 59530, Re_a = 18.51

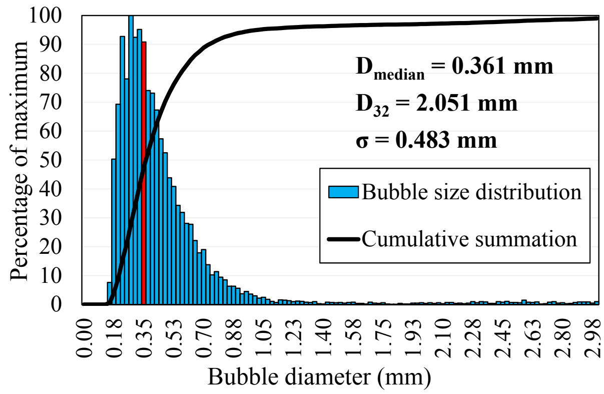

(g) Case 12: Re$_w$= 68930, Re$_a$ = 6.17

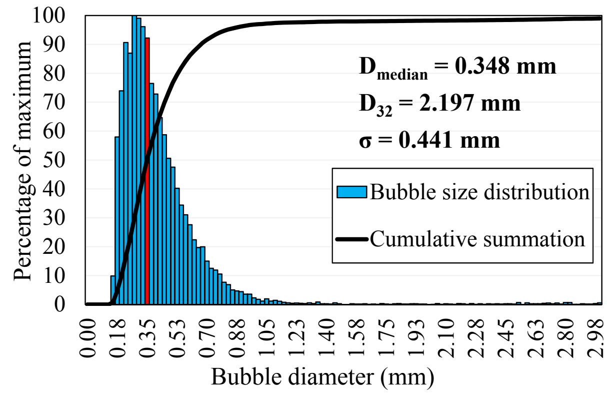

(h) Case 14: Re$_w$= 68930, Re$_a$ = 12.34

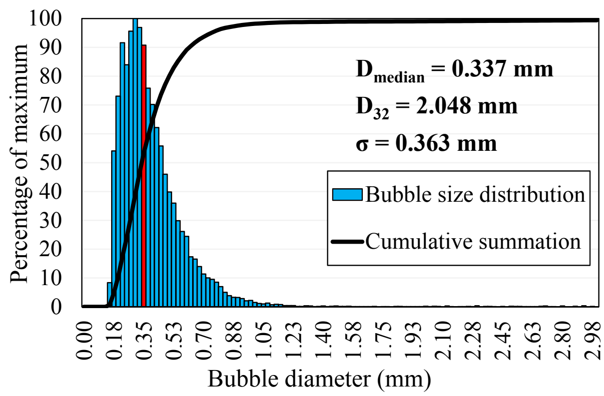

(i) Case 15: Re$_w$= 68930, Re$_a$ = 18.51

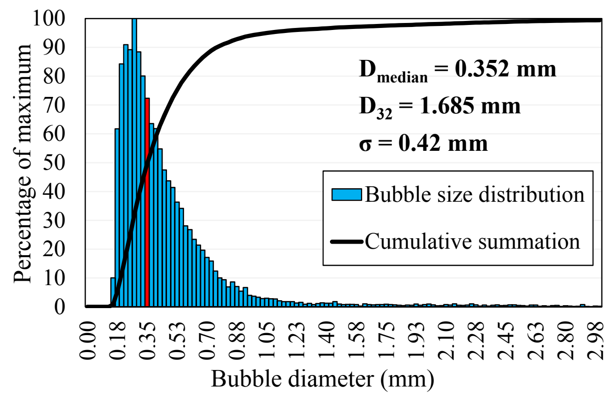

(j) Case 17: Re$_w$= 78330, Re$_a$ = 6.17

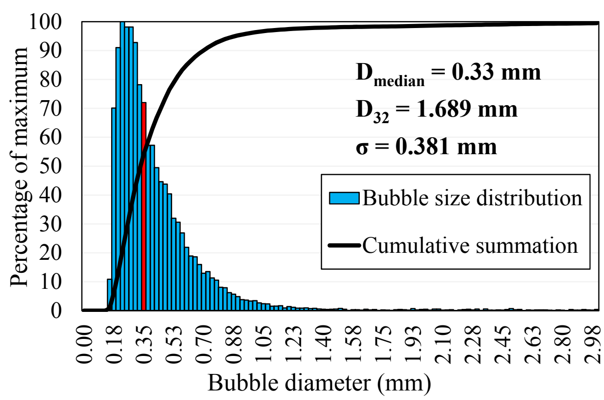

(k) Case 19: Re$_w$= 78330, Re$_a$ = 12.34

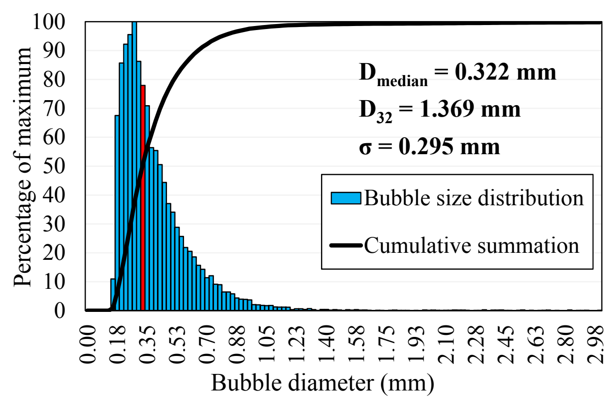

(l) Case 20: Re$_w$= 78330, Re$_a$ = 18.51

Figure 4.17: Inlet bubble size distributions for sample two-phase cases measured by shadowgraphy within a small window at the diffuser inlet.

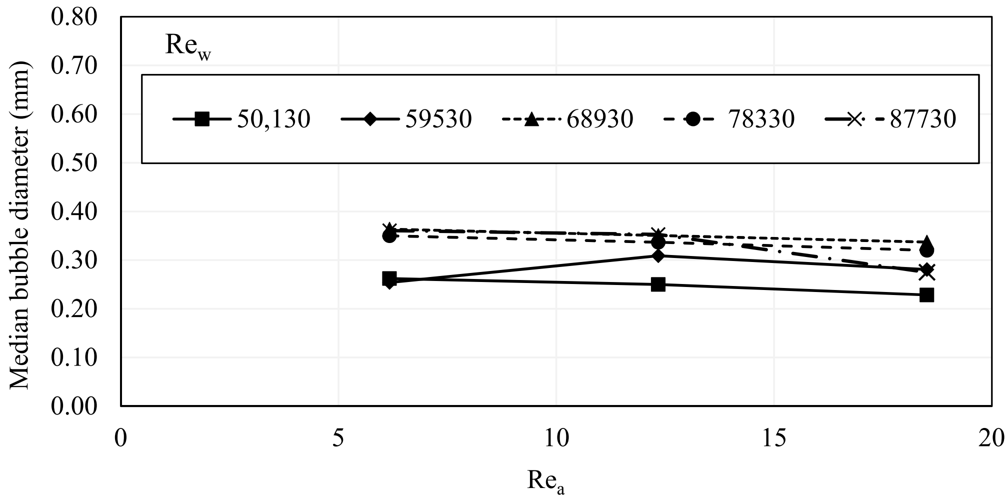

Figure 4.18: Median diameter range of different BSD data.

4.7 Conclusions

Two-phase flows involving air and water have been studied in a horizontal, diverging flow channel with an increasing opening angle. The PIV velocity measurements show two large recirculation zones on the upper and lower sides of the diffuser. As the air phase enters the channel, the bubbles are trapped and accumulate in the upper (lower pressure) recirculation zone. Even for very small air volume fractions (0.05%), a gas pocket is observed. For all the conditions investigated, the accumulated gas size always increases when increasing the superficial air Reynolds number. For $\mathrm{Re}_w = 50,130$, the flow is comparatively slow after the diffuser and stratified air flow is observed at the top of the channel, reducing the growth rate of the gas pocket. However, for higher superficial water Reynolds numbers ($\mathrm{Re}_w = 59,530$, $\mathrm{Re}_w = 68,930$, and $\mathrm{Re}_w = 78,330$), no stratified flow is observed, leading to a sudden increase in the cavity size when the air Reynolds number is increased up to 18.51. Keeping now the air Reynolds number constant, larger gas cavities are observed when increasing the superficial water Reynolds number up to $\mathrm{Re}_w = 68,930$, due to larger recirculation zones. However, increasing further the superficial water Reynolds number to $\mathrm{Re}_w = 87,730$, the increased turbulent fluctuations result in strong bubble break-up at the end of the cavity, hindering a rapid increase of the gas pocket. The accumulated gas strongly affects pressure recovery; a significant decay in pressure recovery is observed across the diffuser when more gas is accumulated. Sample boundary conditions are also measured, including inlet velocity and bubble size distributions, which can be implemented in numerical simulations. These results deliver interesting insights for understanding the complex flow patterns and gas accumulation processes occurring in two-phase gas/liquid flows. Currently, it is found that the accumulated gas can be reduced by 1) avoiding large recirculation zones in the flow, 2) ensuring high enough turbulence levels leading to break-up, and/or 3) choosing a regime leading to a stratified flow after the diverging part, with a connected gas layer along the upper wall.

It is now time to check how the results obtained with this simple, static configuration can be related to those measured in a real centrifugal pump impeller.

Chapter 5

Centrifugal pump experiments: Results and discussions

5.1 Introduction

In this chapter, the two-phase flow transport and the characteristics of a centrifugal pump were investigated for various flow conditions. A closed impeller and a geometrically similar semi-open impeller were employed to compare the flow behavior and corresponding pump performance using each of them. The effect of the tip clearance gap on the performance of the semi-open impeller was investigated by employing a standard and a doubly-increased gap. The flow characteristics and the performance of the semi-open impeller having a standard gap were furthermore examined after installing an upstream axial flow inducer. A rotational speed of 650 rpm was set for all experiments. The performance of the pump was reported and described for either a constant gas volume fraction (ε) or a constant air flow rate (Q_a) at the pump inlet. Possible hysteresis effects due to gas trapping and accumulation in the impeller were studied by approaching the operating conditions using different procedures. The head degradation behavior, the pump surging conditions, and the flow instabilities were considered as well.

Furthermore, the two-phase flow regimes were recorded and identified for all the considered cases using a high-speed recording system. For selected flow conditions, the bubble size distributions were obtained by shadowgraphy measurements and compared for all the different pump settings considered. In addition, flow regime maps have been generated and associated with the pump performance curves for all the considered conditions. This would help to explain the relationship between the two-phase regime found in the impeller and the resulting pump performance. The present analysis and comparisons are also very helpful to choose optimal impeller settings as a function of the desired operating two-phase flow conditions. Moreover, these experimental results are needed to develop and validate suitable numerical procedures in companion CFD studies, as will be shown later in Chapter 6. Some parts of this chapter are based on articles published in Experimental Thermal and Fluid Science and in ASME Turbo Expo 2018 [32, 108]

5.2 Pump performance calculations

In this section, the basic equations and pump parameter calculations are summarized. In the experiments, the density, the volume flow rate, the volume fraction of the air are always defined at the flow conditions of the pump inlet; the suction pressure p_S, and the temperature in the suction line T. The air density is calculated by using the universal gas law, where:

$$\rho_a = \frac{p_S}{RT} \tag{5.1}$$

The air mass flow rate $\dot{m}_a$ and the water volume flow rate Q_w are directly measured by the flow-meter devices installed on the air and water lines, respectively. The air volume flow rate then is defined as:

$$Q_a = \frac{\dot{m}_a}{\rho_a} \tag{5.2}$$

The air (gas) volume fraction is then calculated from:

$$\varepsilon = \frac{Q_a}{Q_t} = \frac{Q_a}{Q_a + Q_w} \tag{5.3}$$

The mass flow rate of the water is calculated after obtaining the water density based on the flow temperature, where:

$$\dot{m}_w = \rho_w \; Q_w \tag{5.4}$$

Then, the air mass fraction (mixture quality) $\dot{\mu}$ is obtained by:

$$\dot{\mu} = \frac{\dot{m}_a}{\dot{m}_t} = \frac{\dot{m}_a}{\dot{m}_a + \dot{m}_w} \tag{5.5}$$

The specific delivery work Υ of the pump is calculated taking the compression work of the air phase into account, assuming isothermal process across the pump, where:

$$\Upsilon = \frac{1-\dot{\mu}}{\rho_w} \; (p_D - p_S) + \dot{\mu} RT \; \ln\left(\frac{p_D}{p_S}\right) + \frac{1}{2} \; \left({V_D}^2 - {V_S}^2\right) + g \; (z_D - z_S) \tag{5.6}$$

The complete derivation of Equation 5.6 is provided in Appendix F. The superficial velocities in the suction and the delivery lines (V_S and V_D) are calculated based on the continuity equation:

$$V_S = \frac{Q_t}{A_S} \tag{5.7}$$

$$V_D = \frac{Q_t}{A_D} \tag{5.8}$$

The suction area A_S and the delivery area A_D are determined at the measurement sections of the suction pressure p_S and the delivery pressure p_D, respectively. The total transferred power from the pump to the conveyed medium is calculated by using the total mass flow rate $\dot{m}_t$ and the specific head of the pump Υ, where:

$$P_P = \dot{m}_t \ \times \Upsilon \tag{5.9}$$

while the motor shaft power P_{Sh} is determined by using the measured shaft torque τ and rotational speed n, where

$$P_{Sh} = \tau \times \omega = \tau \times \frac{2\pi n}{60} \tag{5.10}$$

Finally, the efficiency of the pump η is calculated from:

$$\eta = \frac{P_P}{P_{Sh}} \tag{5.11}$$

Table 5.1 summarizes the considered flow conditions of the present experiments. Based on the accuracy of the measuring instruments given in Table 3.3, the experimental uncertainties were calculated using the method of sequential perturbation described by Moffat [104]. The analysis delivers root mean square values of uncertainty better than 1.45%, 3.2%, 4.7%, and 4.95% in the pump specific delivery work Υ, the gas volume fraction ε, the shaft power P_{Sh}, and the pump efficiency η, respectively. The complete analysis for error propagation and experimental uncertainty calculations are described in Appendix C.

In all experiments, the pump was operated under low suction pressure conditions. As shown in Table 5.1, the suction pressure range was kept in the range between 1.14 and 1.28 bar. Therefore, the universal gas law was applied to calculate the air density, since air can be treated as ideal gas for pressures up to 5 bar without expecting significant errors [109]. The resulting error has been checked by comparing the obtained density values with those of the models of Peng-Robinson [110] or Soave-Redlich-Kwong [111]; this error never exceeded 0.1%, and is thus negligible.

Table 5.1: Flow conditions of the experiments.

Gas volume fraction, ε	$0 - 15$	%
Suction pressure, p_S	$1.14 - 1.28$	bar
Suction temperature, T	299 ± 2	K
Rotational speed, n	650	rpm

5.3 Single-phase flow pumping performance

The single-phase performance curves (specific delivery work, efficiency, and shaft power) of all the considered cases are compared in Figure 5.1a, 5.1b and 5.1c. The performances of the closed impeller and the semi-open impeller with the standard gap are initially similar when transporting a single-phase flow. However, the pump performance of the closed impeller is slightly higher than the semi-open impeller, particularly in overload conditions (2%-4.5% higher). The efficiency curve of the closed impeller is overall 1 to 3% higher than for the semi-open impeller with the standard gap, due to the volumetric loss of the semi-open impeller.

When the semi-open impeller is used with the standard gap, the peak point of the efficiency curve is slightly shifted to a higher volume flow rate because of the volumetric loss. Nevertheless, with the increased gap, the volumetric loss significantly increases, which reduces the efficiency in the overload range, shifting the peak point back to a lower volume flow rate. The increase of the clearance gap of the semi-open impeller results in a reduction of 9% to 40% in the specific delivery work, 1% to 14% in the efficiency, and 7% to 8% in the shaft power, when compared to the standard-gap case.

When the inducer is installed upstream of the semi-open impeller with a standard gap, the pump performance is slightly improved in part-load conditions. However, a performance reduction occurs in overload conditions. This happens mainly due to the increase in shock losses as a result of the intensified vortices that occur through the inducer at high flow rates [112, 113]. This effect is further investigated by CFD numerical simulations and discussed in details in Chapter 6. The conditions corresponding to the best efficiency point (optimal conditions, Q_{opt}, Υ_{opt}, and $P_{Sh\ opt}$) of each case are used for normalization in most of the following sections.

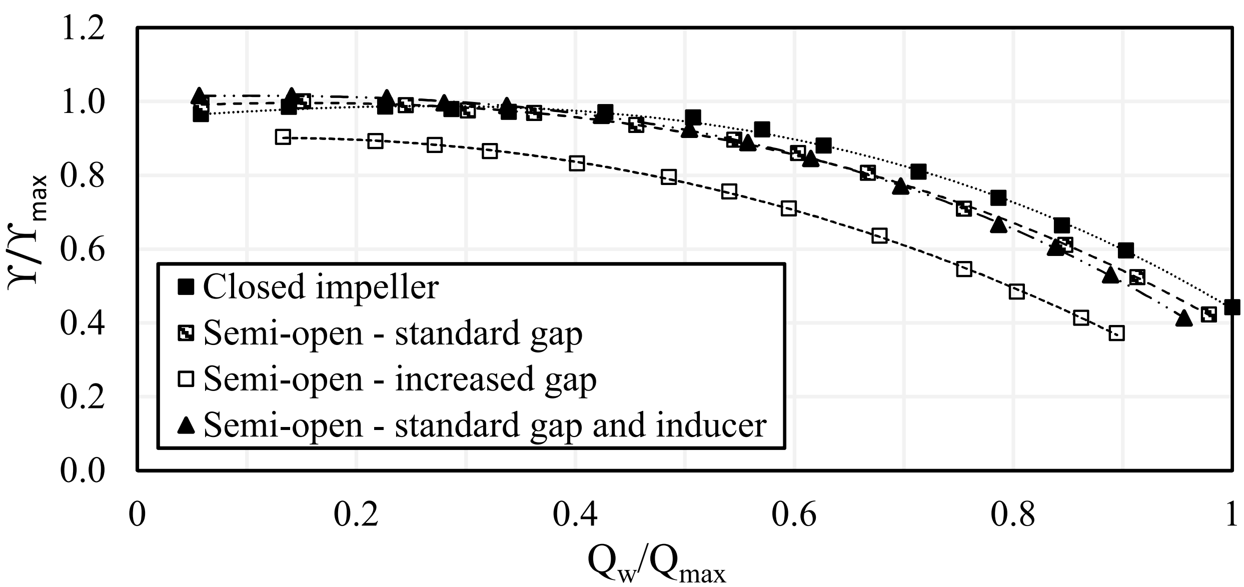

(a) Specific delivery work

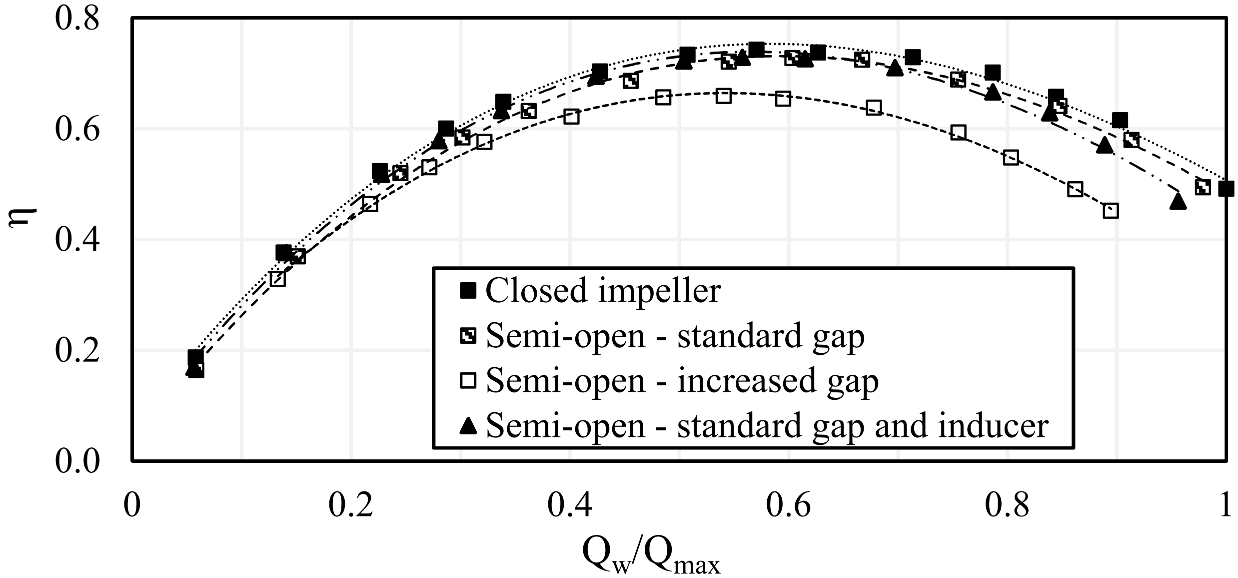

(b) Efficiency

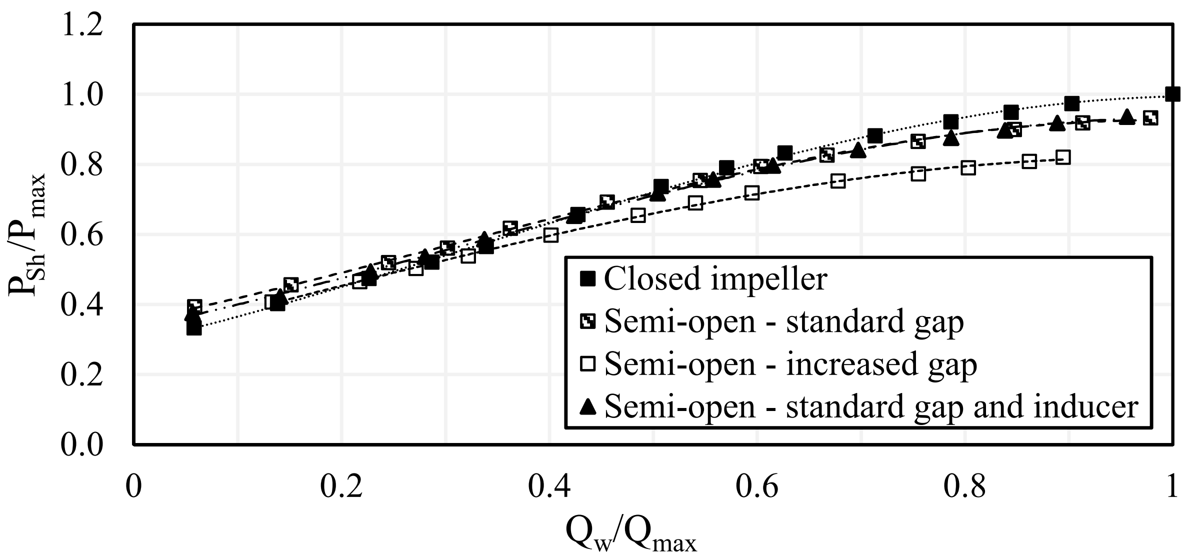

(c) Shaft power

Figure 5.1: Comparison of the single-phase performance curves.

5.4 Two-phase flow pumping performance

As mentioned previously, the possible hysteresis effects due to air accumulation in the impeller passages were examined by comparing in a systematic manner three different experimental procedures to set the desired flow conditions. The steps of each procedure are described in Figure 5.2 and listed below:

- First procedure ("left to right" approach shown in Figure 5.2a)
  1. The motorized gate valve was completely closed.
  2. Then, the water volume flow rate was gradually increased from zero by opening the valve.
  3. The air volume flow rate was finally increased until the required gas volume fraction was reached, and the data points were recorded after reaching steady-state.

- Second procedure ("right to left" approach shown in Figure 5.2b)
  1. The motorized gate valve was completely opened.
  2. Then, the air volume flow rate was increased until the required gas volume fraction was reached for the starting point.
  3. The air volume flow rate was reduced again to move to the next point.
  4. The water volume flow rate was decreased till the required gas volume fraction was reached, and the data points were recorded after reaching steady-state.

- Third procedure (cross tests shown in Figure 5.2c)
  1. An initial single-phase flow of water was set. The water gate valve was not adjusted anymore during the whole data recording.
  2. The air volume flow rate was gradually increased and the data were recorded after reaching steady-state while passing through each desired gas volume fraction.
  3. Then, the data points were recorded again after reaching steady-state in a similar manner, while gradually decreasing the air volume flow rate.

In the following, comparisons are shown for results obtained by three procedures. If not stated further, the first procedure was used as a standard.

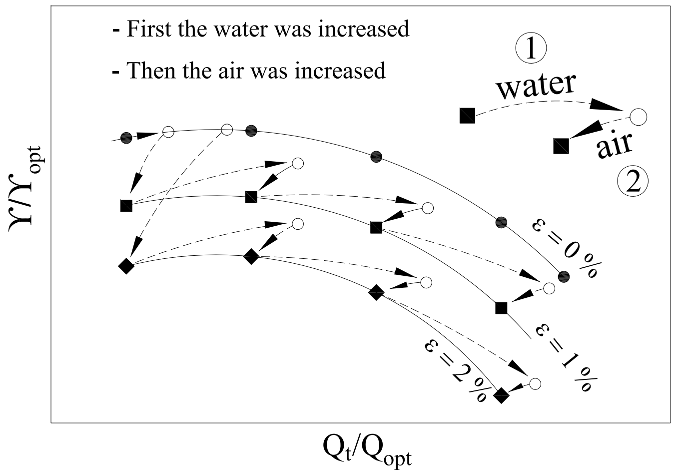

(a) First procedure

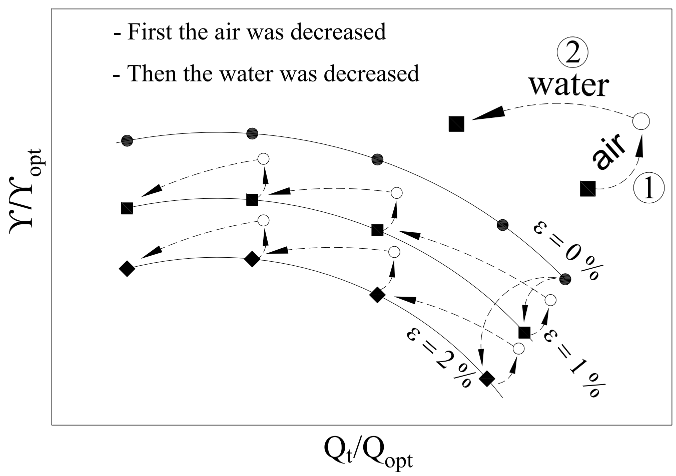

(b) Second procedure

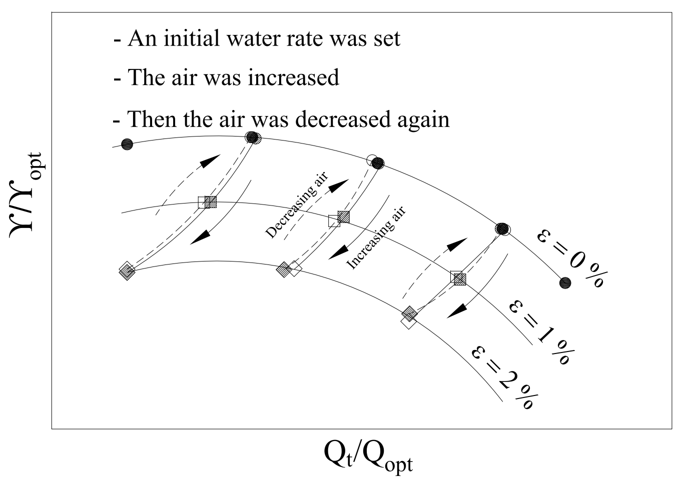

(c) Third procedure

Figure 5.2: Different experimental procedures considered.

5.4.1 Closed impeller

Performance curves

The normalized specific delivery work, the efficiency, and the normalized shaft power curves of the closed impeller are shown in Figure 5.3a, 5.3b, and 5.3c, respectively. In Figure 5.3 the results obtained by the first and the third experimental approaches described above are shown simultaneously. The black-filled symbols represent the experimental data points obtained by the first procedure, while the hatched symbols show the data points recorded while increasing the air flow rate in the third approach, whereas the empty symbols donate the data recorded while decreasing back the air flow rate. Additionally, gray-filled symbols indicate the occurrence of strong flow instabilities. The trend lines of the data points of the first procedure are shown as dotted lines for each gas volume fraction.

As shown in Figure 5.3a, 5.3b, and 5.3c, by increasing the percentage of entrained air in the flow mixture, the pump parameters (Υ, η, and P_{Sh}) are continuously reduced. In addition, the operating flow range of the pump becomes generally narrower. For instance, in part-load operation for Q_t/Q_{opt} approximately lower than 0.5, the pump break-down phenomenon is very likely to happen, where the pump is not able anymore to suck and convey the mixture. Furthermore, the maximum pump capacity is continuously decreased as the percentage of gas fraction increases, where the transfer of kinetic energy is reduced.

Important observations concerning pump operation (breakdown, surging, and cavitation) are also shown in Figure 5.3a and Figure 5.4. In the breakdown region, the pump is not able anymore to convey the mixture. Surging indicates the occurrence of large instabilities in the delivery, accompanied by strong system vibrations. As indicated in Fig. 5.4, cavitation occurs near the maximum flow rate of single-phase operation. However, as soon as a very small amount of air enters the pump, cavitation is damped. A similar effect was reported and discussed in [36, 56]. It was even shown in [36] that an amount of air between 0.3 to 1% can dramatically damp the suction pressure pulsation due to cavitation by a factor of 5.

Comparing the points recorded by the different procedures, no significant hysteresis effects could be observed for the closed impeller. Figure 5.4 shows a comparison between the data points of the normalized specific delivery work recorded by the first and the second procedure. The data of the first procedure are donated by filled symbols and dotted curves for the trend lines; while the data of the second procedure are shown by empty symbols and dashed curves for the trend lines. Again, the data of the two procedures are very similar, showing no important hysteresis effects.

Pump surging and flow instabilities

The results show that for $\varepsilon > 4\%$ some instabilities occur in the flow, particularly for overload operation ($Q_t/Q_{opt} > 1$). Moreover, for $\varepsilon = 6\%$ and $Q_t/Q_{opt} > 1.1$, very strong operational instability occurs, where the pump performance fluctuates between two duty points at the same time. This phenomenon is known as pump "Surging", which generally happens when the system curve could intersect with the pump characteristic curve at two different operational points. The data points which indicate pump surging are shown in Figure 5.3 by gray-filled symbols.

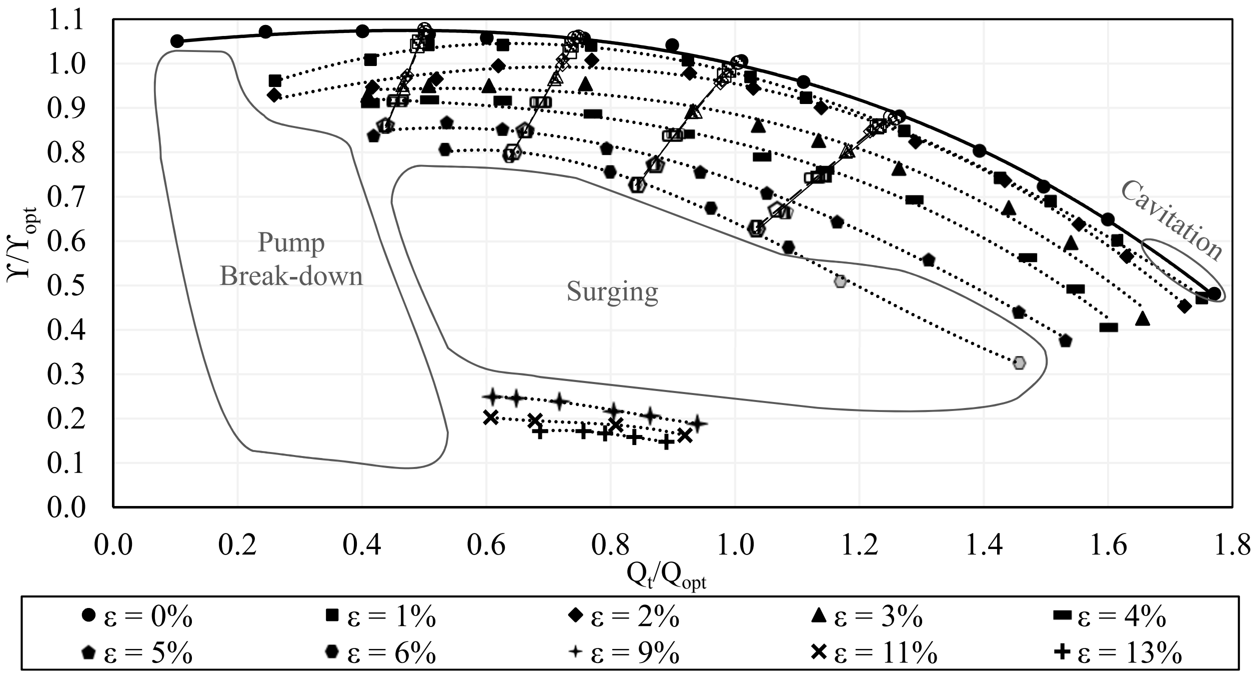

(a) Normalized specific delivery work

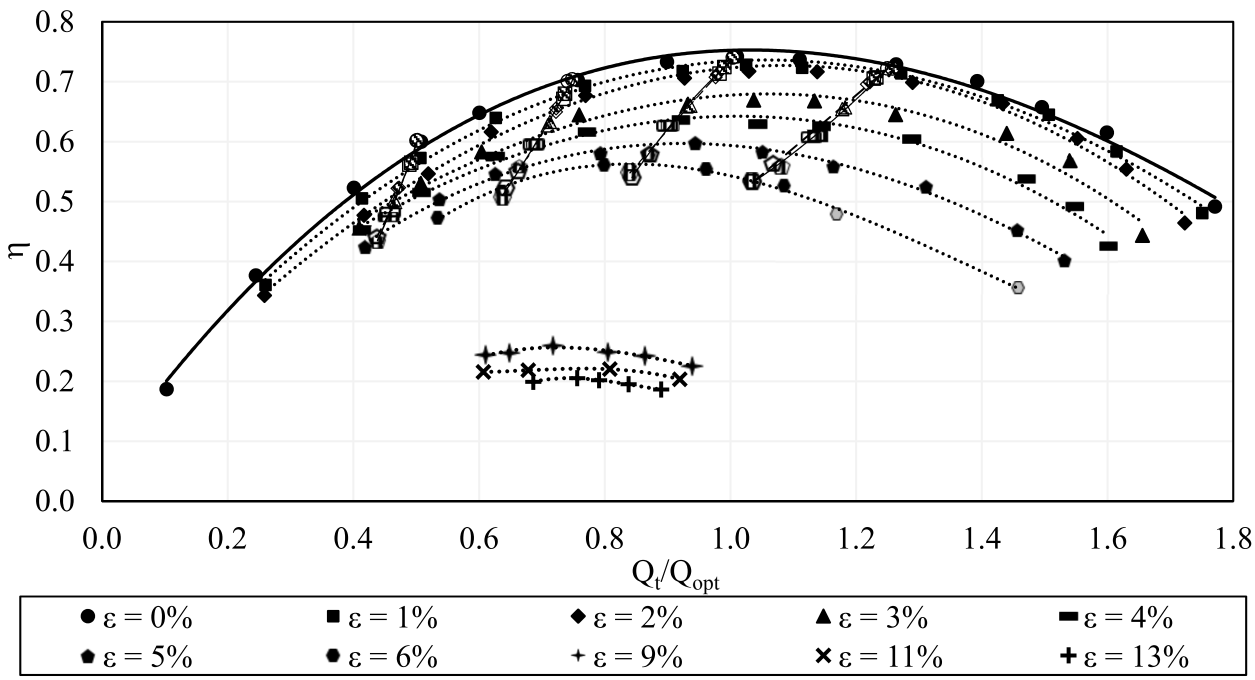

(b) Efficiency

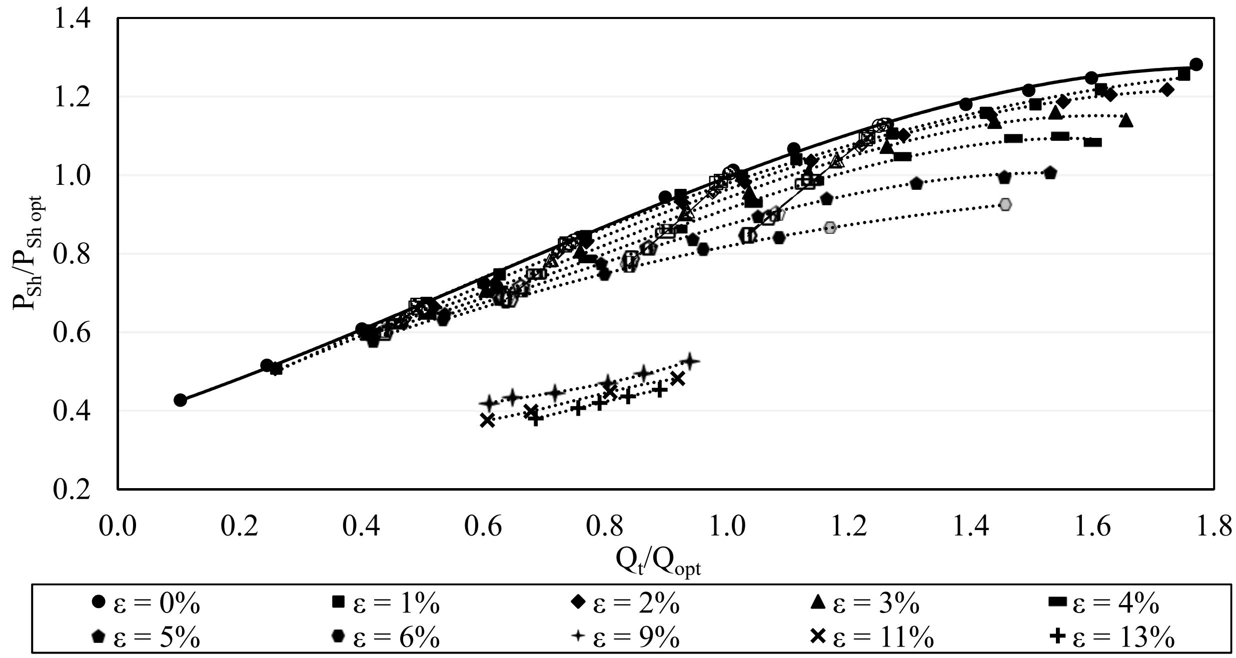

(c) Normalized shaft power

Figure 5.3: Performance curves of the closed impeller for constant gas volume fractions.

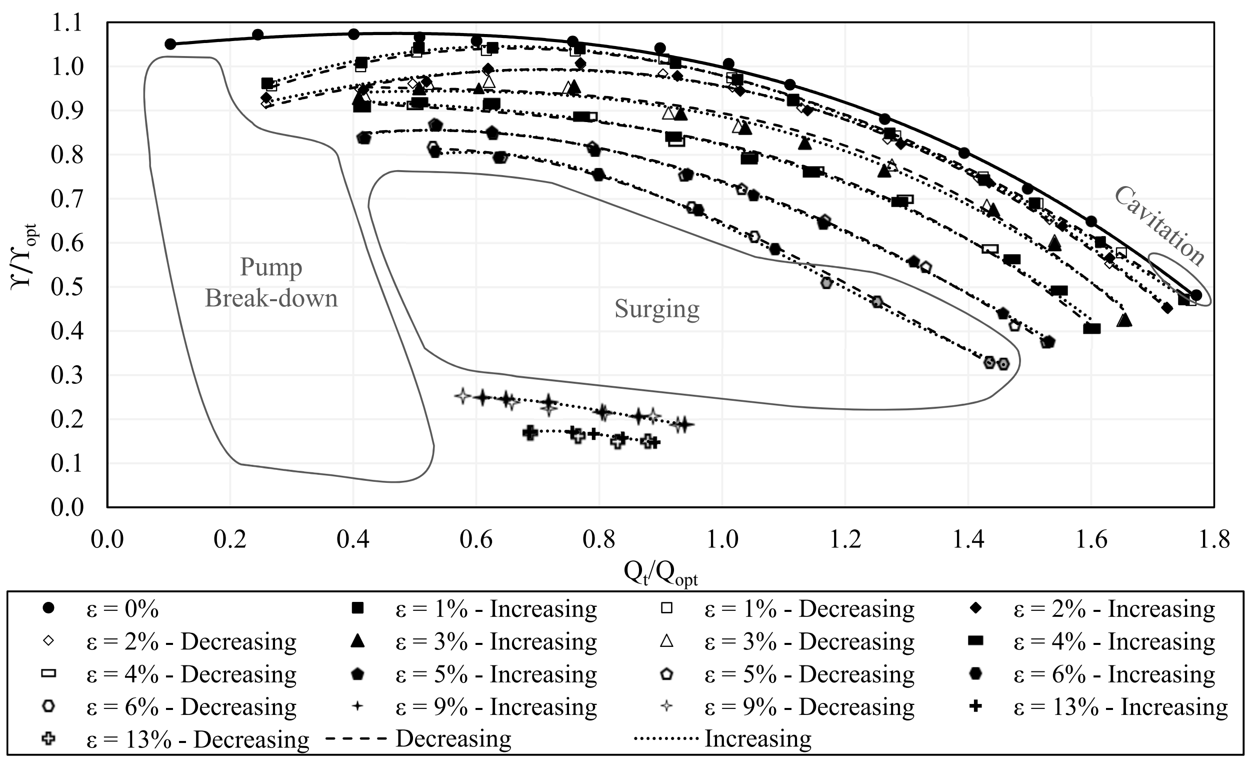

Figure 5.4: Performance of the closed impeller recorded by the 1[st] procedure (filled symbols and dotted curves) and the 2[nd] procedure (empty symbols and dashed curves).

5.4.2 Semi-open impeller with a standard gap

Performance curves

The normalized specific delivery work, the efficiency, and the normalized shaft power curves of the semi-open impeller with a standard gap are shown in Figure 5.5. Similar to the closed impeller, the performance curves are getting narrower as the gas volume fraction is increased. Up to $\varepsilon = 3\%$, the pump parameters are only very slightly reduced, showing a better behavior in this range compared to the closed impeller. However, starting from $\varepsilon = 4\%$ the pump performance is strongly decreased by increasing the gas volume fraction up to $\varepsilon = 6\%$. This effect is less pronounced in the range of $0.4 \leq Q_t/Q_{opt} \leq 0.6$ as the pump could keep quite well its performance. Thereafter, for $\varepsilon > 6\%$ the semi-open impeller shows again a slightly better performance compared to the closed impeller.

Unlike the closed impeller, at some flow conditions, significant hysteresis effects can be observed for the semi-open impeller by comparing the results of the different measurement procedures. This is found in particular while reducing the air flow in the third measurement procedure for $\varepsilon = 4\%$ and $\varepsilon = 6\%$, where the data points are far from the points recorded by the first measurement procedure. For example, starting from $Q_t/Q_{opt} = 1.25$ at $\varepsilon = 4\%$, the percentage reduction of the specific delivery work and the flow of the pump are 20% and 11%, respectively, when comparing the third and the first procedures. In the third procedure (reducing air volume fraction from an initially high value), a large amount of air has been allowed to accumulate in the impeller passages before starting the measurement, and cannot easily be evacuated. Large gas pockets occur mainly due to flow separation, leading to low-pressure zones where air bubbles get trapped. After reducing the air flow rate, large gas accumulations cannot simply be evacuated with the flow; often, they will stay on the blades. To get rid of these large pockets, the air flow must be very significantly reduced, or high turbulence levels should be maintained for a sufficient time, as shown in Chapter 4. Therefore, the pump shows, in this case, a much lower performance for the third procedure compared to the first and the second procedure for exactly the "same" flow conditions.

Additionally, comparing the first and the second procedure as shown in Figure 5.6, hysteresis can again be seen. In this figure, the data of the first procedure are shown by filled symbols and dotted-curves trend lines; while the data of the second procedure are donated by empty symbols and dashed-curves trend lines. Here, considerable hysteresis can be seen, particularly at $\varepsilon = 4\%$ and $\varepsilon = 5\%$ in overload operation.

Pump surging and flow instabilities

The flow instabilities and pump surging are generally lower and less likely to occur in the semi-open impeller. It was only observed near the maximum value of Q_t/Q_{opt} for $\varepsilon = 4\%$ and $\varepsilon = 5\%$ as shown in Figure 5.5a. The surging points are presented in Figure 5.5 by gray-filled symbols.

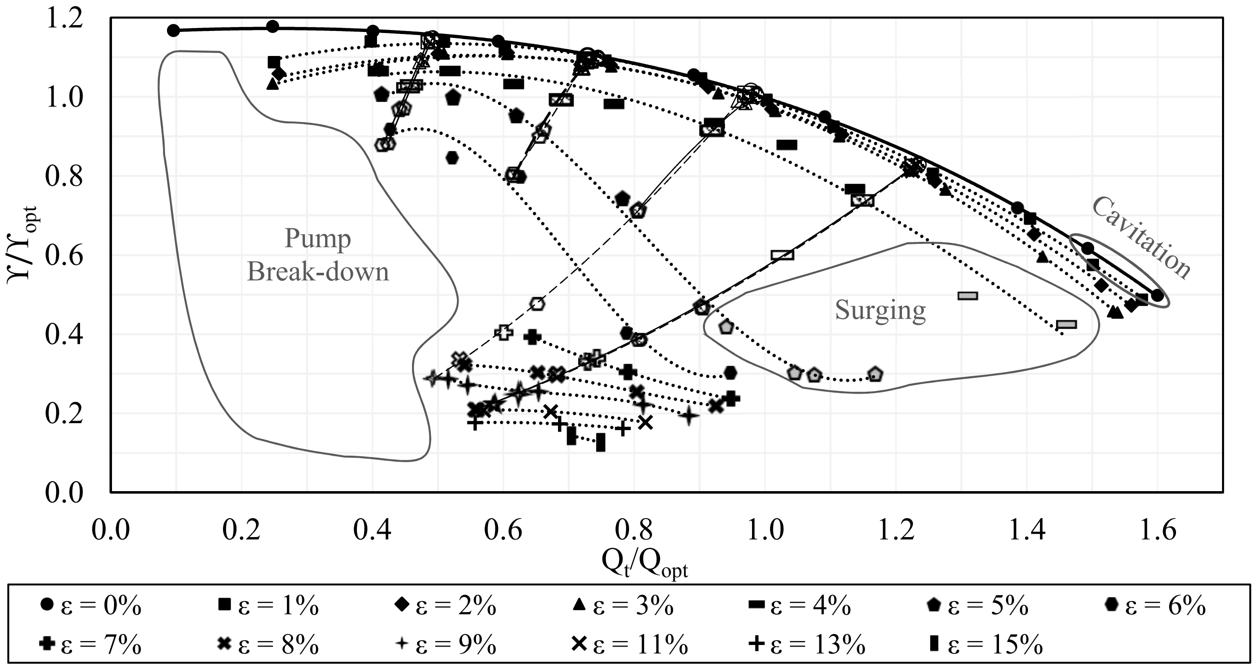

(a) Normalized specific delivery work

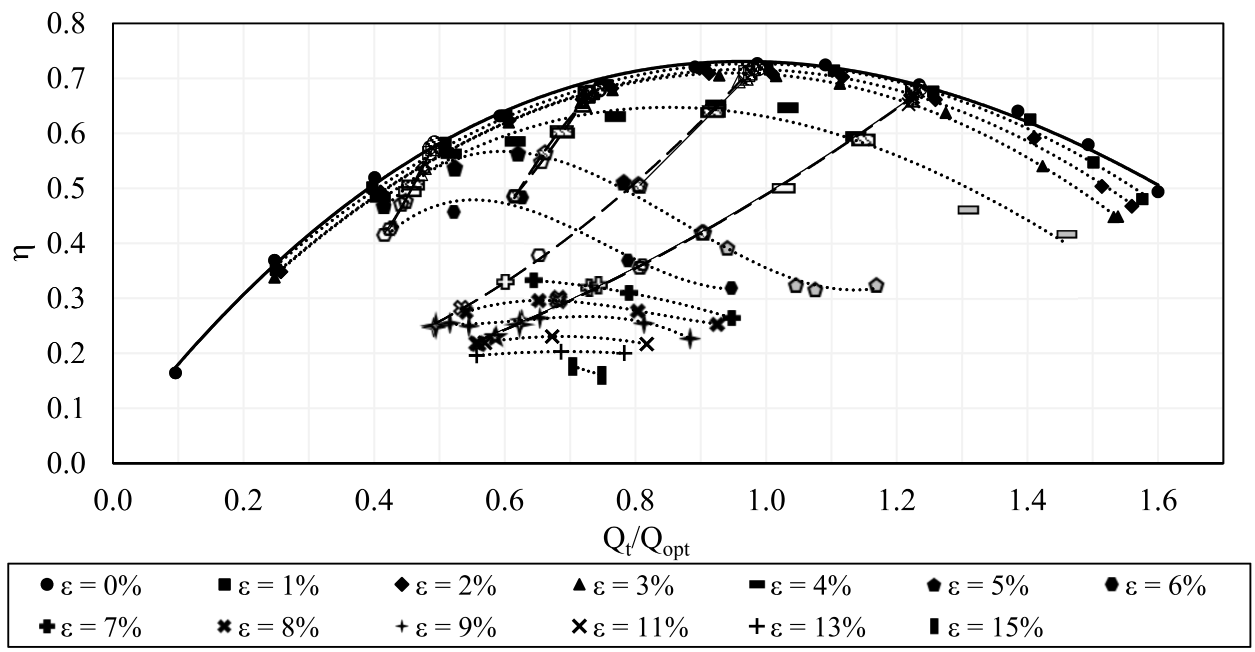

(b) Efficiency

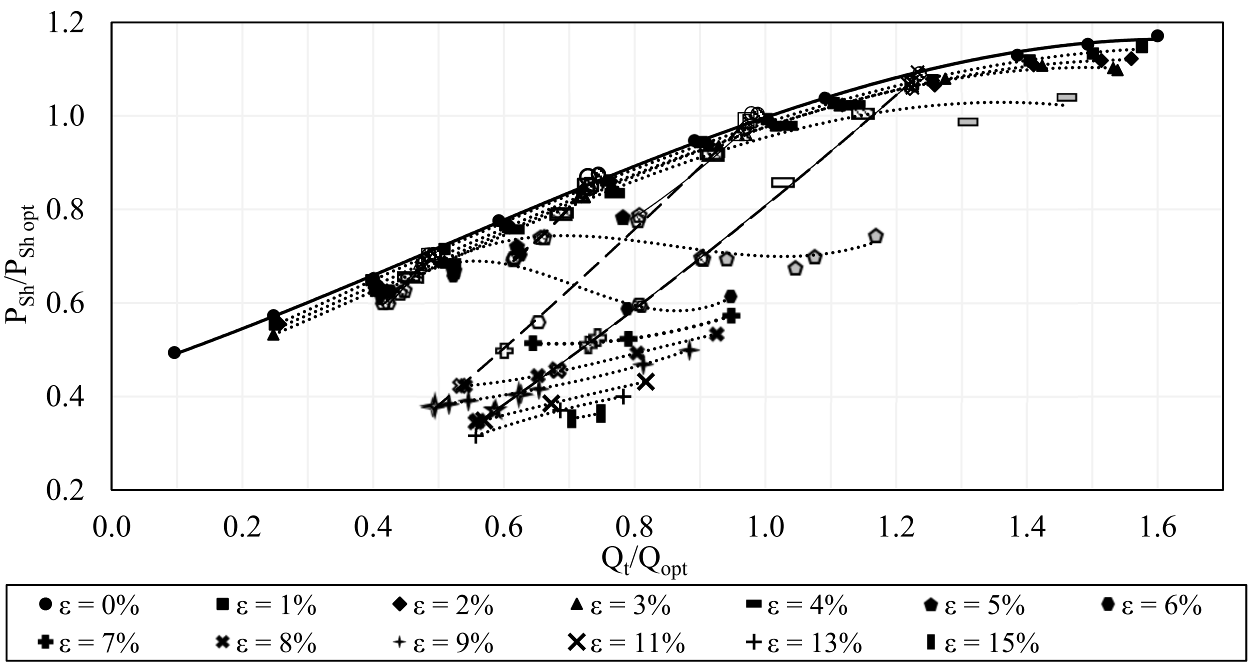

(c) Normalized shaft power

Figure 5.5: Performance curves of the semi-open impeller with the standard gap for constant gas volume fractions.

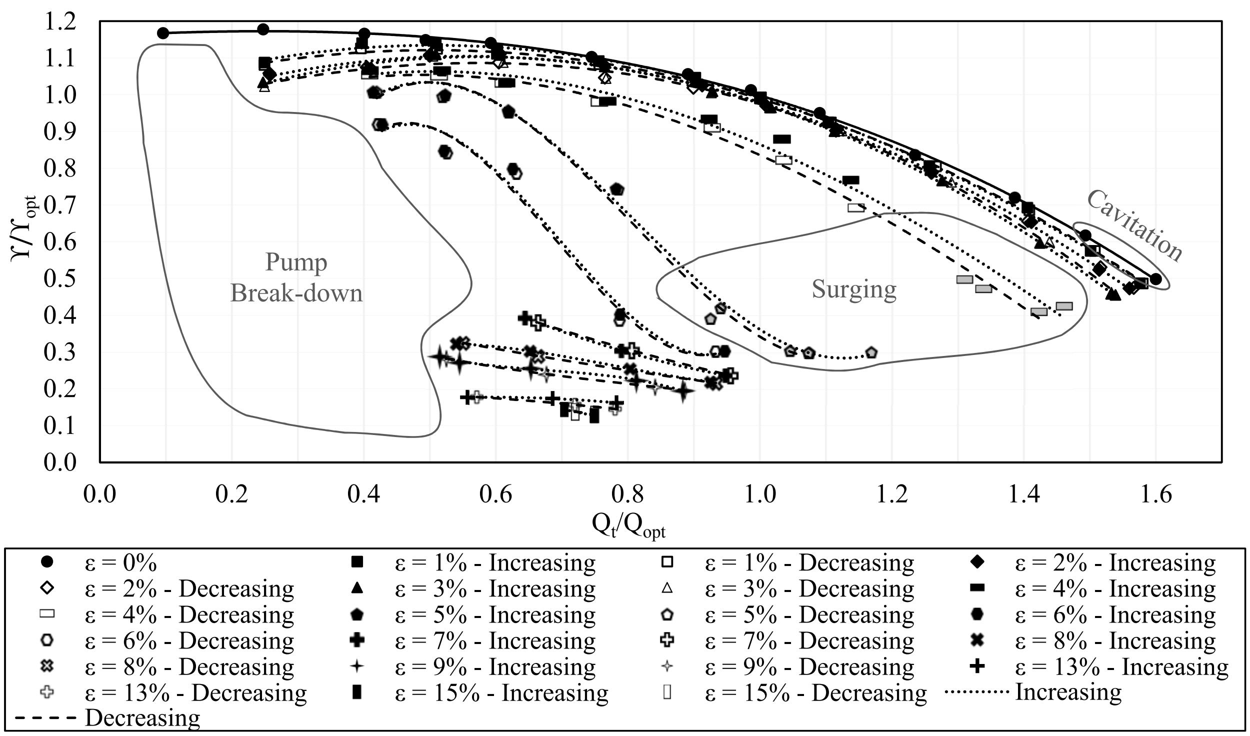

Figure 5.6: Performance of the semi-open impeller with the standard gap recorded by 1st (filled symbols & dotted curves) and 2nd (empty symbols & dashed curves) procedures.

5.4.3 Semi-open impeller with an increased gap

Performance curves

The normalized specific delivery work, the efficiency, and the normalized shaft power curves of the semi-open impeller with an increased tip clearance gap are shown in Figure 5.7. The performance is overall reduced due to the increased secondary flow through the gap. However, the increased leakage flow across the impeller blades provides in this case much higher resistance to gas accumulation. Subsequently, the performance deterioration is considerably more gradual, allowing the pump to keep its performance till higher gas volume fractions (up to $\varepsilon = 7\%$). Comparing Figure 5.5a and Figure 5.7a, it can be seen that for $5\% \leq \varepsilon \leq 7\%$, the semi-open impeller with the increased gap is a lot better than the standard-gap case, as the abrupt performance degradation is now revoked. Both cases show comparable performance in the range of $9\% \leq \varepsilon \leq 15\%$. Comparing data points of the first and the third experimental procedures, that are shown together in Figure 5.7, no hysteresis at all could be observed for the increased-gap case.

Figure 5.8 compares the normalized specific delivery work obtained by the first and the second procedures of the semi-open impeller with the increased tip clearance gap. Again, the important advantage of increasing the gap is that the curves of both procedures are almost identical, i.e. the performance hysteresis is here entirely eliminated. The increased secondary flow doesn't allow the air to accumulate in the impeller in all the considered experimental approaches.

Pump surging and flow instabilities

Further, the onset of pump surging and strong flow instabilities is delayed to higher gas contents for the increased gap. Nevertheless, the surging and the pump breakdown regions become here undesirably bigger. Finally, based on the observed tip clearance gap influence, the standard gap is recommended for single-phase flow and low gas volume fractions up to 3% or 4%, while the several advantages of the increased gap become very useful for $\varepsilon \geq 5\%$.

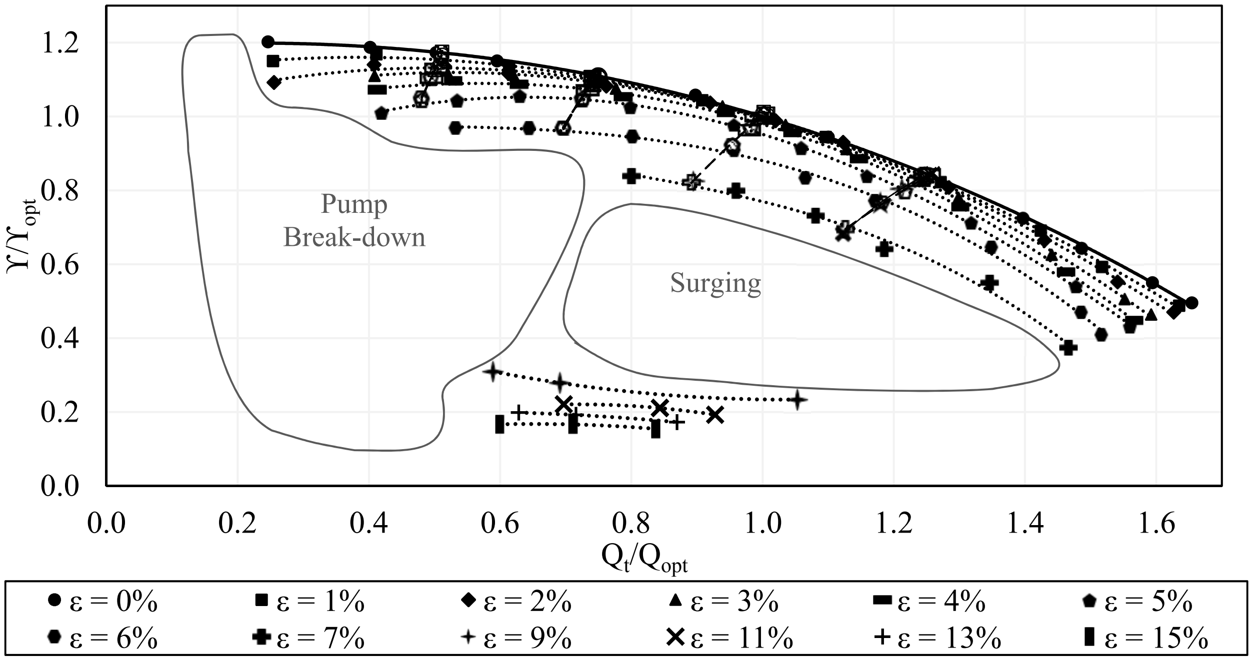

(a) Normalized specific delivery work

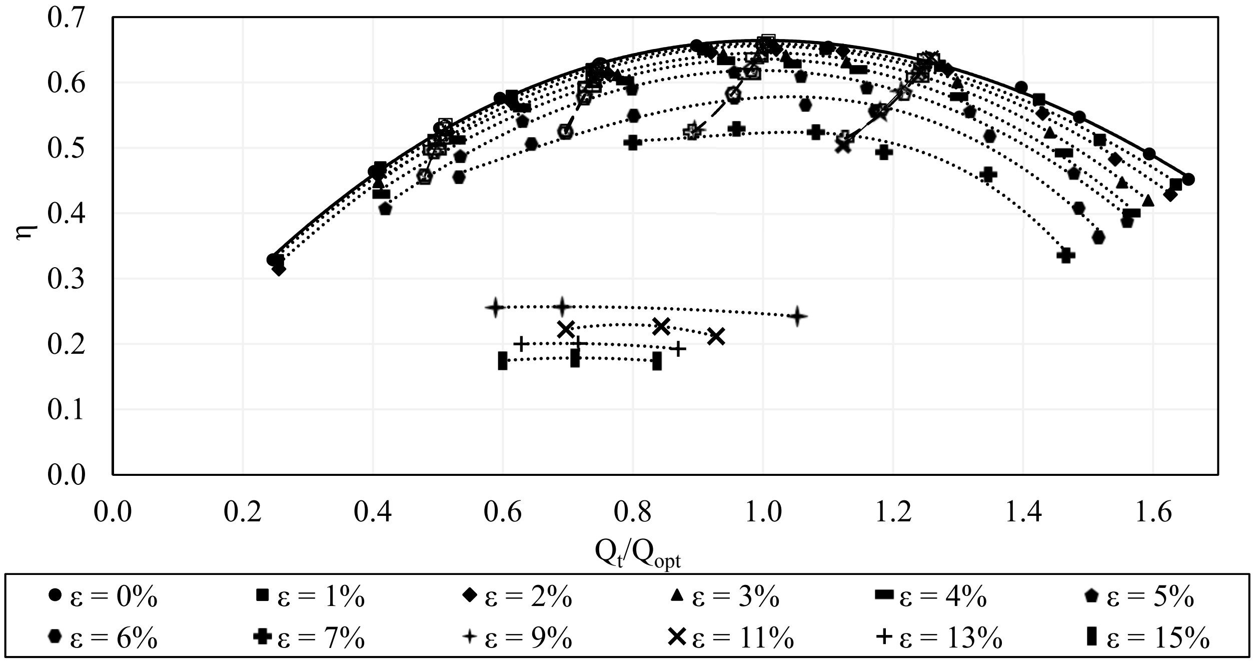

(b) Efficiency

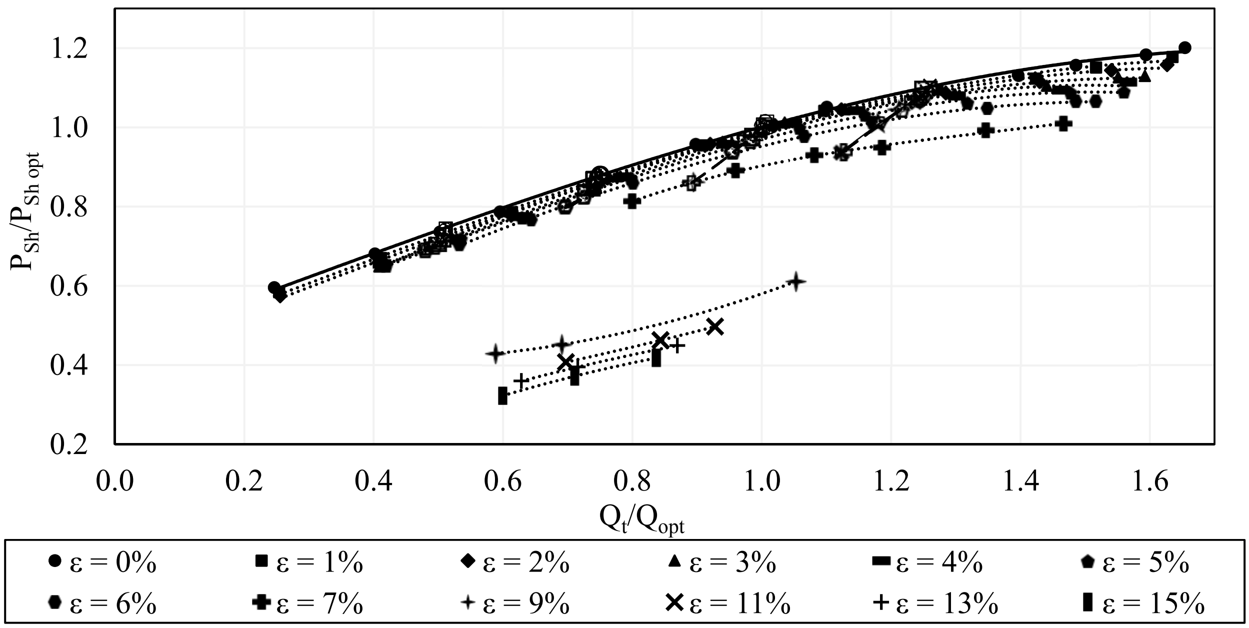

(c) Normalized shaft power

Figure 5.7: Performance curves of the semi-open impeller with the increased gap for constant gas volume fractions.

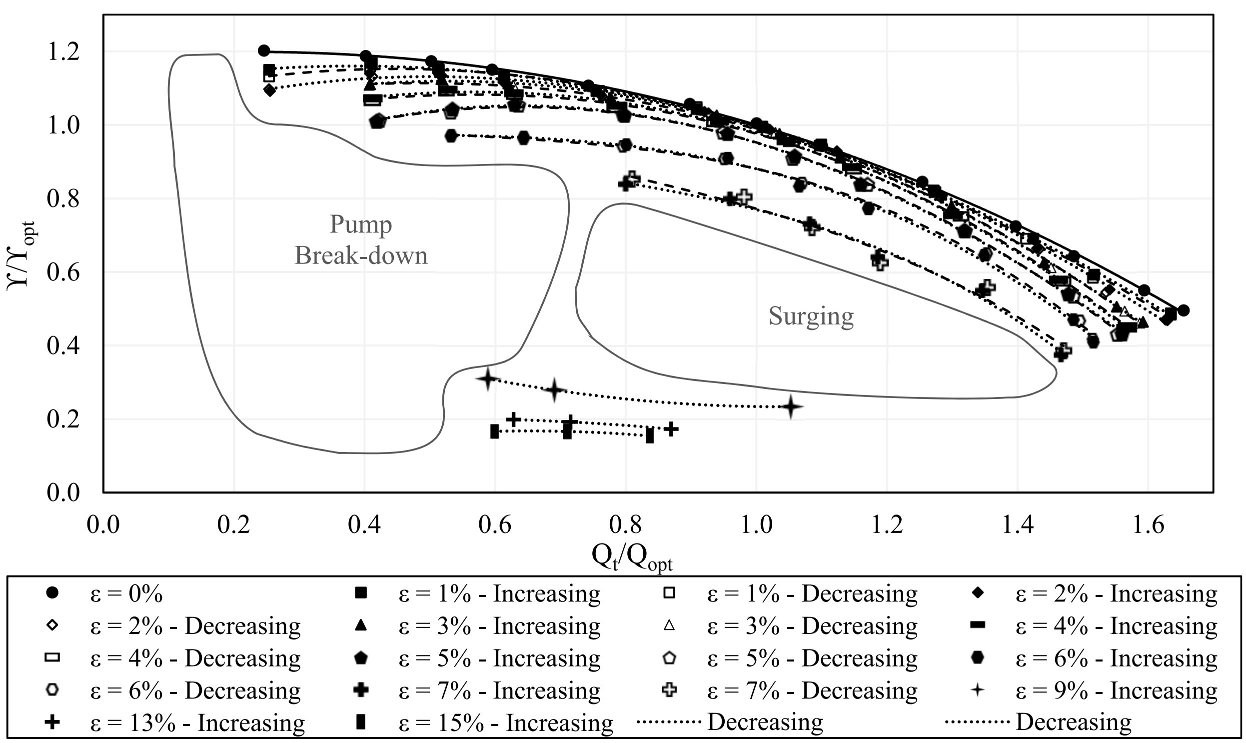

Figure 5.8: Performance of the semi-open impeller with the increased gap recorded by 1[st] (filled symbols and dotted curves) 2[nd] (empty symbols and dashed curves) procedures.

5.4.4 Semi-open impeller with a standard gap and inducer

Performance curves

The performance curves of the semi-open impeller with a standard gap and upstream inducer are shown in Figure 5.9. The results obtained by the first and the third experimental approaches are shown simultaneously in the figure. Again, the black-filled symbols represent the experimental data points obtained by the first procedure, while the hatched symbols show the data points recorded while increasing the air flow rate in the third approach, whereas the empty symbols donate the data recorded while decreasing back the air flow rate. Additionally, gray-filled symbols indicate the occurrence of strong flow instabilities. The trend lines of the data points of the first procedure are shown as dotted lines for each gas volume fraction.

As shown in Figure 5.9a, 5.9b, and 5.9c, by installing the upstream inducer the gas handling capability is to some extent improved along the whole flow range and in particular for $\varepsilon = 4\%$ and 5%. The performance is also considerably enhanced in the part-load range since the pump could keep its performance up to a gas volume fraction of $\varepsilon = 7\%$. However, for $\varepsilon \geq 8\%$ the performance is only insignificantly affected. The inducer increases the mixture pressure at the inlet of the impeller, which reduces the volume occupied by the gas phase in the impeller, delaying the performance deterioration. It offers furthermore a strong rotary action at the impeller inlet, preventing gas-phase to separate and accumulate at the top of the inlet pipe and at the impeller inlet, and thus providing better phase mixing for the pump. The reason that the inducer offers better enhancement in part-load conditions compared to that in overload conditions could be explained by using numerical simulations as shown later in Chapter 6. Analyzing the flow details in the inducer in overload conditions, it was found that the flow separates and forms several, axially-propagating vortices within the inducer, leading to a sudden fall in inducer's efficiency. Further, the two-phase simulations of the inducer showed that the mixing of the two phases, downstream the inducer, is very effective only in part-load conditions. However, in overload conditions, the residence time of the flow is much lower, and the inertia force is very high compared to the centrifugal force, reducing strongly the ability of the inducer to mix the two phases before the impeller inlet.

Comparing performance curves obtained by the first and the second procedure as shown in Figure 5.10, only weak performance hysteresis can be seen for $\varepsilon = 6\%$ and 7%. Therefore, the strong hysteresis effects of the semi-open impeller could be effectively damped for the cross-tests curves by installing the inducer. Similar to the previous figures, in Figure 5.10 the data of the first procedure are donated by filled symbols and dotted curves for the trend lines; while the data of the second procedure are shown by empty symbols and dashed curves for the trend lines.

Pump surging and flow instabilities

Here the results show that the upstream inducer could positively delay the pump surging to higher gas volume fractions, as shown in Figures 5.9a and 5.10. Nevertheless, the pump breakdown region is only slightly decreased as a result of installing the inducer. In Figures 5.9 and 5.10, the data points which indicate pump surging are shown by gray-filled symbols.

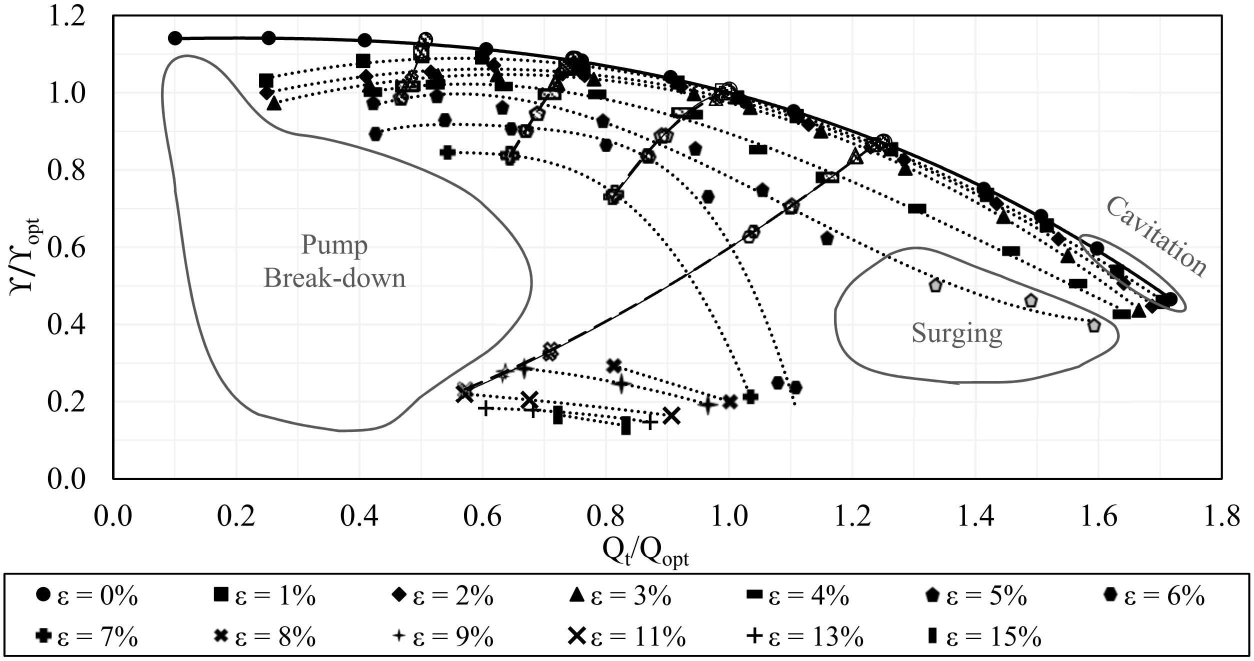

(a) Normalized specific delivery work

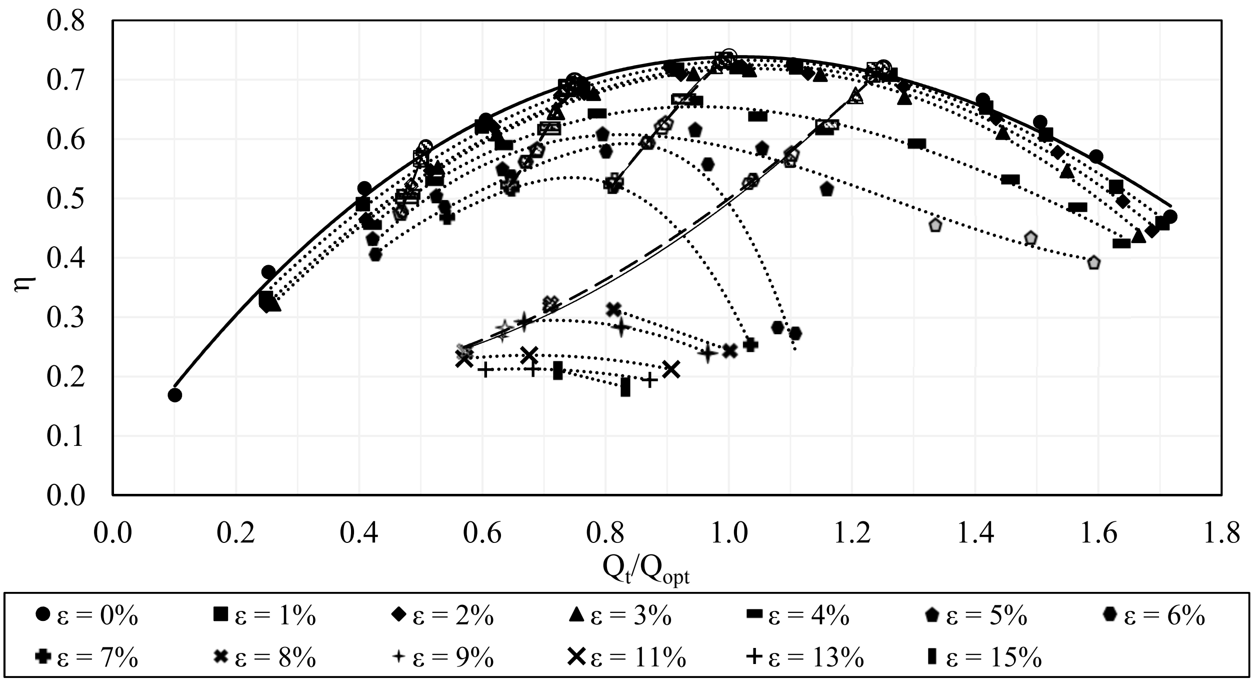

(b) Efficiency

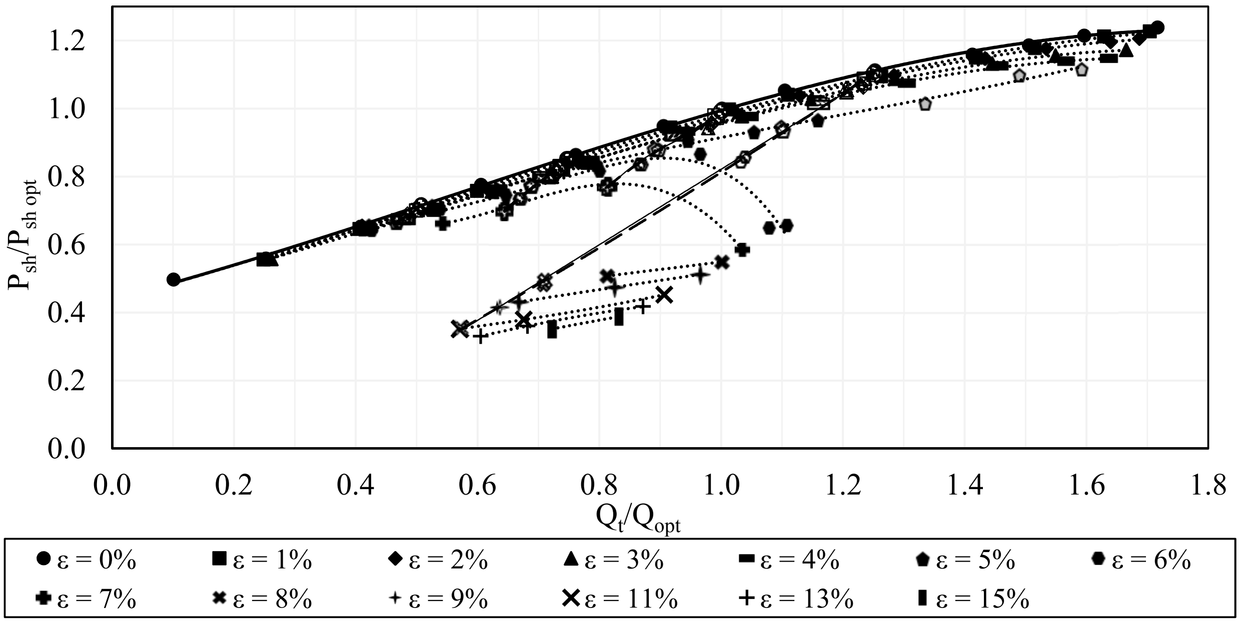

(c) Normalized shaft power

Figure 5.9: Performance curves of the semi-open impeller with the standard gap and inducer for constant gas volume fractions.

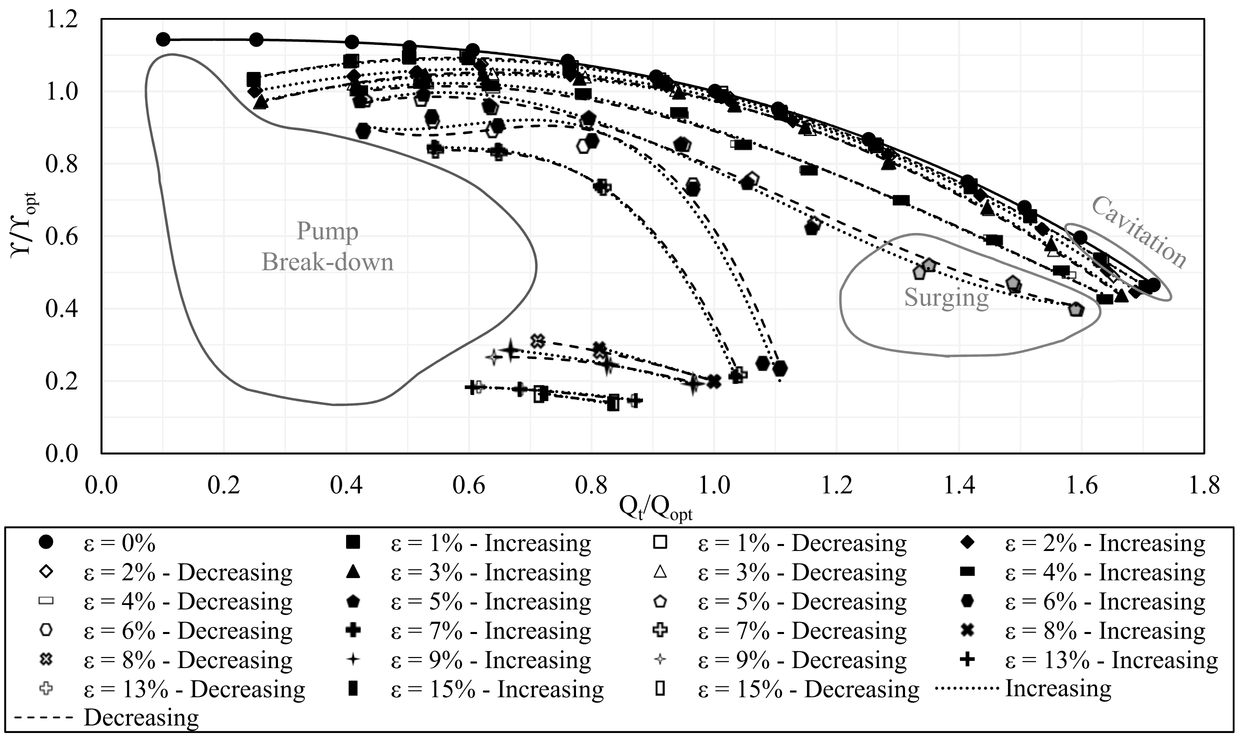

Figure 5.10: Performance of the semi-open impeller with the standard gap and inducer recorded by 1[nd] (filled symbols and dotted curves) and 2[nd] (empty symbols and dashed curves) procedures.

5.5 Performance degradation

The degradation behavior of the normalized specific delivery work of all cases is compared in Figure 5.11 when the gas volume fraction is increased. As shown in Figure 5.11a the normalized specific delivery work of the closed impeller is decreasing with a higher slope compared to the other cases, due to the easier gas accumulation. This happens up to a gas volume fraction of 6%, before strong flow instabilities and pump surging occur. Additionally, the slope of the degradation becomes slightly bigger in overload operation ($Q_w/Q_{opt} = 1.25$).

In Figure 5.11b the pump performance is almost flat up to a gas volume fraction of 3%. In this range, the normalized specific delivery work of the semi-open impeller is only slightly reduced in comparison to the single-phase conditions because of the gas accumulation resistance. However, for $\varepsilon \geq 4\%$, the pump performance sharply drops, since big pockets start to form quickly along the blades, reducing the ability of the pump to convey the mixture. In that event, the secondary flow is not high enough to disturb the rapid accumulation of gas.

As shown in Figure 5.11c, the performance degradation of the semi-open impeller with the increased gap shows more robust behavior up to $\varepsilon = 7\%$, before the pump surging starts afterwards. Again, for $\varepsilon \geq 8\%$, the semi-open impeller shows to some extent a better performance than the closed impeller, particularly when the increased tip clearance gap is employed. Now considering the semi-open impeller with the standard gap and inducer shown in Figure 5.11d, the inducer delays the sharp performance degradation to $\varepsilon = 5\%$ and $\varepsilon = 6\%$ for overload and nominal flow conditions, respectively. Furthermore, the inducer boosts the pump to have a very gradual performance reduction up to $\varepsilon = 7\%$ in part-load conditions, before a steep falling occurs at $\varepsilon \geq 8\%$.

No data points are shown for some specific gas volume fractions in the middle range in Figure 5.11, since the pump operation is characterized in this range by even stronger surging and severe vibrations, which could be destructive for the mechanical parts of the acrylic glass pump; therefore, such conditions could not be maintained for a sufficiently long time, hindering measurements.

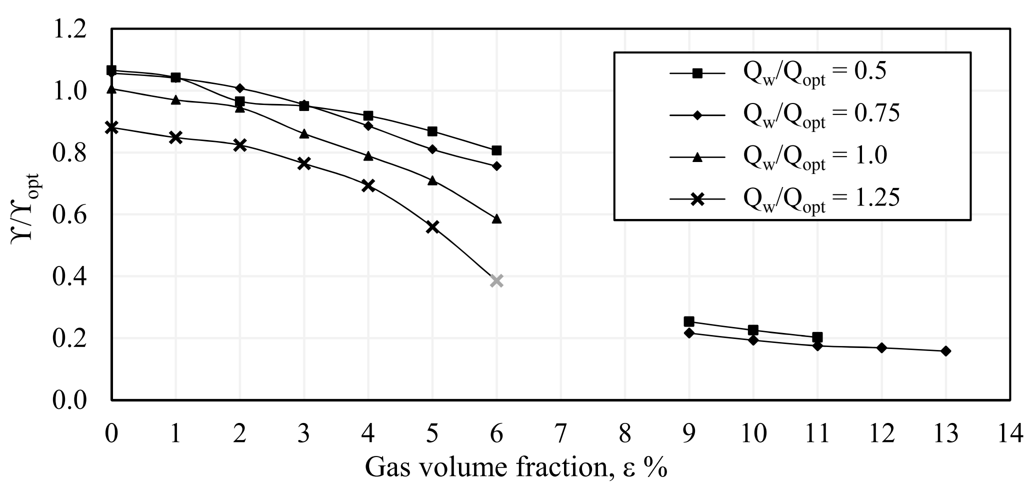

(a) Closed impeller

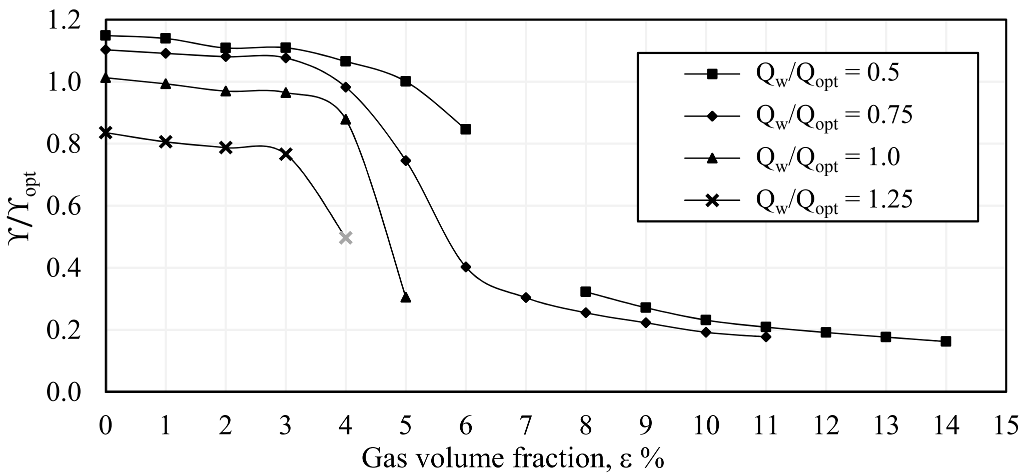

(b) Semi-open impeller with the standard gap

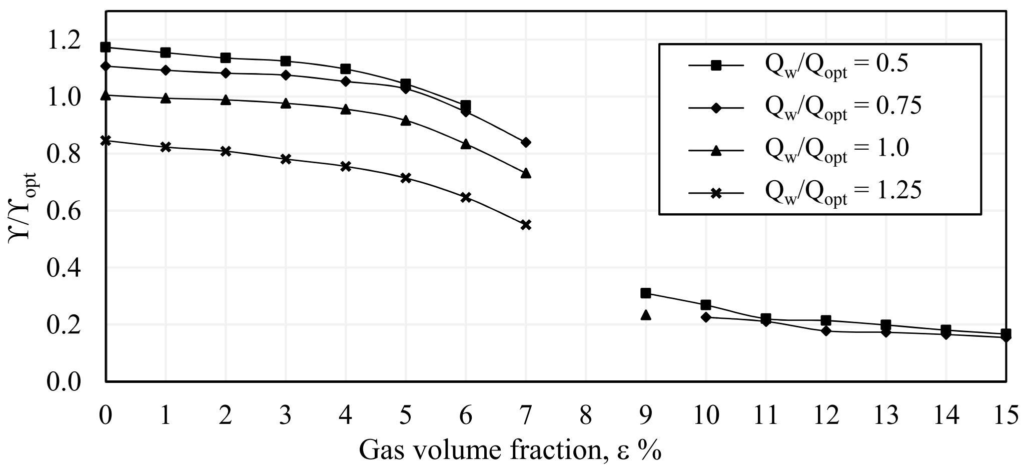

(c) Semi-open impeller with the increased gap

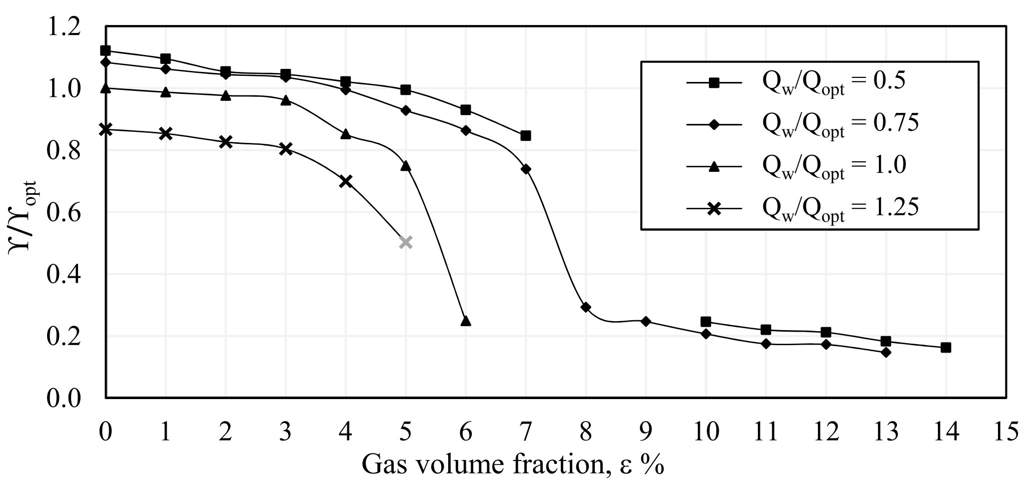

(d) Semi-open impeller with the standard gap and inducer

Figure 5.11: Degradation of the pump specific work as a function of gas volume fraction (gray symbols indicate surging conditions).

5.6 Pump surging and flow instabilities

To clarify how strong the flow instabilities are under surging conditions, they are compared to fluctuations induced by turbulence. Figure 5.12 shows the standard deviation of Q_w for the four cases. Initially, some tests were carried out to determine a suitable recording time and the number of sampling data for calculating standard deviations. At the end of these tests, it was found that 200 data points recorded at a frequency of 4 Hz are sufficient under conditions without surging. While, for data points in surging conditions, a longer sampling series (500 values, acquired at the same frequency of 4 Hz) was found to be necessary to track appropriately the strong, low-frequency flow variations under such conditions.

It can be seen that the standard deviation of the suction-water flow due to flow turbulence is usually around 0.5 m^3/h for single-phase flow and surging-free two-phase flow. In Figure 5.12a the standard deviation is slightly higher for $\varepsilon > 4\%$, which indicates increased instabilities in the flow. Then, the standard deviation abruptly jumps to values higher than 4.5 m^3/h for $\varepsilon > 5\%$, corresponding to the surging conditions mentioned above. For $\varepsilon \geq 9\%$, the pump performance and operational range significantly drop down, while the instabilities become weaker. For these conditions, the pump is no more capable of raising the head of the mixture as the impeller passages are mostly blocked by huge air cavities. The operation regime is known in this case as "Gas-Locking".

The flow instabilities are generally lower in the semi-open impeller for the whole range of gas volume fraction. Additionally, pump surging is less likely to occur. It was only observed in the semi-open impeller with the standard gap near the maximum value of Q_t/Q_{opt} for $\varepsilon =$ 4% and $\varepsilon = 5\%$, as shown in Figure 5.12b. Even in surging conditions, the standard deviation of the water flow for the semi-open impeller is lower than that for the closed impeller (note the different vertical scales). Furthermore, as shown in Figure 5.12c when the increased gap is used, the pump surging is delayed to higher gas volume fractions ($\varepsilon > 7\%$). By installing the inducer upstream of the semi-open impeller with the standard gap, the possible surging is delayed and strongly reduced to very low values as shown in Figure 5.12d. Therefore, to avoid the undesirable flow instabilities and pump surging, the semi-open impeller would be always recommended, and even better with an increased gap or an upstream inducer.

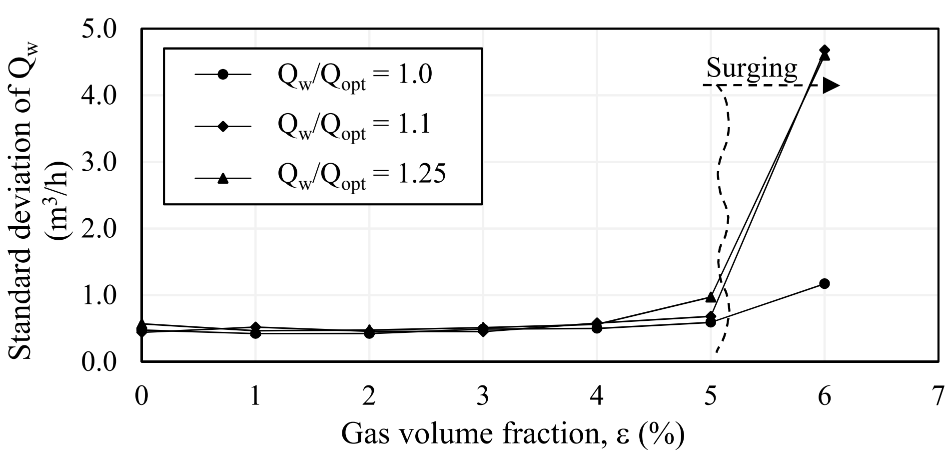

(a) Closed impeller

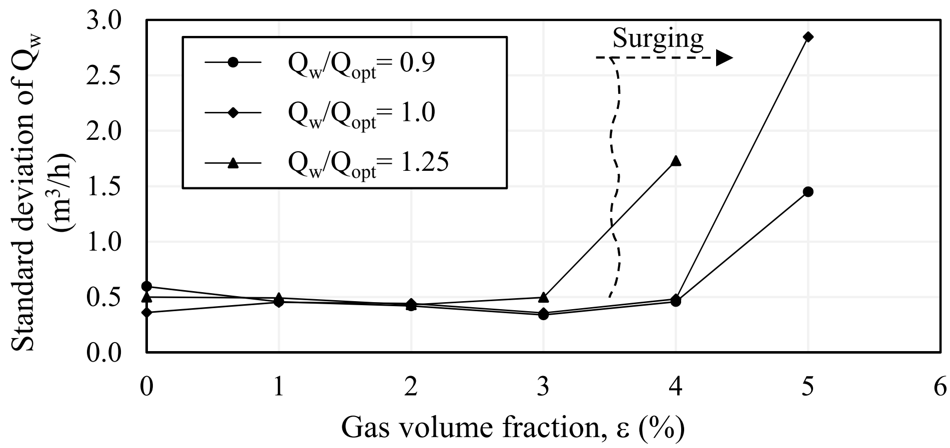

(b) Semi-open impeller with the standard gap

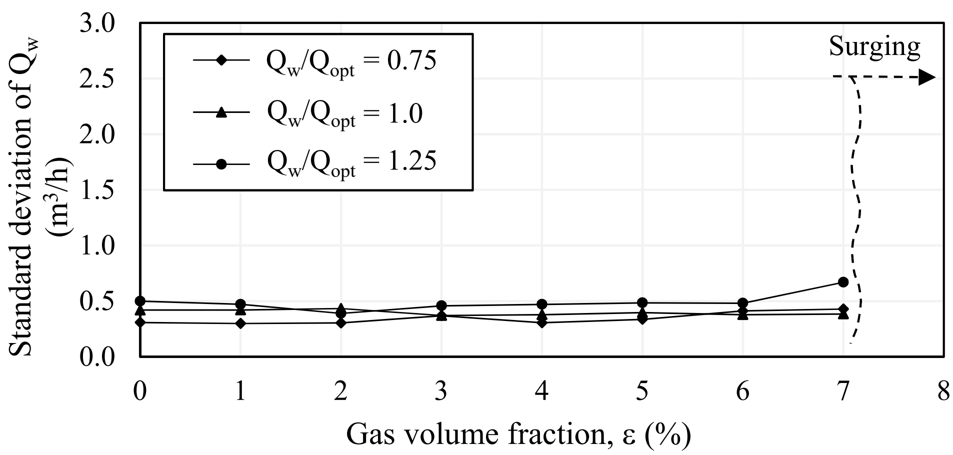

(c) Semi-open impeller with the increased gap

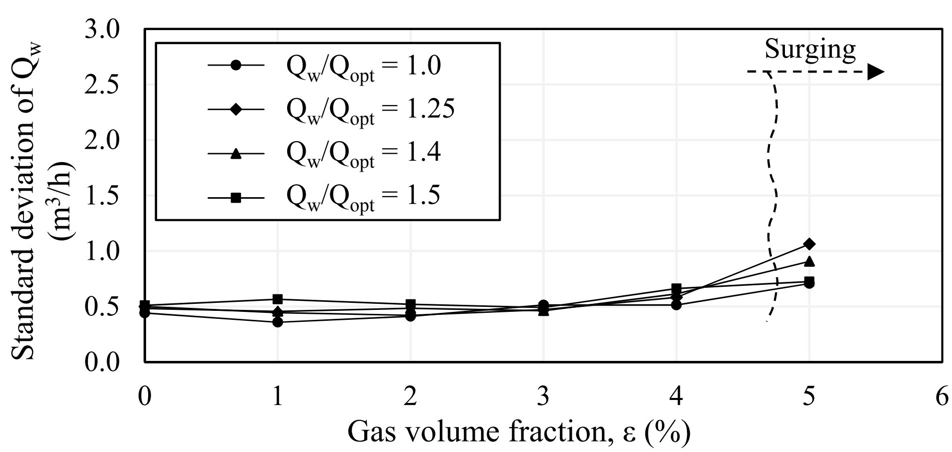

(d) Semi-open impeller with the standard gap and inducer

Figure 5.12: Standard deviation of the suction-water flow as a measure of flow instabilities.

5.7 Performance curves for constant air flow rates

Figure 5.13 shows the pump performance curves obtained for constant volume flow rates of inlet air. The performance curves of the closed impeller shown in Figure 5.13a become strongly unstable for high flow rates of air (Q_a = 80L/min), leading to system curves with two different operational points. This indicates that for high gas volume fractions, the pump surging can easily occur in the closed impeller.

Regarding the semi-open impeller with the standard gap, the characteristics curves show a reversed behavior at high air volume flow rates (Q_a = 60L/min and Q_a = 80L/min), as shown in Figure 5.13b. Nevertheless, the curves are not strongly unstable, confirming that the possibility of pump surging is, in general, lower in the semi-open impeller.

For the semi-open impeller with the increased gap as shown in Figure 5.13c, there are no significant unstable curves, and all curves are very close to the single-phase flow. Additionally, the surging is beneficially delayed to higher air contents as discussed before.

Now regarding the semi-open impeller with the standard gap and inducer, the generally improved performance is obviously seen when comparing Figure 5.13d with Figure 5.13b. The inducer allows the pump to transport higher flow rates of air with effective performance. Nevertheless, for very high flow rates of air (Q_a = 80L/min), there is no significant improvement in gas handling capability of the pump.

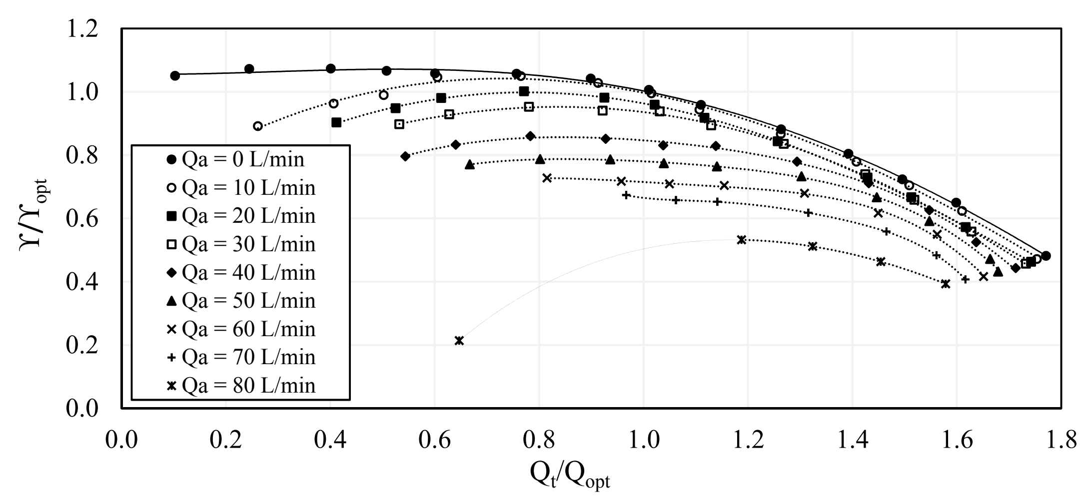

(a) Closed impeller

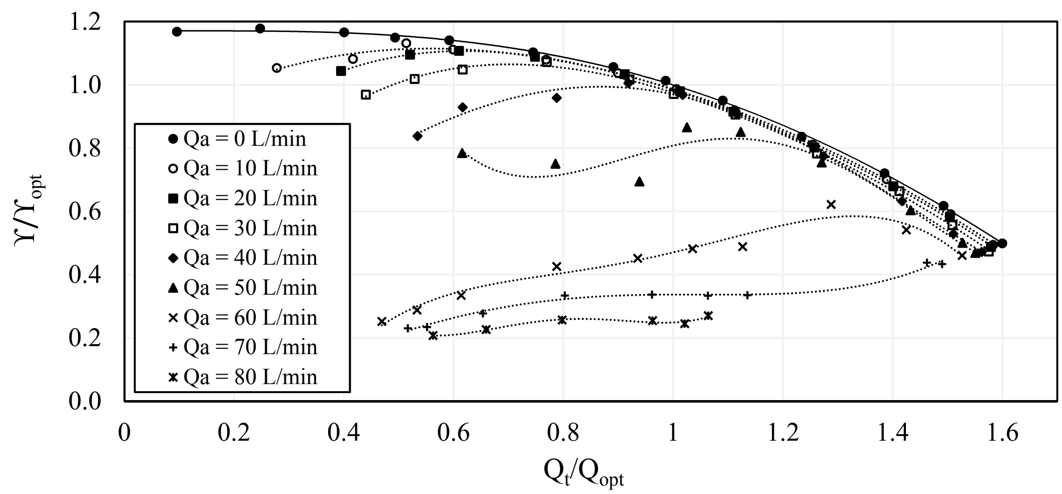

(b) Semi-open impeller with the standard gap

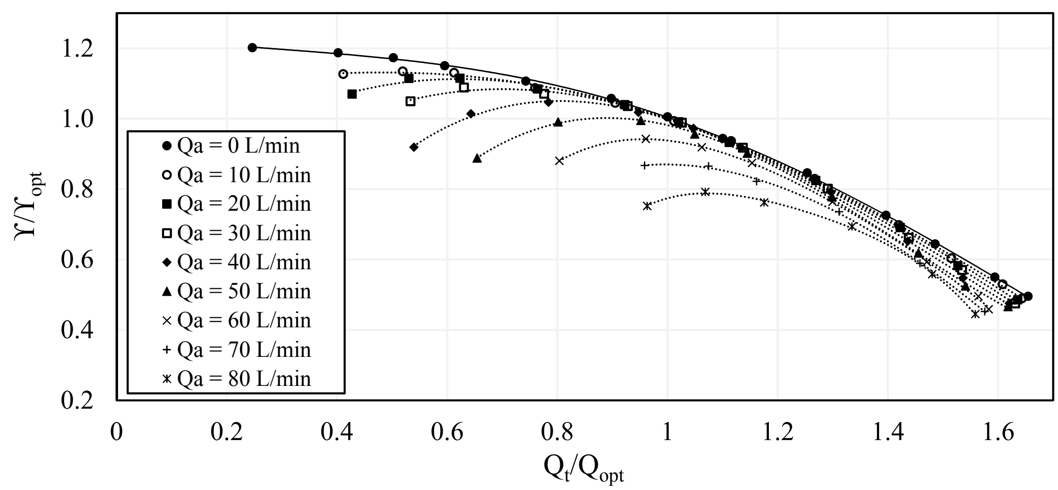

(c) Semi-open impeller with the increased gap

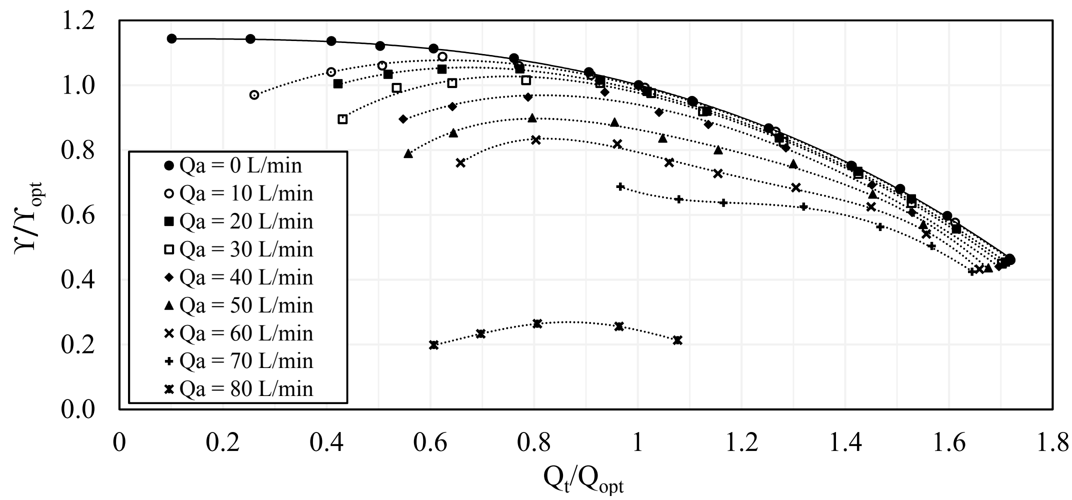

(d) Semi-open impeller with the standard gap and inducer

Figure 5.13: Normalized specific delivery work for constant flow rates of inlet air.

5.8 Visualization of flow regimes

As mentioned before, the whole pump casing and the impellers were manufactured from acrylic glass to allow a thorough flow visualization. The flow details have been observed and recorded by using a high-speed camera (Model: Imager pro HS 4M CCD) with a resolution of 2016 x 2016 pixels. Four LED lamps were installed peripherally around the pump casing to illuminate the flow (see Figure 3.5b). In this way, the gas-liquid interfaces appear brighter due to light reflections, making the bubbles and the accumulated gas clearly observable. For all the four cases considered in the present study, the two-phase flow regimes in the impeller passages are classified into five different flow regimes based on previous literature studies, which are shown in Figure 5.14, 5.15, 5.16, and 5.15. Not all the flow regimes were found when the semi-open impeller was employed. The performance of the pump depends strongly on the two-phase flow regime in the impeller. The important features of each flow regime are described below:

- **Bubbly flow** - The air bubbles are dispersed almost everywhere in the impeller passages without significant interaction between them. In most cases, the bubbles are denser near the suction side of the blades (see for example Figure 5.16a).
- **Agglomerated bubbles flow** - The air bubbles start to interact with each other by coalescence, forming bigger bubbles near both sides of the blades, and are usually denser near the suction side as shown in Figures 5.14b, 5.15b, 5.16b, and 5.17b.
- **Pocket flow** - A large gas pocket (cavity) steadily stands on the suction side of all blades, with only a slight fluctuation of its size.
- **Alternating pocket flow** - Appearance of a large gas pocket near to the blade entrance part, mostly on the blade suction side with strong unsteady properties (large oscillations, appearing/disappearing..). The pump performance is characterized in this regime by significantly increased instabilities.
- **Segregated flow** - The gas pocket is big enough to be connected throughout the blades till the impeller outer diameter. This regime was observed only in the closed impeller and did not occur in the semi-open impeller. Sometimes, an asymmetric gas ring was observed in front of the closed impeller, as can be seen in Figures 5.14e. Similar observations regarding the asymmetric gas ring were reported by A. Poullikkas [14].

Figures 5.14, 5.15, 5.16, and 5.17 compare sample images for all the possible flow regimes in each impeller, and when possible at similar flow conditions. As shown, the phase interaction and the shape of the accumulated gas are quite different among the four cases. Comparing all cases, the increased gas accumulation resistance of the semi-open impeller can be observed. For example in the bubbly flow regime shown in Figures 5.14a, 5.15a, 5.16a, and 5.17a, the mixture is more homogeneous in the semi-open impeller, since the bubbles are almost dispersed everywhere in the impeller. This effect is further enhanced in the case of increasing the gap or installing the inducer. Similar observations can be seen in the agglomerated bubbles and the pocket flow regimes.

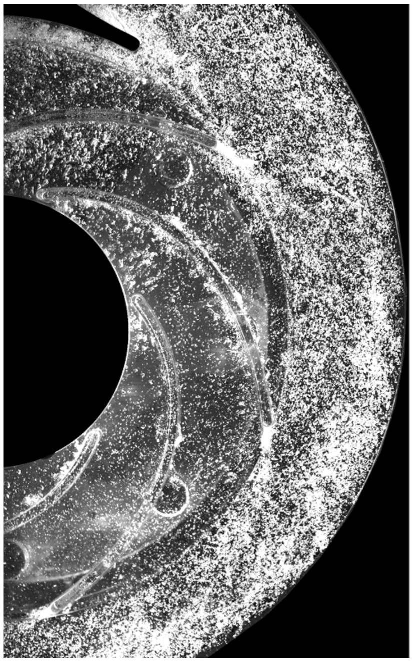

$\varepsilon = 1\%$, $\frac{Q_t}{Q_{opt}} = 1.5$

(a) Bubbly

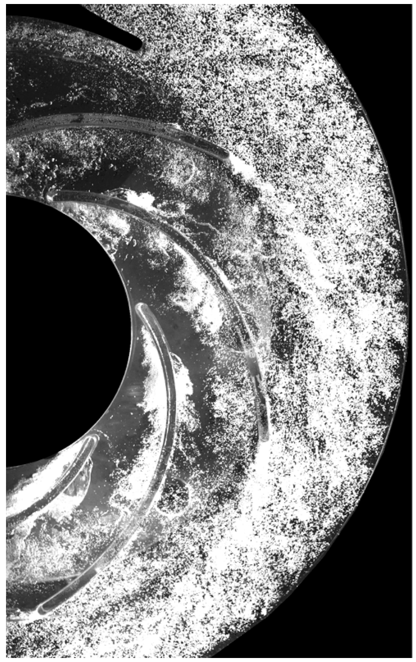

$\varepsilon = 2\%$, $\frac{Q_t}{Q_{opt}} = 0.9$

(b) Agglomerated bubbles

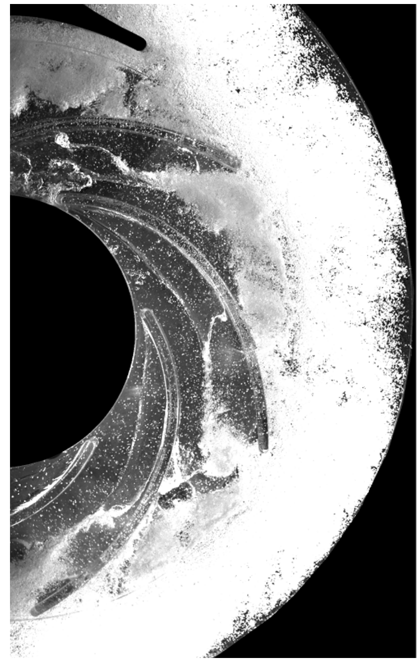

$\varepsilon = 6\%$, $\frac{Q_t}{Q_{opt}} = 0.8$

(c) Pocket

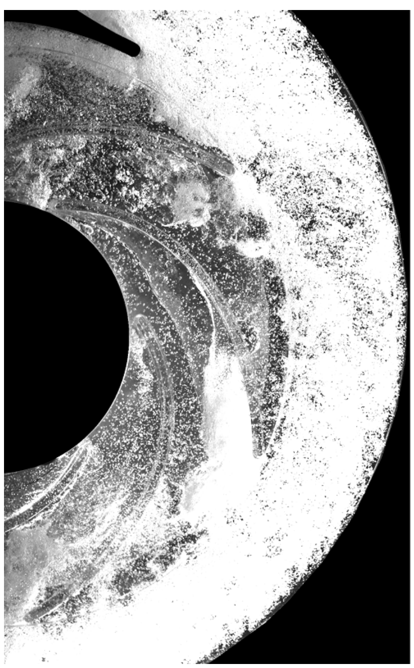

$\varepsilon = 4\%$, $\frac{Q_t}{Q_{opt}} = 1.45$

(d) Alternating pocket

$\varepsilon = 9\%$, $\frac{Q_t}{Q_{opt}} = 0.6$

(e) Segregated

Figure 5.14: Different flow regimes observed in the closed impeller passages.

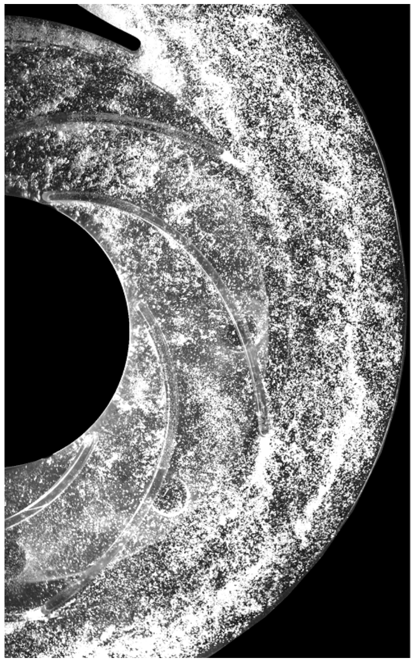

$\varepsilon = 1\%$, $\frac{Q_t}{Q_{opt}} = 1.5$

(a) Bubbly

$\varepsilon = 2\%$, $\frac{Q_t}{Q_{opt}} = 0.9$

(b) Agglomerated bubbles

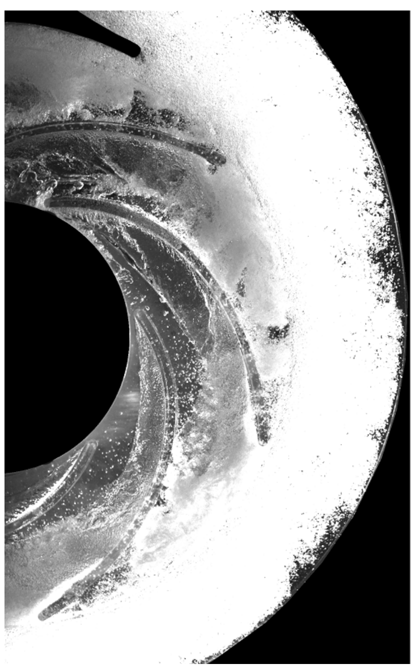

$\varepsilon = 6\%$, $\frac{Q_t}{Q_{opt}} = 0.8$

(c) Pocket

$\varepsilon = 4\%$, $\frac{Q_t}{Q_{opt}} = 1.45$

(d) Alternating pocket

Figure 5.15: Different flow regimes observed in the semi-open impeller passages with the standard gap.

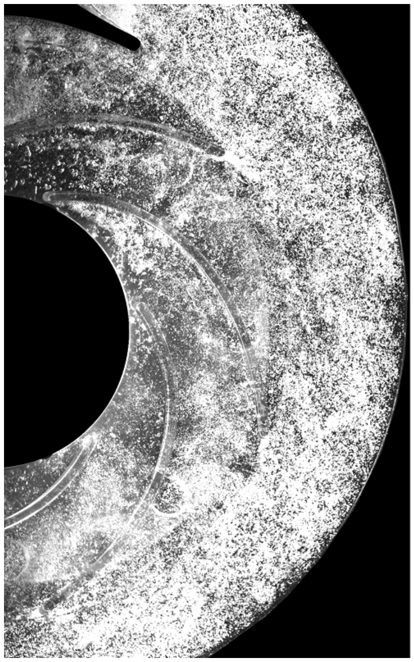

$\varepsilon = 1\%$, $\frac{Q_t}{Q_{opt}} = 1.5$

(a) Bubbly

$\varepsilon = 5\%$, $\frac{Q_t}{Q_{opt}} = 0.9$

(b) Agglomerated bubbles

$\varepsilon = 6\%$, $\frac{Q_t}{Q_{opt}} = 0.8$

(c) Pocket

Figure 5.16: Different flow regimes observed in the semi-open impeller passages with the increased gap.

$\varepsilon = 1\%$, $\frac{Q_t}{Q_{opt}} = 1.5$

(a) Bubbly

$\varepsilon = 2\%$, $\frac{Q_t}{Q_{opt}} = 0.9$

(b) Agglomerated bubbles

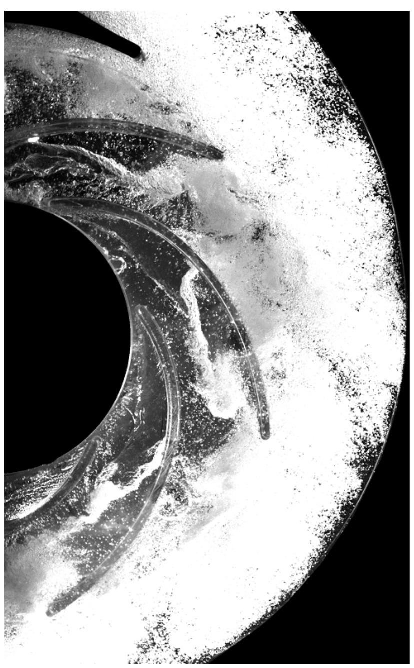

$\varepsilon = 6\%$, $\frac{Q_t}{Q_{opt}} = 0.8$

(c) Pocket

$\varepsilon = 4\%$, $\frac{Q_t}{Q_{opt}} = 1.45$

(d) Alternating pocket

Figure 5.17: Different flow regimes observed in the semi-open impeller passages with the standard gap and inducer.

Figures 5.18, 5.19, 5.20, and 5.21 show detailed maps for the flow regimes located on the performance curves of each case. The undesirable phenomena (breakdown, surging, cavitation…) are also shown, generating a detailed map combined with the pump performance. Accordingly, the behavior and the discontinuities of the performance could be better understood, as a function of the flow regime. Regions, where the pump performance breaks down, can be also highlighted in this way. In Figure 5.18 and Figure 5.19, it can be observed that the two maps show some similarities. The bubbly flow regime occurs in both cases mainly at overload flow conditions and low gas volume fraction ($\varepsilon < 2\%$). Nevertheless, the bubbly flow regime occurs for a wider range of flow conditions in the semi-open impeller, as a result of the higher shear rates exerted on the blades and of the secondary flow.

The alternating pocket flow regimes appear in both impellers in part-load as well as in overload flow conditions. However, the alternating pocket flow regimes are overall smaller in the semi-open impeller, corroborating the reduced flow instabilities. In the closed impeller, there are more bubble interactions; hence, the agglomerated bubbles flow regime is found more often compared to the semi-open impeller. The pocket flow regime appears earlier in the closed impeller, starting from $\varepsilon \approx 3\%$ and showing no remarkable change (no strong discontinuities) in the performance. However, as soon as the pocket appears in the semi-open impeller (starting from $\varepsilon \approx 4\%$), an abrupt reduction in the pump performance can be seen in particular around rated conditions and for overload. Afterwards, as the gas volume fraction is increased from $\varepsilon = 4$ to 7%, the semi-open impeller performance shows several discontinuities in the pocket flow regime. In the surging region of each impeller, the size of the accumulated gas varies strongly as a result of the strongly fluctuating pumping behavior. Just after the surging region for $\varepsilon \geq 9\%$ in the closed impeller, the cavity is large enough to cover the whole length of the blade, reaching down to the outer diameter of the closed impeller. This two-phase flow pattern corresponds to a segregated regime (Figure 5.14e). This regime is not observed in the three other cases of the semi-open impeller because of the intense bubble break-up that occurs near impeller outlet.

Now, increasing the gap causes significant effects on the flow regimes of the semi-open impeller as shown in Figure 5.20. For instance, the secondary flow becomes higher and the gas accumulation resistance increases, resulting in a bigger bubbly flow regime. Here at low gas volume fractions, the bubbly flow regime can take place along the performance curves, even in part-load conditions, which was not possible in case of the standard gap (Figure 5.19). Similar observations can be seen for the agglomerated bubbles flow regime, which is now spread over the full flow range just after the bubble flow regime. Afterwards, the first gas pocket starts only at a gas volume fraction of $\varepsilon = 6\%$, affirming the higher gas accumulation resistance. Additionally, the occurrence of the alternating pocket flow regime is merely limited to the surging region. However, pump performance shows unfavourably larger pump break-down and surging regions compared to the standard gap case.

Comparing Figure 5.21 and Figure 5.19, it can be seen that the upstream inducer causes only minor changes to the location of the flow regimes of the semi-open impeller with the standard gap. The only remarkable change is that part of the bubbly flow regime without inducer is converted to agglomerated flow regime in overload conditions after installing the inducer, due to the slightly reduced performance (flow rate) in this range, as discussed previously. Otherwise, the size and location of other flow regimes are comparable.

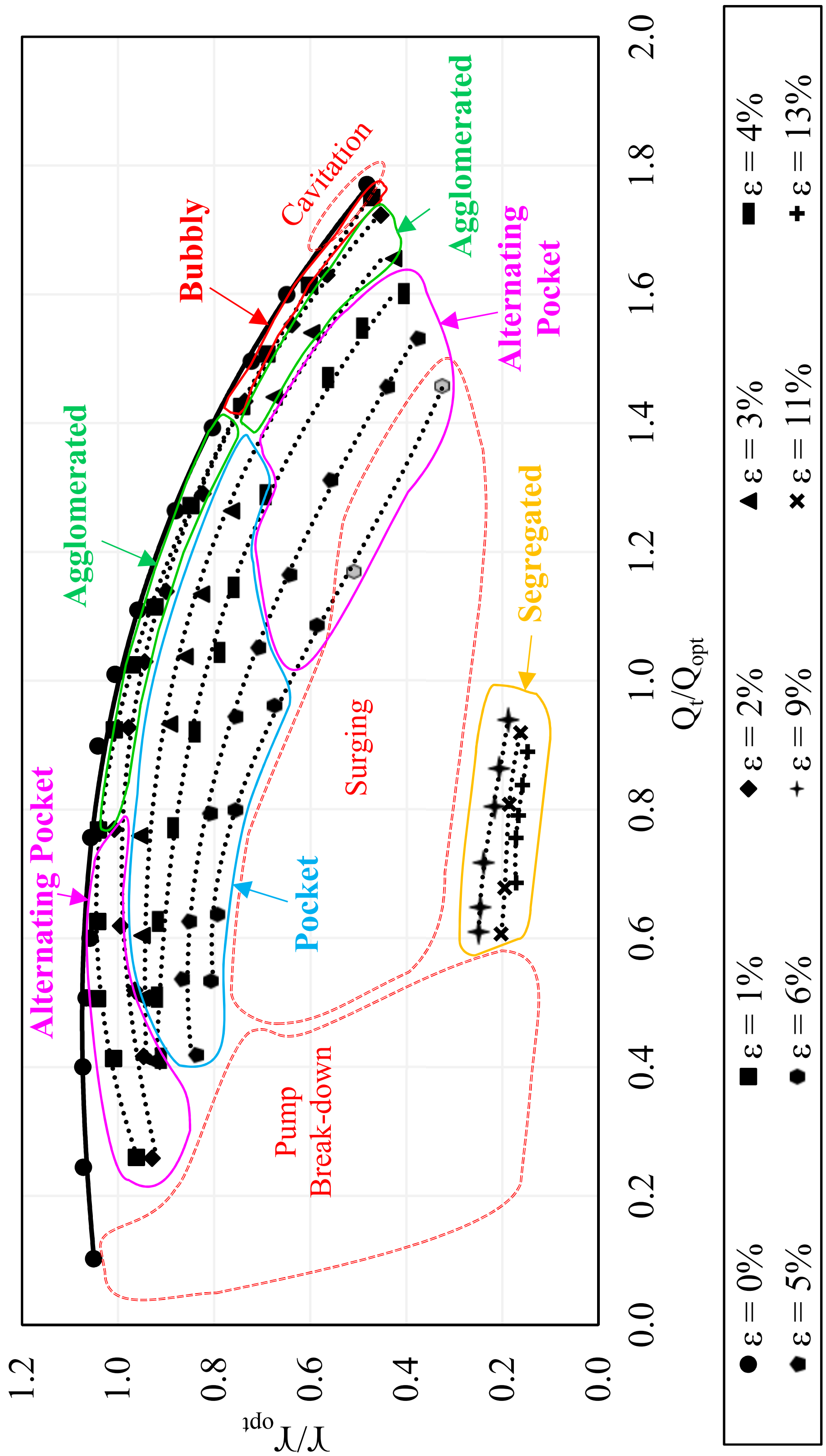

Figure 5.18: Flow regimes of the two-phase flow in the closed impeller.

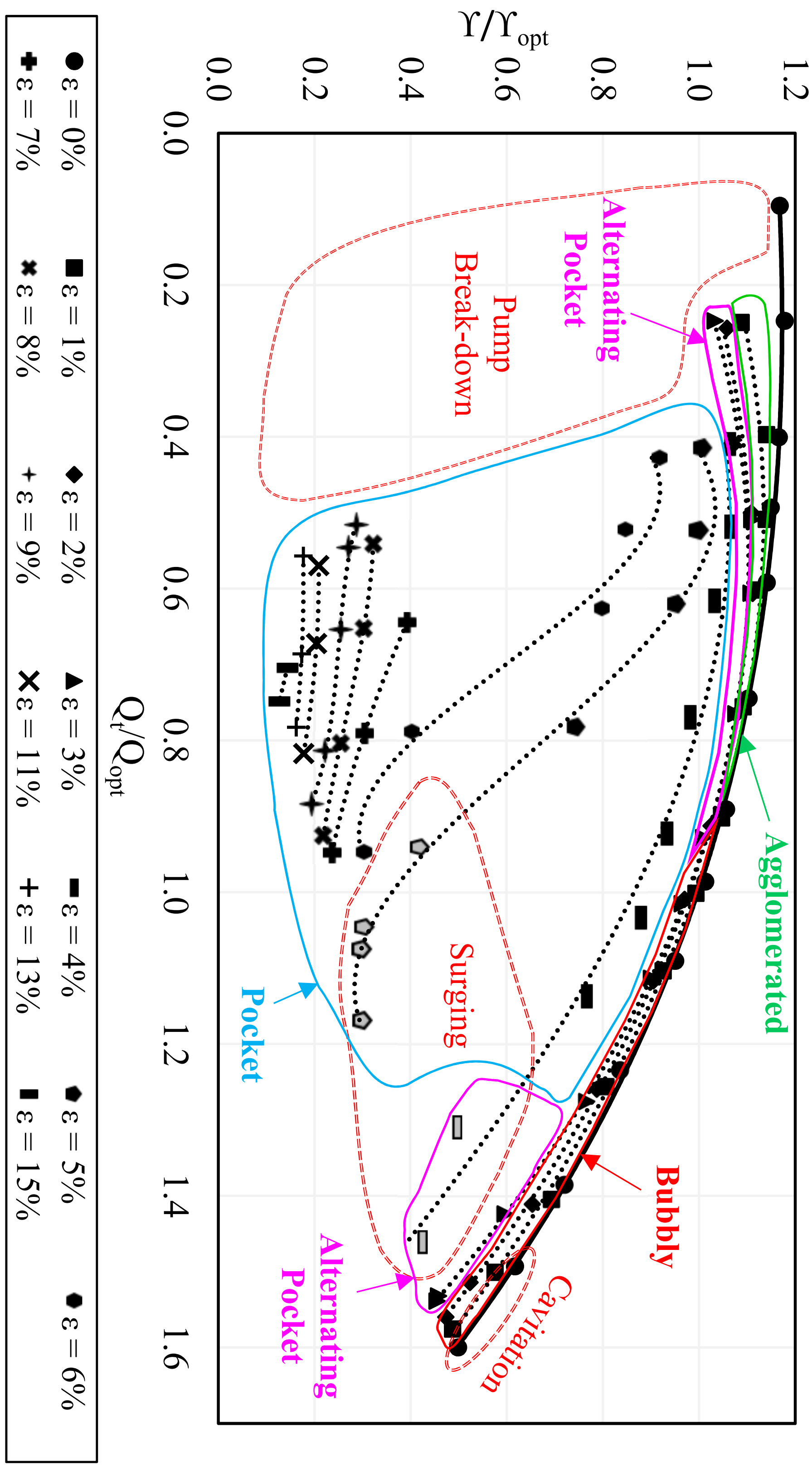

Figure 5.19: Flow regimes of the two-phase flow in the semi-open impeller with the standard gap.

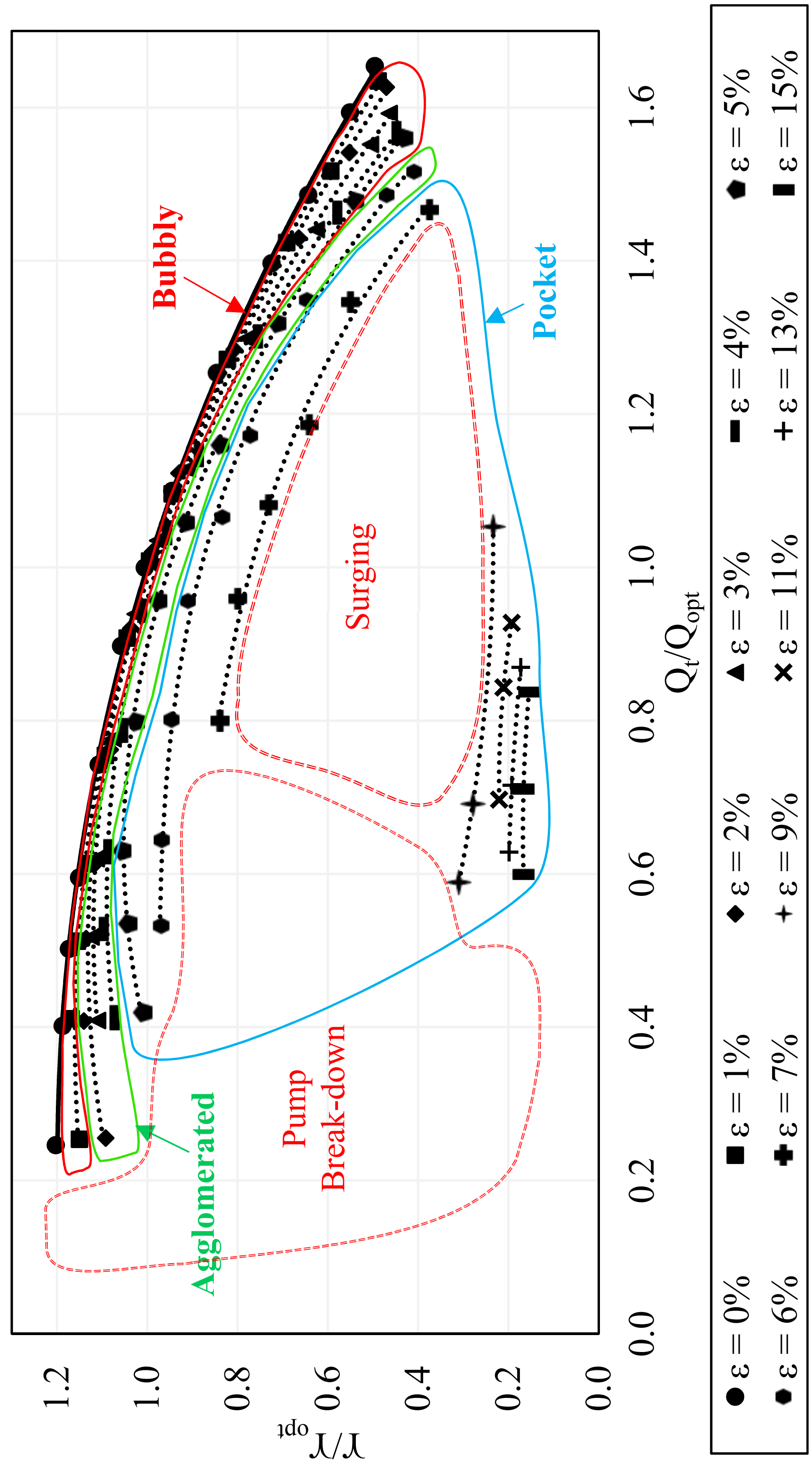

Figure 5.20: Flow regimes of the two-phase flow in the semi-open impeller with the increased gap.

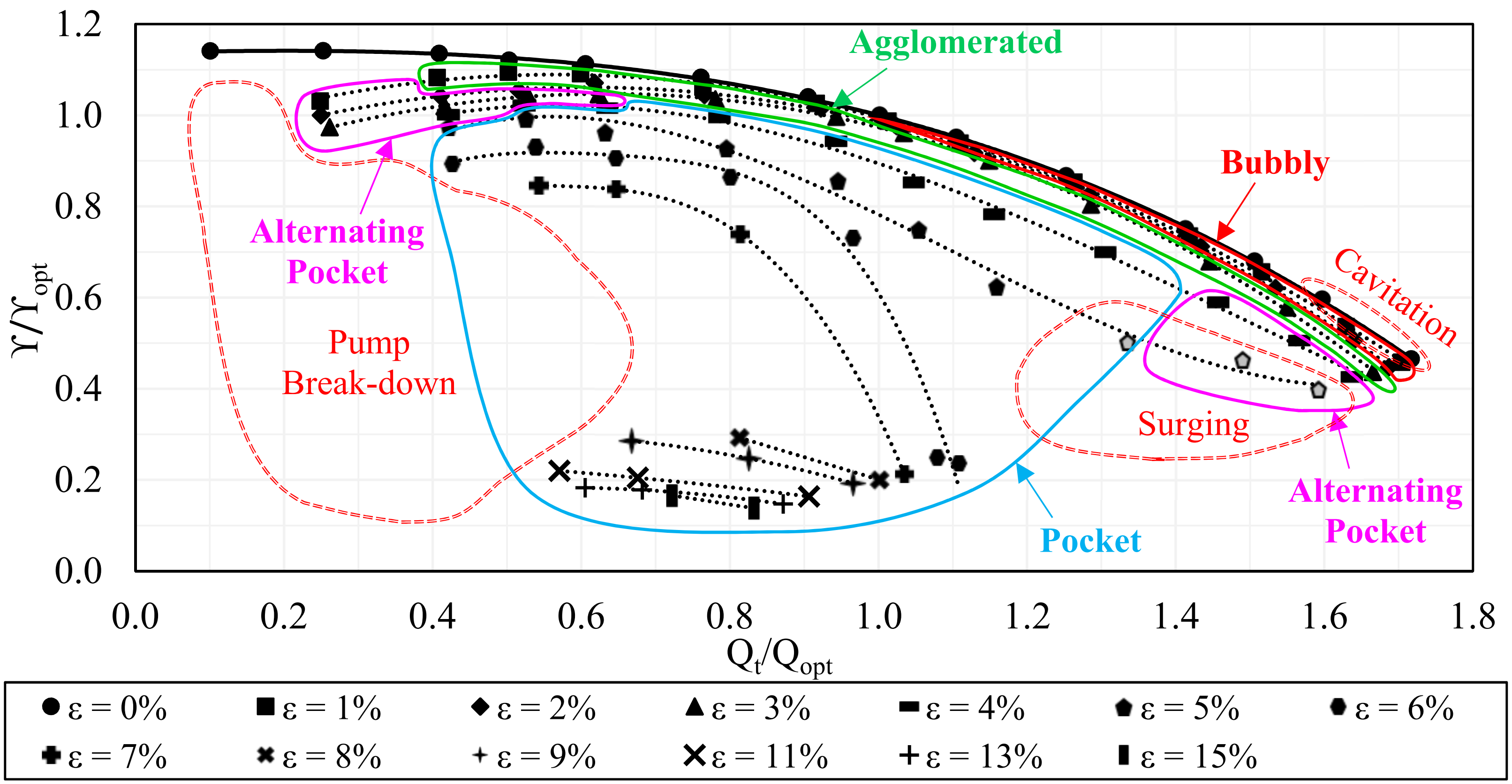

Figure 5.21: Flow regimes of the two-phase flow in the semi-open impeller with the standard gap and inducer.

5.9 Detailed optical measurements

Selected two-phase flow cases are analyzed in this section, providing more details of the flow pattern in the impeller. Particularly, the time-averaged size of gas accumulation in the impeller is obtained. The information shown here is also very convenient to be compared with CFD simulations based on Reynolds-averaged Navier-Stokes equations (RANS equations). To obtain the time-averaged size of the accumulated gas zones in the impeller passages, cyclic image recording is used with the same frequency of impeller rotation, acquiring always one image per rotation. Afterwards, an average image is deduced from 300 recorded images of the flow. The accumulated gas shows in this event almost a stable size with only minor changes in the boundaries. The captured gas accumulations are then colored to make it clearly distinguishable from the water phase.

This averaging technique is similar to that already used previously in Section 4.3 to analyze the size of the accumulated gas in two-phase air-water flows in the diverging channel. Namely, 4 cases in the (steady) pocket flow regime have been selected together with 1 point in the agglomerated bubbles flow regime. The analysis involves three points for the closed impeller in addition to two points for the semi-open impeller with the standard gap. All data points have been considered, when the air percentage is gradually increased starting from the optimal single-phase operation of the pump. Detailed information about those selected points are shown in Table 5.2 and Figure 5.22.

Figure 5.23 to 5.27 show sample instantaneous images and averaged images of all selected points. The gas accumulation is calculated and colored in red, while the total area between two impeller blades (impeller channel area) is hatched by blue lines in the averaged images, which is done by AUTOCAD. The area of the gas accumulation of each point is given in Table 5.2 as a percentage of the impeller channel area. In point 1, a small gas pocket is seen firstly on the pressure side of the blades, which travels to the blade suction surface as the gas volume fraction increases in the pocket flow regime as shown in the images of the further points. This can be due to the change of the incident angle of the flow as shown previously in Figure 2.5.

Table 5.2: Selected points for detailed optical measurements.

Point	Impeller type	Flow regime	Gas volume fraction ε %	Qt/Q_{opt}	Υ/Υ_{opt}	Efficiency η %	Area of gas accumulation per channel area %
1	Closed impeller	Agglomerated bubbles flow	1	0.99	0.98	0.72	0.52
2		Pocket flow	3	0.94	0.89	0.66	5.85
3		Pocket flow	5	0.87	0.78	0.58	10.73
4	Semi-open impeller with standard gap	Pocket flow	4	0.92	0.91	0.64	8.16
5		Pocket flow	5	0.81	0.72	0.51	14.77

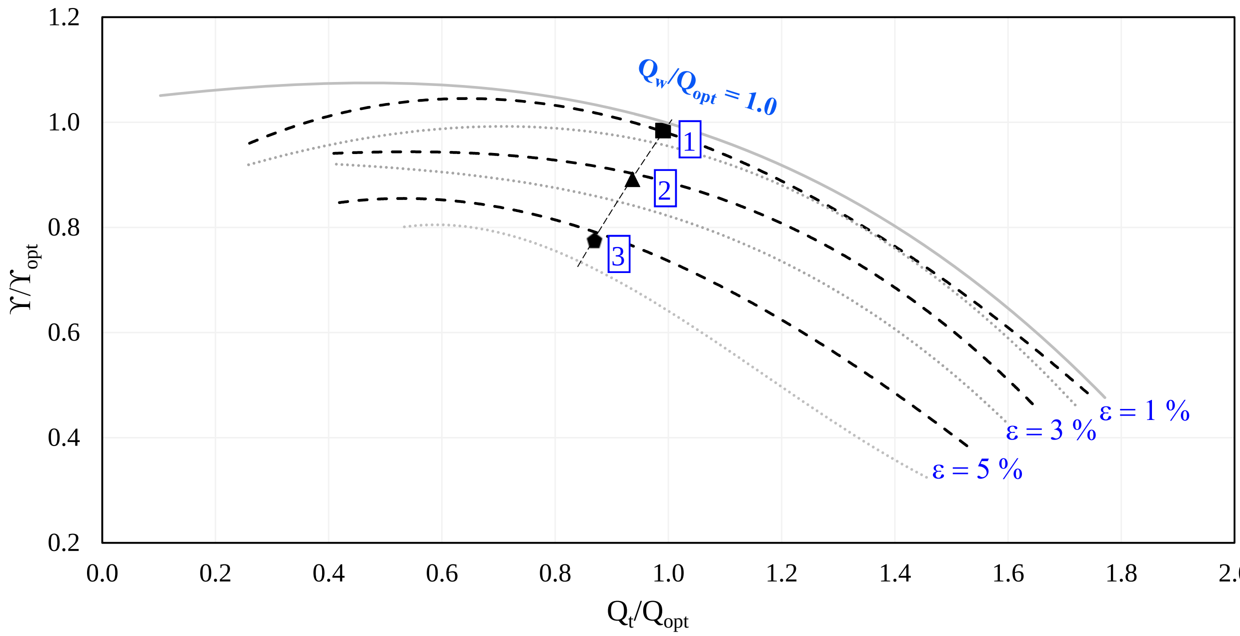

(a) Selected points from closed impeller for detailed optical measurements

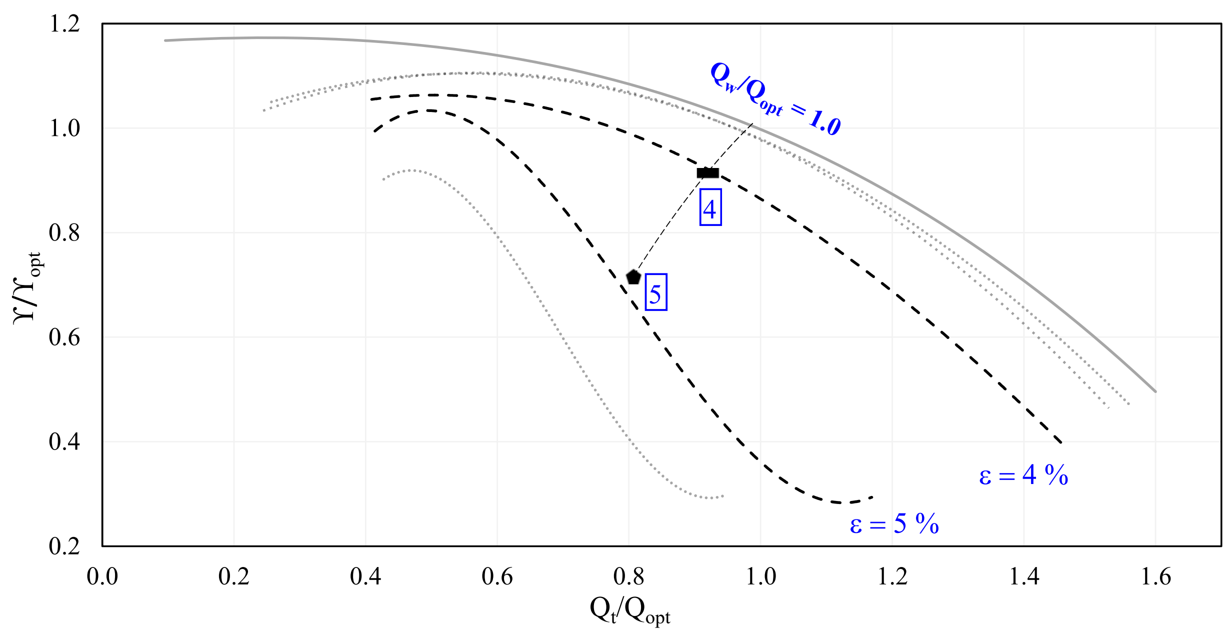

(b) Selected points from semi-open impeller with the standard gap for detailed optical measurements

Figure 5.22: Details of the selected points and gas accumulation (a) Closed impeller (b) Semi-open impeller with the standard gap.

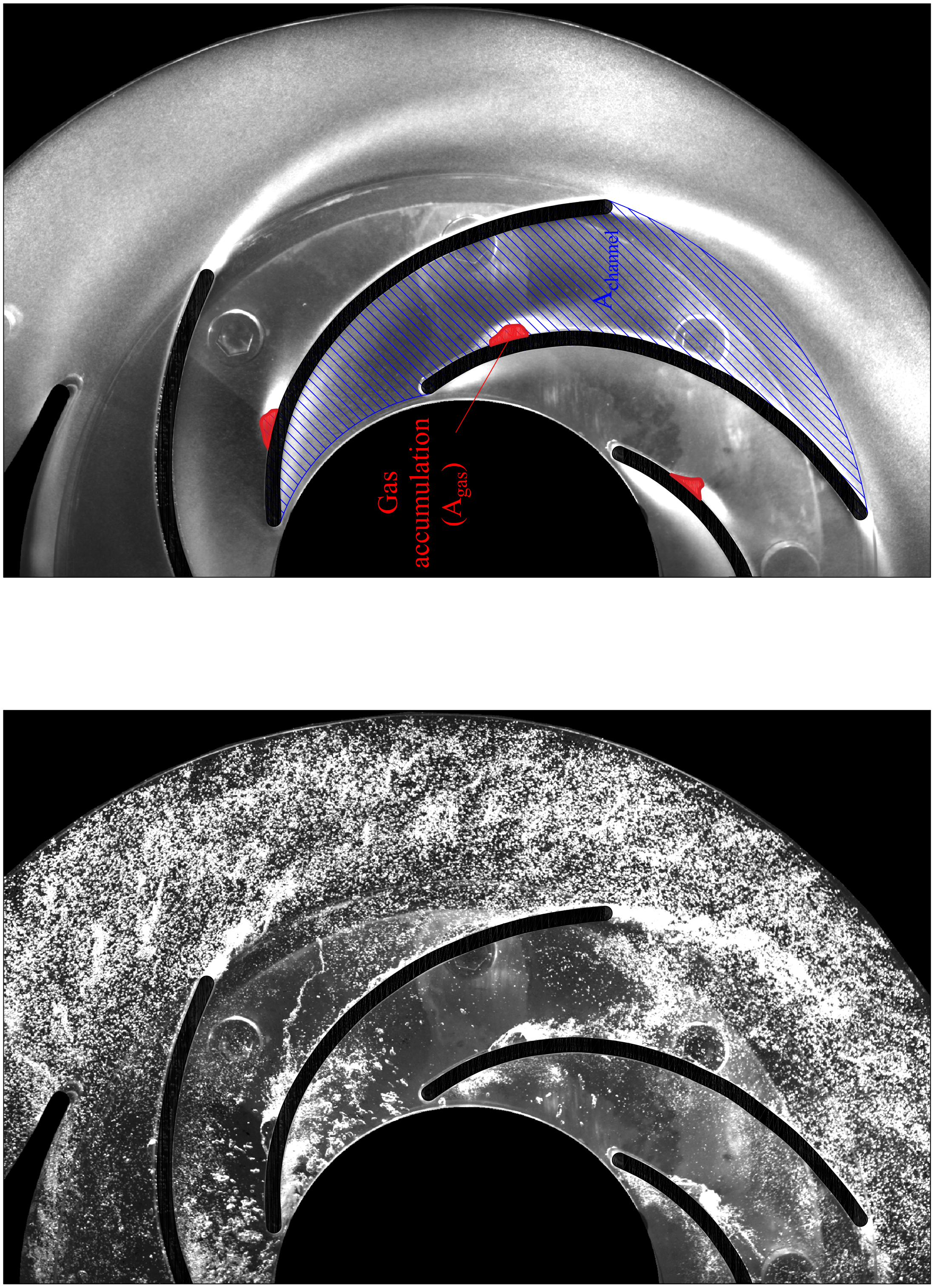

(a) Instantaneous image

(b) Averaged image

Figure 5.23: Details of the flow pattern and gas accumulation for point 1 (a) Sample instantaneous image and (b) Averaged image of 300 instantaneous images.

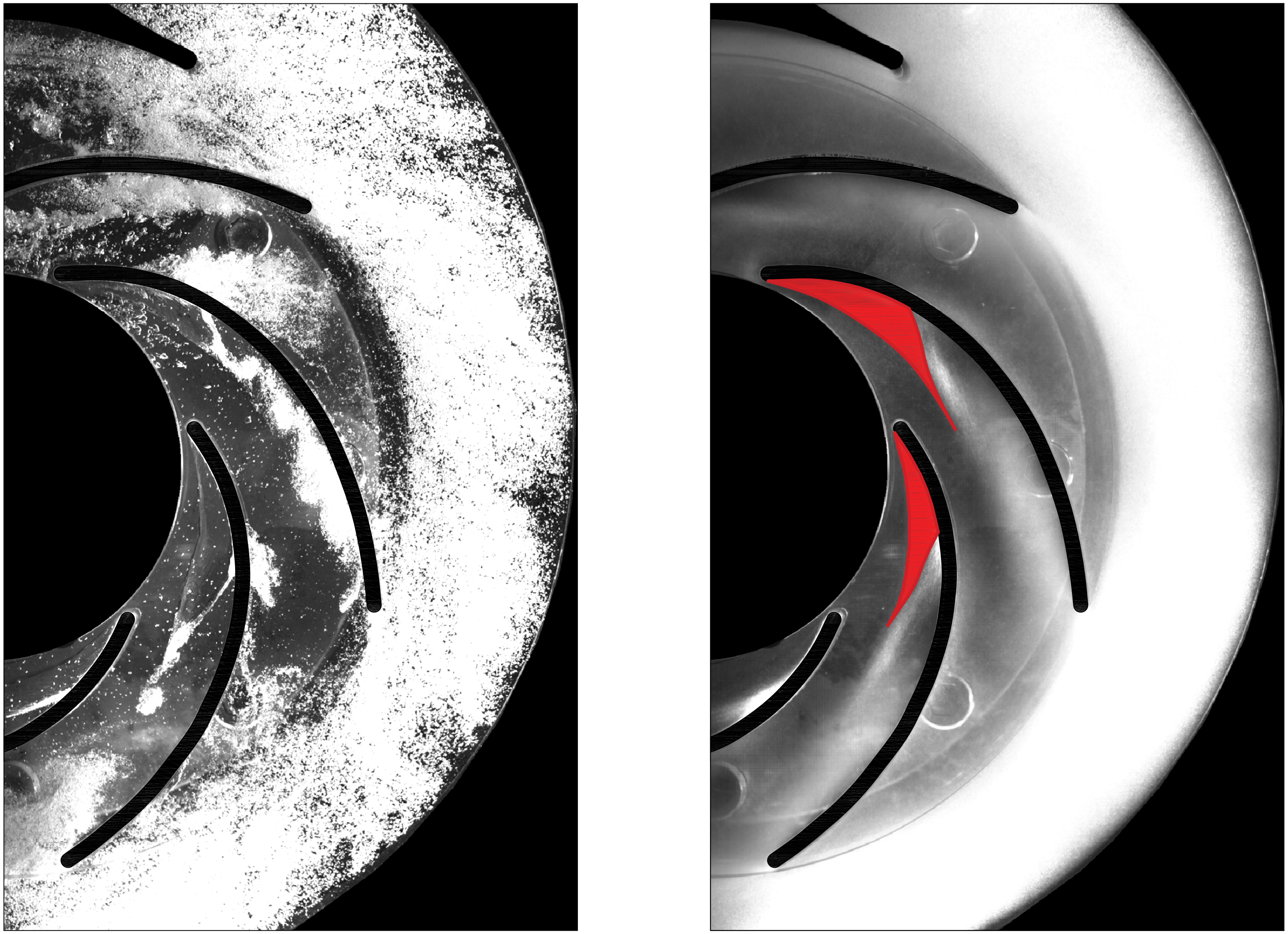

(a) Instantaneous image

(b) Averaged image

Figure 5.24: Details of the flow pattern for point 2 (a) Sample instantaneous image and (b) Averaged image of 300 instantaneous images (Gas accumulation is highlighted in red).

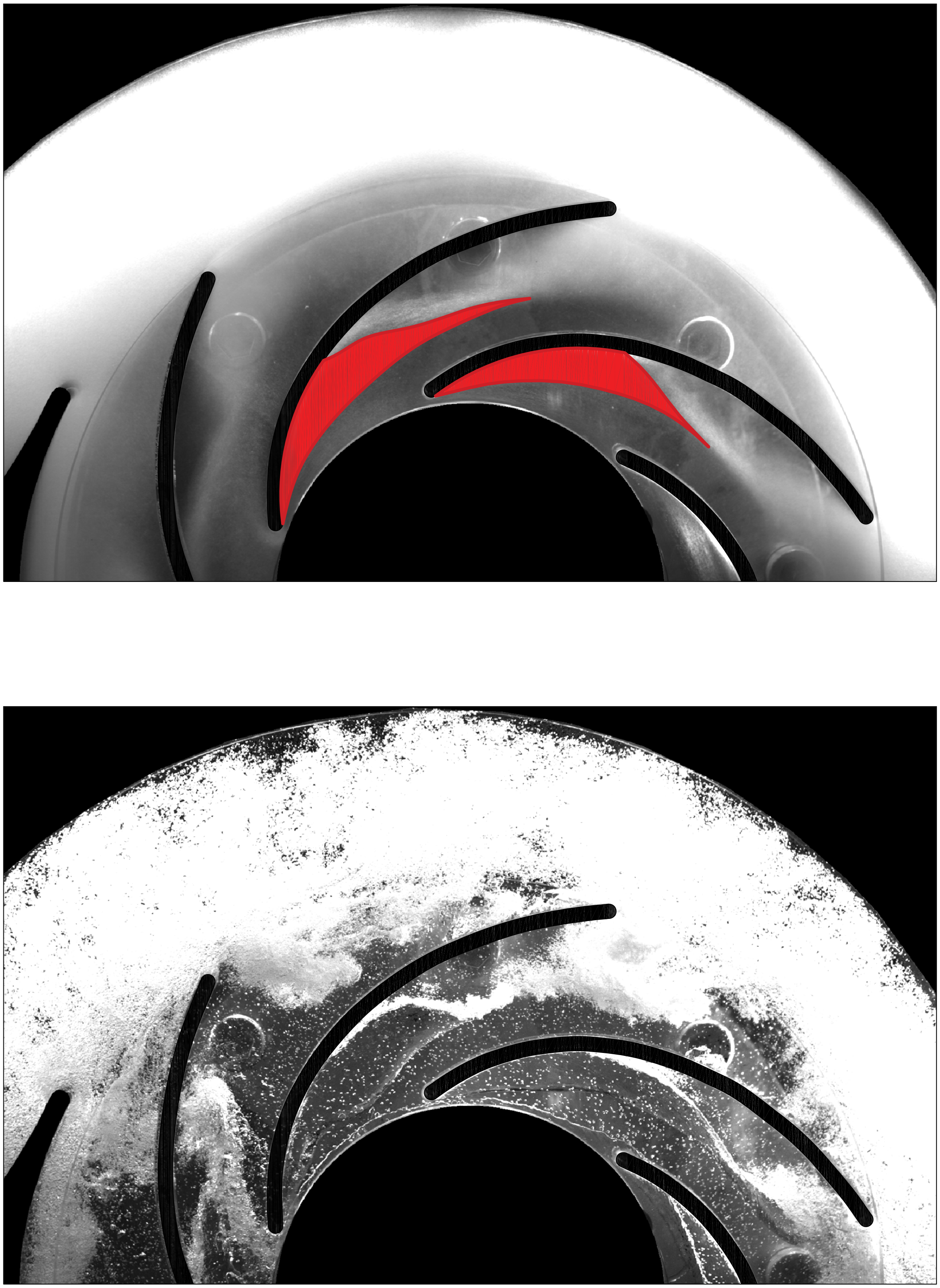

(a) Instantaneous image

(b) Averaged image

Figure 5.25: Details of the flow pattern for point 3 (a) Sample instantaneous image and (b) Averaged image of 300 instantaneous images (Gas accumulation is highlighted in red).

(a) Instantaneous image

(b) Averaged image

Figure 5.26: Details of the flow pattern for point 4 (a) Sample instantaneous image and (b) Averaged image of 300 instantaneous images (Gas accumulation is highlighted in red).

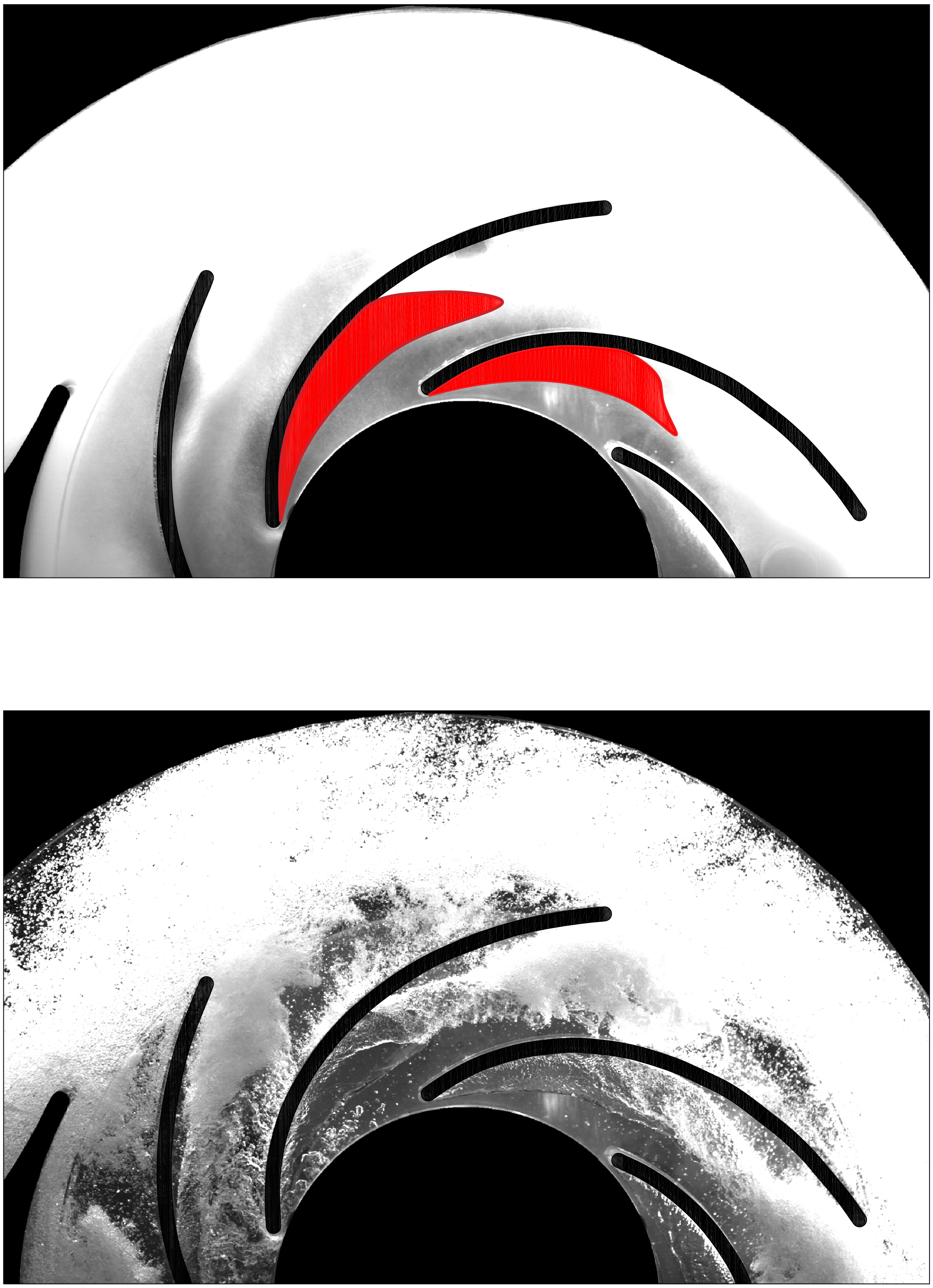

(a) Instantaneous image

(b) Averaged image

Figure 5.27: Details of the flow pattern for point 5 (a) Sample instantaneous image and (b) Averaged image of 300 instantaneous images (Gas accumulation is highlighted in red).

5.10 Video library

In the present work, a detailed video library has been produced for all the pump cases considered. Specifically, the videos are recorded for 4 different approaches while gradually increasing the gas volume fraction. Figure 5.28 shows a description of 4 types of video recording. As shown, in video 1 to 3 the recording was started from $Q_w/Q_{opt} = 0.75$, $Q_w/Q_{opt} = 1.0$ and $Q_w/Q_{opt} = 1.25$, respectively, and the two-phase flow pattern was recorded while passing through each gas volume fraction ($\varepsilon = 1\%, 2\%, 3\%, ...$ and so on). In video 4, the flow patterns were recorded for increasing gas volume fraction of air, while keeping the water flow rate always constant. A tree describing all generated videos is shown in Figure 5.29. The video library is available in the supplementary material of the thesis.

Furthermore, two types of video recording have been generated for each approach, i.e. a time-resolved (1 kHz recording rate) and a cyclic recording (10.83 Hz recording rate). The time-resolved videos provide fine details of the flow in slow motion. In the cyclic recording, 6 images have acquired per impeller revolution, keeping always the impeller blades in place (frozen impeller), which helps to show only the oscillations and changes of the two-phase flow patterns.

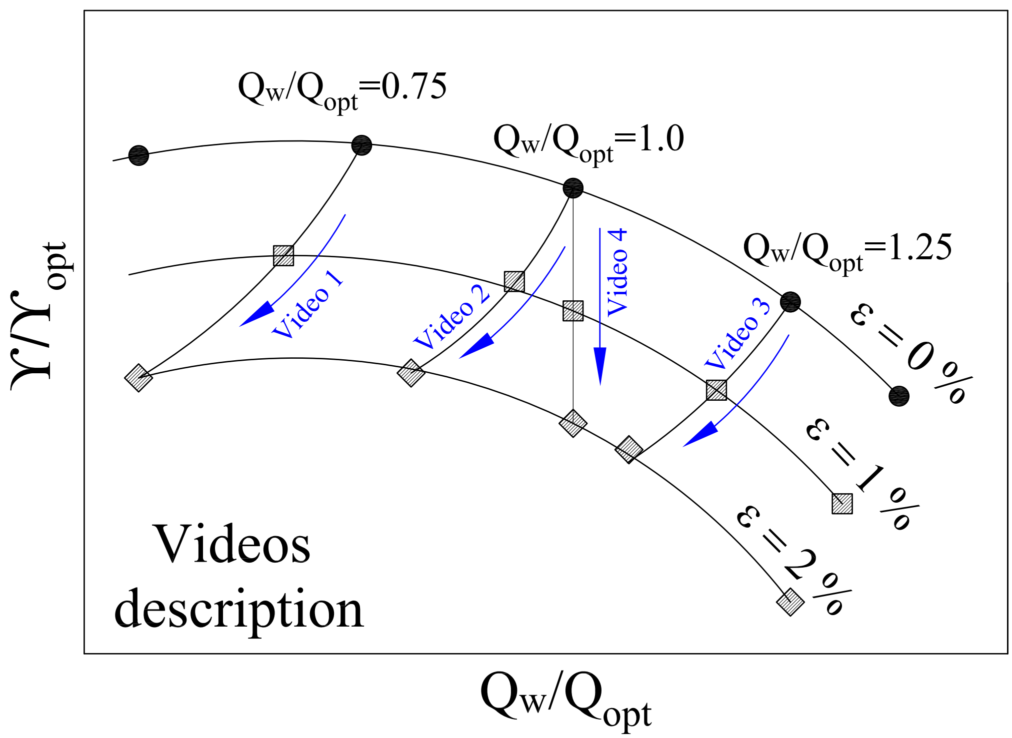

Figure 5.28: Description of the 4 types of recorded videos.

Figure 5.29: Tree of pump video library for all recorded videos.

5.11 Bubble size distribution

In this section, the bubble size distributions (BSD) are compared among all cases studied. The bubble sizes were determined by using shadowgraphy measurements as presented in Figure 3.10a. The shadowgraphy images were obtained by using the same high-speed camera as employed for the flow regimes measurements. A specific window in the impeller channels was selected and considered as a representative area for the BSD. The location of the window, where the bubbles were observed is shown in Figure 3.10b. The bubbles moving through the area marked by the red border in Figure 3.10b were then masked and analyzed.

For the comparison of the bubble size distributions among the four operation cases, two values of gas volume fraction ($\varepsilon = 0.25\%$ and $\varepsilon = 0.5\%$) were considered at overload conditions ($Q_w = 105$ m^3/h). Figure 5.30 shows all the bubble size distributions obtained. As shown, for all cases the median diameter and the standard deviation of the BSD increase when increasing the gas volume fraction from $\varepsilon = 0.25\%$ to $\varepsilon = 0.5\%$. Additionally, the BSD of the closed impeller is generally wider with higher median diameters compared to the other three cases of the semi-open impeller.

Precise comparisons between the four case are shown in Figure 5.31. Again, the bubble sizes in the semi-open impeller channel are generally smaller than that of the closed impeller. This occurs due to the higher shear rates exerted on the blades of the semi-open impeller. Increasing the gap of the semi-open impeller results in slightly lower median diameters and more homogeneous distributions, i.e. lower standard deviations as shown in Figure 5.31b. A similar effect occurs when the upstream inducer is installed. Nevertheless, the BSD of the semi-open impeller with inducer is the narrowest among all cases, having very low standard deviations of the bubble sizes. The reason is that the rotary action of the inducer boosts the phase mixing and makes the BSD more homogeneous.

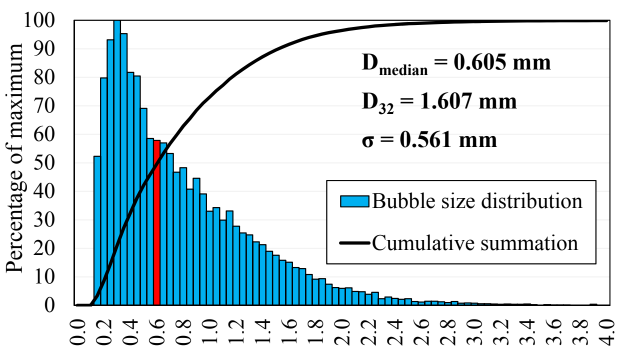

(a) Closed impeller - $\varepsilon = 0.25\%$

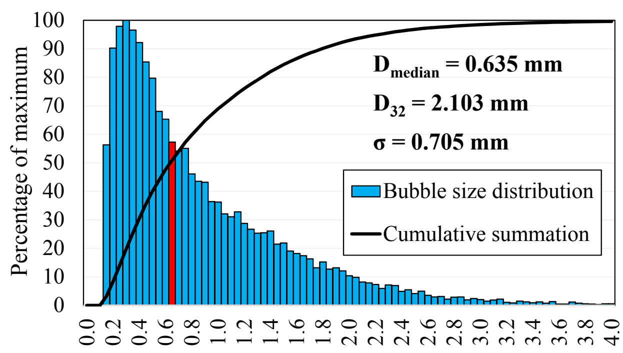

(b) Closed impeller - $\varepsilon = 0.50\%$

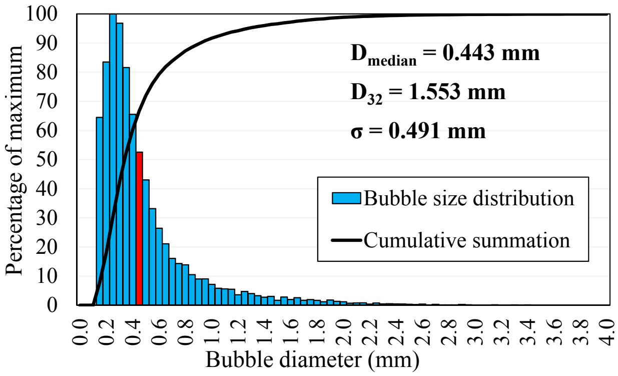

(c) Semi-open impeller with the standard gap - $\varepsilon = 0.25\%$

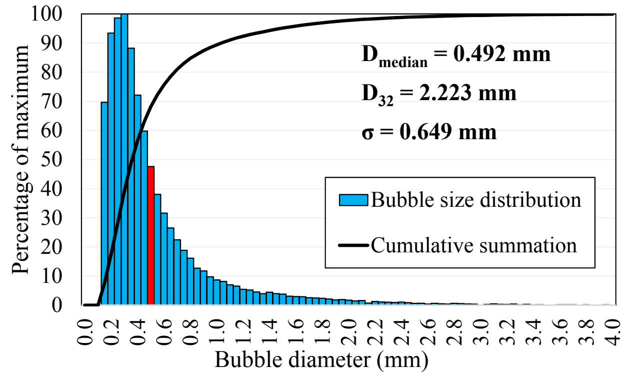

(d) Semi-open impeller with the standard gap - $\varepsilon = 0.50\%$

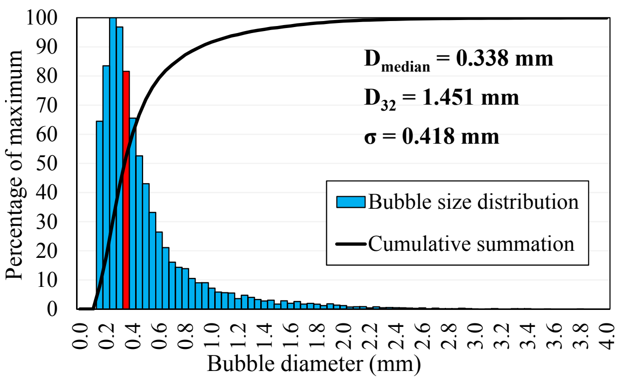

(e) Semi-open impeller with the increased gap - $\varepsilon = 0.25\%$

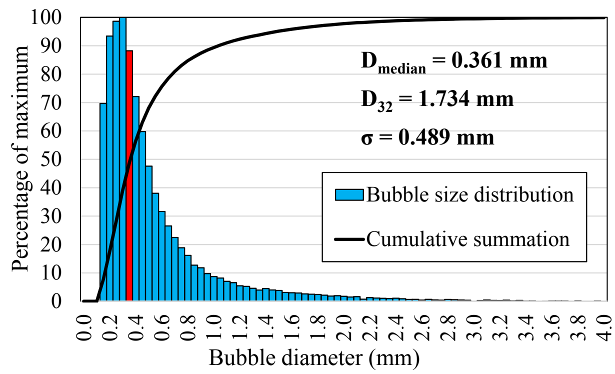

(f) Semi-open impeller with the increased gap - $\varepsilon = 0.50\%$

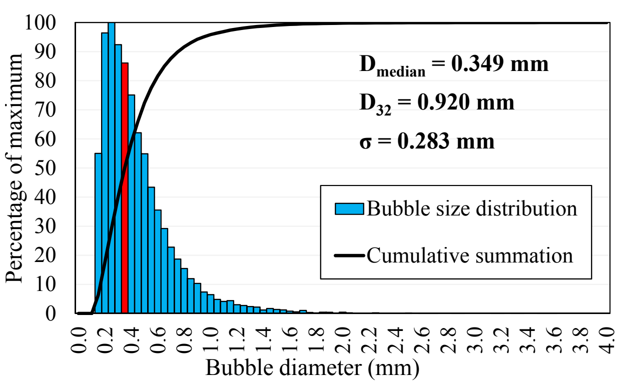

(g) Semi-open impeller with the standard gap and inducer - $\varepsilon = 0.25\%$

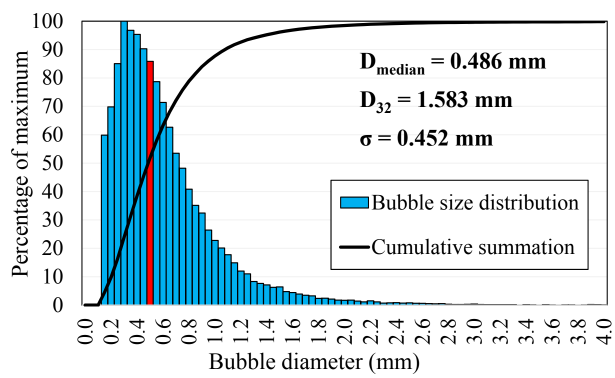

(h) Semi-open impeller with the standard gap and inducer - $\varepsilon = 0.50\%$

Figure 5.30: Bubble size distributions for different operating conditions.

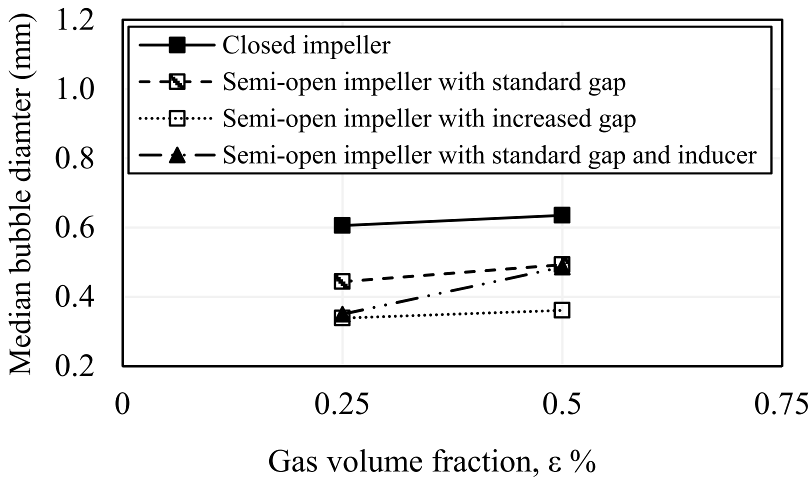

(a) Median diameter of the BSD

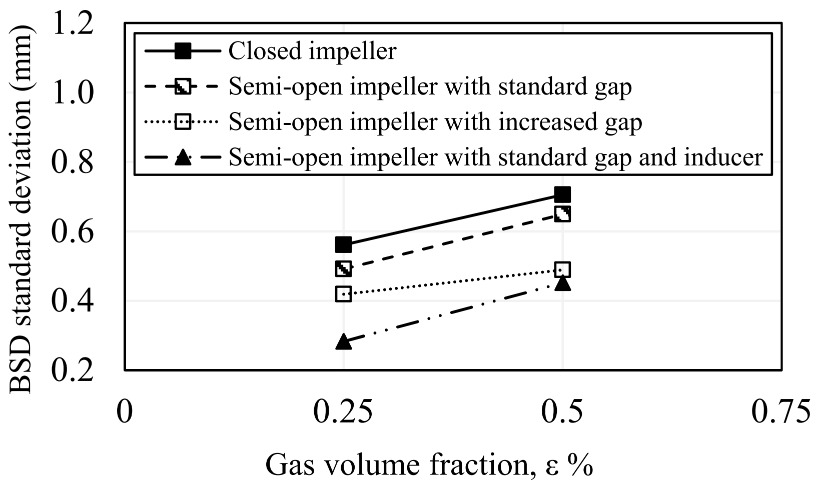

(b) Standard deviation of the BSD

Figure 5.31: Comparison of bubble size distributions.

5.12 Further analysis: Cordier diagram

The performance of the pump is also presented in terms of Cordier-diagram parameters, using the speed number σ and the diameter number δ, which are given by:

$$\sigma = \left(2\pi^2\right)^{0.25} n \frac{\sqrt{Q_t}}{\Upsilon^{0.75}} \tag{5.12}$$

$$\delta = \left(\frac{\pi^2}{8}\right)^{0.25} D_2 \frac{\Upsilon^{0.75}}{\sqrt{Q_t}} \tag{5.13}$$

Plotting the data points on a Cordier diagram as shown in Figure 5.32, it is confirmed that the effective operation of the pump occurs at optimal conditions and at slightly part-load conditions ($Q_t/Q_{opt} = 0.8 : 1$), corresponding to a speed number (σ) range approximately between 0.1 and 0.14. In this range, the pump efficiency is relatively high, where the data points are close to the high-efficiency curve of Cordier. For $\varepsilon \geq 6\%$, the data points are relatively far from Cordier's curve, indicating lower expected efficiency.

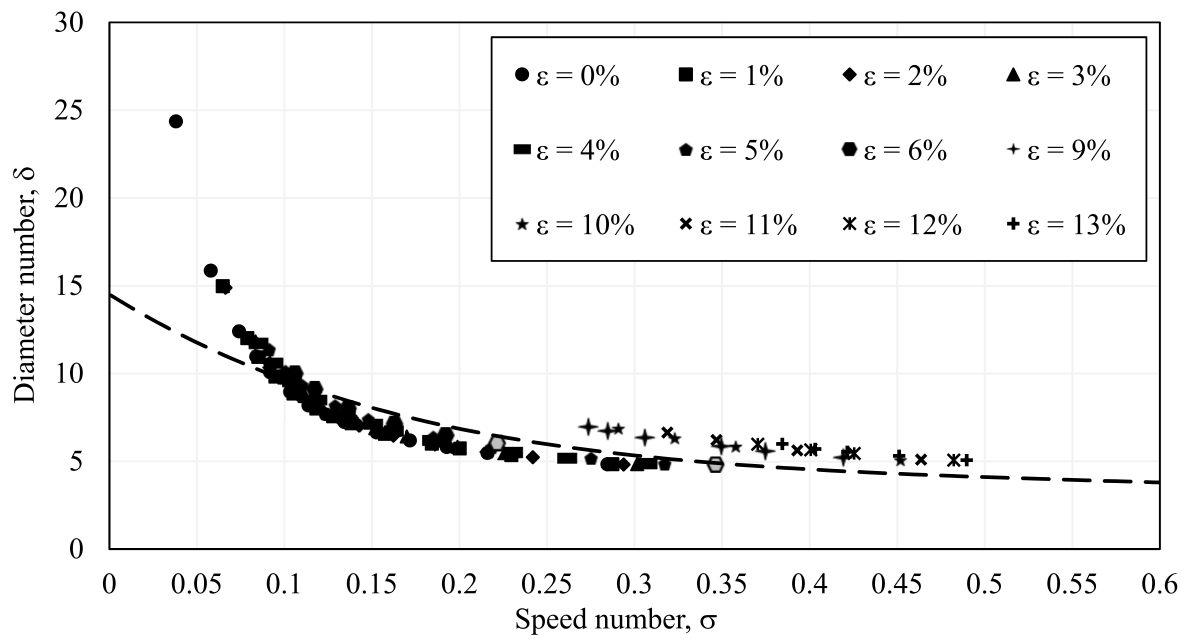

(a) Closed impeller

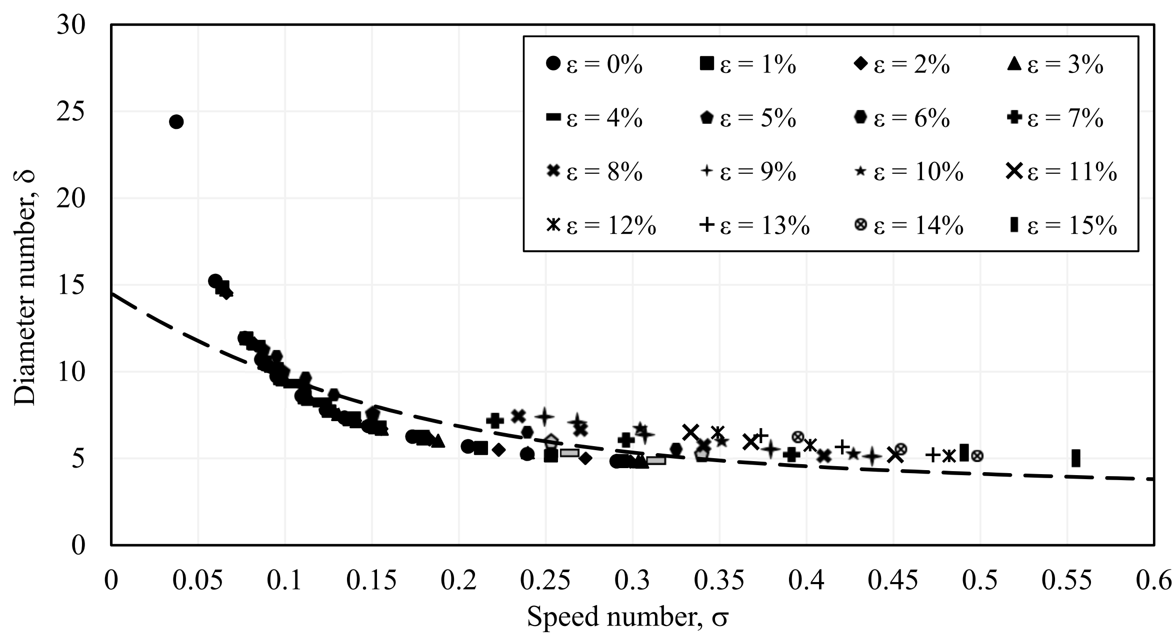

(b) Semi-open impeller with the standard gap

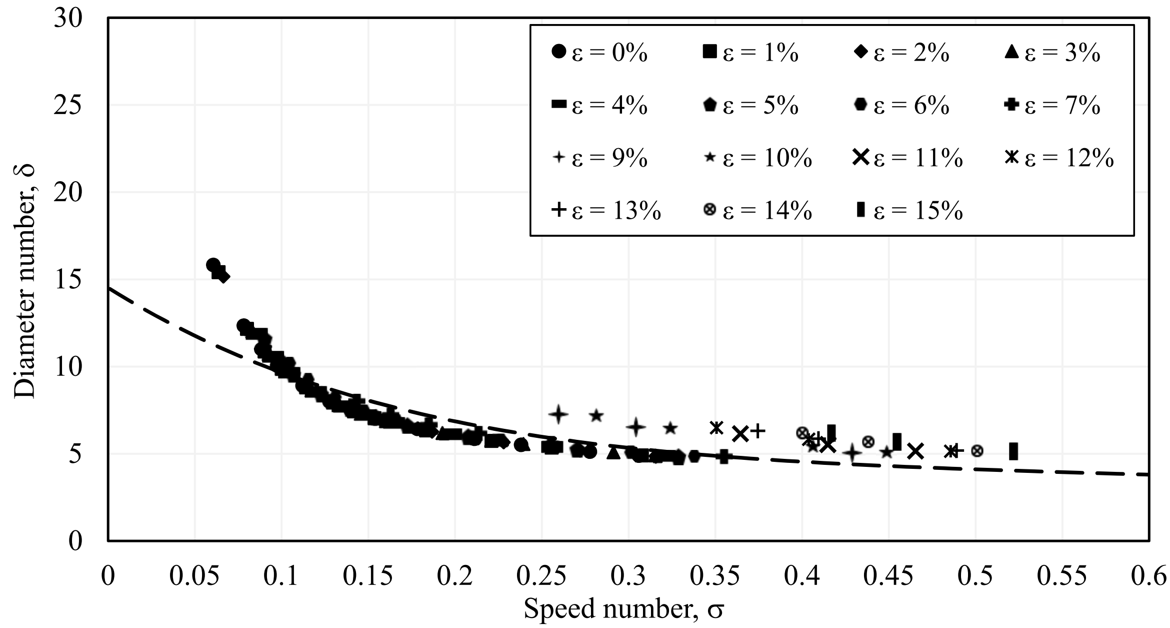

(c) Semi-open impeller with the increased gap

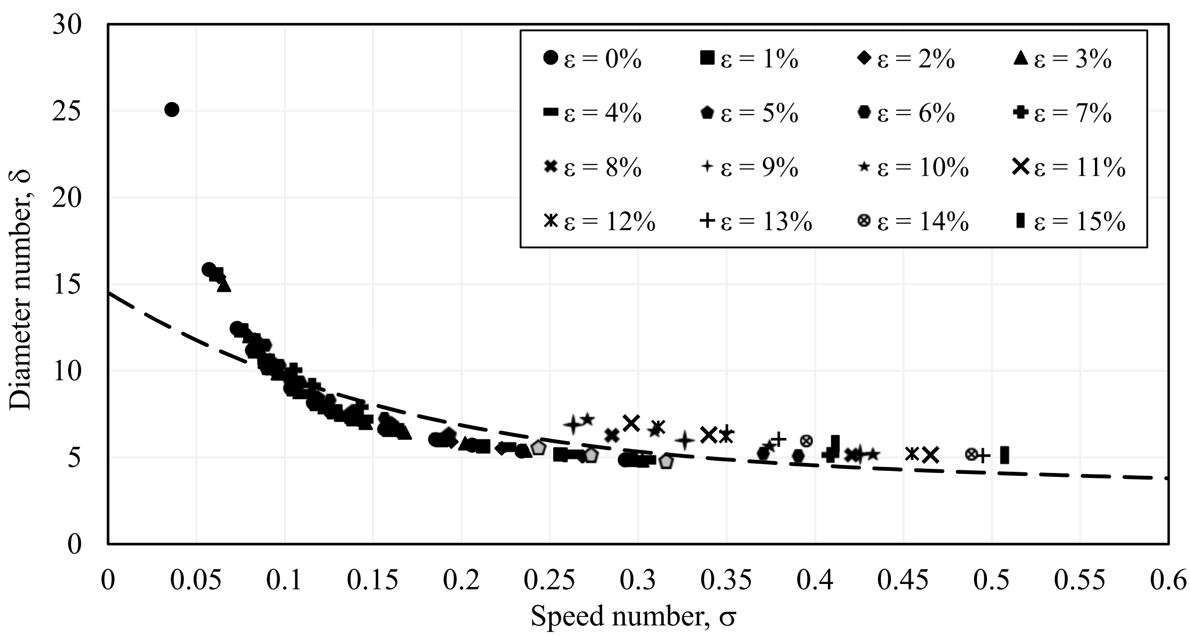

(d) Semi-open impeller with the standard gap and inducer

Figure 5.32: Pump performance on Cordier diagram.

5.13 Conclusions

The performance of a radial centrifugal pump was studied experimentally for gas/liquid two-phase flows, considering either a closed impeller or a semi-open impeller with a standard or an increased tip clearance gap. Additionally, the influence of adding an upstream inducer before the semi-open impeller was also considered. The main observations can be summarized as follows:

- The initial single-phase flow performance of the closed impeller is slightly higher than that of the semi-open impeller with the standard gap. Increasing the gap causes a considerable reduction in the single-phase performance of the semi-open impeller. The reduction is as big as 9% to 40% in specific delivery work, and 1% to 14% in pump efficiency from part-load to overload, respectively. Only insignificant changes could be seen in the single-phase performance curves when the inducer is installed.

- Recording the data by three different procedures in the two-phase performance measurements, no significant hysteresis effects could be observed in the closed impeller. However, obvious hysteresis could be seen in the semi-open impeller with the standard gap between $\varepsilon = 4\%$ and $\varepsilon = 6\%$. This effect is due to previous air accumulation inside the impeller passages. Additionally, increasing the tip clearance gap completely eliminated the performance hysteresis of the semi-open impeller. Similarly, installing the inducer enhanced the inlet mixture of phases and strongly reduced the hysteresis between different procedures.

- For the range of $1\% \leq \varepsilon \leq 3\%$, the deterioration of the pump performance parameters is much lower in the semi-open impeller with the standard gap compared to that of the closed impeller. Nevertheless, in the range between $\varepsilon = 4\%$ and $\varepsilon = 6\%$ the trend is reversed, and the semi-open impeller with the standard gap performance is strongly reduced (due to the onset of the pocket flow regime) compared to the closed impeller, particularly in overload conditions.

- Increasing the semi-open impeller tip clearance gap results in increased secondary flow across the blades, and thus higher bubble break-up. This revokes the abrupt performance drop and provides more robust two-phase pumping up to $\varepsilon = 7\%$, before the beginning of pump surging. Therefore, the standard gap is recommended for single-phase flow and low gas volume fractions $\varepsilon < 4\%$, while increasing further the gap is an advantage when higher gas volume fractions, $\varepsilon \geq 5\%$, are expected. Further, installing the inducer with the semi-open impeller with the standard gap resulted in improved performance in the ranges of $\varepsilon = 4\%$ to 5% and $\varepsilon = 4\%$ to 7% for overload and part-load flow conditions, respectively.

- Measuring the performance for constant air flow inlet, the closed impeller exhibits strongly unstable curves compared to the semi-open impeller. Therefore, the flow instabilities are generally lower in the semi-open impeller; in addition, pump surging can only occur in limited flow conditions compared to the closed impeller. Having the inducer installed could even further damp the flow instabilities and reduce the surging region of the semi-open impeller.

- For $\varepsilon \geq 8\%$, the performance of the semi-open impeller is slightly better in comparison to the closed impeller. There, the flow regime in the closed impeller is segregated, which is never found in the semi-open impeller. In this range, neither increasing the gap nor installing the inducer could significantly improve the performance due to the occurrence of gas-locking.

- The transitions between different flow regimes on the two-phase maps explain the changes and discontinuities of the pump performance in each case. Additionally, the maps reveal the improved gas accumulation resistance of the semi-open impeller, which positively increases with increasing the tip clearance gap. Although the inducer caused improvement in some ranges, it has only a slight influence on the flow regime map of the semi-open impeller.

- The bubble size distributions of the closed impeller are generally wider with higher median diameters compared to the other three cases of the semi-open impeller. When the gap is increased or the inducer is installed, the BSDs of the semi-open impeller are getting narrower, with slightly lower median diameters.

Now, it can be checked if the experimental findings can be correlated to CFD predictions.

Chapter 6

Numerical simulations

6.1 Introduction

As discussed previously in Section 2.3.9, numerical simulations can deliver interesting details of the flow, which are sometimes difficult to be obtained experimentally. This is also done here in order to explain the flow behavior at some specific conditions. The following simulation results also underline the limitations of some common CFD models, when applied to the complex flow in centrifugal pumps or the diverging channel flow under two-phase conditions. Moreover, this chapter highlights even further the importance of the present experimental data for validation and model developments, to improve the prediction accuracy of CFD models. Some parts of this chapter are based on published articles [114, 115].

6.2 Diverging channel simulations

6.2.1 Numerical modeling

The CFD code STAR-CCM+ [116] was employed to simulate the flow. The considered numerical domain for the diverging channel is shown in Figure 6.1. Although the diverging part is the central area of interest, a long domain was employed as shown in Figure 6.1 to avoid unrealistic numerical effects from the boundaries. The boundary conditions of the inlet and outlet are set to velocity inlet and pressure outlet, respectively. After performing a mesh-independence test using the Reynolds-Stress Model (RSM), different turbulence models are compared as well, involving the realizable $k-\epsilon$, the $k-\omega$ shear stress transport (SST), and the Spalart–Allmaras turbulence models. Additionally, the results of a hexahedral and a polyhedral grid with similar resolutions were compared. A steady-state solver was considered for single-phase simulations since the interest is set to the average properties of the flow. However, for two-phase flows, an unsteady solver was always applied together with the Volume of Fluid (VOF) to model the interaction between the two phases (see later Section 6.2.3).

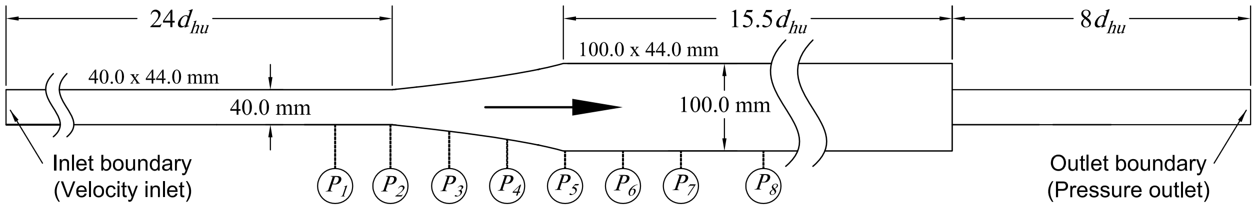

Figure 6.1: Numerical domain used for the diverging channel simulations.

6.2.2 Single-phase simulations

Mesh-independence study

A mesh-independence study was done in terms of the total pressure change across the whole simulation domain to ensure that the solution does not vary after any further refinement of the mesh. The test was done at Re_w = 50,130 using the Reynolds-Stress Model (RSM) for turbulence modeling [117, 118]. The simulations were done for gradually refined mesh resolutions by increasing the number of cells at each step by a factor of approximately 1.2-2, starting from an initial resolution of 2.73 million cells till a final resolution of 9.27 million cells. In total, 5 different meshes were considered as shown in Figure 6.2 and listed in Table 6.1. For all simulations, adequate mesh refinement near the walls was used to ensure accurate resolving for the boundary-layer flow. Additionally, the average value of the dimensionless wall distance y+ was always kept smaller than 1 (y+ $\approx$ 0.5), as can be seen in Table 6.1, to avoid the need for wall models. Figure 6.3 shows the results of the total pressure change and the relative error taking the finest mesh as reference. As can be seen from Figure 6.3, the numerical results of the last two grids (mesh 4 and 5) are very similar, with a relative error lower than 0.2%. Therefore, mesh 4, with 7.36 million cells, was assumed to have a mesh-independent solution, and thus kept for all further simulations.

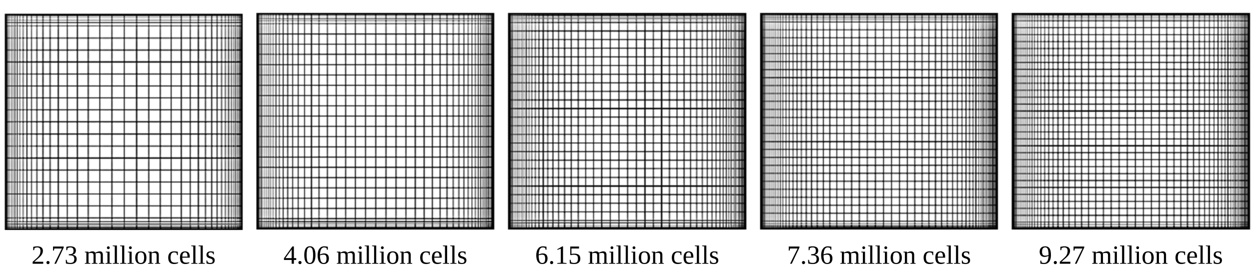

Figure 6.2: Cross-views of different grids used for the mesh-independence study.

Table 6.1: Details of different grids used for the mesh-independence study.

Mesh #	No. of cells (millions)	Average y+	Pressure drop (Pa)	Error %
1	2.73	0.517	732.87	6.637
2	4.06	0.501	738.7	5.789
3	6.15	0.480	768.394	1.701
4	7.36	0.472	779.97	0.192
5	9.27	0.448	781.47	Reference

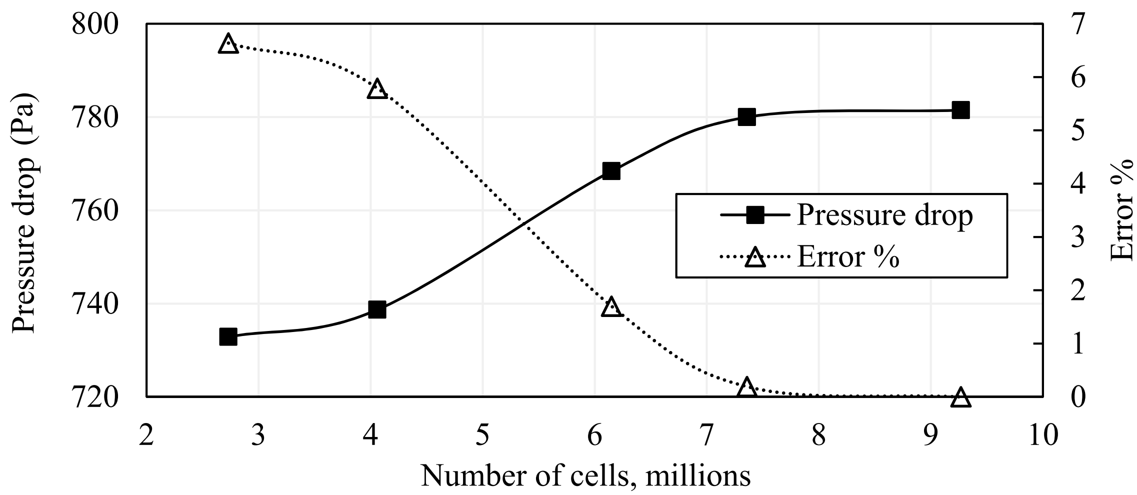

Figure 6.3: Comparison of the numerical results using different meshes at Re_w = 50,130.

Comparison of different types of numerical grids

In this section, the results of the selected hexahedral mesh (7.36 million cells) and a similar-resolution polyhedral mesh (7.92 million cells) are compared against experimental data. This is done to examine the accuracy of both types of mesh. Figure 6.4 compares the axial pressure recovery along the diffuser for both meshes against the experimental values. As done in Section 4.5, pressure sensor number 2, located at the beginning of the diffuser (i.e., at $x = 0$), was always taken as a reference. This means that all pressure values are given by the difference to this reference value.

As can be seen from Figure 6.4, both mesh types show very good agreement with the experimental data. However, in the second half of the diffuser near the separation zone, the hexahedral mesh shows a little higher pressure, since the separation could not be very accurately predicted. This is visible in Figure 6.5 when comparing the fields of the velocity magnitude, where it can be seen that the separation starts slightly later in the hexahedral mesh simulation (Figure 6.5b) with a smaller size compared to the averaged PIV velocity measurements (Figure 6.5c). Here, the average velocity field of the PIV measurements was obtained by using 5000 instantaneous velocity fields recorded with a frequency of 1000 Hz (similar to Section 4.2.2). It is also important to note that the real flow is very unstable and that the averaging leads to a smooth field but not to a real solution. This strong unstable behavior of the velocity field can not be predicted by using steady simulations.

Nevertheless, the numerical model is able to reproduce the hydrodynamic features of the flow. Since the simulations with hexahedral mesh are much faster than those with a polyhedral mesh (the hexahedral mesh consumes about 60% CPU time of the polyhedral mesh) and lead also to a lower average relative error, the hexahedral mesh was further kept for the following simulations. Additionally, in preliminary two-phase simulations with VOF model, it was found that polyhedral grids are more diffusive, which can affect the expected accumulation in the separation zone; this problem can be avoided with hexahedral grids.

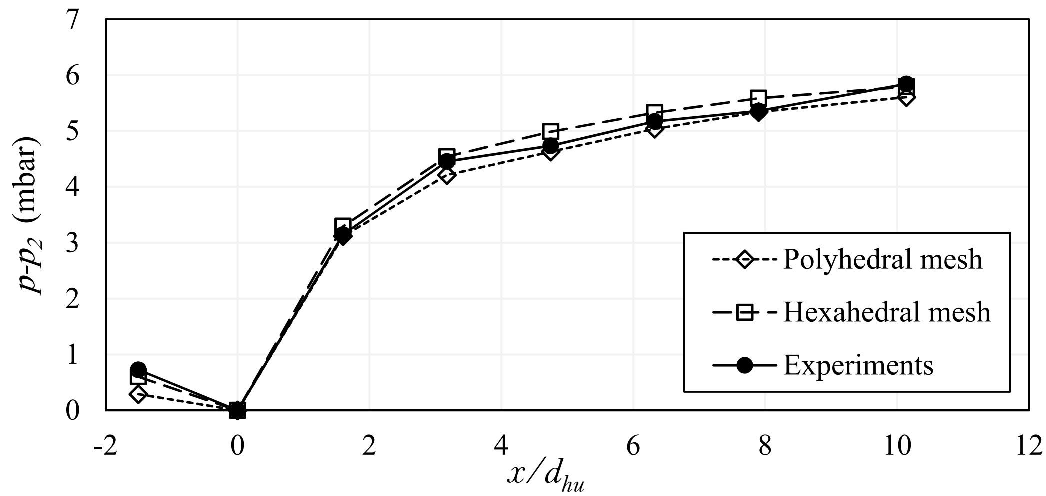

Figure 6.4: Axial pressure change using the selected hexahedral mesh and a similar-resolution polyhedral compared with the experimental data at $\mathrm{Re}_w = 50{,}130$.

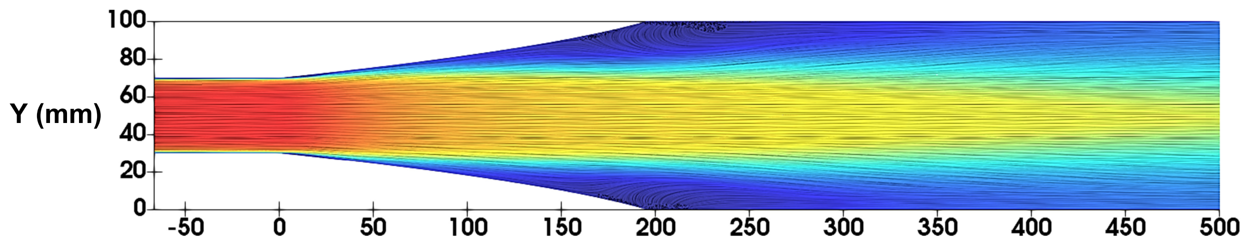

(a) Polyhedral mesh

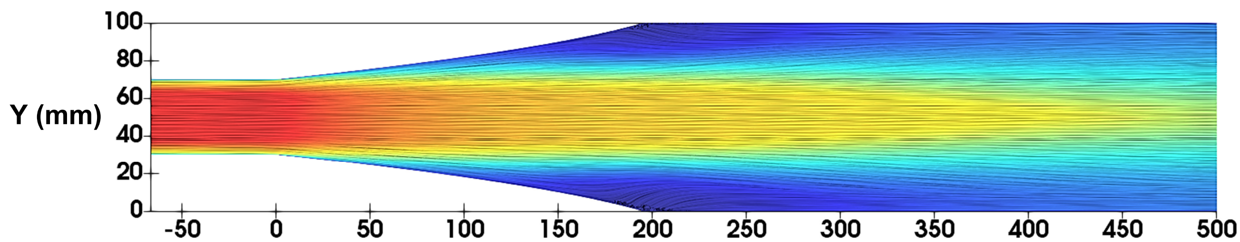

(b) Hexahedral mesh

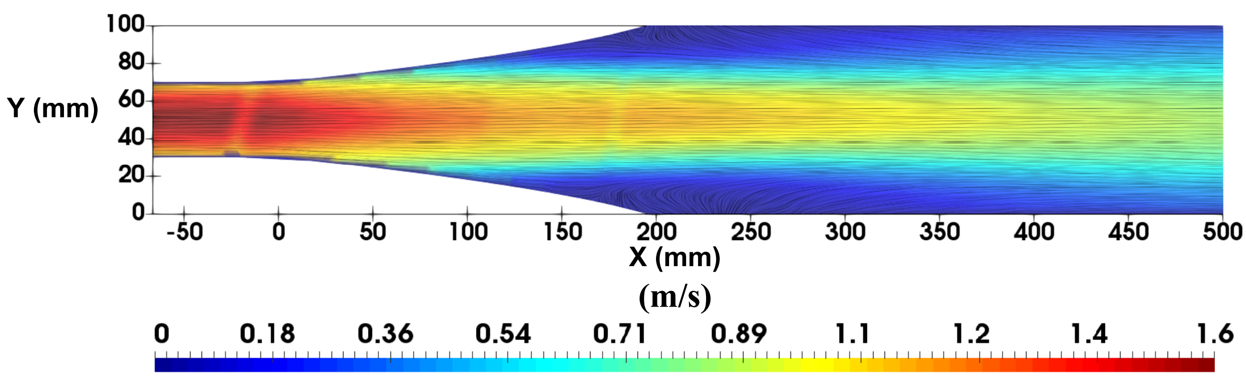

(c) PIV Experiments

Figure 6.5: Velocity fields of (a) Hexahedral mesh, (b) Polyhedral mesh and (c) PIV measurements at the middle plane of the channel for $\mathrm{Re}_w = 50{,}130$.

Comparison of different turbulence models

In this section, a comparison of the numerical results obtained by different turbulence models is presented. This comparison is done not only to select an appropriate turbulence model for further calculations but also to underline the limitations of simulations if the turbulence model is not carefully chosen. This is very important even for single-phase simulations because of the turbulent flow (Re $\geq$ 50,000) with strong separation. Figure 6.6 compares the numerical results of different turbulence models with the experimental data in terms of the axial pressure change along the diverging part, considering in addition to RSM, the realizable $k-\epsilon$ model [119], the $k-\omega$ shear stress transport (SST) model [120], and the Spalart-Allmaras turbulence model [121]. A brief introduction about these turbulence models is given in Appendix G, while the complete formulation of the models can be found in the user manual of STAR-CCM+ [116]. Here, the realizable $k-\epsilon$ was considered rather than the standard $k-\epsilon$, since it can more accurately predicts jet, separated and recirculating flows [122], sometimes also better than the $k-\omega$ SST model [123].

It is clear in Figure 6.6 that the $k-\omega$ SST model and the Spalart-Allmaras model fail to predict the flow; both models show much lower pressure recovery compared to the experiments. In addition to the RSM model, the realizable $k-\epsilon$ model could, however, predict the axial pressure change more precisely. Figure 6.7 presents the velocity fields of all turbulence models along with the experimental velocity field to understand the behavior of pressure recovery. Here, it can be seen that the velocity field of the RSM model is the closest one to the experiments, while the velocity fields of all other models involve deviations. For the $k-\omega$ SST and the Spalart-Allmaras models, the velocity field exhibits strongly accelerated cores through the whole channel, which reduces the pressure recovery in the diffuser as shown in Figure 6.6. This effect is also slightly visible in the velocity field of the realizable $k-\epsilon$ model shown in Figure 6.7a. Additionally, the recirculation zones are poorly captured by the realizable $k-\epsilon$ model, confirming the general limitations of first-order turbulence modeling (i.e., $k-\omega$ SST, realizable $k-\epsilon$, and Spalart-Allmaras).

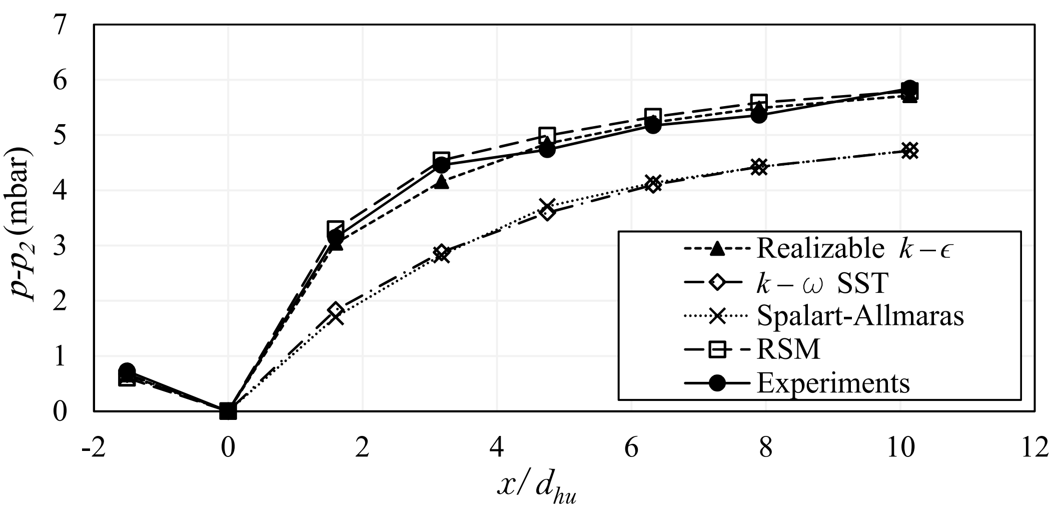

Figure 6.6: Comparison of numerical results obtained by different turbulence models against the experimental data at Re_w = 50,130.

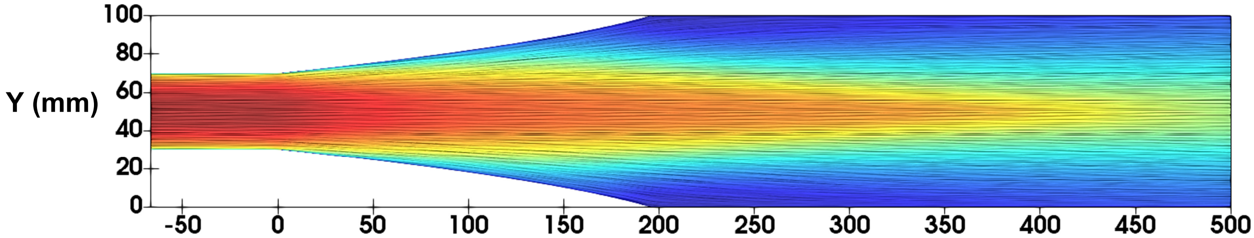

(a) Realizable $k - \epsilon$

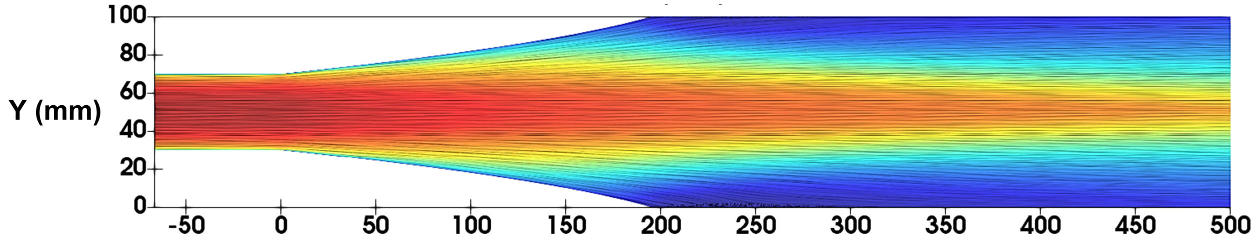

(b) $k - \omega$ – SST

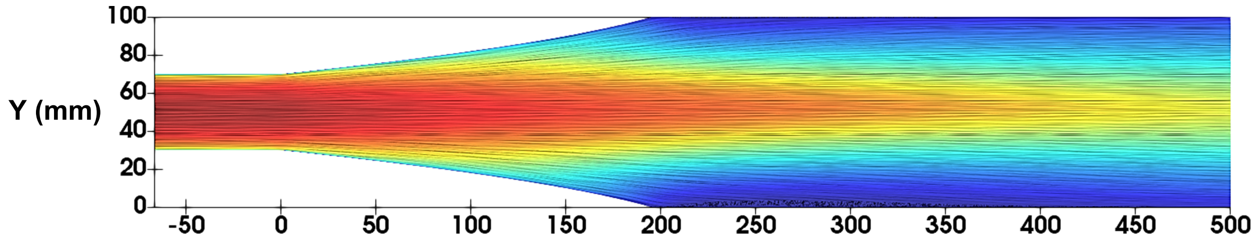

(c) Spalart–Allmaras

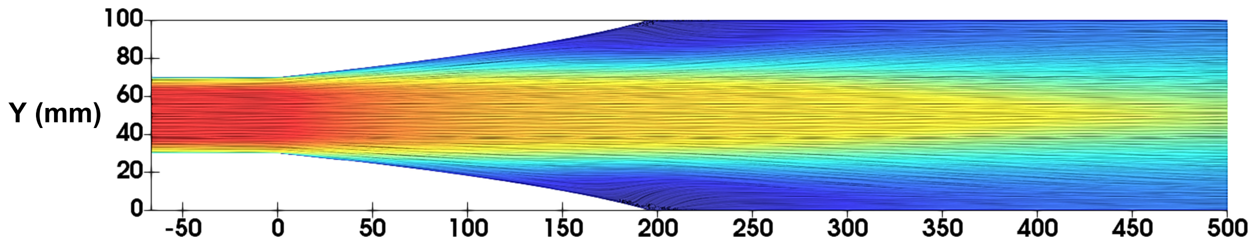

(d) Reynolds stress model – RSM

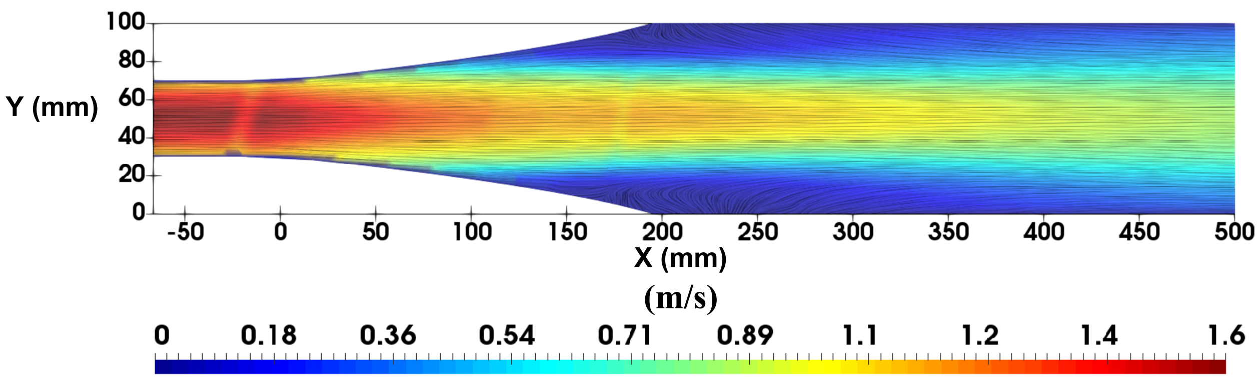

(e) PIV Experiments

Figure 6.7: Velocity fields of different turbulence models, compared to the PIV measurements at the middle vertical plane of the channel for $\mathrm{Re}_w = 50{,}130$.

Because of the strong flow separation, vortices with 3D structures and secondary flows are induced into the flow. Therefore, it is important to check the ability of the models to capture these features, as they could dramatically impact the behaviour under two-phase conditions. Figure 6.8 compares streamlines of the secondary flow at different axial sections. As shown, the vortex structures predicted differ strongly for each turbulence model. Only RSM was able to predict recirculating structures with several strong vortices. Additionally, the $k-\omega$ SST model could predict more curved structures, while all other models fail to predict the secondary vortices, particularly at $x/d_{hu} = -1.5$. The reason for that is the isotropic turbulence assumption of the first-order models.

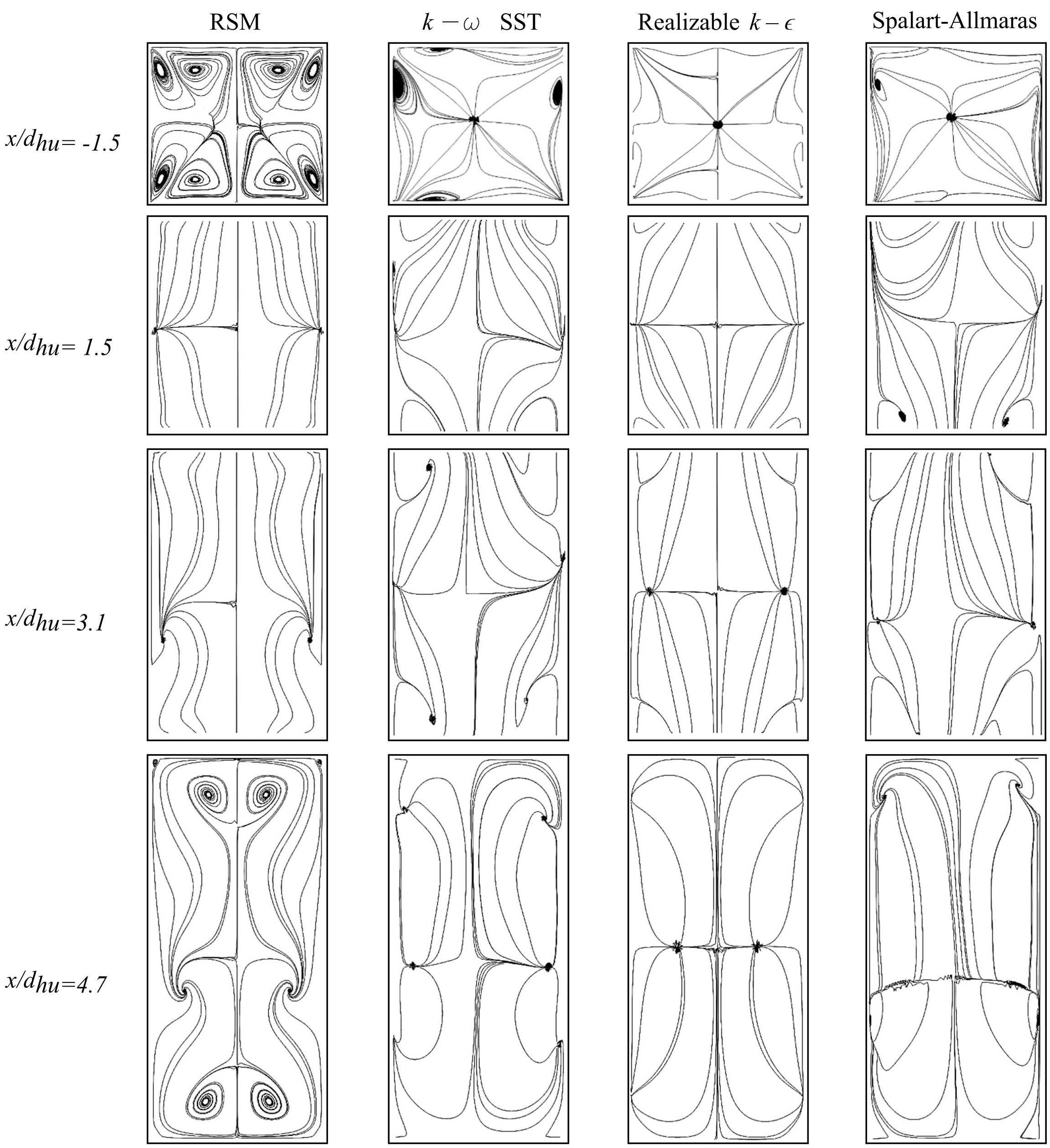

Figure 6.8: Streamlines at different plane sections.

Simplified simulation domain initialized with experimental velocity profile

A trial was done to reduce the computational efforts by cutting the inlet pipe of the domain, removing about 90% of its length and using the measured two-component velocity profiles near the diffuser inlet (Section 4.6.1). Figure 6.9 shows the velocity field of the simplified simulation when initialized with the experimental velocity profile. As shown, this simulation converged to an asymmetric velocity field with one large separation zone, similar to the experiments done with a short inlet pipe (see Figure 4.2). Since the velocity field of the shorter domain is not similar to the one of the full domain, the pressure recovery is likewise different as shown in Figure 6.10. Although the solution is comparable to that of the experimental case with a short inlet pipe, the shorter simulation domain cannot be used to obtain the symmetric velocity profile. The reason is that the flow has a strong 3D behaviour as shown in Figure 6.8, which can not be obtained when the flow is initialized with a two-component velocity profile. Accordingly, the long inlet pipe is needed for the simulation to converge to the symmetric velocity solution, which is necessary to maintain similar gas accumulation behavior in later two-phase flow simulations. Therefore, the full simulation domain was used in all further two-phase simulations.

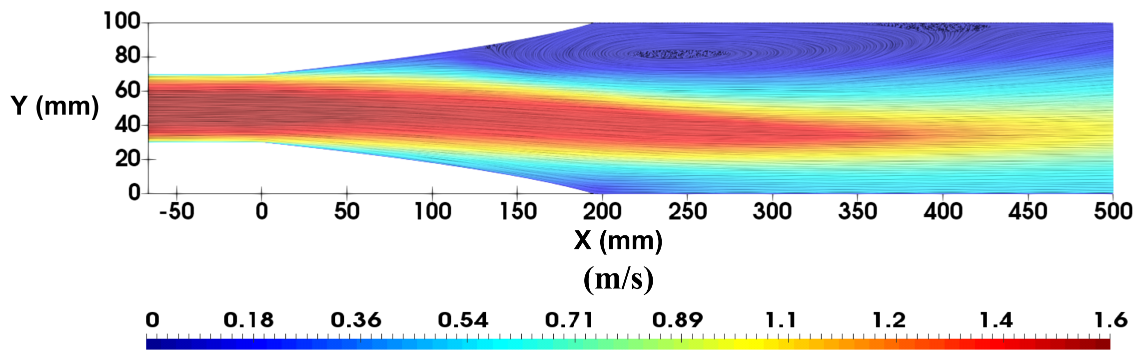

Figure 6.9: Velocity field of the shorter simulation domain at the middle plane of the channel (initialized with experimental velocity profile for Re_w = 50,130).

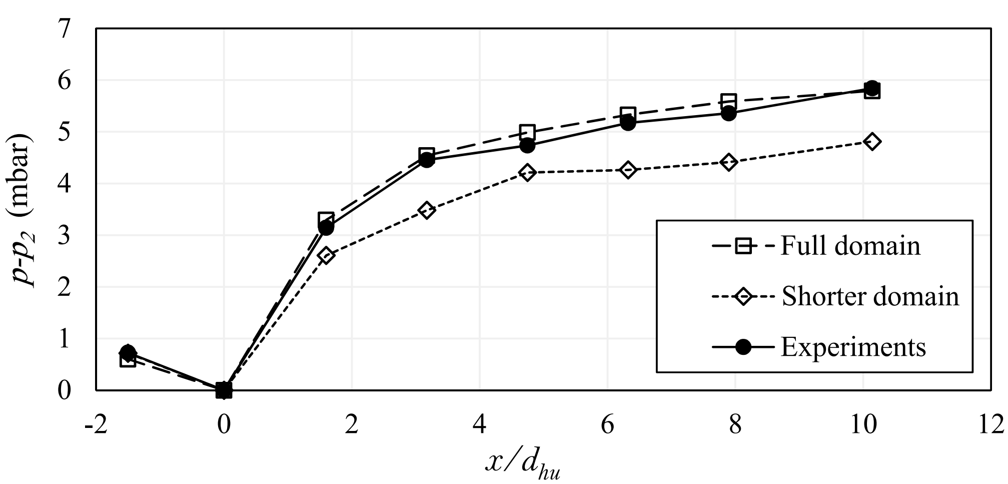

Figure 6.10: Comparison between the full simulation domain (long inlet pipe) and the shorter simulation domain initialized by experimental velocity profile for Re_w = 50,130.

6.2.3 Two-phase simulations

In the two-phase simulations, the interactions between the two phases (air and water) were modeled by using the Volume of Fluid (VOF) method. This method solves one set of conservation equations for both phases, assuming common velocity, pressure and temperature fields, together with one additional equation for the phase volume fraction. The VOF model can be properly used when the mesh size is small enough compared to the resolved length scale of the two-phase interface, which is the case in the present investigations. Both phases were assumed to be incompressible with constant densities. The second-order upwind scheme was employed as a discretization scheme for computing the convective fluxes in the transport equations. A first-order upwind scheme was used for temporal discretization with a maximum time step of 0.2 ms for two-phase simulations. In every time-step, the number of inner iterations was varied between 6 and 40, ensuring always sufficient convergence of all residuals (at least to 5×10^{-6}). The surface tension force between water and air was taken into account with a constant value of 0.072 N/m.

Three two-phase flow cases were selected for the numerical simulations as listed in Table 6.2, where the case number matches those in Chapter 4, Q_w is the water flow rate, Q_a is gas flow rate, Re_w is the superficial water Reynolds number, Re_a is the superficial air Reynolds number, and ε is the gas volume fraction. The cases are selected with increasing liquid Reynolds number Re_w so that the shape and the size of the accumulated gas of each case are considerably different. Accordingly, the ability of the simulations to predict the flow features can be examined under different flow conditions. Unlike the single-phase simulations, all computations presented in this section are unsteady.

Table 6.2: Details of the two-phase flow cases considered.

Case #	Q_w (m^3/h)	Q_a (L/h)	Re_w	Re_a	ε %
4	8	28.28	50,130	12.34	0.352
7	9.5	14.14	59,530	6.17	0.148
11	11	0.707	68,930	3.10	0.064

Comparison of turbulence models

Since RSM and the realizable $k - \epsilon$ models could more accurately match the real single-phase flow behavior (Figure 6.6), they are further employed along with the VOF method and compared now for two-phase flows (Case 4 from Table 6.2). The air volume fraction of the two models is presented in Figure 6.11 after 30 seconds of physical simulation time in comparison with corresponding shadowgraphy experiments. This simulation time was found proper to get steady state flows; simulating further than 30 seconds does not lead to any significant change in the accumulated gas shape or size. The accumulated gas is represented by a (red) iso-surface in Figure 6.11, which shows all grid cells with gas volume fractions higher than 5%, while grid cells with lower values were excluded from the representation. This threshold value was found suitable to clearly visualize the accumulated gas in the simulations and identify the differences among all the considered two-phase simulations.

In Figure 6.11, it can be observed that the position and overall profile of gas accumulation predicted by RSM is qualitatively in better agreement with that of the experiments compared to that of the realizable $k-\epsilon$ model. This is particularly true near the diffuser exit. Nevertheless, the overall size of the gas pocket shows some slight deviations compared to the experiments. On the other hand, the realizable $k-\epsilon$ model performs poorly everywhere, and underestimates the overall size and shape of the gas accumulation, showing also earlier separation. Additionally, the realizable $k-\epsilon$ model failed to predict the stratified flow regime downstream of the diffuser.

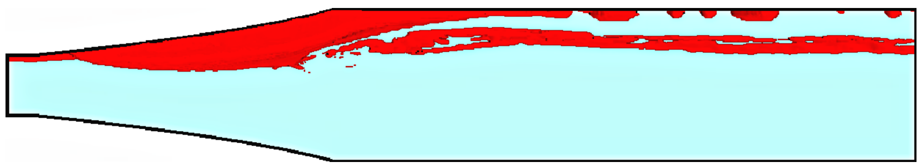

(a) Case 4 - Simulations - Realizable $k-\epsilon$

(b) Case 4 - Simulations - RSM

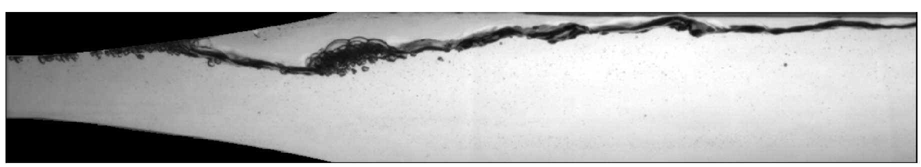

(c) Case 4 - Experiments

Figure 6.11: Comparison between different turbulence models and corresponding experiments for the two-phase flow behaviour (Case 4).

Additional details of the flow can be extracted from the simulations, complementing the experiments. Figure 6.12 shows corresponding velocity fields of the realizable $k-\epsilon$ and RSM models for Case 4 at the longitudinal mid-section plane ($z = 0.022$m). In both cases, the liquid phase is forced to move below the gas cavity. As shown, RSM delivers a more plausible velocity field, showing a gradual deceleration near the gas accumulation region and in the upper part of the channel. On the other hand, the realizable $k-\epsilon$ model exhibits unrealistic sharp gradients with lower velocities only in the stratified region. Additionally, the core flow jet of the realizable $k-\epsilon$ model is more pronounced while exiting the diffuser, leading also to a strong deceleration region in the lower part of the channel. These effects are not visible with RSM, where the velocity profile is smoother and uniformly spread within the channel height.

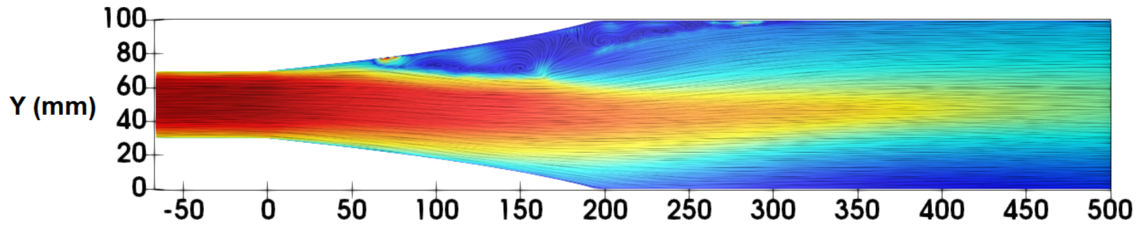

(a) Case 4 - Simulations - Realizable $k - \epsilon$

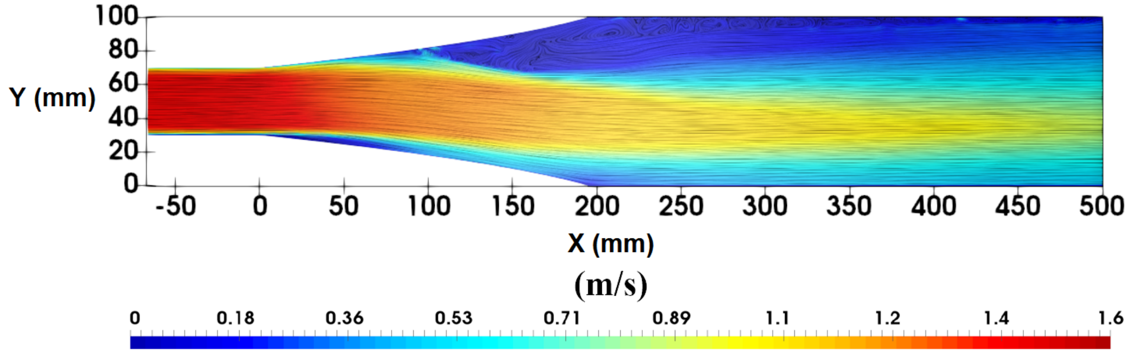

(b) Case 4 - Simulations - RSM

Figure 6.12: Instantaneous two-phase velocity fields for Case 4 predicted by the simulations.

Figure 6.13 compares the pressure recovery (averaged over the last 3 seconds of the simulation time) estimated by the realizable $k - \epsilon$ and RSM models against experimental data. The agreement is quite good despite the fact that $k - \epsilon$ estimated a smaller gas accumulation and an unrealistic velocity field, it shows an even better good agreement for pressure. This is properly the result of multiple errors, compensating each other. Although the values of the pressure recovery obtained by the VOF model coupled with RSM are overall slightly lower than the experiments, the pressure trend is still good.

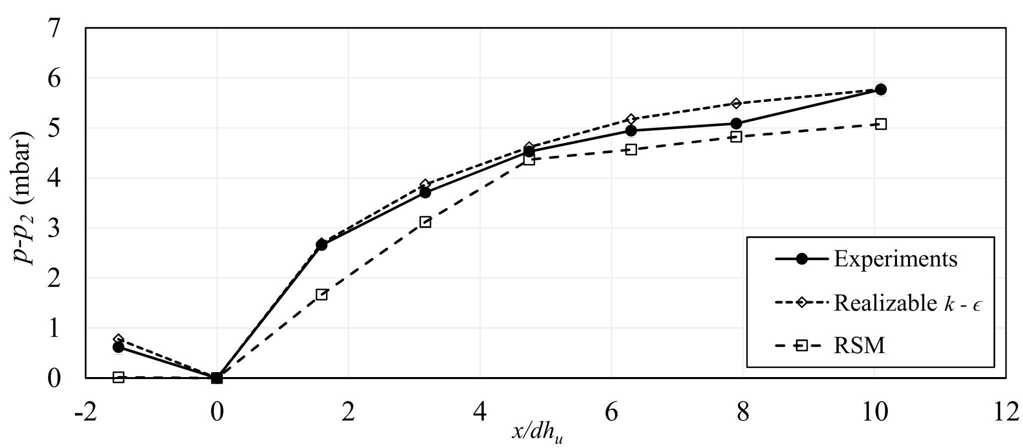

Figure 6.13: Comparison of numerical pressure recovery obtained by the realizable $k - \epsilon$ and RSM at $\mathrm{Re}_w = 50{,}130$ against measurements.

Higher Reynolds numbers

From the comparison of the two turbulence models under two-phase flow conditions, it can be concluded that the RSM-VOF combination could more adequately predict the gas accumulation for the considered superficial liquid Reynolds number ($\mathrm{Re}_w = 50,130$). With this evidence, RSM-VOF combination is further assessed for higher values of Re_w, i.e. Case 7 ($\mathrm{Re}_w = 59,530$) and Case 11 ($\mathrm{Re}_w = 68,930$) in Table 6.2. When the superficial water Reynolds number is increased, the flow is not segregated anymore downstream of the channel as was previously for Case 4 (Figure 6.11). After the diffuser, the air moves mostly as slug flow with agglomerated bubbles. The reason is that the turbulence levels are high enough to suppress the connected stratified flow of air, leading to strong bubble break-up. In this case, the gas accumulations behave unsteady, tending to move instantaneously towards one of the side walls in an alternative manner.

The two-phase flow regimes are presented in Figure 6.14 for Case 7 and Case 11. As can be seen, the flow separates earlier in the simulations for both cases, shifting the beginning of the predicted gas cavity upstream in the diffuser. That is why the shape and the size of the gas accumulation in the simulation are also not completely matching the corresponding experiments, affecting the prediction of the pressure recovery in the diffuser as well. This can be explained by the combined limitations of both turbulence model and the two-phase model.

Figure 6.15 shows the corresponding two-phase velocity fields for Case 7 and Case 11. As can be seen, the separation zone is generally getting bigger as the Reynolds number increases. The wavy velocity field of Case 7 shown in Figure 6.15a is an instantaneous behavior due to the splitting of large gas bubbles. However, the velocity field is smooth for most of the time. Figure 6.16 shows the pressure recovery for Case 11 in table 6.2. Similar to Case 4, it is observed that the simulation results has a slightly lower pressure recovery, yet with a very similar trend to the experiments.

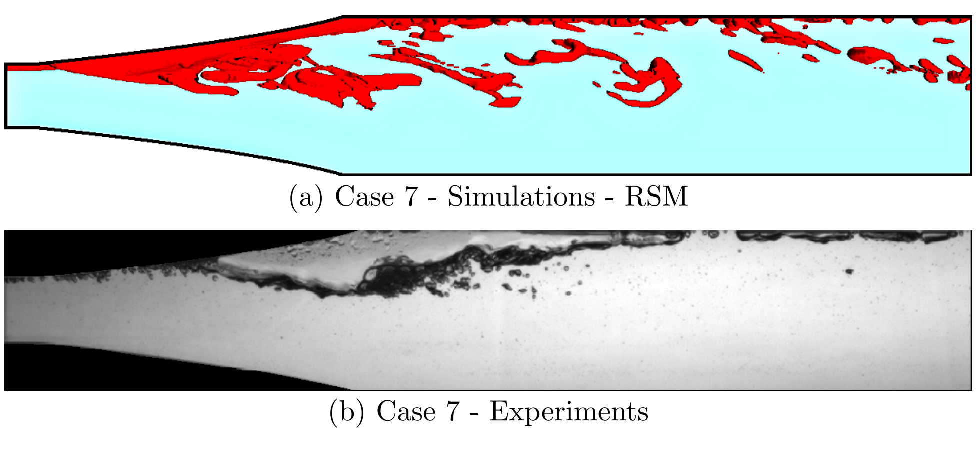

(a) Case 7 - Simulations - RSM

(b) Case 7 - Experiments

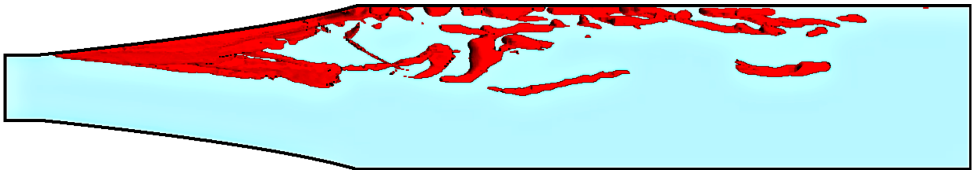

(c) Case 11 - Simulations - RSM

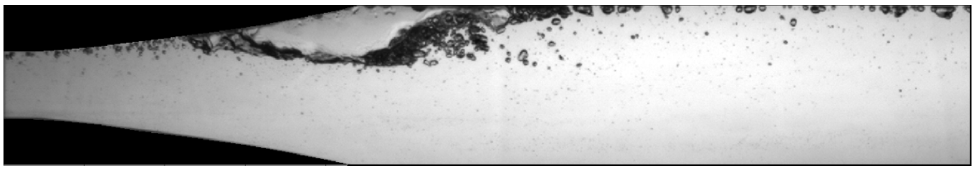

(d) Case 11 - Experiments

Figure 6.14: Comparison of gas accumulations for Case 7 and Case 11.

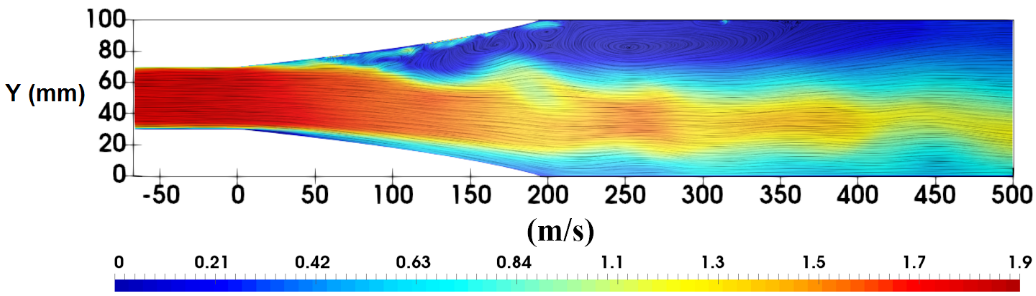

(a) Case 7 - Simulations - RSM

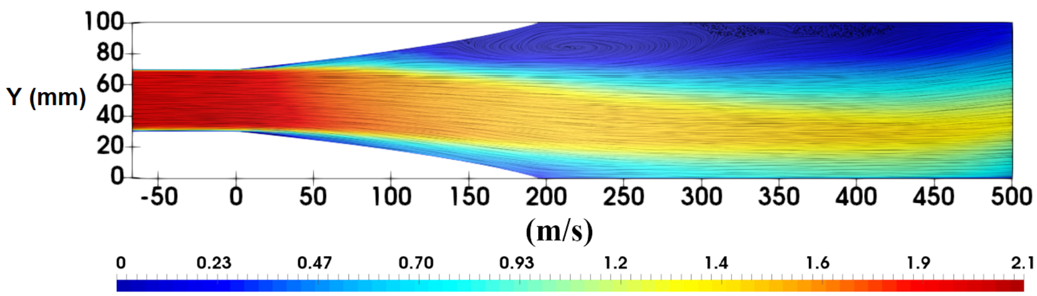

(b) Case 11 - Simulations - RSM

Figure 6.15: Instantaneous two-phase velocity fields predicted by RSM.

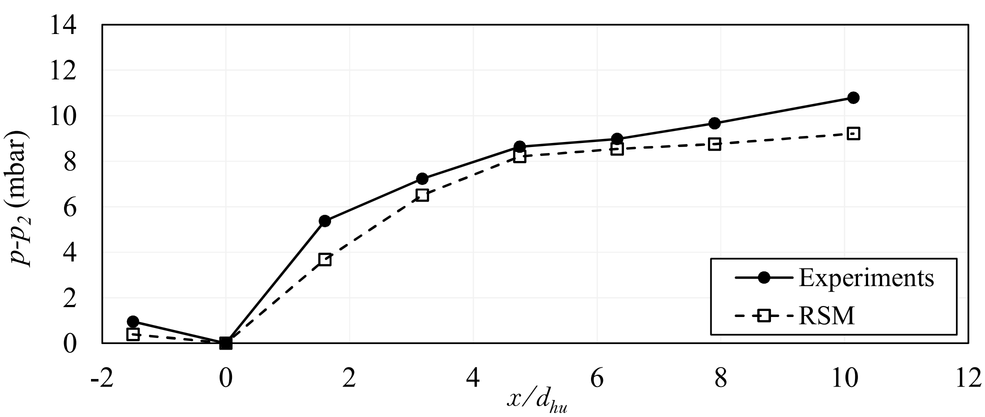

Figure 6.16: Comparison of experimental and RSM pressure recovery at Re_w = 68,930.

6.2.4 Summary

For the diverging channel simulations, only the realizable $k - \epsilon$ and RSM models predicted the single-phase water flow with good accuracy. Overall, for two-phase simulations, the results with RSM and VOF show good agreement with the experiments concerning the gas accumulation and the pressure recovery. The $k - \epsilon$ - VOF combination failed to estimate the cavity size and also the flow field. Very accurate results regarding the size, the shape, and the position of the gas accumulations are difficult to obtain numerically in such highly turbulent, two-phase, separated flows. Reynolds stresses are most sensitive to the parameterization of the triple-velocity correlation where local turbulent production is negligible and turbulence is mainly sustained by the flux transport term [124]. As suggested in [125], it is necessary to treat the right-hand side term in the Reynolds stress transport model with much higher closure models to improve accuracy concerning pressure. Additionally, the VOF model is not fully able to capture accurately the coalescence and break-up of small bubbles [126]. Altogether, the two effects lead to some deviations in the simulations. A better agreement could perhaps be obtained by using higher-order turbulence models like Large-Eddy Simulations (LES), combined with Euler-Euler (two-fluid) models [127]. Corresponding simulations would require a much higher computational power. Accurate experimental data are necessary to quantify the accuracy of the obtained results.

6.3 Inducer simulations

In this section, the flow details within the inducer are investigated using CFD simulations, considering a simplified 3D model. The following analysis is useful to understand the best operating range of inducers when used for improving two-phase pumping. Further, the simulations could explain the disparate influences of the inducer on the two-phase performance in part-load and overload conditions. The presented comparisons between numerical and experimental results are also useful for selecting suitable numerical models for such a complex flow since the impact of the employed numerical settings is also discussed.

6.3.1 Numerical modeling

For the inducer simulations, steady-state as well as transient simulations with different turbulence models (Realizable $k-\epsilon$, $k-\omega$ SST, Spalart-Allmaras, and Reynolds-Stress Model – RSM) were compared using STAR-CCM+. The steady simulations were done using a frozen-rotor approach with a Moving Reference Frame (MRF) for single-phase flow, while the transient approach was implemented using a moving mesh approach for two-phase flows. The MRF approach is very effective for modeling the time-averaged properties of a moving flow field, by moving the observer coordinates. It can model the motion by steady simulations, yet it eliminates the need for rotating the inducer body or moving the mesh, which reduces computational cost. In MRF simulations, a constant grid flux (i.e., a Coriolis force that is induced by the rotation) is imposed in the source term of appropriate conservation equations for the defined rotating domain (where the inducer is placed). In the transient two-phase simulations, air-water interactions are modeled again by the Volume of Fluid (VOF) method. Likewise, the flow is considered to be incompressible, since the average change of the air density, for the whole pressure range considered, is limited only to 3.2%. The simulations were stopped after simulating 1.0 second of physical time, corresponding to more than 10 complete revolutions of the inducer, which are sufficient to reach statistically steady conditions.

The considered domain focuses mainly on the inducer as shown in Figure 6.17. All dimensions are given as a function of the suction pipe diameter (D_s). Two pressure probes are used in the simulation across the inducer, at the same locations as in the experiments. Sensor 2 is set at the end of the blades because it was not possible experimentally to move it further downstream since the impeller is directly installed behind the inducer. The domain is split into two equal parts, i.e. a stationary domain (before the inducer) and a rotating domain (around the inducer). The tangential speed of the pipe wall is kept zero in the whole domain with respect to the stationary reference frame, allowing only the inducer to rotate. For two-phase simulations, the inlet surface is divided into two inlet boundaries, one for each phase. The inlet surface of air is centered on the pipe axis and maintained so that both the air and water phases have identical velocities ($V_a = V_w$) in all simulations, which is comparable with the way the air is injected in the experiments. To satisfy the condition $V_a = V_w$, the diameter of the air inlet surface is set to $D_s\sqrt{\varepsilon}$, where ε is the gas volume fraction. Gas volume fractions from 0% up to 5% were studied for the complete range of flow rates.

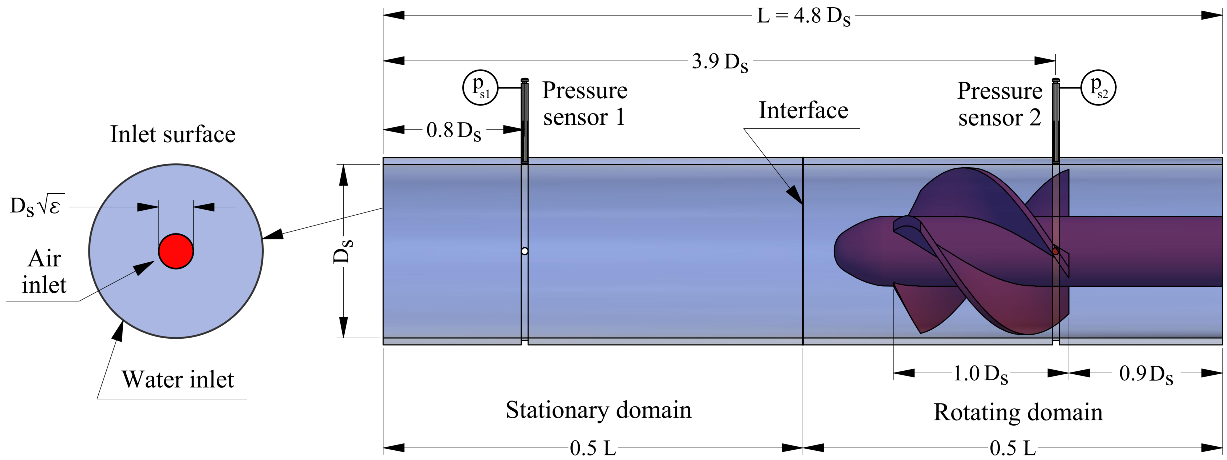

Figure 6.17: Numerical domain used for the inducer simulations.

Mesh-independence study

A polyhedral mesh was generated for the whole domain, considering an in-place interface between the stationary and the rotating domain. A total of 8 prism layers were generated along all walls, for an accurate resolution of the boundary layer flow. To confirm that the numerical results are mesh-independent, a mesh-convergence study was performed, considering different mesh resolutions. The mesh-independence study was carried out for two-phase flow conditions at $Q_w/Q_{opt} = 0.5$ and $\varepsilon = 3\%$ using the Reynolds Stress Model (RSM) for turbulence modeling. The details of the different mesh resolutions used for the mesh study are given in Table 6.3. As shown, the average non-dimensional wall distance (y+) was kept always lower than 1 by adapting the height of the first cell near the wall. Accordingly, the boundary layer can be accurately resolved without activating any wall model.

Considering different grids, Figure 6.18a shows the numerical pressure change between the two sensors ($p_{s2} - p_{s1}$) and across the simulation domain ($p_{out} - p_{in}$) averaged over one inducer rotation. As shown, no significant differences are found in the flow properties when using 3.25 million cells or more (meshes 3 to 5). The maximum difference between the last 3 meshes is limited merely to 83 Pa, which is negligible for the considered pressure range. Therefore, mesh 3 with 3.25 million cells was kept for all single-phase simulations. However, for two-phase simulations, mesh 4 with 5.11 million cells is employed to ensure a more accurate resolution of small-scale gas structures, as shown in Figure 6.18b by gas volume fraction scenes corresponding to different meshes near the inlet at $x = 0.083L$. Sample images of the final grids used for single and two-phase simulations are shown in Figure 6.19.

Table 6.3: Details of different grids used for the inducer mesh-independence study.

Mesh #	No. of cells (millions)	Average y+
1	0.46	0.81
2	2.25	0.33
3	3.25	0.26
4	5.11	0.21
5	8.25	0.18

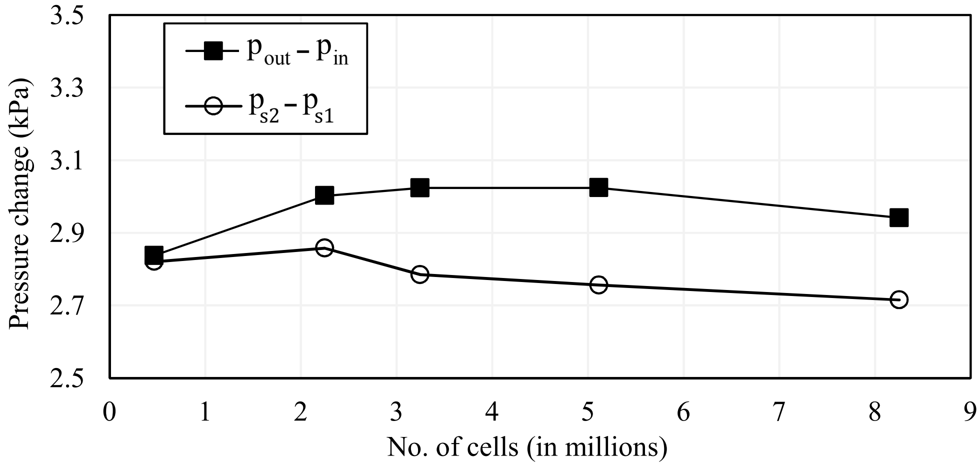

(a) Pressure change

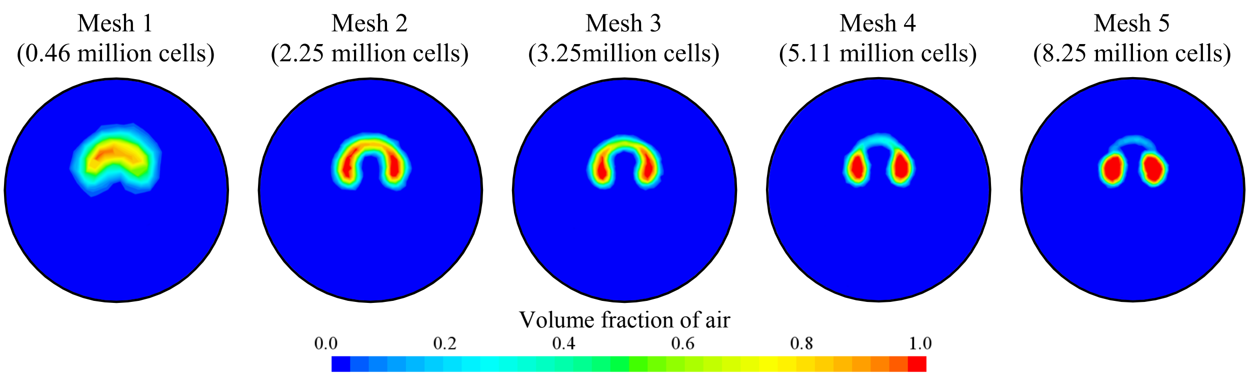

(b) Air volume fraction at $x = 0.083L$

Figure 6.18: Comparison of the numerical results for different mesh resolutions at $Q_w/Q_{opt} = 0.5$ and $\varepsilon = 3\%$.

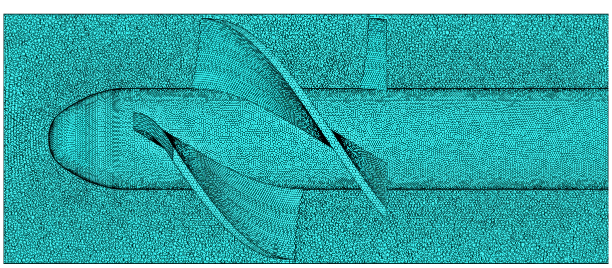

(a) Single-phase mesh (3.25 million cells)

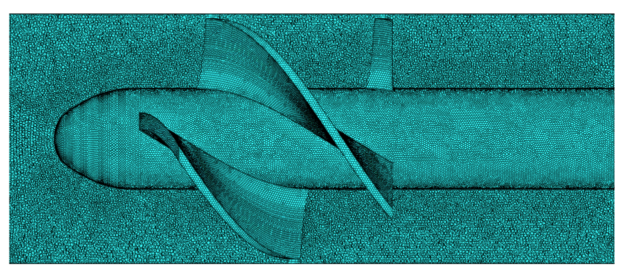

(b) Two-phase mesh (5.11 million cells)

Figure 6.19: Numerical grids for single and two-phase flow.

Timestep test

The discretization in time is important as well. Therefore, the impact of the retained timestep has been checked. The obtained pressure changes across the simulation domain were compared using 4 different time steps, corresponding to 0.5°, 1.0°, 2°, and 4° angle rotations per time step. A sample value of $\varepsilon = 3\%$ was used, together with the maximum flow rate ($Q_w/Q_{opt} = 1.6$, overload), ensuring that all other, lower flow rates are also well resolved in time. Figure 6.20 presents the pressure change across the simulation domain ($p_{out} - p_{in}$) averaged over two inducer rotations for all time steps considered. As shown, the numerical results of 0.5° (0.128 ms) and 1.0° (0.256 ms) are almost identical. Accordingly, a time step of 1.0° was selected for all further simulations. Additionally, a total number of 80 inner iterations were found suitable for two-phase simulations, leading to a drop of at least three magnitudes of the residuals. Finally, the two-phase simulations were stopped after simulating 1.0 second of physical time, corresponding to more than 10 complete revolutions of the inducer. This simulation time is sufficient to reach statistically stable conditions in all cases.

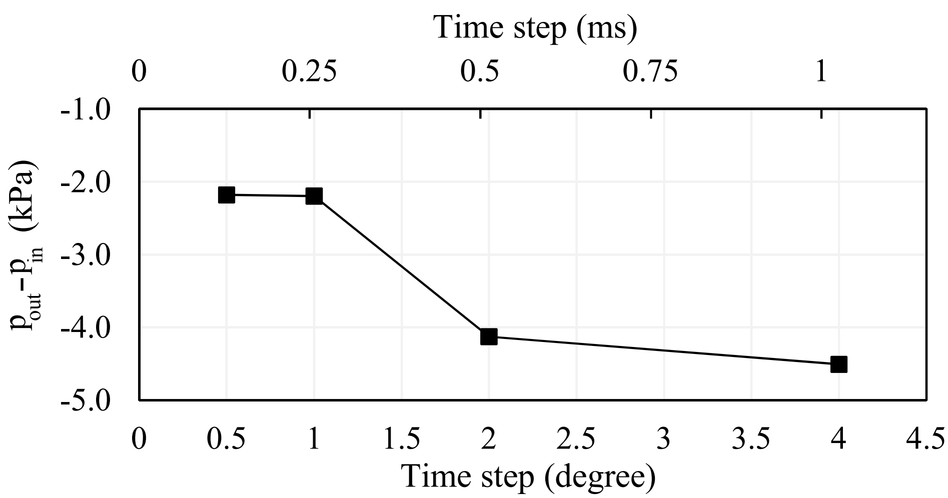

Figure 6.20: Numerical results for pressure difference corresponding to different time steps at $Q_w/Q_{opt} = 1.6$ and $\varepsilon = 3\%$.

6.3.2 Single-phase analysis for the inducer performance

Firstly, a comparison for the numerical results obtained with different turbulence models is shown together with the measured single-phase performance of the inducer. This is done to decide an appropriate turbulence model for the further two-phase simulations. Figure 6.21 compares the numerical results corresponding to different turbulence models with the experimental data, considering the realizable $k - \epsilon$, the $k - \omega$ SST, the Spalart–Allmaras and the RSM turbulence models. Compared to the experiments, it is clear from Figure 6.21 that most models can generally predict correctly the pressure change across the inducer, particularly near the optimal flow rate of the pump. However, at $Q_w/Q_{opt} = 0.4$, the realizable $k - \epsilon$, $k - \omega$ SST and Spalart-Allmaras models deviate obviously from the measured data. Additionally, in overload conditions, all first-order turbulence models slightly overestimate the experimental curve. Nevertheless, RSM can predict the axial pressure change very precisely, since it matches quite perfectly the measured data almost along the whole flow rate range. In Figure 6.21, also unsteady single-phase simulations with RSM are shown to ensure that the results of both steady and unsteady simulations are similar. Here, the numerical results of the unsteady simulations are averaged over one complete inducer rotation. It can be seen that both the steady MRF and the transient moving mesh simulations with RSM lead to very similar values.

It can also be seen in Figure 6.21 that the performance (pressure change) of the inducer is mainly negative for overload conditions. In this case, the air would expand and occupy more space in the impeller channels as a result of such reduced pressure after the inducer. This is one of the main reasons for the considerably decreased positive influence of the inducer on the two-phase pumping performance in overload conditions. Nevertheless, it is important to mention here that the inducer still has the ability to slightly improve the two-phase pumping capacity up to $\varepsilon = 4 - 5\%$ in overload conditions, even with such a negative pressure change across the inducer. The justification for this improvement is discussed later by analyzing the results of the two-phase simulations. Now, to understand these changes in inducer performance, the flow is further analyzed by examining the velocity fields at radial and axial sections across the blades of the inducer. Figure 6.22 illustrates the location of the sections used for this analysis. The axial section was set vertically in the middle of the pipe, while the radial section was placed at a distance of $x = 0.72L$ from the inlet surface of the simulation domain (approximately mid-length of the blades).

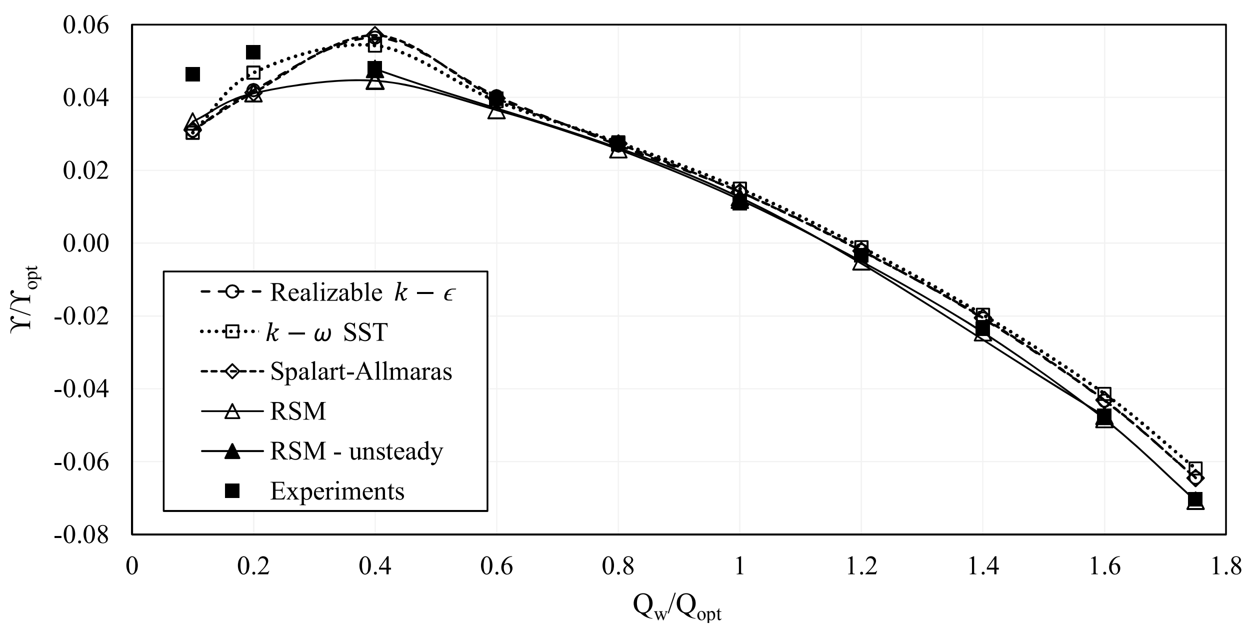

Figure 6.21: Comparison of numerical results obtained by different turbulence models against the experimental data (single-phase flow).

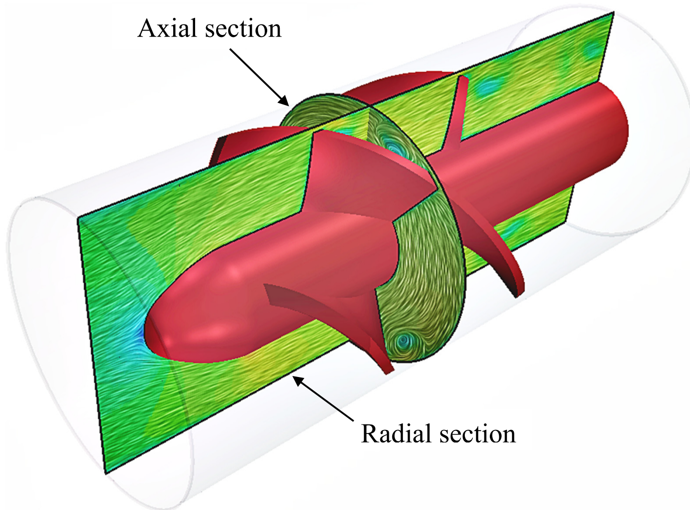

Figure 6.22: Illustration of the axial and radial sections used for the analysis of velocity fields.

Figure 6.23 presents the velocity fields at the axial section for the different turbulence models applied. The first, the second and the third columns correspond to part-load ($Q_w/Q_{opt} = 0.4$), optimal ($Q_w/Q_{opt} = 1.0$) and overload ($Q_w/Q_{opt} = 1.6$) conditions, respectively. As shown, the flow streamlines are quite smooth in the longitudinal direction for optimal and overload conditions. Additionally, no significant differences can be seen in the velocity fields obtained by different turbulence models for optimal and overload conditions. However, tangential vortices occur for part-load conditions (at $Q_w/Q_{opt} = 0.4$). These vortices can be generally predicted by all turbulence models. However, RSM captures more vortices, with higher streamline curvatures and more apparent structures compared to other models. The pressure change of RSM is very close to the corresponding measured value at $Q_w/Q_{opt} = 0.4$, while the other models deviate, as shown previously in Figure 6.21.

Similarly, Figure 6.24 compares the velocity fields at the radial section for different turbulence models and flow rates. In the radial section, only slight changes can be seen when different turbulence model are compared. For optimal and part-load flow conditions, the flow is moderately smooth with some curved streamlines at part-load conditions due to the presence of tangential vortices shown previously in Figure 6.23, leading also to high-velocity gradients as can be seen in Figure 6.24 (note the blue and the red colors shown in part-load flow conditions).

For overload conditions, the simulation results reveal that the flow obviously separates and forms strong vortices near the blades. These vortices can be captured by all turbulence models, as shown in the last column of Figure 6.24. The presence of the flow separation and such strong vortices justifies the negative pressure change across the inducer and the reduced performance at overload flow conditions. Additionally, the separated flow in overload conditions explains the sudden reduction of the two-phase pumping performance when employing the inducer, restricting most of its positive effect to part-load flow conditions. Based on this presented velocity analysis, RSM was further kept for all the following two-phase simulations.

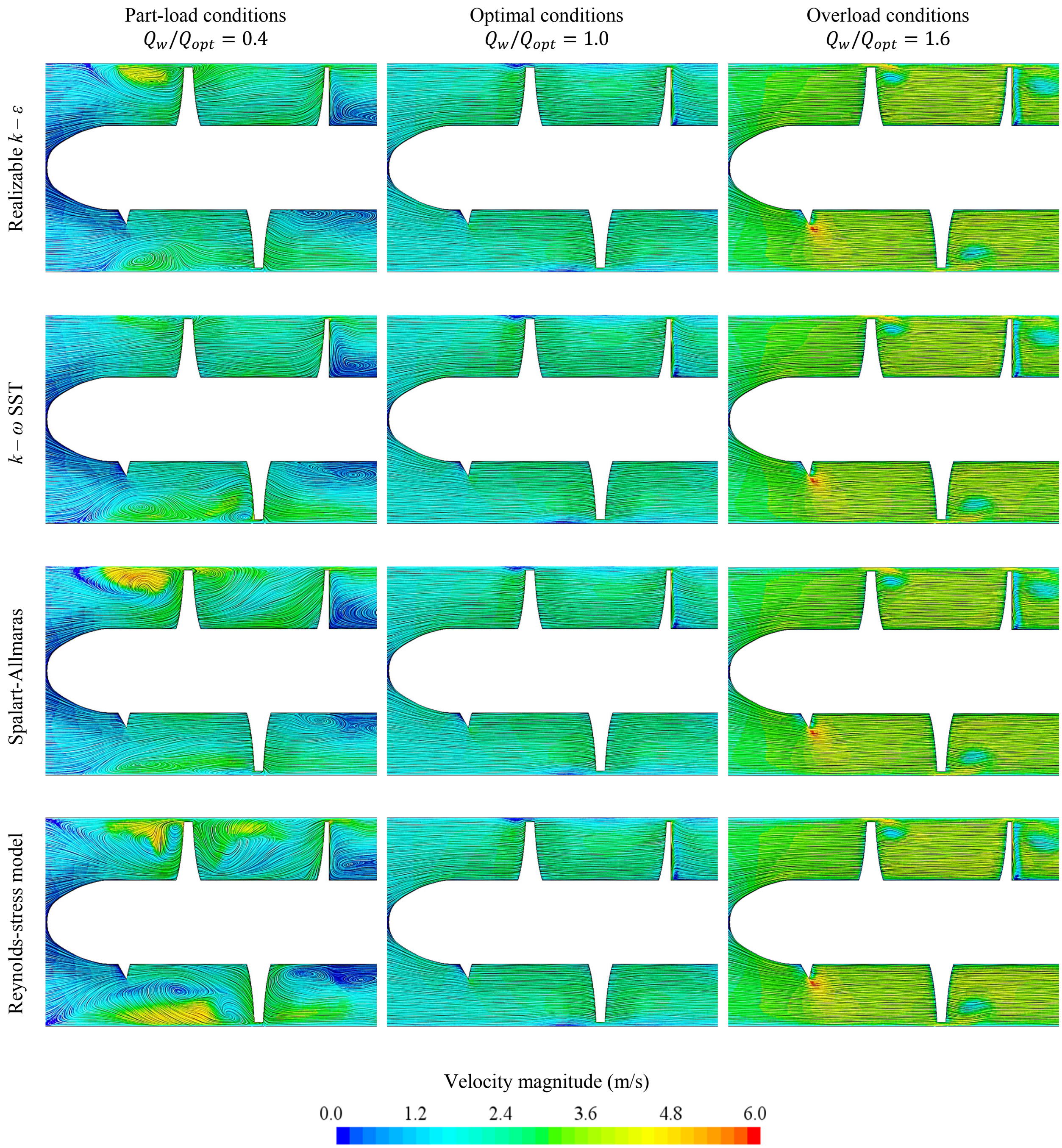

Figure 6.23: Average velocity fields along the axial plane for different turbulence models and flow rates.

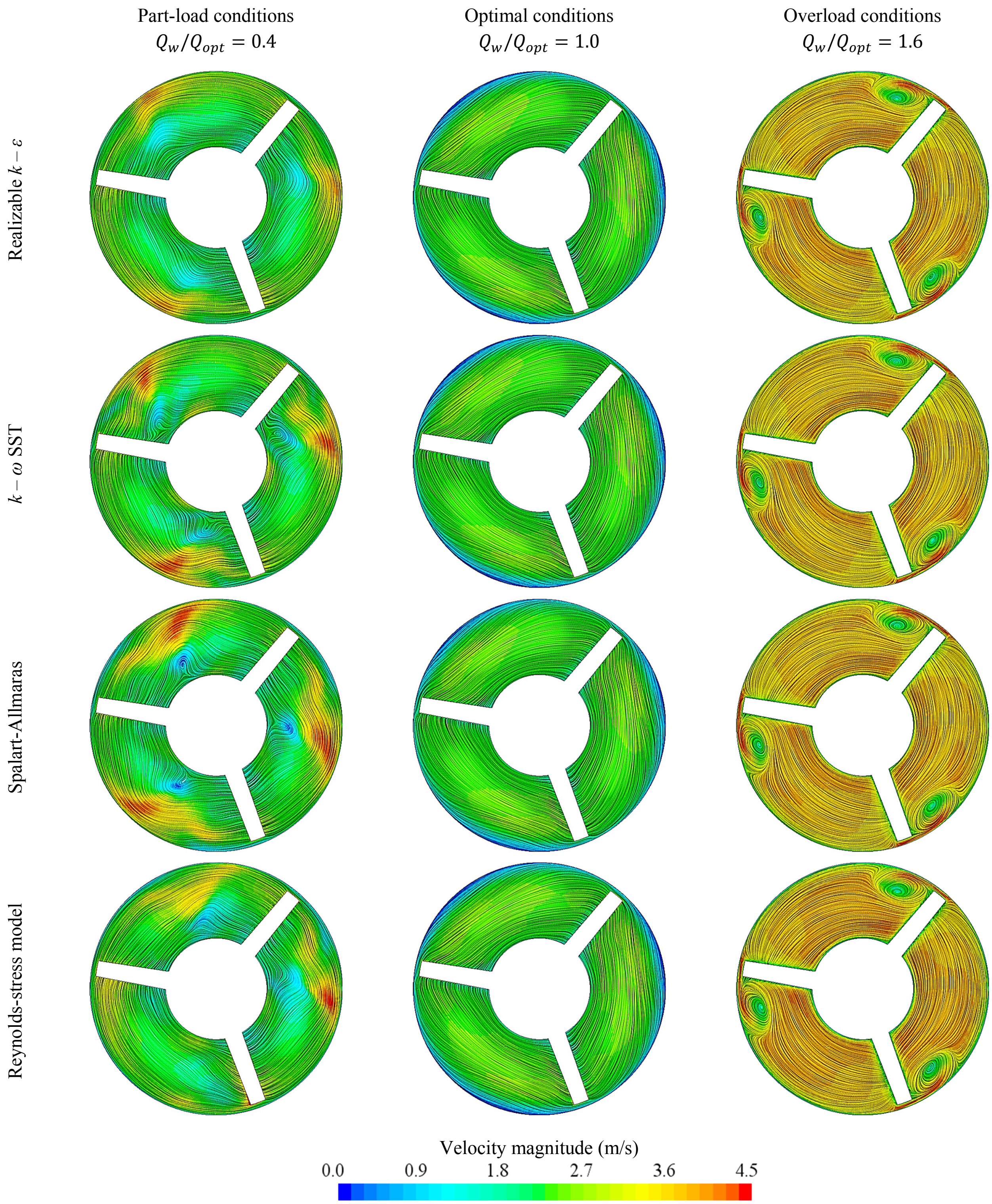

Figure 6.24: Average velocity fields along the radial plan ($x = 0.72L$) for different turbulence models and flow rates.

6.3.3 Two-phase analysis for the inducer performance

The two-phase simulations were carried out for different gas volume fractions (1%, 3%, and 5%), considering similarly part-load ($Q_w/Q_{opt} = 0.5$), optimal ($Q_w/Q_{opt} = 1.0$) and overload ($Q_w/Q_{opt} = 1.6$) conditions. Figure 6.25 presents a comparison between the numerical and experimental results of the two-phase performance of the inducer. The numerical results shown in Figure 6.25 are averaged over one complete inducer rotation, while the experimental data are deduced from 200 instantaneous measurements recorded over a period of 50 seconds (4 Hz). Compared to the experimental points, it is clear from Figure 6.25 that the RSM-VOF combination can very well predict the specific work of the inducer, considering also different gas volume fractions. Figure 6.25d compares the numerical results of the inducer performance for different gas volume fractions. As can be seen, the presence of the gas phase has only a moderate influence on the specific work of the inducer in part-load and optimal conditions, while the effect is much more pronounced at overload, particularly so at $\varepsilon = 5\%$. The reason for this increased performance deterioration is explained later by analyzing the flow field.

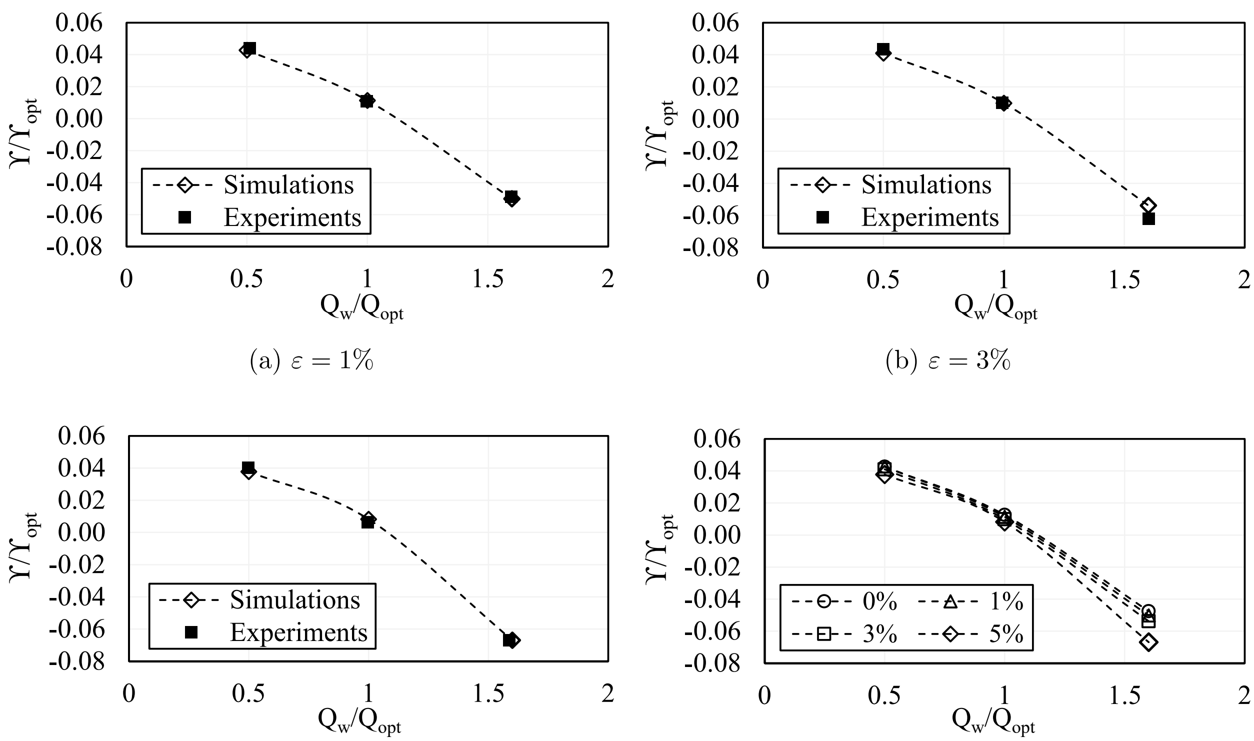

(a) $\varepsilon = 1\%$ (b) $\varepsilon = 3\%$

(c) $\varepsilon = 5\%$ (d) Performance deterioration

Figure 6.25: Comparison between numerical and experimental results of the inducer performance for different gas volume fractions.

Figure 6.26 presents the velocity fields along the radial section, for two-phase flow conditions. Again, for part-load ($Q_w/Q_{opt} = 0.5$) only weak vortex structures can be seen in the considered radial section, while the velocity fields are mostly smooth at optimal conditions ($Q_w/Q_{opt} = 1.0$). For overload conditions ($Q_w/Q_{opt} = 1.6$), the strong flow separation with axial vortices still prevails, with more complex structures for higher gas volume fractions. The velocity "spots" shown in Figure 6.26 indicate the presence of the gas phase, which significantly changes the local velocity.

Figure 6.27 shows the Q-criterion of the flow in part-load and overload conditions for different gas volume fractions to clarify further the influence of the gas phase on the vortices. The Q-criterion is a three-dimensional, scalar indicator that can be used to visualize a vortex as a spatial region [128]. As can be seen in Figure 6.27 for part-load conditions, some vortices appear around the hub of the inducer already at $\varepsilon = 0\%$. However, these vortices are disrupted by the inducer and are transported downstream as disconnected, small-scale structures. The increase of gas volume fraction from 0% to 5% does not change significantly this observation, explaining the satisfactory performance of the inducer in part-load conditions (Figure 6.25).

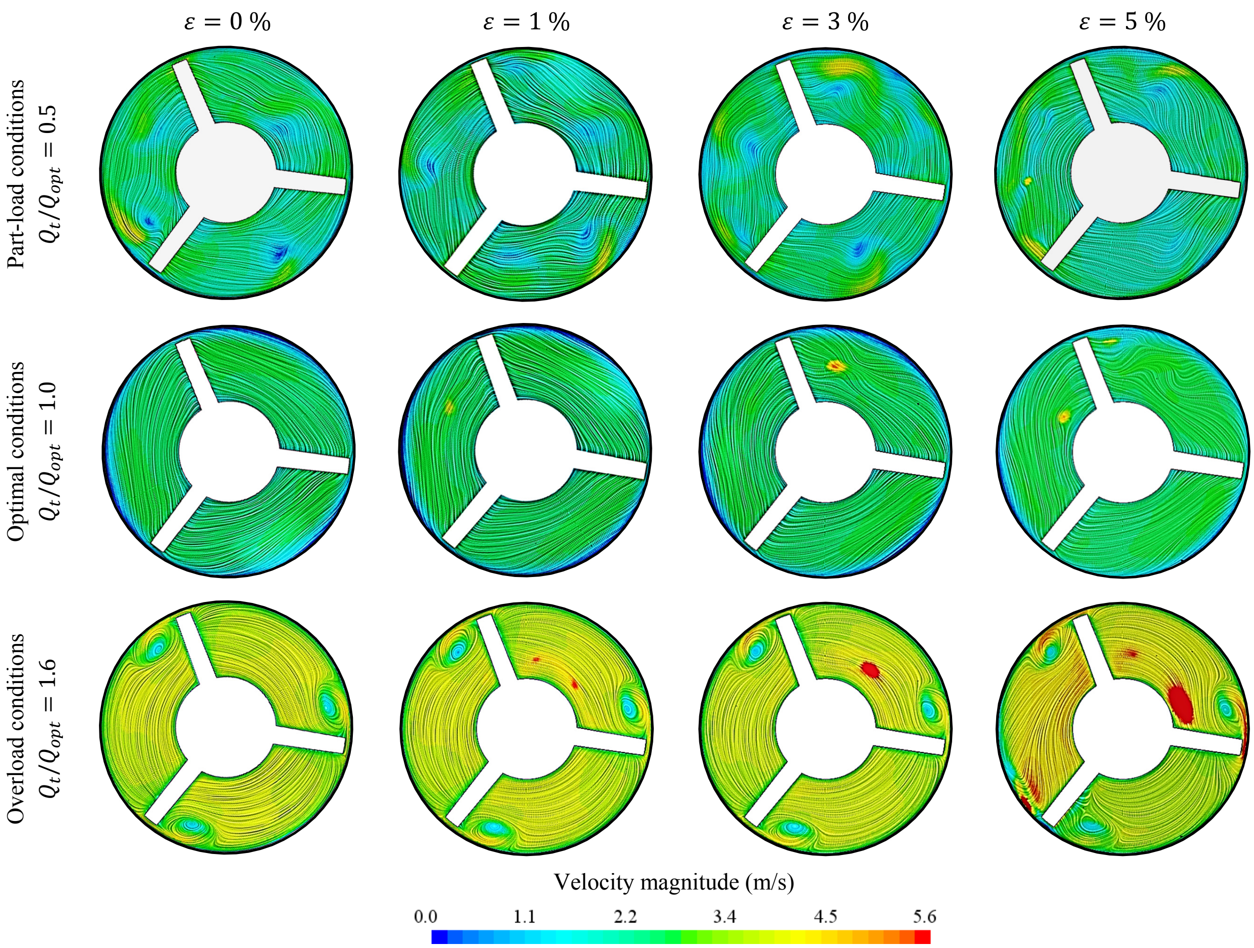

Figure 6.26: Instantaneous radial velocity fields at $x = 0.72L$ for different gas volume fractions.

On the other hand, for overload conditions, the induced vortices appear as long coherent structures within the inducer along the whole length of the blades, hindering the inducer from increasing pressure. Additionally, the increase in gas volume fraction considerably strengthens flow separation, leading to the formation of additional vortices that continuously reduce the pressure downstream of the inducer, as shown previously in Figure 6.25. This explains the performance deterioration of the inducer for $\varepsilon \geq 5\%$ observed for overload conditions.

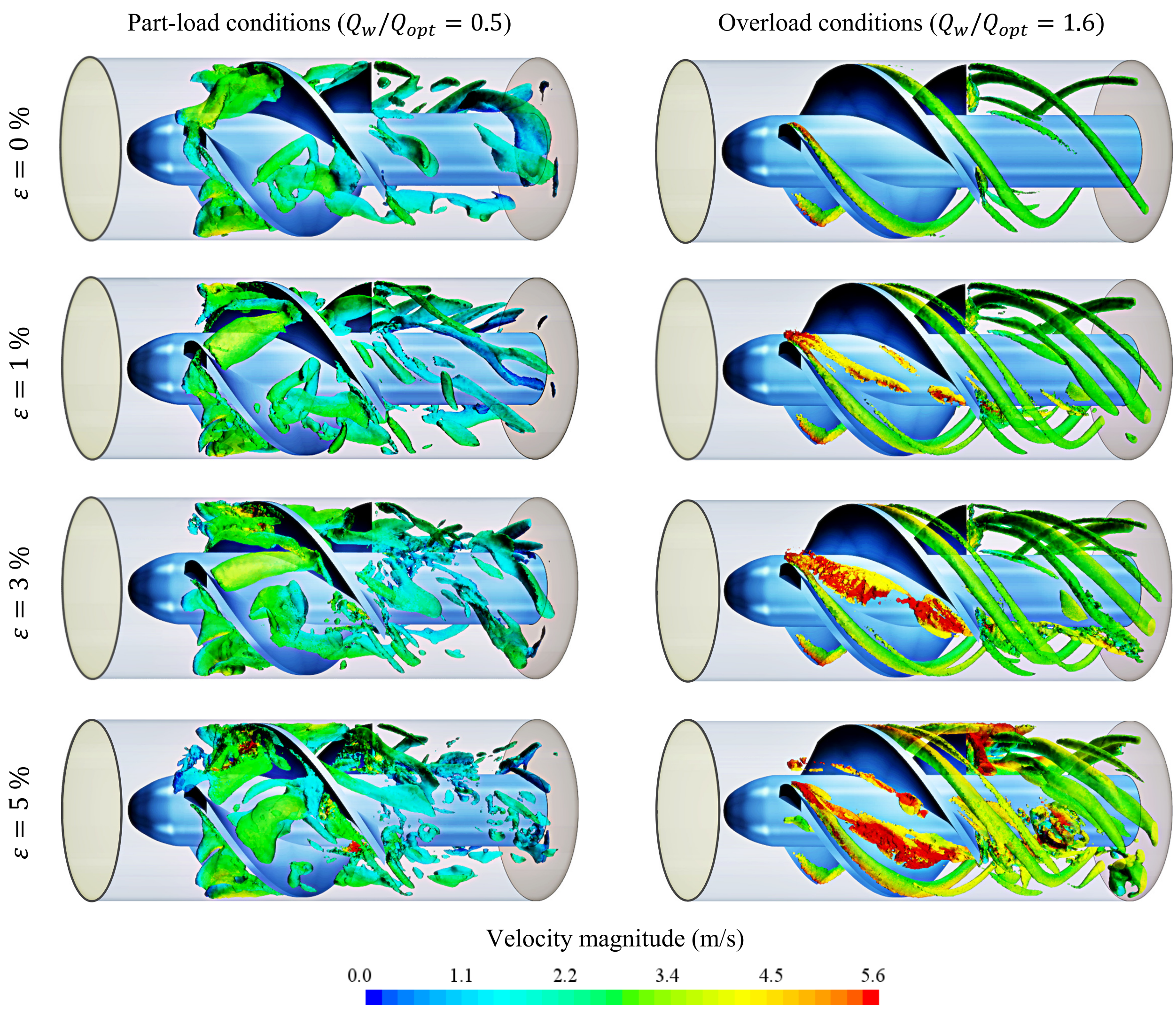

Figure 6.27: 3D views of the vortex structures represented by Q-criterion (threshold value is $Q_{cr} = 6000\ s^{-2}$) for gas volume fractions at part-load (left) and overload conditions (right).

Two-phase flow patterns

The two-phase flow behaviour across the inducer and the ability of the inducer to mix the two phases are analyzed in this section. Figure 6.28 shows the distribution of the air phase represented by a (red) iso-surface at $Q_w/Q_{opt} = 0.5$ for three different gas volume fractions along the inducer and at the domain outlet surface after 1.0 second of simulation time (approximately 11 inducer rotations). Here, the iso-surface shows all cells which have gas volume fractions higher than 5%, while cells involving lower values than this threshold were excluded from the representation. This threshold value was found suitable to visualize the two-phase flow patterns and identify corresponding differences of the patterns among all the considered two-phase simulations.

As shown in Figure 6.28, the flow is quite slow for part-load conditions and air accumulates mostly at the top side of the pipe due to buoyancy before it reaches the inducer. It is worth mentioning here that such a separated flow behaviour makes the gas accumulation easier at the impeller inlet and increases the performance deterioration when the pump runs without inducer. However, the inducer can effectively disturb the air accumulation and strongly mix back the two phases, producing a much more homogeneous mixture at the impeller inlet. Even when the gas volume fraction is increased up to $\varepsilon = 5\%$, the inducer preserves its ability to provide a very uniform two-phase mixture behind it, as shown in Figure 6.28. Therefore, the inducer can generally improve the two-phase pump performance significantly in such low-flow conditions. Furthermore, the pressure change across the inducer is mostly positive for part-load conditions, which decreases the volume occupied by the air phase at the impeller inlet, delaying the pump performance degradation. This effect together with the presented flow patterns in Figure 6.28 explain clearly the efficient influence of inducer on two-phase pumping in part-load conditions.

Considering now the flow behavior at optimal and overload flow conditions as presented in Figure 6.29 and 6.30, respectively, it can be seen that the inducer mixing becomes less effective compared to the part-load flow; the two phases are now far less uniform at inducer outlet. Since the flow is now faster, several large attached gas pockets can still be seen downstream of the inducer, the residence time being now insufficient to obtain proper phase mixing. The reason for the considerably reduced mixing is that most of the gas phase passes through the upper part of the inducer blades (no gas can be seen under the inducer blades for all cases shown in Figure 6.29 and 6.30), revealing the insufficient residence time of the flow across the blades.

In these cases, the fluid flow rate is higher, and the inertia force of the flow is more significant compared to the centrifugal force produced by the inducer. Therefore, the inducer mostly fails to provide significant improvement of the two-phase pump performance for such high flow rate conditions. Moreover, the negative pressure change occurring across the inducer at overload conditions due to flow separation will simultaneously allow the air to expand and occupy more space in the impeller channels. The combined effects of reduced mixing and lower pressure explain the sudden drop of inducer performance at overload conditions. The overall pump performance is still slightly improved due to the (low) additional phase mixing produced by the inducer.

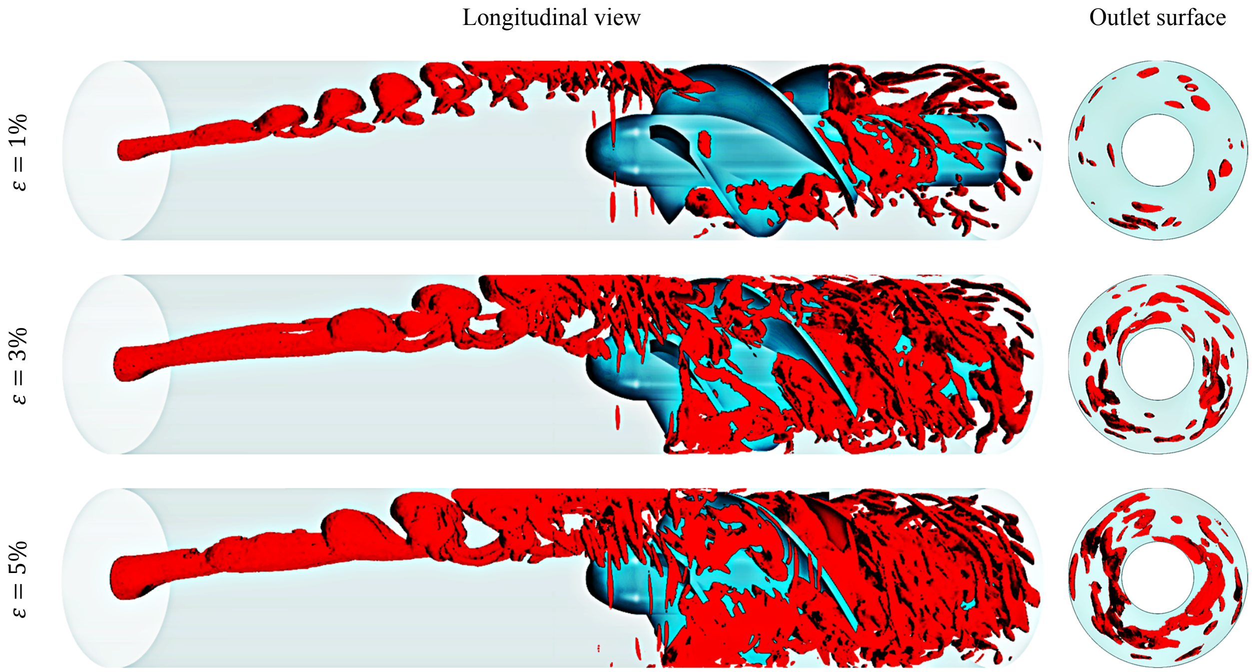

Figure 6.28: Two-phase flow patterns at part-load conditions ($Q_w/Q_{opt} = 0.5$).

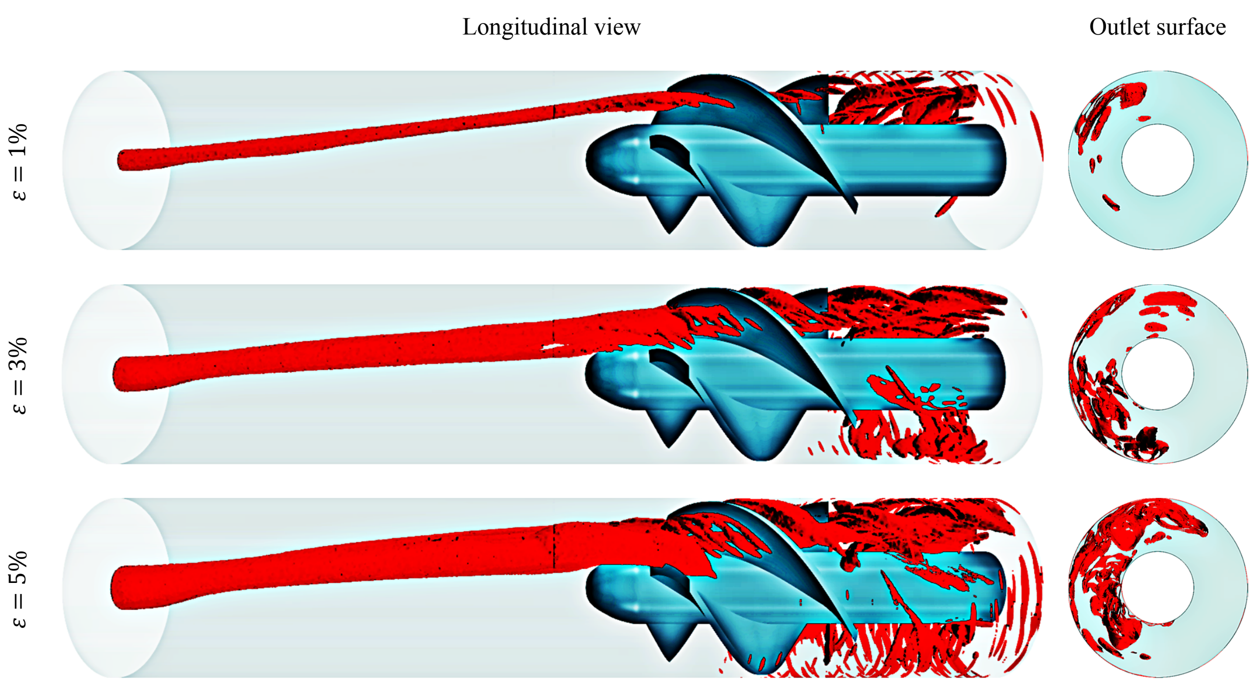

Figure 6.29: Two-phase flow patterns at optimal conditions ($Q_w/Q_{opt} = 1.0$).

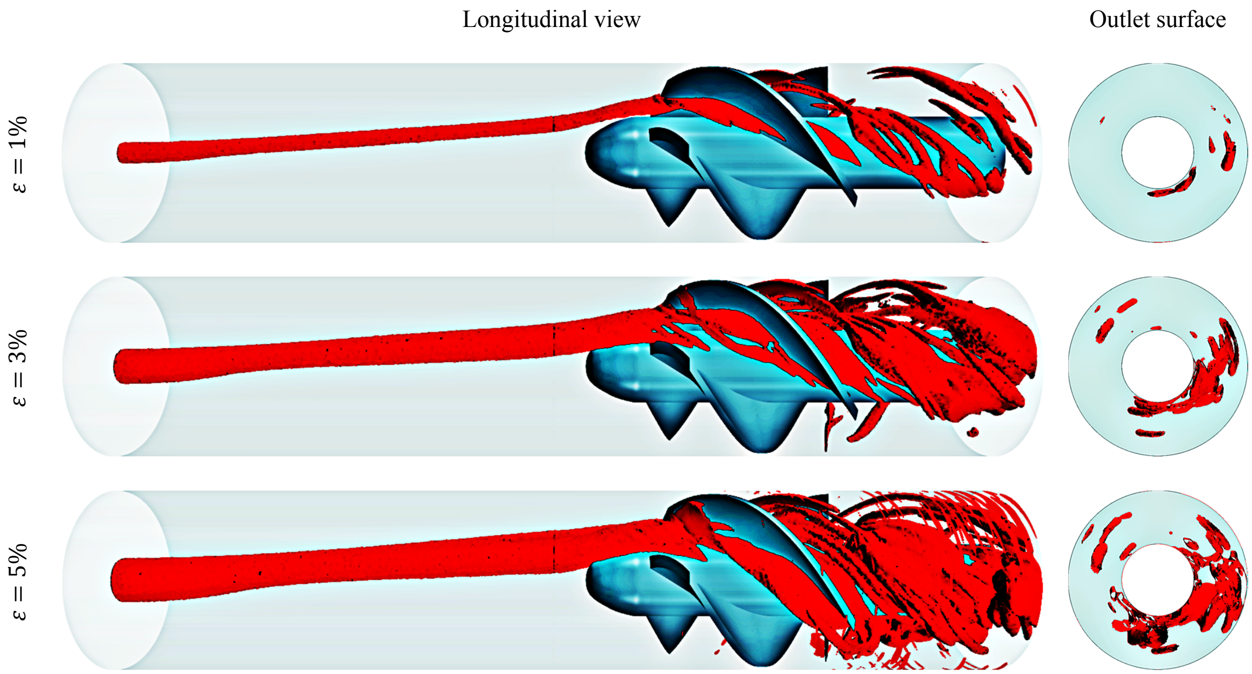

Figure 6.30: Two-phase flow patterns at overload conditions ($Q_w/Q_{opt} = 1.6$).

Mixing performance

In this last section, the axial evolution of the two-phase flow mixing is investigated to precisely compare the different conditions. Figure 6.31 shows the radial distributions of gas volume fraction on a series of sections distributed along the simulation domain for different flow rate conditions, considering $\varepsilon = 3\%$ as exemplary gas volume fraction. For part-load, it is clear from Figure 6.31 that most of the gas phase is accumulated at the top side of the pipe at $x = 0.5L$ before it becomes strongly mixed with water at higher values of x. For optimal and overload conditions, the gas phase slightly moves upwards but is still far from the upper wall. In the range of $x = 0.64L - 0.75L$, no gas can be seen on the lower side of the inducer, due to the lower residence time. Downstream of the inducer, Figure 6.31 highlights the much-improved distribution of air at part-load conditions compared to the two other flow cases.

Now, to quantify the mixing of the two phases, the surface uniformity in terms of the gas volume fraction is obtained on a series of radial sections distributed axially. The surface uniformity (uniformity index) represents how uniform the air is distributed on a specific surface based on the air volume fraction, and can be calculated by Equation 6.1. In this equation, c is the local volume fraction of air, $\bar{c}$ is the average volume fraction over the area A, and A_f is the area of an elementary cell face. The average volume fraction $\bar{c}$ can be calculated by Equation 6.2. The maximum value of S_u is 1.0 and its minimum value ($S_{u,min}$) occurs at the inlet, where the two phases are completely separated.

$$S_u = 1 - \frac{\sum_f |c - \bar{c}| \, A_f}{2 \, |\bar{c}| \sum_f A_f} \tag{6.1}$$

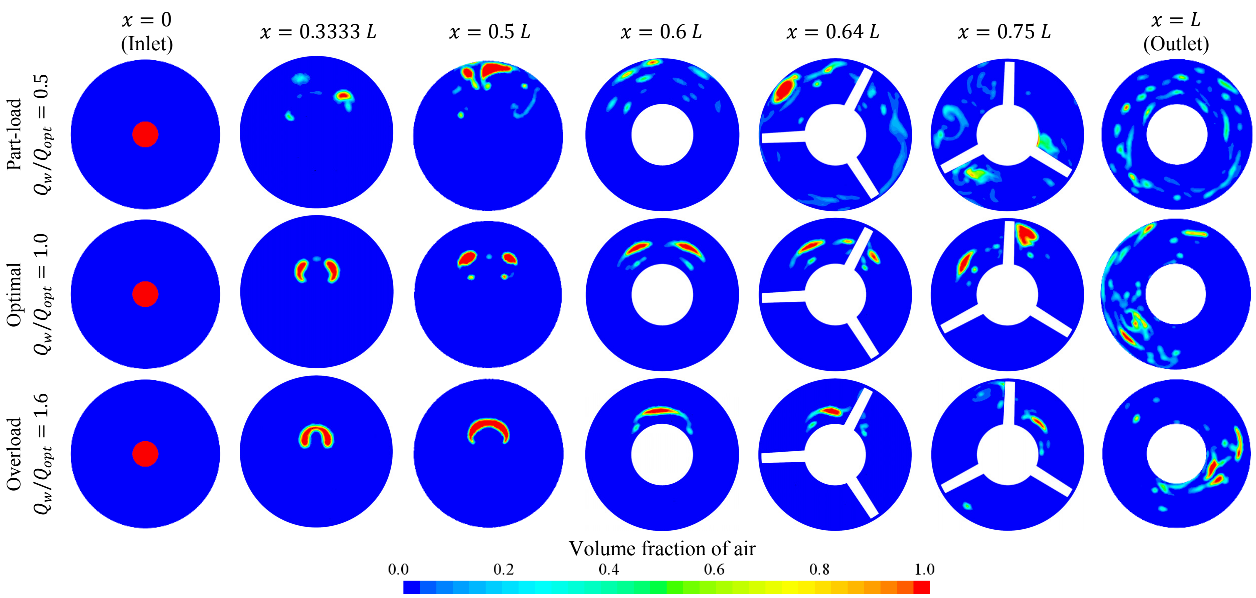

Figure 6.31: Distribution of air volume fraction for different flow conditions at $\varepsilon = 3\%$.

$$\bar{c} = \frac{1}{A}\int c \, dA \tag{6.2}$$

Even more useful than the surface uniformity is the mixing coefficient M_c, with $0 \leq M_c \leq 1$, where 0 indicates no mixing at all between the two phases (0% mixing), and 1 indicates complete mixing (100% mixing), see [129, 130]. This quantity can be computed using Equation 6.3.

$$M_c = \frac{S_u - S_{u,min}}{1 - S_{u,min}} \tag{6.3}$$

Figure 6.32 presents the axial evolution of the mixing coefficient for the three different flow conditions at a gas volume fraction of $\varepsilon = 3\%$. As shown, the value of the mixing coefficient is always higher in part-load along the whole length of the simulation domain. Before the inducer, the mixing coefficient in part-load conditions is also slightly better than the other cases, since the gas phase rises up due to buoyancy, giving rise to instabilities and entraining water. Additionally, the air becomes strongly mixed with the main stream of water once it reaches the blades of the inducer at part-load. Therefore, the mixing coefficient jumps quickly to values between 20% and 26%. This cannot be seen for either optimal or overload flow conditions, where the air distribution remains quite non-uniform and the corresponding mixing coefficient values are limited to a low range between 10% and 18% at outlet. Though small, this improvement of two-phase mixing is the only reason for the slight improvement of two-phase pumping at overload conditions, although the pressure is reduced by the inducer in this case. Inducers are indeed much more useful in part-load and near optimal conditions for significantly improving the two-phase pumping performance.

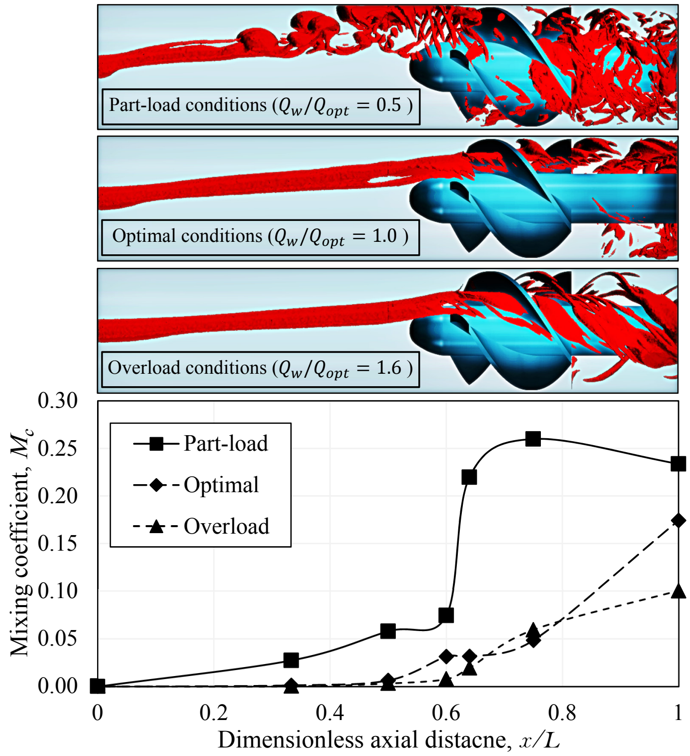

Figure 6.32: Axial development of mixing coefficient for different flow conditions at $\varepsilon = 3\%$.

6.3.4 Summary

This section presents the main concluding remarks of the inducer simulations. After setting a proper numerical model including discretization in space and time, the numerical results show excellent agreement with companion experimental data concerning the inducer performance. The results show that the increase of the gas volume fraction moderately reduces the inducer performance for part-load and optimal conditions, while the performance is considerably reduced in overload conditions. Only weak vortices occur around the inducer hub for part-load conditions, while at overload conditions, strong flow separation occurs along the leading edge of the blades, forming several long vortices in the axial direction. The increase of the gas volume fraction causes no significant change in the structure of the vortices in part-load flow. However, the axial vortices appearing in overload conditions grow and increase in number as the gas volume fraction increases, which reduces the pressure further downstream of the inducer. This explains the sudden drop of the pump performance in overload conditions for high gas volume fraction. For the whole range of gas volume fraction considered, the inducer can effectively mix the two phases at part-load, producing a very homogeneous mixture downstream, improving the pump performance significantly in such low-flow conditions. For optimal and overload conditions, the flow is much faster, and the mixing level reached by the inducer is much lower. Though small, the flow mixing level resulting from the inducer for overload conditions can still provide a slight improvement of the two-phase pumping performance, more than compensating the reduction in pressure due to flow separation in the inducer. These observations explain why inducers can only noticeably improve two-phase pumping performance at part-load, roughly up to optimal conditions.

6.4 Pump simulations

In this last section, the whole pump domain was simulated for single-phase and two-phase flows to asses the ability of the numerical models to predict the pump performance under different flow conditions.

6.4.1 Numerical Modeling

Similar to the previous numerical sections, the commercial CFD code Siemens STAR-CCM+ V13.02 [116] was used to perform the simulations. A transient set-up was always used together with a moving-mesh approach to model the impeller rotation. Unfortunately, it is not possible yet to use the more accurate RSM model for simulating the whole pump, since the required computational resources are not available. Accordingly, for these simulations, the $k-\omega$ shear stress transport (SST) model [120] was used for turbulence modeling to reduce the computational cost. This model was also often used in the literature for pump simulations. It can predict strong pressure gradients and the expected flow separations in the impeller [95, 131–134]. Additionally, in some cases, the $k-\omega$ SST model resulted in very good agreement with experiments concerning air-water two-phase flow in pipes compared to other turbulence models [135]. A second-order upwind convection scheme was used together with a segregated solver. In all pump simulations, the VOF model was used, where water was modeled as an incompressible fluid, while the compressibility of air was considered using the ideal gas equation.

Simulation domain

In accordance with the present experiments, three pump configurations were considered, i.e. the semi-open impeller with the standard gap, the semi-open impeller with the increased gap, and the semi-open impeller with the standard gap and inducer. The three cases are compared in detail to examine the pump performance and the improved flow mixing provided by the inducer and by the increased gap. Figure 6.33 presents the details of the considered simulation domain. As shown, the simulation domain was basically divided into 3 parts; (1) the inlet pipe, (2) the rotating zone surrounding either the impeller or the impeller together with the inducer, and (3) the volute with the exit pipe, considering in-place interfaces between them. Similar to the experiments, pressure probes were placed at corresponding locations upstream and downstream of the impeller.

Same as the inducer simulations (see Figure 6.17), the inlet face was divided into 2 surfaces for two-phase simulations; one for each phase, using a center circle as air inlet as can be seen in Figure 6.33. The radius of the air inlet surface was regulated based on the gas volume fraction value so that the inlet velocities of air and water remain always equal ($V_a = V_w$) for all simulations. Concerning the boundary conditions of the simulation, a mass flow inlet boundary and a pressure outlet boundary were applied at the inlet and outlet surfaces, respectively. The outlet pressure value obtained from the experiments was specified in the simulations to accurately model the air compressibility.

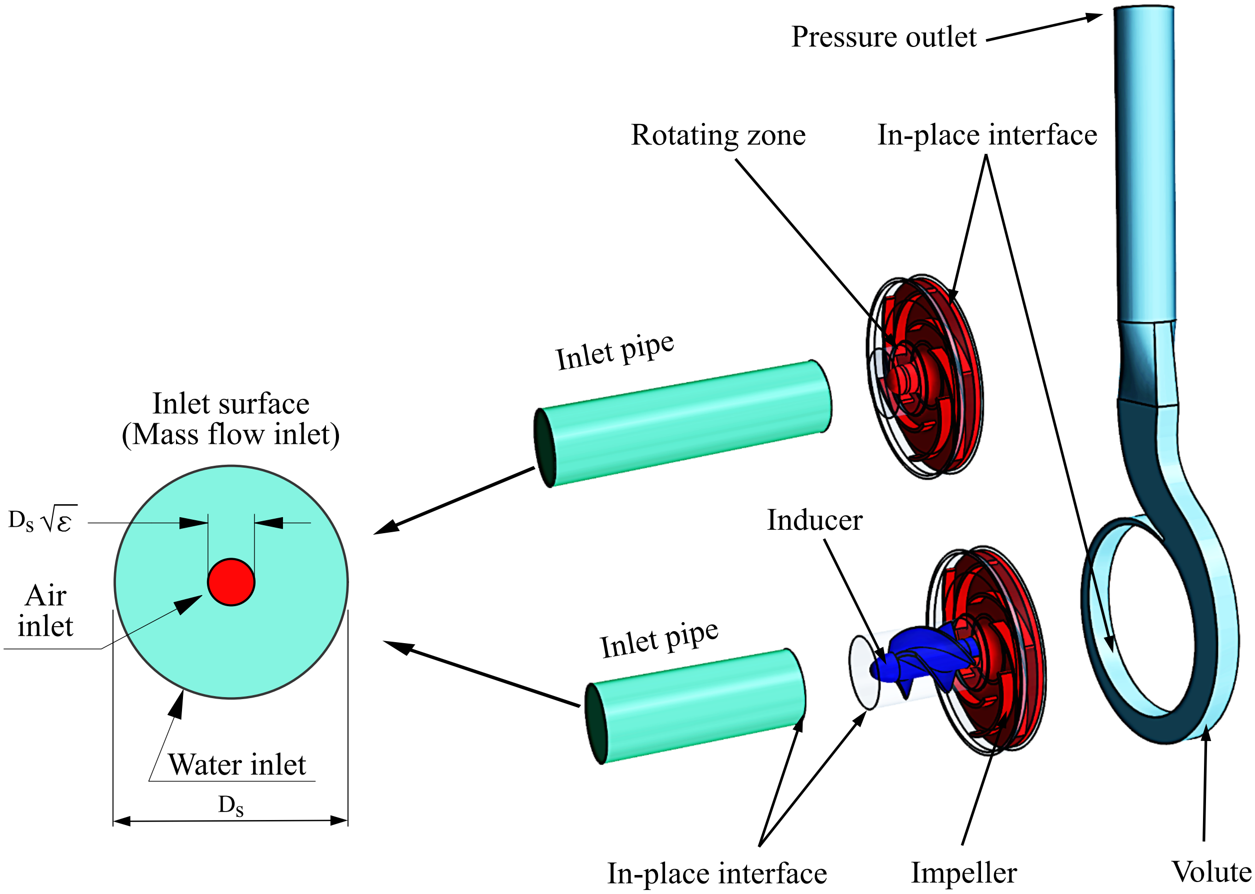

Figure 6.33: Numerical domain used for the pump simulations.

Mesh-independence test

For the whole pump domain, polyhedral elements were generated with 8 prism layers along all walls to ensure adequate resolving of the boundary layer flow. Additionally, to eliminate the use of wall models, the thickness of the first layer was kept sufficiently small in order to always keep the average value of the dimensionless wall distance (y+) lower than 1. A slight additional mesh refinement was applied in the rotating zone, i.e. around the impeller and the inducer to improve the prediction in this zone of central interest. A mesh-independence test was first carried out for single-phase flow, to minimize the numerical errors of space discretization. The test was done at the maximum flow rate considered, i.e. $Q_w/Q_{opt} = 1.6$ (overload conditions). The details of the meshes used in the test are given in Table 6.4.

Figure 6.34 shows the numerical results of the different meshes considered in terms of the normalized pressure change across the pump ($\Delta p/\Delta p_{opt}$). The pressure change shows a constant behaviour between mesh 4 and mesh 5 with an error of less than 0.2%. Accordingly, the fourth mesh with 5.5 million cells was assumed to deliver sufficient accuracy and used for all single-phase simulations. However, a second test was done to examine the ability of the meshes to resolve the bubbles under two-phase conditions in the inlet pipe. Again, the maximum flow rate was considered ($Q_w/Q_{opt} = 1.6$), together with a gas volume fraction of 3% as a sample value. The numerical results of all meshes are presented in Figure 6.35 in terms of the gas volume fraction for a sample section located at a distance of $2D_S$ from the inlet surface. As can be seen, the air-water interface is mostly smeared for the low-resolution meshes (mesh 1 to mesh 4). It is best resolved using mesh 5, with a very low gradient compared to all other meshes. Therefore, mesh 5 with 9.0 million cells was employed for two-phase simulations. This mesh is illustrated in Figure 6.36.

Table 6.4: Details of grids used for the mesh-independence test of the pump simulations.

Mesh #	Total No. of cells (millions)	Average y+
1	0.7	0.97
2	1.5	0.69
3	2.5	0.53
4	5.5	0.35
5	9.0	0.27

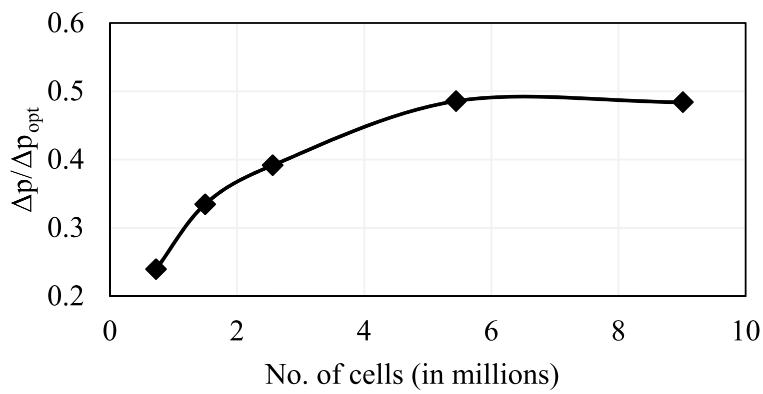

Figure 6.34: Normalized pressure change for different grid resolutions.

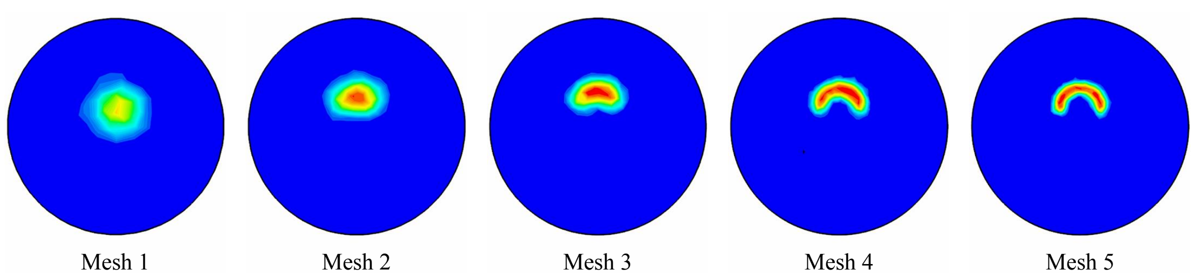

Figure 6.35: Comparison of the air volume fraction obtained with different mesh resolutions.

Timestep independence test

The timestep of the simulation solver is also assessed by performing a test, taking into consideration 3 different timesteps, namely 0.5° (0.128 ms), 1.0° (0.256 ms), and 2.0° (0.512 ms) angle rotations per timestep. The maximum flow rate of $Q_w/Q_{opt} = 1.6$ was considered, ensuring time-independence at all other, lower flow rates as well.

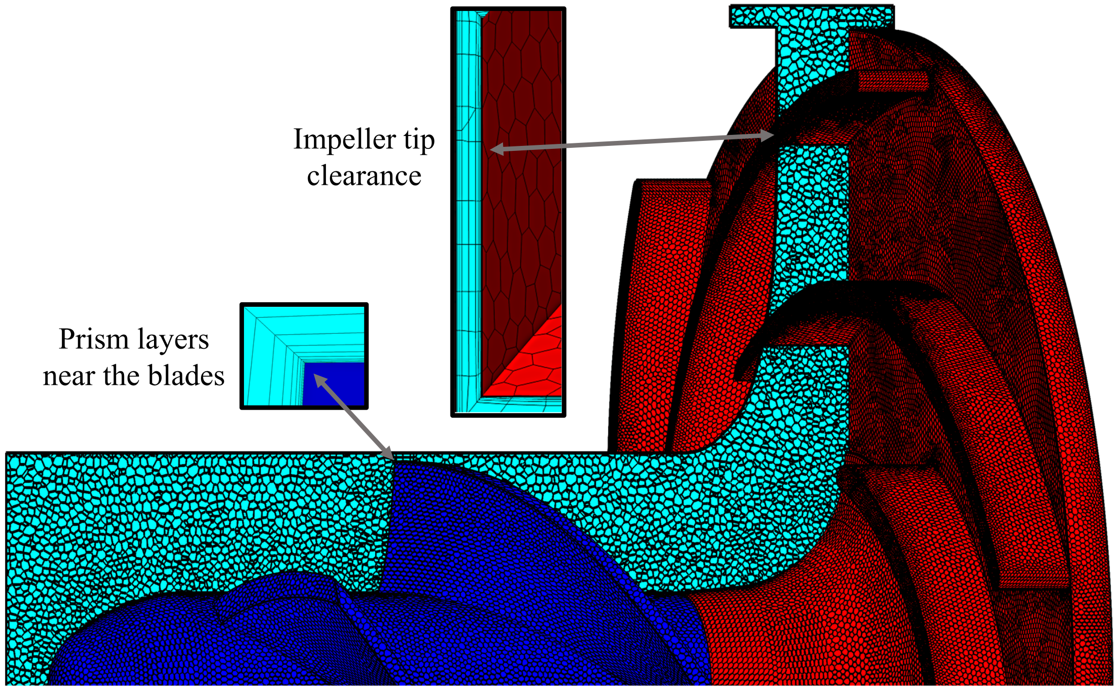

Figure 6.36: Mesh resolution used for two-phase simulations (9.0 million cells).

Figure 6.37 shows the normalized pressure change across the pump for different timesteps. It can be seen that the difference in the pressure values between 1.0° and 0.5° is very limited. Therefore, the angle rotation of 1.0° per timestep was considered to be sufficiently accurate and kept for all further simulations. Additionally, a number of 25 inner iterations were set to ensure convergence of all residuals at each time-step by a drop of at least three magnitudes. The total physical time considered in single-phase simulations is 0.5 seconds, which corresponds to more than 5 complete impeller rotations, while the two-phase simulations were stopped after at least 1.0 second of physical time. For two-phase simulations at part-load condition ($Q_w/Q_{opt} = 0.5$), 1.5 seconds for the physical time (more than 16 impeller rotations) are required to ensure that the air phase reaches the domain outlet.

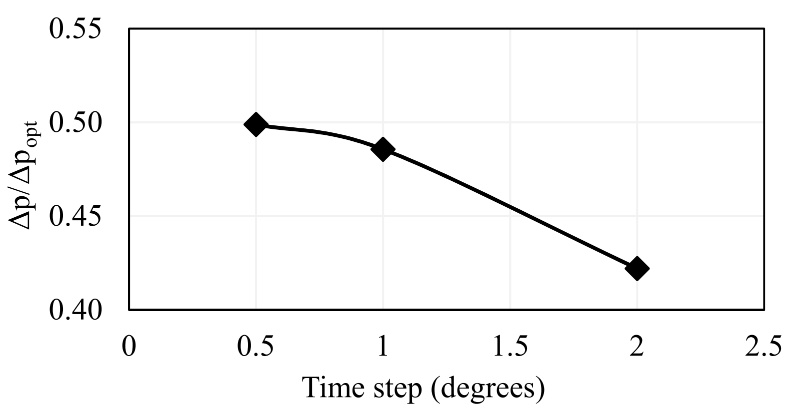

Figure 6.37: Normalized pressure change for different timesteps.

All the numerical results shown later were averaged over one complete rotation of the pump (approximately 0.1 seconds) to obtain statistically stable values for all cases considered. Figure 6.38 shows pressure and torque results as a function of time, normalized by optimal values (of single-phase flow), for different flow conditions (part-load, optimal, and overload) and $\varepsilon = 3\%$ as a sample value, together with their cumulative averaged values over the last 0.2 seconds of the physical time. Here, the instantaneous fluctuations of the pressure exhibit typically a slightly increasing behaviour with the flow rate, while the torque fluctuations are higher for part-load and overload compared to those of optimal flow, due to the increased shock losses. As shown, the cumulative averaged properties reach constant values for all flow cases after approximately 0.1 seconds, confirming proper averaging.

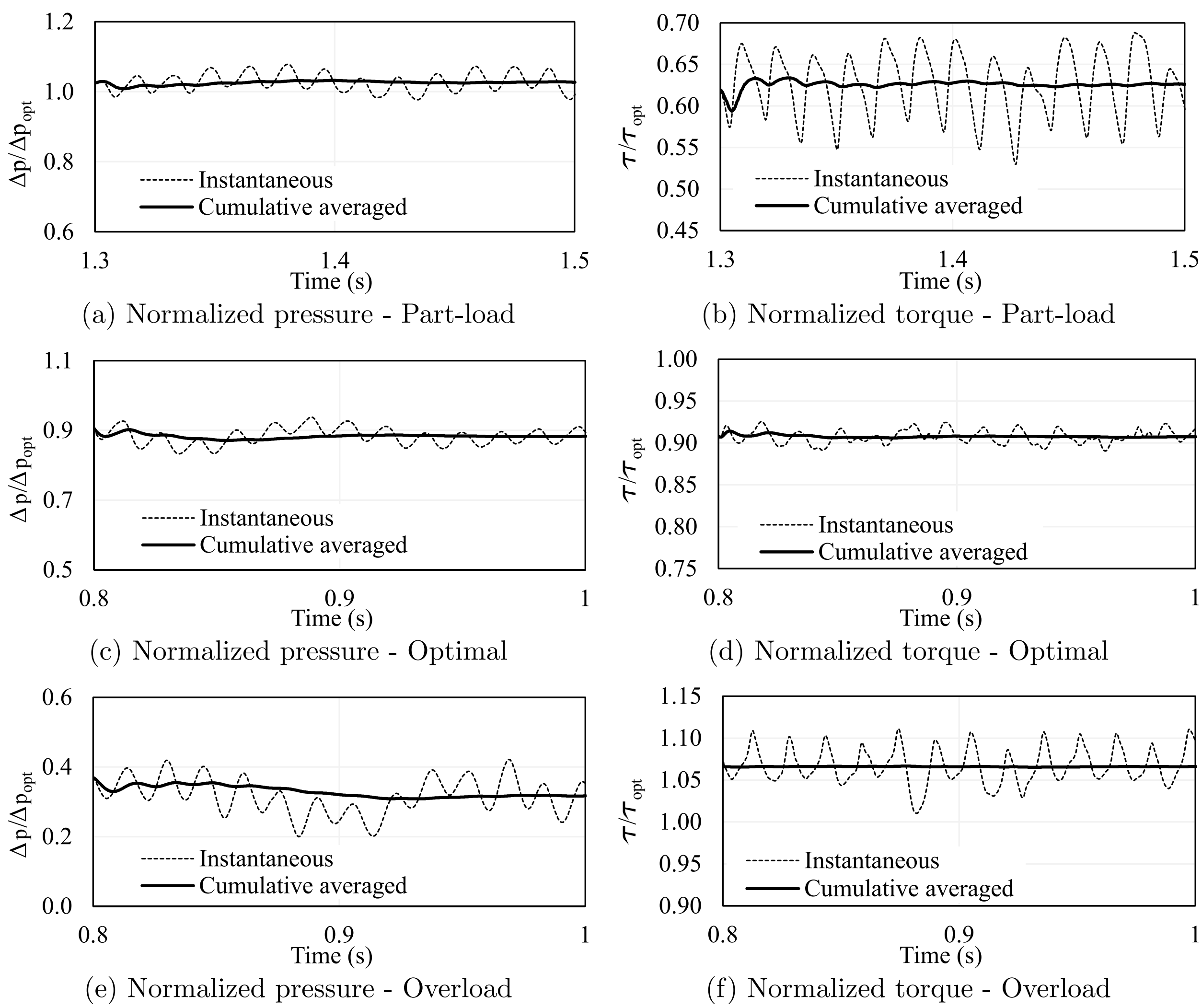

(a) Normalized pressure - Part-load
(b) Normalized torque - Part-load
(c) Normalized pressure - Optimal
(d) Normalized torque - Optimal
(e) Normalized pressure - Overload
(f) Normalized torque - Overload

Figure 6.38: Instantaneous and cumulative averaged values of normalized pressure and torque for the last 0.2 seconds of physical time.

6.4.2 Analysis of pump performance

Now, the numerical and experimental pump performances are compared. Figure 6.39 and Figure 6.40 show the normalized specific delivery work (Υ/Υ_{opt}) and the pump efficiency (η), respectively, as a function of the normalized volume flow rate (Q_w/Q_{opt}) for all the considered simulation cases. The simulation results were always averaged over the last 0.1 seconds as discussed in the previous section, while the experimental results were obtained from 200 instantaneous measurements recorded over a period of 50 seconds (4 Hz acquisition frequency). The simulations show generally good agreement with the experiments in the range of $\varepsilon = 0\%$ to $\varepsilon = 3\%$. In some single-phase flow cases the simulation shows a slight overestimation compared to the experiments, particularly for the increased gap. The reason can be an inaccurate representation of the increased secondary flow across the tip clearance gap. Additionally, the simulations underestimate the experiments for a few two-phase conditions probably due to the limited accuracy of the VOF model to resolve the small bubbles.

The agreement between the simulations and the experiments is generally better for part-load and optimal conditions, while the simulations points deviate more at overload conditions. This can be justified by the limitation of numerical models to accurately predict the strong flow separation at the volute nose occurring at these conditions. The flow separation will be shown later by visualizing the flow field in the pump.

For $\varepsilon = 5\%$, the simulation results show comparable performance to the experiments only at part-load conditions, while the sudden performance drop occurring at higher flow rates could not be predicted by the simulation. Accordingly, the simulation points deviate significantly from the experimental curve. For the increased gap, the pump does not experience a sudden performance drop for $\varepsilon = 5\%$ in the experiments, since the drop occurs only at $\varepsilon \geq 7\%$ (see Figure 5.7). The simulation results are still comparable to the experiments in this case. Overall, the averaged relative errors in the normalized specific delivery work between the simulations and the experiments for part-load, optimal, and overload flow are 3.8% and 10.4% and 45%, respectively. The presented performance curves confirm that the accuracy of the simulation is limited to low to moderate flow rates (part-load to optimal flows) as well as low gas volume fractions ($\varepsilon < 5\%$).

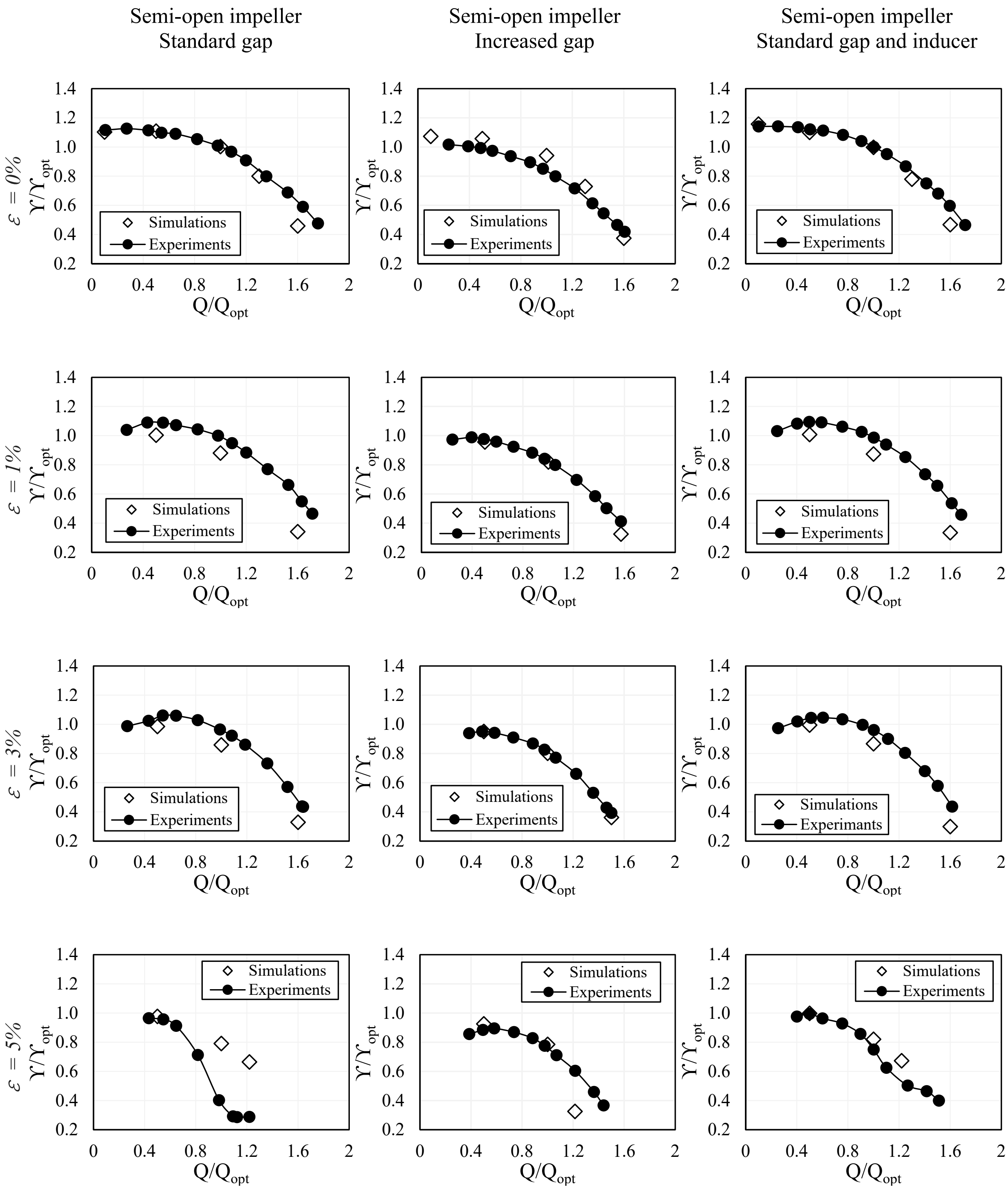

Figure 6.39: Comparison of experimental and numerical specific delivery work for various pump configurations and gas volume fractions.

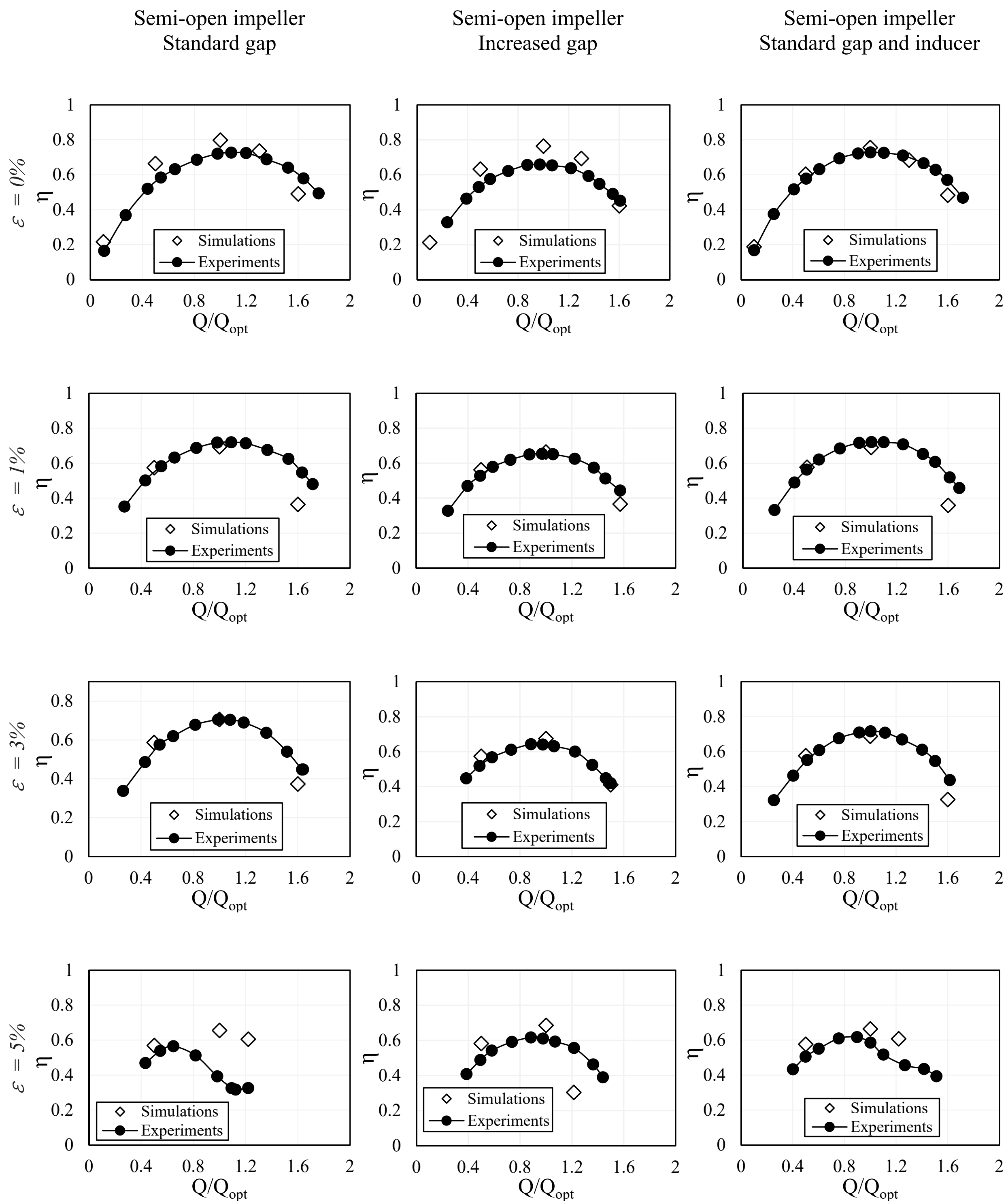

Figure 6.40: Comparison of experimental and numerical efficiency for various pump configurations and gas volume fractions.

6.4.3 Internal flow and pressure contours

Now, the internal flow of the pump is visualized and discussed. Figures 6.41, 6.42, and 6.43 illustrate the normalized static pressure contours and surface streamlines at midspan of the impeller for different pump configurations and gas volume fractions at part-load, optimal, and overload conditions, respectively. Additionally, 3D iso-surfaces of Q-criterion are shown (in black) for the region starting from the impeller inlet till the midspan of the impeller. The Q-criterion is again used here to exhibit the wake regions. A threshold value of $Q_{cr} = 20000$ s^{-2} for the Q-criterion iso-surfaces was found appropriate to represent the wakes in the impeller, highlighting also the differences among all cases. In the presented range of $\varepsilon = 0\%$ to $\varepsilon = 3\%$, the pressure contours are very comparable for the standard gap with and without the inducer since the performances are comparable, while a drop in the pressure can be seen for all flow conditions when the gap is increased.

For part-load conditions shown in Figure 6.41, evident flow separations occur on the blade suction sides near the leading edge (indicated by Separation 1 on Figure 6.41), in addition to some weaker separations on the blade pressure sides near the trailing edge (indicated by Separation 2 on Figure 6.41). The separations are more obvious for the standard gap case compared to the other two cases, where the streamlines show more recirculation zones. Looking now at Figures 6.41, 6.42, and 6.43, it can be observed generally that the Q-criterion iso-surfaces become more apparent when the gap is increased, showing also a discrete manner, as a result of the interaction between increased secondary flow and the impeller rotation. The increase in Q-criterion iso-surfaces is also an indicator of the improved mixing of the two phases within the impeller when the gap is increased. On the other hand, the Q-criterion iso-surfaces are slightly reduced when the inducer is installed, since it allows for a better incidence of the flow on the impeller blades, while mixing is improved yet before the impeller. Accurate comparisons for flow mixing are shown later in Section 6.4.4.

For optimal and overload conditions the flow shows a smoother behavior in the impeller compared to the part-load case; the streamlines are mostly aligned with the impeller blades. Nevertheless, a significant flow separation occurs at the volute nose for overload. A wrong prediction of this volute separation is assumed to be the reason for the worse agreement between simulations and experiments at overload. Again, the wake regions are slightly increased when the gap is increased and slightly reduced when the inducer is used. The discontinuous behaviour of the Q-criterion for the increased gap is very evident at optimal conditions, particularly for $\varepsilon = 1\%$ and $\varepsilon = 3\%$, indicating that the secondary flow is increased, and interacts in a quite complex way with the impeller rotation. Generally, as the gas volume fraction increases for all flow conditions, it can be seen that the pressure values are getting lower, while the Q-criterion structures are mostly getting bigger.

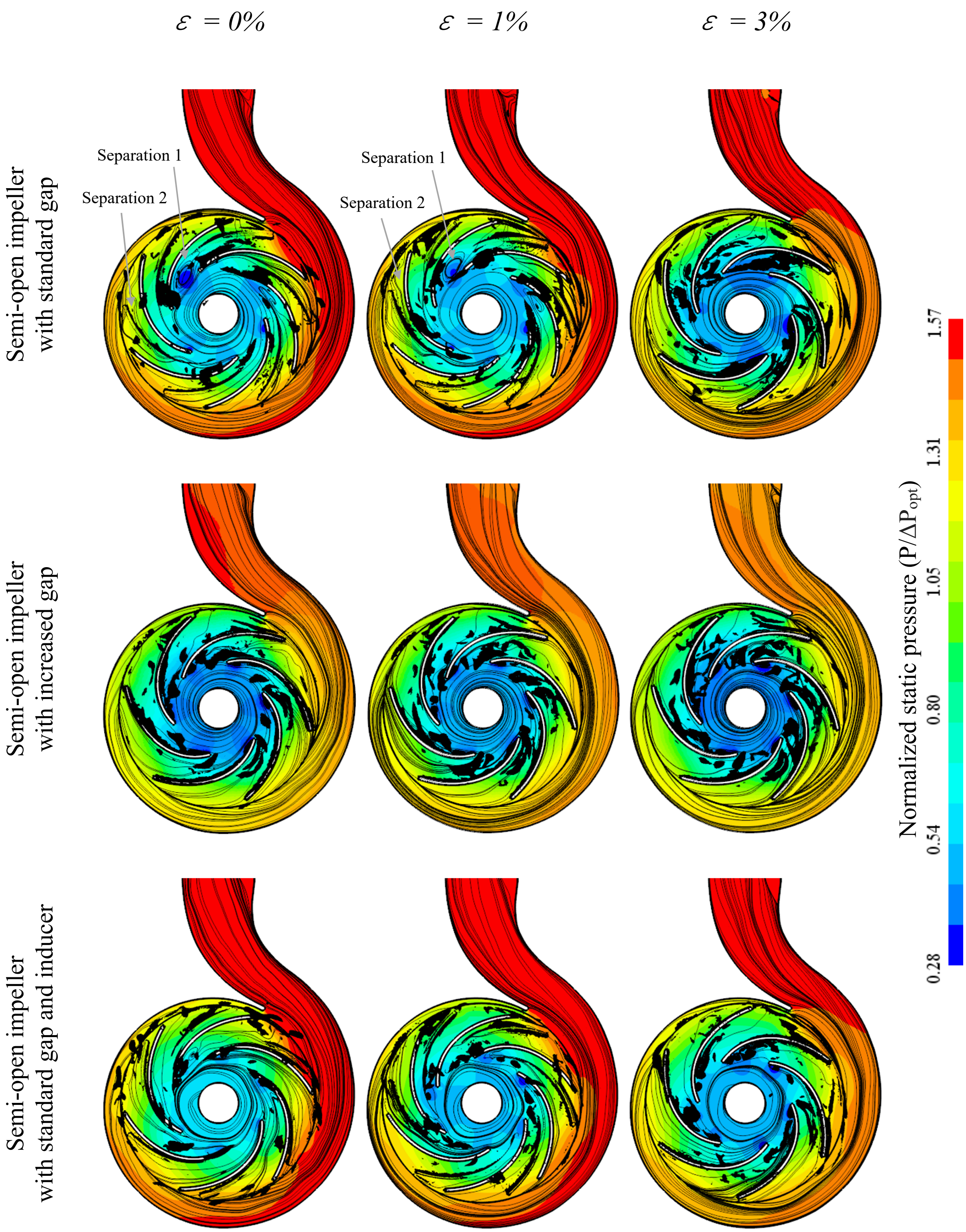

Figure 6.41: Normalized static pressure contours (colours), surface streamlines (thin black lines), and Q-criterion within the impeller (black) at part-load conditions.

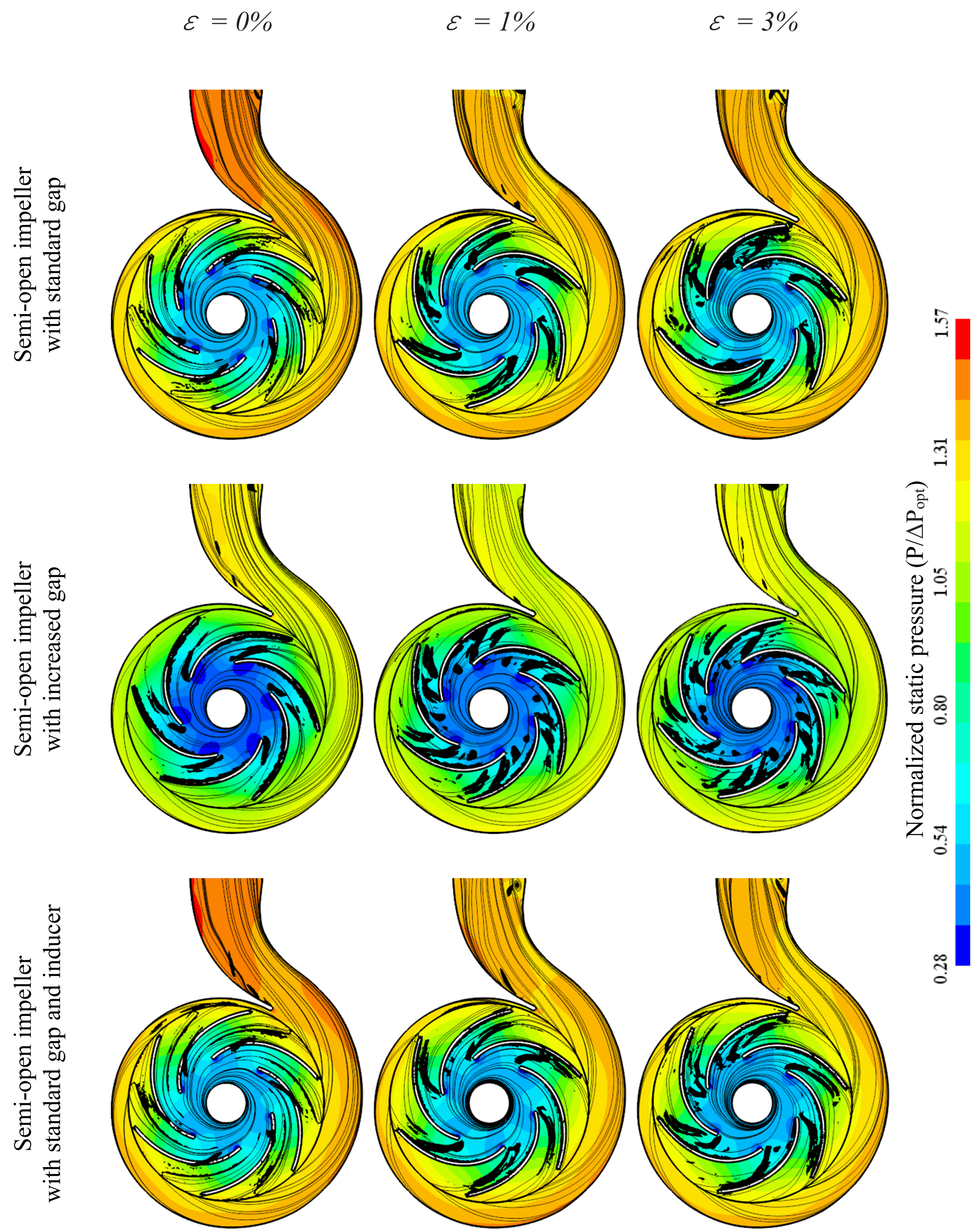

Figure 6.42: Normalized static pressure contours (colours), surface streamlines (thin black lines), and Q-criterion within the impeller (black) at optimal conditions.

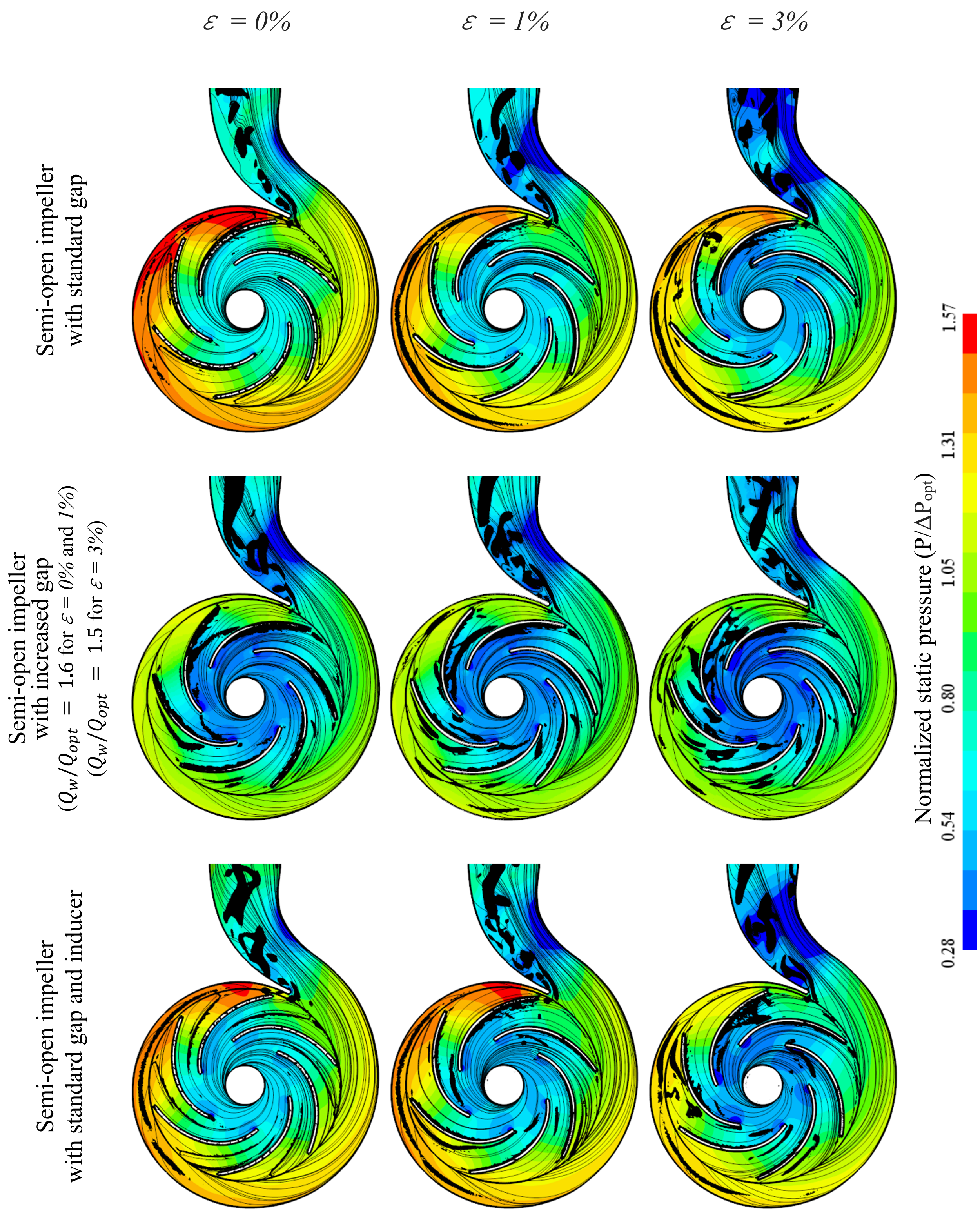

Figure 6.43: Normalized static pressure contours (colours), surface streamlines (thin black lines), and Q-criterion within the impeller (black) at overload conditions.

6.4.4 Comparisons of two-phase flow regimes

Figures 6.44, 6.45, 6.46 show sample instantaneous flow fields obtained by the high-resolution camera from the experiments in comparison with the corresponding instantaneous flow patterns obtained in simulations using the VOF model. The air phase is represented in the simulation images by volume fraction iso-surfaces, which show all cells with air volume fraction higher than 5%. Again, this value is suitable to highlight the differences among various cases. To be comparable with the experimental images, the numerical results are shown for the whole impeller depth. Although fine flow details are difficult to be obtained numerically, the simulations are able to predict distinct regimes for different conditions.

For $\varepsilon = 1\%$, the experimental flow regime is bubbly flow; the simulations show correspondingly dispersed and mostly disconnected air iso-surfaces. Nevertheless, since the VOF model is an interface tracking method, very fine bubbles can be resolved only by using an extremely high-resolution mesh. This is another general limitation of two-phase simulations when fine interactions are needed to be resolved. For $\varepsilon = 3\%$ and $\varepsilon = 5\%$, the simulations could predict the right location of the gas accumulations as in the experiments, i.e. the blade suction sides. Strong deviations can occur concerning pump performance if the location of the gas accumulation is not accurately predicted [95, 133].

Comparing different flow rate conditions, it can be seen that the air is generally more dispersed for part-load conditions compared to the optimal or overload conditions. The reason for this better mixing is the higher residence time available for the flow at such low-flow conditions. For overload conditions, the simulations show a non-uniform distribution of the gas phase within the impeller, where some impeller channels have considerably less gas compared to other channels. This effect can be more evidently seen for $\varepsilon = 1\%$ and $\varepsilon = 3\%$. This reveals the reduced mixing due to the insufficient residence time since the flow is very fast.

When the gap is increased or the inducer is installed, the distribution of the gas becomes slightly more uniform. This can be seen for example by comparing the simulation results of the first row ($Q_w/Q_{opt} = 0.5$) for $\varepsilon = 1\%$ in Figure 6.44 with corresponding conditions in Figure 6.46. Quantitative comparisons for the mixing efficiency in the impeller under different conditions are shown in the next section.

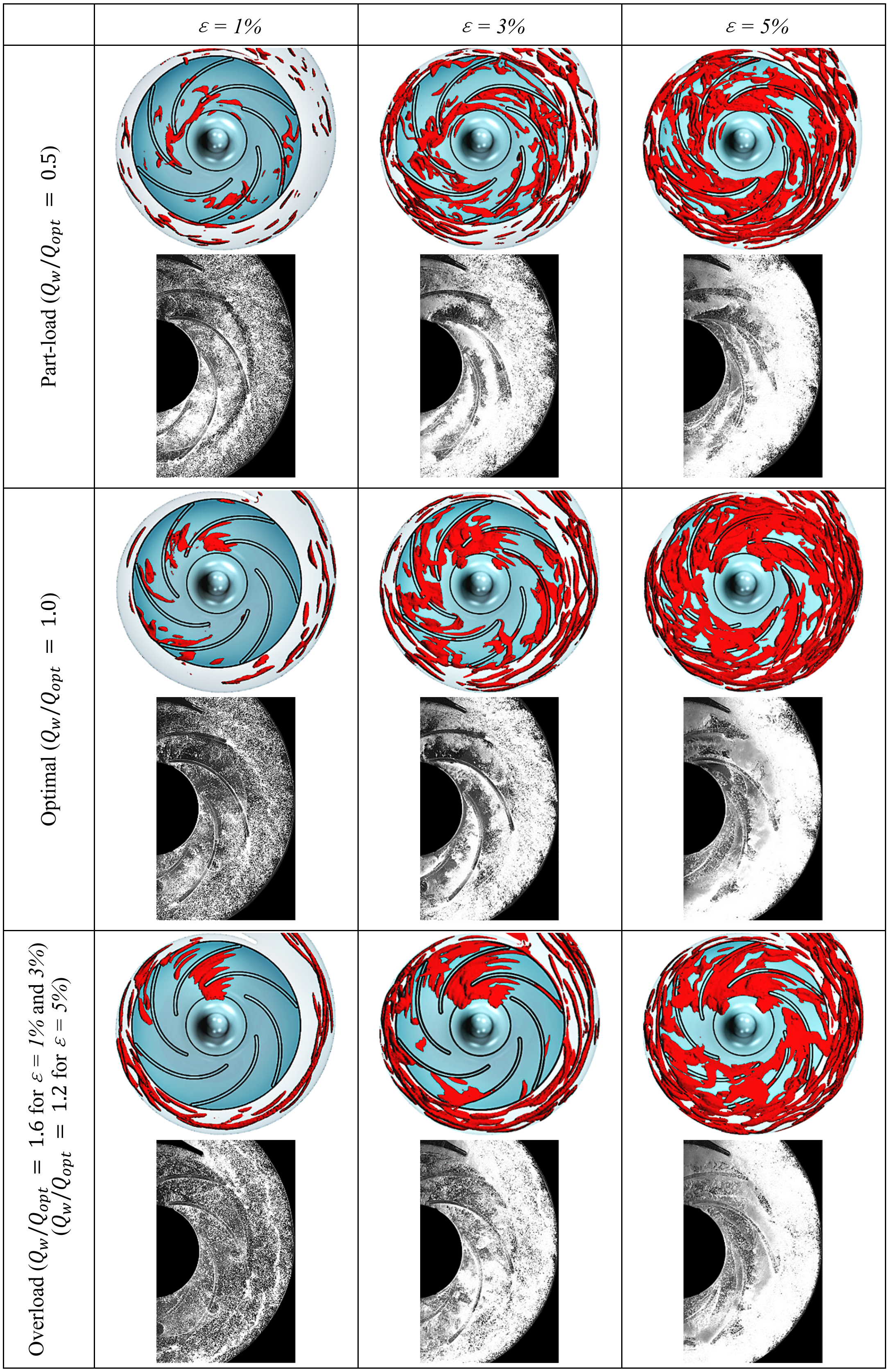

Figure 6.44: Flow regimes for the semi-open impeller with the standard gap.

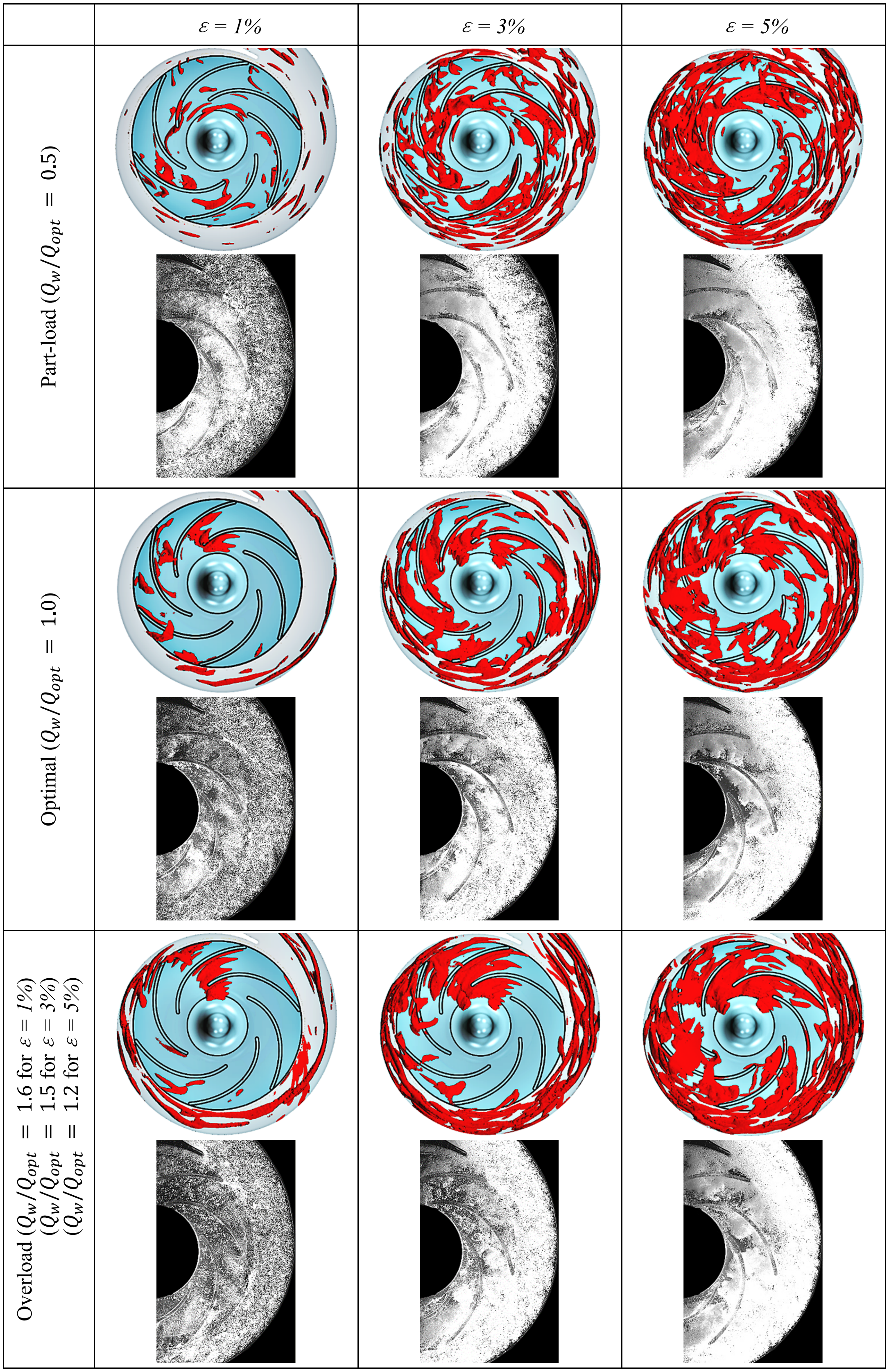

Figure 6.45: Flow regimes for the semi-open impeller with the increased gap.

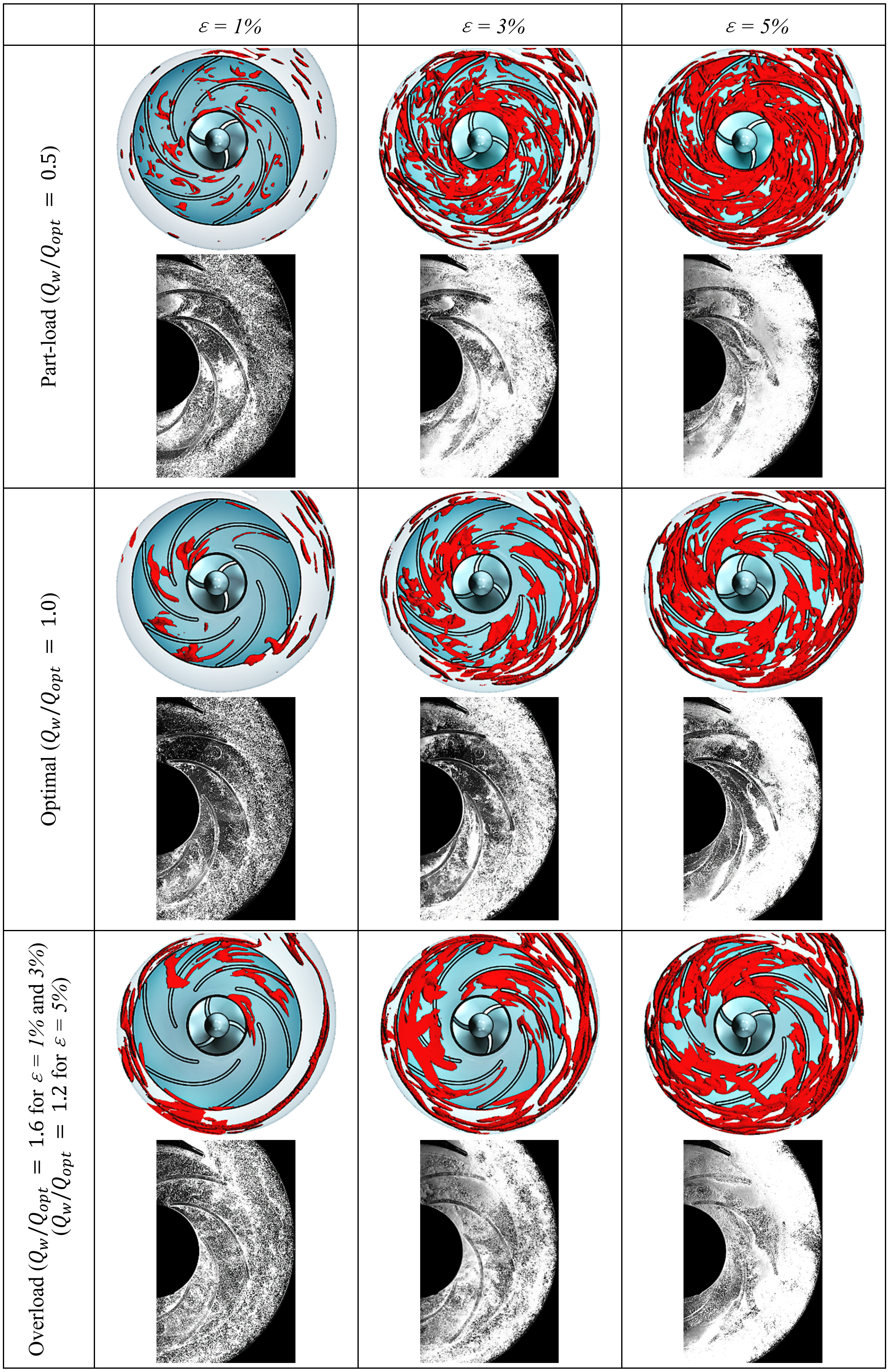

Figure 6.46: Flow regimes for the semi-open impeller with the standard gap and inducer.

Mixing performance

Lastly, the two-phase flow mixing is analyzed in the impeller under different conditions. For that, the mixing coefficient (Equation 6.3) is calculated and compared among different cases at midspan of the impeller for $\varepsilon = 3\%$ as a sample value for the gas volume fraction. Figure 6.47 presents the average values of the mixing coefficient over one rotation, together with variation bars representing the fluctuation range of the mixing coefficient in each case. As shown, the mixing is generally decreasing with the increase of the flow rate due to the reduced residence time.

Additionally, the mixing of the two phases within the impeller is always better when the gap is increased or the inducer is installed compared to the standard gap case. Confirming previous observations, the inducer improves the mixing in the impeller strongly at part-load conditions, reaching values higher than 0.37. However, the improvements are lower for optimal and overload conditions. Similarly, the increased gap results in slight improvements in the mixing at part-load and optimal conditions, while the mixing is considerably improved at overload conditions with the increased gap despite the reduced residence time, justifying the very good pump performance at overload conditions up to $\varepsilon = 7\%$.

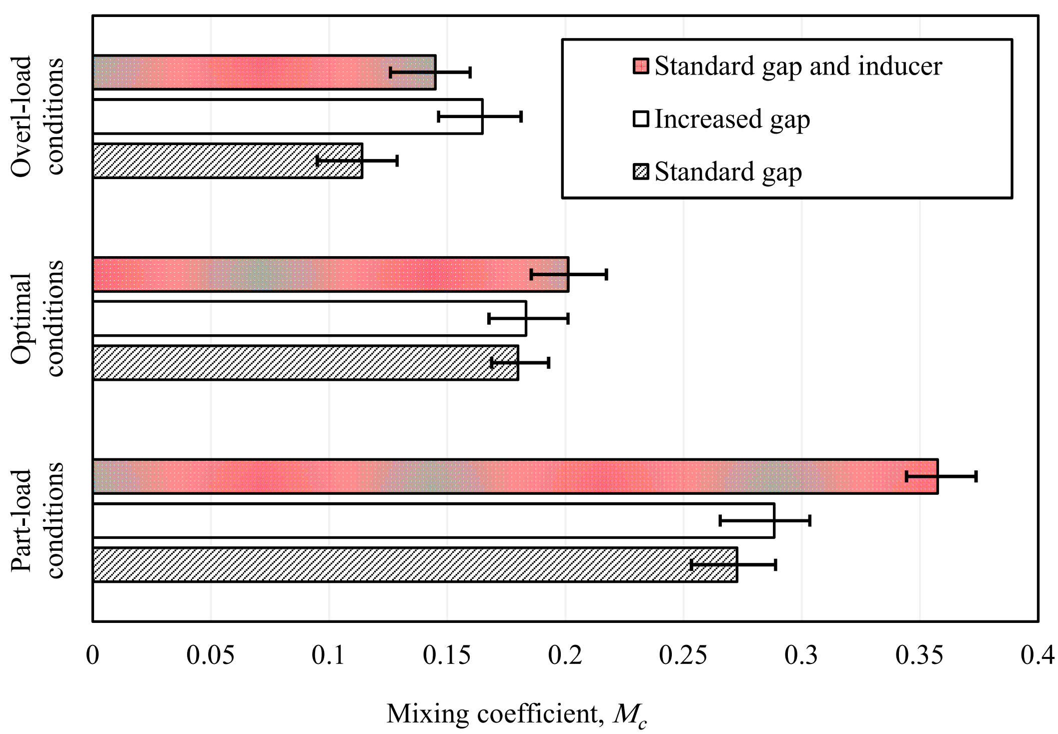

Figure 6.47: Mixing coefficient for different pump configurations and flow conditions at $\varepsilon = 3\%$.

6.4.5 Summary

Systematic 3D transient numerical simulations were performed for the whole pump using the moving-mesh approach for impeller motion, the $k-\omega$ SST model for turbulence modeling, and the VOF model for two-phase modeling. The discretization in space and time were selected after performing corresponding tests. Three pump configurations were considered, i.e. the semi-open impeller with the standard gap, the semi-open impeller with the increased gap, and the semi-open impeller with the standard gap and inducer. For the range of $0 \geq \varepsilon \geq 3\%$, the numerical results show generally good agreement with the experimental data, with higher deviations at overload conditions. However, for $\varepsilon = 5\%$, the simulations failed to predict the sudden performance drop occurring at overload conditions, showing only good agreement with the experiments at part-load conditions (before the sudden performance drop). Additional information concerning the flow in the pump could be obtained by the simulations, including flow separations and wake regions in the impeller and the pump volute, explaining some experimental observations. The flow regimes obtained by simulations are generally comparable with the experimental images. The gas accumulation could be correctly predicted in the simulations, i.e. on the blade suction sides. Nevertheless, fine bubbles and minute two-phase interactions could not be resolved by VOF simulations. This could only be obtained by an extremely fine mesh. Finally, the improved mixing of the two phases as a result of increasing the tip clearance gap or installing the inducer could be predicted by the simulations.

6.5 Conclusions

In this chapter, CFD simulations for the diverging channel, the inducer, and the whole pump with three different semi-open configurations are presented. Some important findings concerning the effect of gas accumulations, the upstream inducer, and the tip clearance gap were deduced from the simulations. Additionally, different numerical models and settings were employed, and their accuracy was analyzed and compared against experiments. The presented results highlight some common limitations of CFD models and the need for model improvements, confirming further the importance of the detailed experimental data obtained in this thesis. However, careful simulations relying on high-quality models can already deliver useful information, but at a high computational cost.

Chapter 7

Conclusions and Outlook

7.1 Conclusions

This dissertation discussed the complex transport of gas-liquid two-phase flows in centrifugal pumps in order to provide comprehensive investigations for the phenomenon of gas accumulation (phase segregation), pump performance degradation, performance hysteresis, pump surging and flow instabilities. After discussing some fundamentals and corresponding research challenges of gas-liquid two-phase flows, the scientific literature and related studies have been reviewed, emphasizing several gaps and the need for performing additional research with more advanced techniques. For that, two experimental test-rigs (i.e., a static diverging channel and a centrifugal pump) have been specially developed and equipped with all required measuring instruments to accomplish the main research objectives.

In the diverging channel experiments, the parameters leading to phase segregation and large gas accumulation have been observed and discussed. These results deliver interesting insights for understanding the complex flow patterns and gas accumulation processes occurring in two-phase gas/liquid flows. Using PIV velocity measurements, it was shown that the presence of large recirculation zones can lead to gas bubble trapping and rapid accumulation. Even for very small air volume fractions (0.05%), large gas pockets were observed due to the low pressure of the recirculation zone. Using shadowgraphy measurements, the accumulated gas size could be quantified for various two-phase flow conditions. The accumulated gas size was always increased as a result of increasing the superficial air Reynolds number. Further, It was found that the accumulated gas can be reduced or minimized by 1) avoiding large recirculation zones in the main liquid flow, 2) ensuring high enough turbulence levels leading to break-up, which can be done by strongly increasing the superficial water Reynolds number and/or 3) choosing a regime leading to a stratified flow after the diverging part, with a connected gas layer along the upper wall, which can be achieved at very low superficial water Reynolds number. It was also shown that the accumulated gas strongly affects pressure recovery; a significant decay in pressure recovery is observed across the diffuser when more gas is accumulated.

To provide possible comparisons with CFD simulations, sample boundary conditions were also measured, including inlet velocity and bubble size distributions, which can be directly implemented in numerical simulations. The developed experimental data of these experiments will help also to examine the accuracy of available two-phase models.

Concerning the centrifugal pump, the transport of two-phase flows and the corresponding pump performance were studied for different flow conditions and pump impeller settings. The mixture transport was investigated for a closed impeller and a geometrically similar semi-open impeller with a standard or an increased tip clearance gap. The influence of adding an upstream inducer before the semi-open impeller was also considered.

Due to the secondary flow across the tip clearance gap, the initial single-phase flow performance of the semi-open impeller with the standard gap is slightly lower than that of the closed impeller. The difference is considerably larger when the gap is increased. However, when the inducer is installed, only insignificant changes could be seen in the single-phase performance curves of the semi-open impeller.

For two-phase flows, the semi-open impeller with a standard gap can generally resist gas accumulation in the range of $1\% \leq \varepsilon \leq 3\%$, showing better performance than that of the closed impeller. However, for ε between 4 % and 6 %, the trend is reversed, due to flow separation and the accumulation of huge pockets in the semi-open impeller with the standard gap, particularly in overload conditions. Therefore, in this range, the performance of the closed impeller is higher compared to that of the semi-open impeller with the standard gap.

The increase in the semi-open impeller tip clearance gap leads to increased secondary flow over the blades, enhancing bubble break-up and retarding gas accumulation. Therefore, the larger gap revokes the abrupt performance drop and provides more robust two-phase pumping up to $\varepsilon = 7\%$, before the beginning of pump surging and strong flow instabilities. Accordingly, the standard gap is recommended for single-phase flow and low gas volume fractions $\varepsilon < 4\%$, while an increased gap would be preferable when higher gas volume fractions, $\varepsilon \geq 5\%$, are expected. Further, installing the inducer with the semi-open impeller with the standard gap resulted in improved performance in the ranges of $\varepsilon = 4\%$ to 5% and $\varepsilon = 4\%$ to 7% for overload and part-load flow conditions, respectively.

In the experimental investigations, it was also interestingly shown that the pump can exhibit substantially different two-phase pumping performances based on the history of the operation. Here, the data was recorded by three different experimental procedures to set the desired two-phase conditions (i.e. the flow rate of air and water). No significant hysteresis effects (no noticeable difference in the pump performance) could be observed in the closed impeller. However, obvious hysteresis could be seen in the semi-open impeller with the standard gap for gas volume fractions between $\varepsilon = 4\%$ and $\varepsilon = 6\%$, specially for the third experimental procedure, in which the air is reduced from an originally high flow rate. As it was obtained from the diverging channel experiments, large gas pockets occur mainly due to large recirculation zones, leading to low-pressure zones where gas bubbles get trapped. Further, when reducing the air flow rate, the large accumulated gas pockets cannot simply be evacuated with the flow; often, they will stay on the blades. To dispose of these large pockets, the gas flow must be very significantly reduced, or high turbulence levels should be maintained for a sufficient time. Therefore, the pump shows, in this case, a much lower performance for the third procedure compared to the first and the second procedure for exactly the “same” flow conditions. Nevertheless, increasing the tip clearance gap was found able to completely eliminate the performance hysteresis of the semi-open impeller. On the other hand, installing the inducer ahead of the semi-open impeller results in enhanced phase mixing at the inlet, reducing strongly the hysteresis between different experimental approaches.

The pump surging and flow instabilities were also studied for the different pump settings considered. Measuring the performance for constant air flow inlet, the closed impeller exhibits strongly unstable curves compared to the semi-open impeller. Therefore, the flow instabilities are generally lower in the semi-open impeller; in addition, pump surging can only occur in limited flow conditions compared to the closed impeller. Furthermore, having the inducer installed could even further damp the flow instabilities and reduce the surging region of the semi-open impeller.

The whole pump was made of transparent acrylic glass, providing high-quality flow visualization. The two-phase flow regimes were recorded and identified using a high-speed camera for all considered pump cases. The two-phase flow maps for the flow regimes were directly associated with the performance curves of each case. Additionally, the undesirable phenomena (breakdown, surging, cavitation...) are also shown, generating a detailed map combined with the pump performance. Accordingly, the behavior and the discontinuities of the performance could be better understood and related to the existing flow regime in the pump. The transitions between different flow regimes on the two-phase maps explain the changes and discontinuities of the pump performance in each case. Additionally, the maps reveal the improved gas accumulation resistance of the semi-open impeller, which positively increases with increasing the tip clearance gap. Although the inducer caused improvement in some ranges, it has only a slight influence on the flow regime map of the semi-open impeller. For very high gas volume fractions ($\varepsilon \geq 8\%$), the performance of the semi-open impeller is slightly better in comparison to the closed impeller. There, the flow regime in the closed impeller is segregated, which is never found in the semi-open impeller. In this range, neither increasing the gap nor installing the inducer could significantly improve the performance due to the occurrence of Gas-locking.

Additionally, some selected two-phase flow cases have been even further analyzed to provide more details of the flow pattern in the impeller and the gas accumulation shape and size. For this purpose, time-averaged images of the gas accumulation in the impeller were obtained for those selected cases. The time-averaged images are very useful to compare with CFD simulations, helping to check the accuracy of different available two-phase models. A complete video library including high-speed time-resolved recordings and cyclic recordings has been generated in this work, producing finally 42 different videos for the flow regimes. The videos involve 115 various two-phase flow conditions.

Using shadowgraphy measurements, the bubble size distributions have been also recorded, which can also be implemented for two-phase flow simulations. It was shown that the bubble size distributions (BSD) of the closed impeller are generally wider with higher median diameters compared to the other three cases of the semi-open impeller. When the gap is increased or the inducer is installed, the bubble size distributions of the semi-open impeller are getting narrower, with slightly lower median diameters.

Performing CFD simulations, some flow details could be clarified, complementing the experimental observations. The comparison between the numerical and experimental results highlights the limitations of CFD results, even for single-phase flows, due to the complexity of the flow and the phase interaction when adding the gas.

7.2 Outlook and Recommendations

In future work, several investigations can be done to improve further the general understanding of the complex interaction of two-phase gas-liquid flows. Corresponding recommendations are listed as follows:

- In the present investigation, a specific diffuser geometry has been used to deliver basic information about the phase segregation and the gas accumulation behavior of two-phase flows. However, the measurements can also be applied to variable diffuser configurations, together with a sudden expansion singularity, in order to investigate the corresponding influence on the gas accumulation phenomenon.

- The present experiments can be extended to consider also the influence of some additional parameters, which have not been considered in the present work. For instance, the effect of increased suction pressures and different rotational speeds would make the results more general. A rotational speed of 650 rpm was kept here in this study, since in our primary tests, strong system vibrations occurred at higher speeds, which could, together with the possible occurrence of pump surging, be destructive for the acrylic parts of the present test rig. Additionally, at higher rotational speeds, cavitation occurred in the volute casing for a wide range of flow conditions in overload. As a consequence, 650 rpm was the maximum limit for safe operation. Therefore, in future investigations, higher rotational speeds and increased suction pressures should be considered, after modifications of test rig and impeller.

- It would be also very interesting to know how gap size would affect the pump performance at higher rotational speeds and increased suction pressures.

- The inducer geometry and its blade configuration can be changed or optimized to maximize the phase mixing before the pump, extending the range in which the two-phase pumping performance is improved.

- In the present analysis, the considered experimental test-rigs are completely made of acrylic glass and simplified to some extent to provide thorough flow visualization. However, it would be of course very appealing to investigate whether different impeller shapes could affect the gas bubble attachment in future studies and how much different the behavior of a more sophisticated 3D impeller can be.

- Based on the experimental and numerical results shown in the present dissertation, additional and more advanced numerical simulations can be done to examine and develop the predicting accuracy of different two-phase models, possibly in combination with different turbulence models. As a result, it should be possible to improve those models and their corresponding prediction of the transport of two-phase flows.

Appendices

A Overview of Particle Image Velocimetry (PIV)

Particle image velocimetry (PIV) is an optical method used to obtain instantaneous velocity fields in fluid flows. PIV systems can provide 2D or even 3D instantaneous flow-field velocity measurements. Time-resolved velocity fields of the flow can be in this event obtained by the use of modern cameras and high-speed computing hardware.

Figure A.1 shows a schematic sketch for the working principle of a typical Particle Image Velocimetry system. As shown, the PIV system consists of several components, including a (double-pulsed) laser, a laser sheet optics, the investigated fluid, seeding particles, a CCD camera, a synchronizer and a computer where the signals are analyzed and the post-processing is done. Seeding (tracer) particles are added to the fluid, which should be sufficiently fine to accurately follow the flow dynamics, and sufficiently big to scatter enough light, generating a good signal. For air flows, the seeding particles are typically oil drops in the range 1 µm to 5 µm, while for water flows, the tracer particles can be typically polystyrene, polyamide, nylon or hollow glass spheres with sizes in the range of 5 µm to 100 µm. In the present experiments, the mean diameter of the employed tracer particles is 50 µm (VESTOSINT 1164 white nylon particles). Additionally, the number density of the particles or the number of particles in the flow should be appropriate to ensure a good signal peak in the cross-correlation. Normally, each interrogation area should contain about 10 to 25 particles.

The seeded fluid is illuminated twice by high-power lights (mostly laser sheets) so that particles are clearly visible, representing the fluid motion. The laser and the camera are synchronized, where the particles illuminated with the first and second light pulse are captured separately on image frame 1 and on image frame 2, respectively. The time between the two laser pulses (Δt) is usually very short to track all flow variations (typically less than 100 microseconds). Evaluating the PIV data, the image frame is divided into small subregions known as interrogation areas. The interrogation areas are cross-correlated considering each pair of image frames (frame 1 and frame 2), obtaining the particle displacement vector. The displacement of the seeding particles is used to calculate speed and direction (the velocity field) of the flow being studied, where the velocity vector is defined as

$$\vec{V} = \frac{\Delta \vec{X}}{\Delta t} \tag{8.1}$$

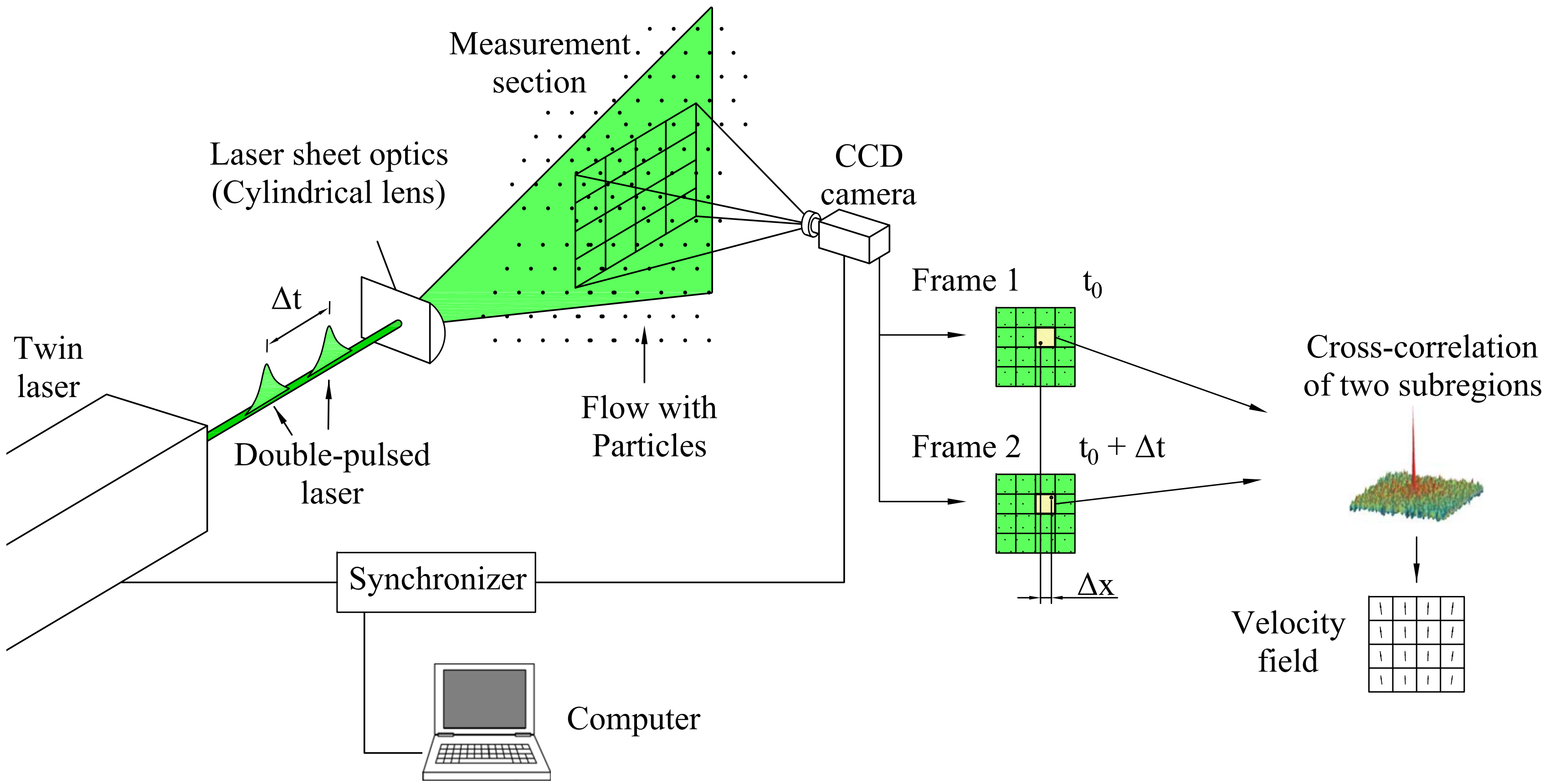

Figure A.1: Schematic sketch of Particle Image Velocimetry (PIV).

B Refraction calibration for Laser Doppler Anemometry (LDA) measurements

B.1 Overview of Laser Doppler Anemometry (LDA)

Laser Doppler Anemometry (LDA) is a method that can measure the velocity of a flow precisely. Actually, it measures the velocity of small tracer particles moving with the fluid flow. The method is non-intrusive, i.e. it does not disturb the flow during the measurement process. The LDA provides a single-point measurement, usually of one component of the flow velocity. The method was originally invented by Yeh and Cummins in 1964 [136].

Figure B.2 shows a simple sketch, which explains the basic principle of the LDA system. As shown, a laser is split into two beams that are focused on a point, where the velocity will be measured. The intersection of the two beams forms the measurement volume, which is typically about 0.5 to 1.0 mm in size. Therefore, LDA measurements can provide very high spatial resolution.

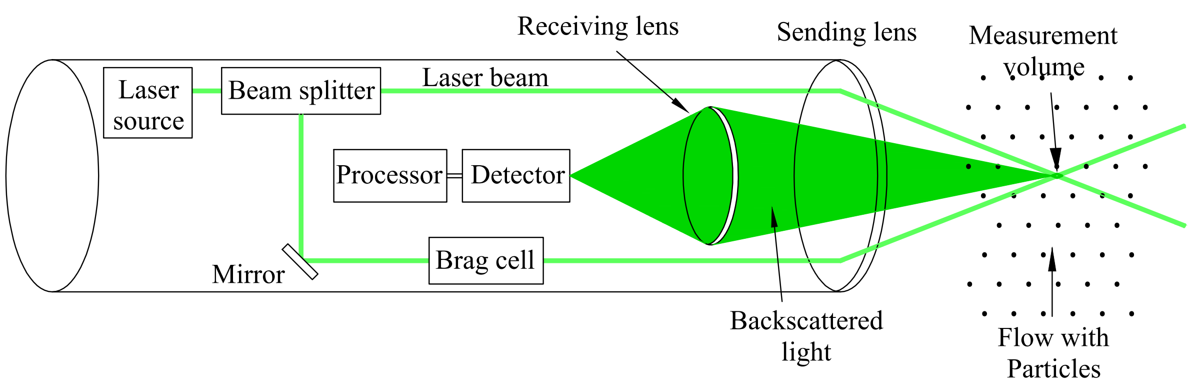

Figure B.2: Schematic sketch of laser Doppler Anemometry.

The laser light is coherent, which means that the light is all in phase, i.e. the peaks and troughs of the waves are aligned. The peaks of the wavefronts are shown by thin lines in each beam in Figure B.3. When the two beams cross, an interference pattern is formed with the wavefront peaks and troughs of the two beams aligning in the horizontal direction (the peaks are shown by the green lines in Figure B.3). The spacing of the fringes is given by d_{fringe}.

When particles pass the intersection region of the two beams (the measurement volume), light is scattered from the stationary fringes. As the particle crosses the fringes, an oscillating signal in time is generated as shown in Figure B.3. The time between peaks in the scattered light corresponds to the time that it takes a particle to travel a distance of d_{fringe}. Afterwards, the velocity can be easily calculated by dividing the distance d_{fringe} by the period of the scattered light oscillation.

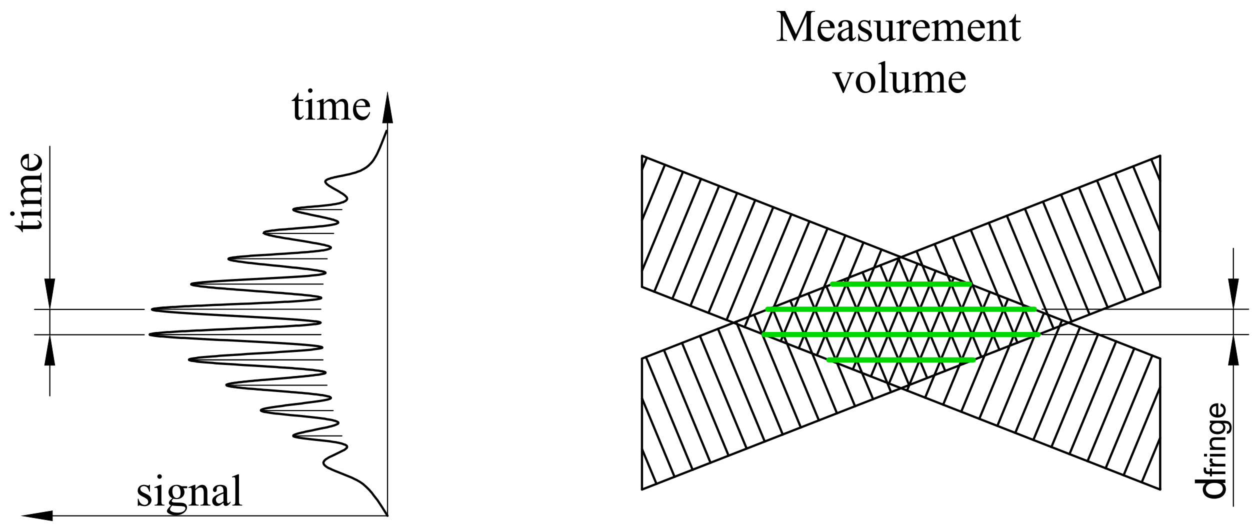

Figure B.3: Description of measuring principle of Laser Doppler Anemometry.

The technique is widely used due to its advantages. However, transparent pipes or transparent windows in the test-rig and tracer particles are always required. Additionally, care must be taken to account for the actual location of the beams intersection, which is shifted due to light refraction at the interface between different mediums. The calibration done in the present experiments is explained in what follows.

B.2 Refraction Calibration

Refractive index (index of refraction)

The refractive index (n_r) of a medium represents a dimensionless number that describes the propagation of light through that medium. It is defined as:

$$n_r = \frac{c}{\nu} \tag{B.1}$$

where c is the speed of light in vacuum and ν is the phase velocity of light in the medium.

The refractive index of a medium determines the refraction of light when light enters this medium. The refraction angle can be described by Snell's law of refraction. Assuming the example shown in Figure B.4, where light is refracted at the interface between two media (air and acrylic glass), the refraction angle can be then determined by Snell's law of refraction, where:

$$n_{r1} \sin\theta_1 = n_{r2} \sin\theta_2 \tag{B.2}$$

In this equation, θ_1 is the angle of incidence, measured between the incident light beam and the normal to the interface between the two media, θ_2 is the angle of refraction of a beam crossing the interface between the two media, measured between the refracted light beam and the normal to the interface between the two media, n_{r1} is the refractive index of the first medium (air), and n_{r2} is the refractive index of the second medium (acrylic glass).

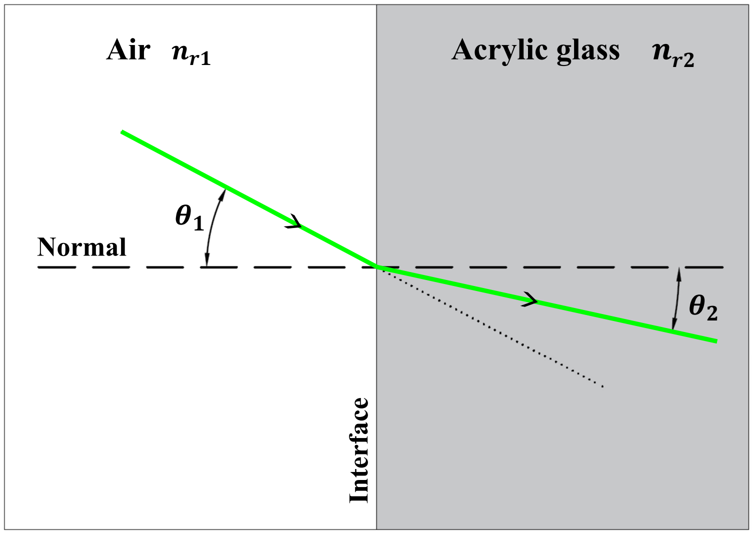

Figure B.4: Refraction of a light beam at the interface between two media.

Calculation of the actual position of the LDA measurement point

We now consider, the refraction of the laser beams through the acrylic glass and water shown in Figure B.5, as done in the present experiments. The actual position of the LDA measurement point in the water is x_w, which will be calculated as a function of the input distance x, as shown in Figure B.5.

The sending lens of LDA system used has a focal length of $L_f = 250$ mm, and a beam distance $B = 45$ mm. The refractive indices of air, acrylic glass, and water obtained from [137] are $n_{r1} = 1.000293$, $n_{r2} = 1.491$, and $n_{r3} = 1.333$, respectively. From Figure B.5, the following equation can be written to calculate the refraction angle θ_1:

$$\sin\theta_1 = \frac{B/2}{\text{Length of incident beam in air}} \tag{B.3}$$

$$\sin\theta_1 = \frac{B}{2\sqrt{0.25B^2 + {L_f}^2}} \tag{B.4}$$

From Snell's law of refraction:

$$n_{r1}\sin\theta_1 = n_{r2}\sin\theta_2 = n_{r3}\sin\theta_3 \tag{B.5}$$

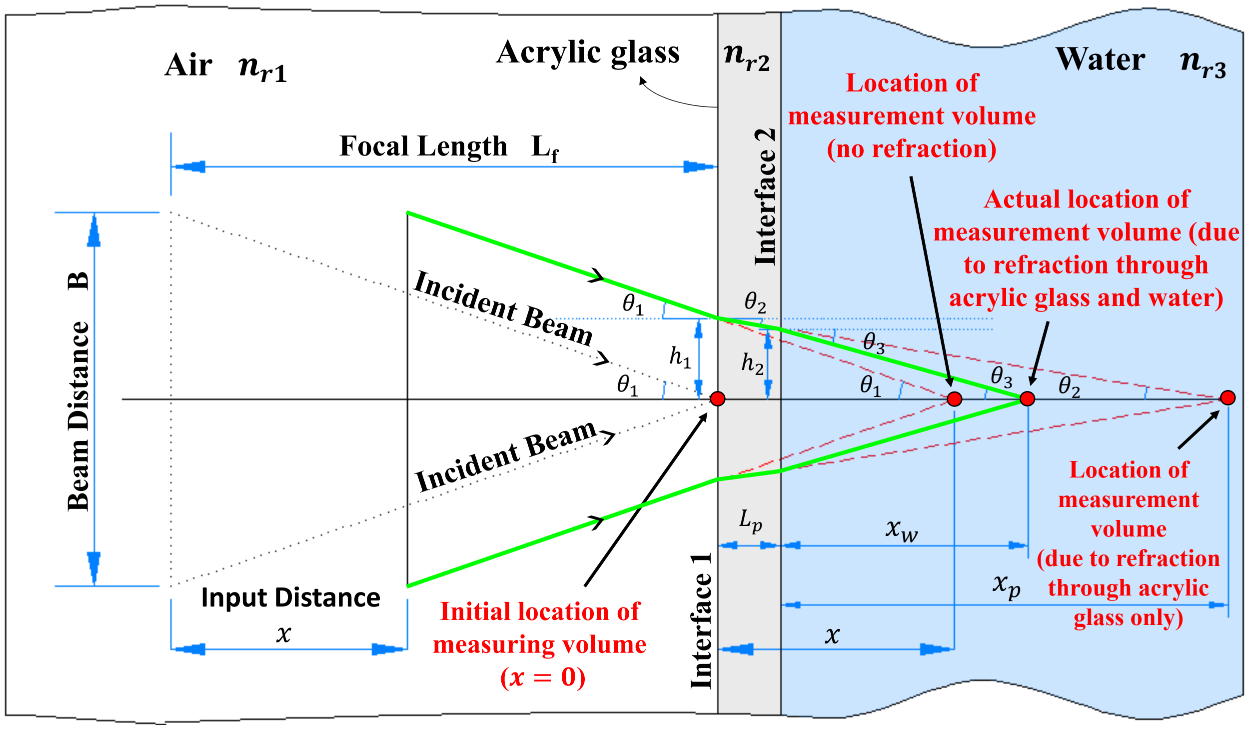

Figure B.5: Refraction of a light beam at the interface between two media.

$$\sin\theta_2 = \frac{n_{r1}}{n_{r2}}\sin\theta_1 = \frac{n_{r1}}{n_{r2}}\frac{B}{2\sqrt{0.25B^2 + {L_f}^2}} \tag{B.6}$$

$$\theta_2 = \sin^{-1}\left[\frac{n_{r1}}{n_{r2}}\frac{B}{2\sqrt{0.25B^2 + {L_f}^2}}\right] = 3.4476648 \tag{B.7}$$

Similarly θ_3 can be calculated by:

$$\theta_3 = \sin^{-1}\left[\frac{n_{r1}}{n_{r3}}\frac{B}{2\sqrt{0.25B^2 + {L_f}^2}}\right] = 3.8569007 \tag{B.8}$$

Now, the position of the LDA measurement point x_p due to the refraction at the interface between the air and acrylic glass (only) is obtained as a function of the input distance x. From trigonometry in Figure B.5, the following equations can be written:

$$\tan\theta_2 = \frac{h_1}{x_p + L_p} \tag{B.9}$$

$$\tan\theta_1 = \frac{h_1}{x} = \frac{B}{2L_f} \tag{B.10}$$

$$h_1 = (x_p + L_p)\tan\theta_2 = \frac{xB}{2L_f} \tag{B.11}$$

$$x_p = \frac{xB}{2L_f \tan\theta_2} - L_p \tag{B.12}$$

where L_p is the thickness of the acrylic glass plate. Then, the final (actual) position of the LDA measurement point x_w due to the second refraction at the interface between the acrylic glass and water can be similarly calculated as a function of the input distance x:

$$\tan\theta_2 = \frac{h_2}{x_p} \tag{B.13}$$

$$\tan\theta_3 = \frac{h_2}{x_w} \tag{B.14}$$

$$h_2 = x_w \;\tan\theta_3 = x_p \;\tan\theta_2 \tag{B.15}$$

$$x_w = \frac{\tan\theta_2}{\tan\theta_3}\, x_p \tag{B.16}$$

Substituting from Equation B.12 into Equation B.16, x_w can be finally calculated by:

$$x_w = \frac{\tan\theta_2}{\tan\theta_3}\left[\frac{xB}{2L_f \tan\theta_2} - L_p\right] \tag{B.17}$$

$$x_w = \left[\frac{xB}{2L_f \tan\theta_3} - L_p \frac{\tan\theta_2}{\tan\theta_3}\right] \tag{B.18}$$

Knowing the refraction index of all materials (n_{r1}, n_{r2} and n_{r3}), together with the focal length (L_f) and the beam distance (B), Equation B.7 and B.8 can be used to calculate the refraction angles of the laser beam θ_2 and θ_3. Afterwards, the final position of the LDA measurement point x_w after the second refraction can be obtained using Equation B.18.

C Error propagation and uncertainty analysis of the experiments

In this Appendix, the calculation steps of the uncertainty of the experiments are given, based on the method of sequential perturbation described by Moffat in [104]. The target is to calculate the uncertainty (error) of the calculated variables in the experiments, resulting from the uncertainties of the measured variables. The uncertainties of the measured variables can be obtained by two methods:

- Directly from the measuring device specifications

  Usually, every measuring device provides the measured variable within a specific range of accuracy due to some unavoidable experimental uncertainty. This accuracy represents the uncertainty. The accuracy of most instruments is given either as a percentage of full scale (% FS) or as a percentage of reading (% RD). If the accuracy is given as % FS, the absolute error value is constant regardless of the measured value. However, if the accuracy is given as % RD, the absolute error is now dependent on the measured value and will increase as the measured value increases. Figure C.6 shows the difference between the two accuracy specifications, by comparing two pressure sensors having uncertainties of 0.25 % FS and 0.5 % RD.

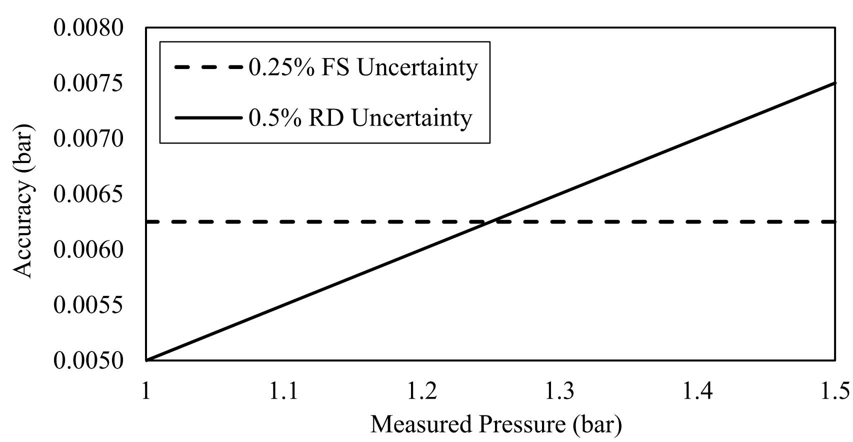

Figure C.6: Difference between % FS and % RD in accuracy specifications.

- Statistically from the measured values

  If the instrument accuracy is not available, then the uncertainty can be obtained statistically from the standard deviation of some sequentially recorded values of the measured variable. The recording time should be large enough (might be 1 or 2 minutes) to observe all possible variations in the observed variable. An adequate frequency of recording should also be considered to track all variations.

The standard analysis of the uncertainty of a calculated variable is done by obtaining the partial derivatives with respect to each measured parameter. For instance, assume that x and y are two measured variables having uncertainty values of dx and dy, respectively. If a variable z is then calculated from these two measured variables, then the uncertainty of the calculated variable dz is:

$$dz = \sqrt{\left(\frac{\partial z}{\partial x}\right)^2 dx^2 + \left(\frac{\partial z}{\partial y}\right)^2 dy^2} \tag{C.1}$$

In the present measurements, the main calculated variables are the pump specific delivery work Υ, the pump efficiency η, the shaft power P_{Sh}, the total flow rate Q_t, and the gas volume fraction ε. Additionally, five different measured variables (signals) are used in calculations, which are the pressure difference across the pump $(p_D - p_S)$, the air mass flow rate $\dot{m}_a$, the water volume flow rate Q_w, the flow temperature T, and the pump suction pressure p_S. To follow the error propagation, each calculated variable should be written as a function of the measured variables to obtain the partial derivatives. For example, the equation of pump specific delivery work Υ is given by:

$$\Upsilon = \frac{1-\dot{\mu}}{\rho_w}\ \Delta p + \dot{\mu} RT\ \ln\left(\frac{p_D}{p_S}\right) + \frac{1}{2}\ \left({V_D}^2 - {V_S}^2\right) + g\ (z_D - z_S) \tag{C.2}$$

This should be written as $\Upsilon = f(\Delta p, \dot{m}_a, Q_w, T, p_S)$, where:

$$\begin{aligned}\Upsilon = \frac{\Delta p}{\rho_w} - \frac{\Delta p \dot{m}_a}{\rho_w \dot{m}_a + {\rho_w}^2 Q_w} + \frac{\dot{m}_a}{\dot{m}_a + \rho_w Q_w}\ RT\ \ln\left(\frac{\Delta p + p_S}{p_S}\right) \\ + \frac{1}{2}\left(\frac{1}{A_D^2} - \frac{1}{A_S^2}\right)\left(\frac{RT\dot{m}_a}{p_S} + Q_w\right)^2 + g\ (z_D - z_S)\end{aligned} \tag{C.3}$$

Now, the partial derivatives of Equation C.3 with respect to each measured variable are deduced:

$$\frac{\partial \Upsilon}{\partial \Delta p} = \frac{1}{\rho_w} - \frac{\dot{m}_a}{\rho_w \dot{m}_a + {\rho_w}^2 Q_w} + \frac{RT\dot{m}_a}{\Delta p(\dot{m}_a + \rho_w Q_w)} \tag{C.4}$$

$$\frac{\partial \Upsilon}{\partial \dot{m}_a} = -\frac{\Delta p Q_w}{\dot{m}_t^2} + \frac{\dot{m}_w}{\dot{m}_t^2}\ RT\ \ln\left(\frac{\Delta p + p_S}{p_S}\right) + \frac{Q_t}{\rho_a}\left(\frac{1}{A_D^2} - \frac{1}{A_S^2}\right) \tag{C.5}$$

$$\frac{\partial \Upsilon}{\partial Q_w} = \frac{\Delta p \dot{m}_a}{\dot{m}_t^2} - \frac{\dot{m}_a \rho_w}{\dot{m}_t^2}\ RT\ \ln\left(\frac{\Delta p + p_S}{p_S}\right) + Q_t\left(\frac{1}{A_D^2} - \frac{1}{A_S^2}\right) \tag{C.6}$$

$$\frac{\partial \Upsilon}{\partial T} = \dot{\mu}R\ \ln\left(\frac{\Delta p + p_S}{p_S}\right) + \frac{Q_t R \dot{m}_a}{p_S}\left(\frac{1}{A_D^2} - \frac{1}{A_S^2}\right) \tag{C.7}$$

$$\frac{\partial \Upsilon}{\partial p_S} = -\dot{\mu}RT\ \left(\frac{\Delta p}{p_S(\Delta p + p_S)}\right) - \frac{Q_t RT \dot{m}_a}{{p_S}^2}\left(\frac{1}{A_D^2} - \frac{1}{A_S^2}\right) \tag{C.8}$$

Then, the uncertainty of the pump specific delivery work $d\Upsilon$ can be finally calculated from:

$$d\Upsilon = \sqrt{\left(\frac{\partial \Upsilon}{\partial \Delta p}\right)^2 d\Delta p^2 + \left(\frac{\partial \Upsilon}{\partial \dot{m}_a}\right)^2 d\dot{m}_a{}^2 + \left(\frac{\partial \Upsilon}{\partial Q_w}\right)^2 dQ_w{}^2 + \left(\frac{\partial \Upsilon}{\partial T}\right)^2 dT^2 + \left(\frac{\partial \Upsilon}{\partial p_S}\right)^2 dp_S{}^2} \tag{C.9}$$

Similarly, the gas volume fraction ε equation is rewritten from:

$$\varepsilon = \frac{Q_a}{Q_a + Q_w} \tag{C.10}$$

to be a function of the measured variables $\varepsilon = f(\dot{m}_a, Q_w, T, p_S)$, so that:

$$\varepsilon = \frac{\dot{m}_a RT}{\dot{m}_a RT + Q_w p_S} \tag{C.11}$$

Likewise, the partial derivatives of Equation C.11 with respect to each measured variable are deduced, where:

$$\frac{\partial \varepsilon}{\partial \dot{m}_a} = \frac{Q_w RT}{(p_S Q_w + \dot{m}_a RT)^2} \tag{C.12}$$

$$\frac{\partial \varepsilon}{\partial Q_w} = -\frac{RT p_S \dot{m}_a}{(p_S Q_w + \dot{m}_a RT)^2} \tag{C.13}$$

$$\frac{\partial \varepsilon}{\partial T} = \frac{Q_w R p_S \dot{m}_a}{(p_S Q_w + \dot{m}_a RT)^2} \tag{C.14}$$

$$\frac{\partial \varepsilon}{\partial p_S} = -\frac{RT Q_w \dot{m}_a}{(p_S Q_w + \dot{m}_a RT)^2} \tag{C.15}$$

Then, the uncertainty of the gas volume fraction $d\varepsilon$ can be calculated from:

$$d\varepsilon = \sqrt{\left(\frac{\partial \varepsilon}{\partial \dot{m}_a}\right)^2 d\dot{m}_a{}^2 + \left(\frac{\partial \varepsilon}{\partial Q_w}\right)^2 dQ_w{}^2 + \left(\frac{\partial \varepsilon}{\partial T}\right)^2 dT^2 + \left(\frac{\partial \varepsilon}{\partial p_S}\right)^2 dp_S{}^2} \tag{C.16}$$

Similarly, the shaft power P_{Sh} equation can be written as:

$$P_{Sh} = \tau \times \omega = \tau \times \frac{2\pi n}{60} \tag{C.17}$$

The partial derivatives of P_{Sh} are:

$$\frac{\partial P_{Sh}}{\partial n} = \frac{2\pi\tau}{60} \tag{C.18}$$

$$\frac{\partial P_{Sh}}{\partial \tau} = \frac{2\pi n}{60} \tag{C.19}$$

The uncertainty of the shaft power dP_{Sh} can be calculated from:

$$dP_{Sh} = \sqrt{\left(\frac{\partial P_{Sh}}{\partial n}\right)^2 dn^2 + \left(\frac{\partial P_{Sh}}{\partial \tau}\right)^2 d\tau^2} \tag{C.20}$$

Lastly, the pump efficiency η equation can be written as:

$$\eta = \frac{P_P}{P_{Sh}} = \frac{\dot{m}_t \Upsilon}{P_{Sh}} = \frac{(\dot{m}_a + \rho_w Q_w)\,\Upsilon}{P_{Sh}} \tag{C.21}$$

Then, the partial derivatives of η are:

$$\frac{\partial \eta}{\partial \dot{m}_a} = \frac{\Upsilon}{P_{Sh}} \tag{C.22}$$

$$\frac{\partial \eta}{\partial \Upsilon} = \frac{(\dot{m}_a + \rho_w Q_w)}{P_{Sh}} \tag{C.23}$$

$$\frac{\partial \eta}{\partial Q_w} = \frac{\rho_w \Upsilon}{P_{Sh}} \tag{C.24}$$

$$\frac{\partial \eta}{\partial P_{Sh}} = \frac{(\dot{m}_a + \rho_w Q_w)\,\Upsilon}{P_{Sh}{}^2} \tag{C.25}$$

Then, the uncertainty of the pump efficiency $d\eta$ can be calculated from:

$$d\eta = \sqrt{\left(\frac{\partial\eta}{\partial\dot{m}_a}\right)^2 d\dot{m}_a{}^2 + \left(\frac{\partial\eta}{\partial\Upsilon}\right)^2 d\Upsilon^2 + \left(\frac{\partial\eta}{\partial Q_w}\right)^2 dQ_w{}^2 + \left(\frac{\partial\eta}{\partial P_{Sh}}\right)^2 dP_{Sh}{}^2} \tag{C.26}$$

Using the uncertainty of the measuring devices given in Table 3.3, the uncertainty of the calculated variables are obtained by Equations C.9, C.16, C.20, and C.26. The final uncertainties are given in Table 8.1 as root mean square values of all measurement points recorded by the first experimental procedure (Figure 5.2a) for different pump settings. As can be seen, for different cases, the analysis delivers root mean square values of uncertainty better than 1.45%, 3.2%, 4.7%, and 4.95% in the pump specific delivery work Υ, the gas volume fraction ε, the shaft power P_{Sh}, and the pump efficiency η, respectively. Figure C.7 shows the error bars of the normalized pump specific delivery work, the normalized shaft power, and the pump efficiency η of the closed impeller.

Table 8.1: Uncertainties of calculated variables as root mean square values.

Variable	Closed impeller	Semi-open impeller standard gap	Semi-open impeller increased gap
$d\Upsilon$ %	1.23	1.43	1.39
$d\varepsilon$ %	2.86	2.96	3.16
dP_{Sh} %	4.23	4.61	4.69
$d\eta$ %	4.43	4.86	4.92

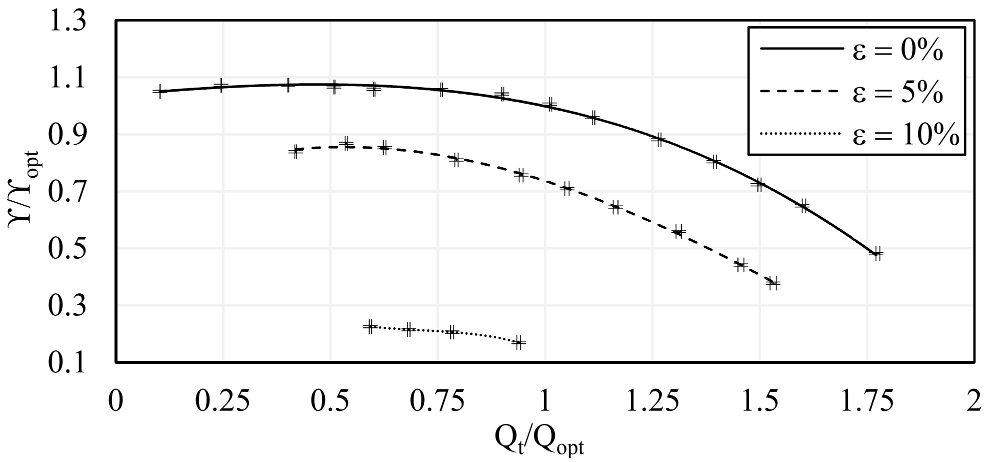

(a) Normalized specific delivery work

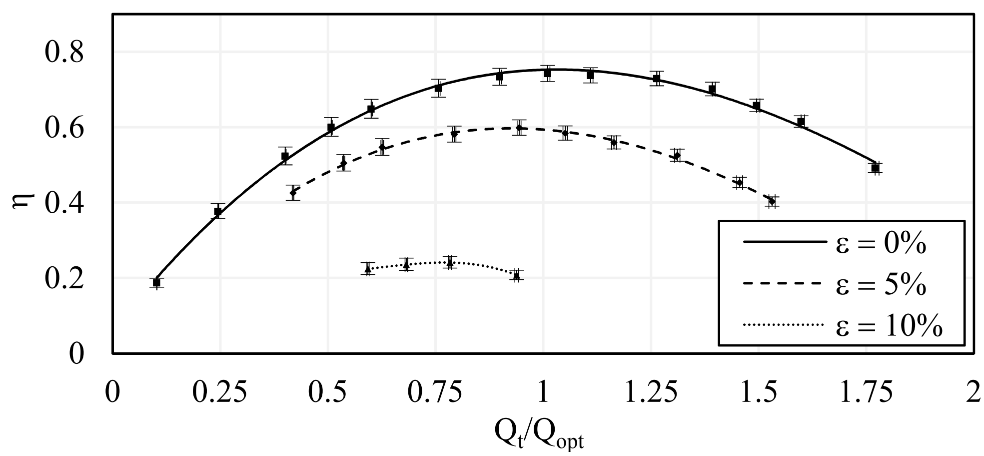

(b) Efficiency

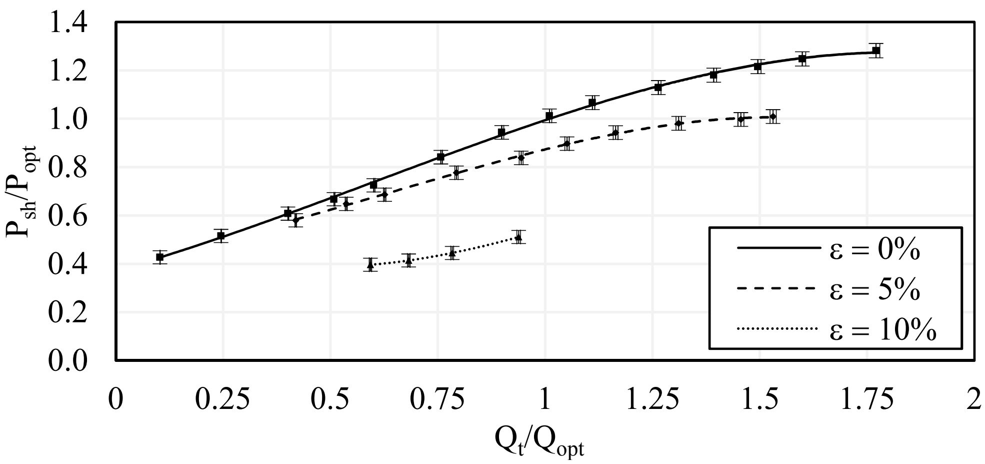

(c) Normalized shaft power

Figure C.7: Error bars of the performance curves of the closed impeller.

D MATLAB script for calculating the size of gas accumulation in the diverging flow channel

In this Appendix, the MATLAB script used to calculate the gas accumulation size in the diverging flow channel is given (see Section 4.3). The script is divided into several parts, including:

- Reading the averaged images
- Converting the images to grayscale
- Calculating the average boundary of the cavity
- Correcting the average boundary of the cavity
- Calculating the separation (starting) point and the cavity dimensions
- Calculating cavity area and size
- Printing the cavity boundary images
- Exporting the data to an Excel file

MATLAB Script

```
clc, clear all, close all,
%————————————————————————————————

%% Read the averaged images
% Get all the png images in the current directory
pngFiles = dir('*.png');
% Obtain the number of images
numFiles = length(pngFiles);
% Read image from graphics files
mydata = cell(1,numFiles);
for k = 1:numFiles;
A{k,1} = imread(pngFiles(k).name);
end
%————————————————————————————————

% % Converting the images to grayscale and printing the new images
for k = 1:numFiles;
A{k} = im2bw(A{k}, 0.99);
% Printing the images in binary format
pngName{k} = getfield(pngFiles(k,1),'name');
pngNewName2 = strrep(pngName{k},'.png','_BW.bmp');
pngNewName2 = fullfile('G:\Shadowgraphy \Black and white images\',pngNewName2 );
imwrite((A{k}), pngNewName2);
end
%————————————————————————————————
```

```
%% Starting the calculations
% Obtaining the size of the image in pixels
[sy,sx]=size(A{1});
% Obtaining the coordinates of the black pixels
for k=1:numFiles
[y{k},x{k}]=find(A{k}¡1);
mat{k}=[x{k},(sy-y{k})];
[nx{k},ny{k}]=size(mat{k});
end
%——————————————————————————

%% Calculating the average boundary of the cavity
for k=1:numFiles
j=1;
i=1;
while i¡(nx{k}-1);
s=1;
ys=mat{k}(i,2);
d=(mat{k}(i,2))-(mat{k}(i+1,2));
while (d==1);
if mat{k}(i+1,1) > mat{k}(i,1);
break
end
ys=ys+mat{k}(i+1,2);
s=s+1;
i=i+1;
if i > (nx{k}-1);
break
end
d=mat{k}(i,2)-mat{k}(i+1,2);
end
if i > (nx{k}-1);
break
end
yav{k}(j,2)= ys/s;
yav{k}(j,3)= yav{k}(j,2);
yav{k}(j,1)=mat{k}(i,1);
u=mat{k}(i,1)-mat{k}(i+1,1);
if u==0 ;
i=i+1;
s=1;
ys=mat{k}(i,2);
d=mat{k}(i,2)-mat{k}(i+1,2);
while (d==1);
if mat{k}(i+1,1) > mat{k}(i,1);
break
end
ys=ys+mat{k}(i+1,2);
s=s+1;
i=i+1;
if i > (nx{k}-1);
break
```

```
end
d=mat{k}(i,2)-mat{k}(i+1,2);
end
yav{k}(j,3)= ys/s;
end
Lowerlimit{k}(j,1)=j;
Lowerlimit{k}(j,2)=mat{k}(i,2);
i=i+1;
j=j+1;
if j > sx;
break
end
end
end
%————————————————————————————————

%% Correcting the average boundary of the cavity by:
% 1- removing the wrong points inside the cavity boundary if any
% 2- removing the wrong points after the cavity
for k=1:numFiles
yavm{k}=yav{k};
[nm{k},pm{k}]=size(yavm{k});
i=1;
while (i ¡(nm{k}-1));
if (yavm{k}(i,1)==yavm{k}(i+1,1));
yavm{k}(i,3)=yavm{k}(i+1,3);
yavm{k}([i+1], :) = [];
end
if (yavm{k}(i,3) > (sy-4));
yavm{k}(i:nm{k}, :) = [];
[nm{k},pm{k}]=size(yavm{k});
break
end
i=i+1;
[nm{k},pm{k}]=size(yavm{k});
end
end
%————————————————————————————————

%% Calculating the separation (starting) point and the cavity dimensions
%pixel scale (mm/pixel)
ps=0.454837;
for k=1:numFiles
for i=1:400;
if (yavm{k}(i,2) > yavm{k}(i,3));
xsep{k}=yavm{k}(i,1)-40;
ysep{k}=yavm{k}(i-40,3);
break
else
[ysep{k},xsep{k}]= max(yavm{k}(1:320,2));  % separation point
end
end
```

```
%————————————————————————————————

%% Setting the end of the cavity before the stratified flow
for k=1:numFiles;
yavmc{k}=yavm{k};
for u=400:nm{k}
if (yavmc{k}(u,3) > yavmc{k}(nm{k},3))&&((sx-5)leqnm{k});
yavmc{k}(u:nm{k}, :) = [];
break
end
end
[nmc{k},pmc{k}]=size(yavmc{k});
end
%————————————————————————————————

%% Editing the average boundary of the cavity by setting the boundary to maximum before the separation
point
for k=1:numFiles
t=1;
for r=1:xsep{k};
if (mat{k}(t,1)==yavmc{k}(r,1));
yavmc{k}(r,3)=mat{k}(t,2);
end
while (mat{k}(t,1)==mat{k}(t+1,1));
t=t+1;
end
t=t+1;
end
end
%————————————————————————————————

%% Calculations of Areas
% Total area of the image
At=sx*sy;
for k=1:numFiles;
% Area of water before the cavity
Abc{k}=0;
% A loop for summing the area before the cavity
for q=1:xsep{k};
% Area of water before the cavity
Abc{k}=Abc{k}+(yavmc{k}(q,3)) ;
end
% Area of water under the cavity
Auc{k}=0;
% A loop for summing the area under the cavity
for m=xsep{k}:nmc{k};
% Area of water under the cavity
Auc{k}=Auc{k}+(yavmc{k}(m,3)) ;
end
% Area of water after the cavity
Aac{k}=sy*(sx-m+1);
% Area diffuser (calculated by AutoCAD directly in pixel)
```

```
Ad{k}=3375/(ps*ps);
% Area of the cavity in pixel
Ac{k}=At-(Auc{k}+Abc{k}+Aac{k}+Ad{k});
% Area of the cavity in mm2
Acmm{k} = Ac{k}*ps*ps;
end
%————————————————————————

%% Showing the cavity boundaries
for k =1:numFiles;
Am{k}=zeros(sy,sx)+1;
for h=1:nmc{k};
Am{k}(round(yavmc{k}(h,3)),h)= 0;
end
% Flips the rows, making an upside-down image
Am{k} = flipdim(Am{k},1);
An{k}=1-A{k};
Amn{k}=1-Am{k};
c{k} =1-(An{k}-Amn{k});
end
%————————————————————————

%% Printing the cavity boundary images
for k = 1:numFiles;
% Printing the images in binary format
pngName{k} = getfield(pngFiles(k,1),'name');
pngNewName2 = strrep(pngName{k},'.png','_CB.bmp');
pngNewName2 = fullfile('G:\Shadowgraphy \Cavity-boundary images \',pngNewName2 );
imwrite((c{k}), pngNewName2);
end
%————————————————————————

%% Exporting the data to an excel file
% Assigning the titles to string variables
txtN= {'Image Name'};
txtAt = {'Area of image'};
txtAd={'Area Diffuser'};
txtAbc={'Area before the cavity'};
txtAuc={'Area under the cavity'};
txtAac={'Area after the cavity'};
txtAc={'Area cavity pixels'};
txtAcmm={'Area cavity mm2'};
% Printing the titles in the first row of the excel file
xlswrite('test.xlsx',txtN,'Sheet1','A1')
xlswrite('test.xlsx',txtAt,'Sheet1','B1')
xlswrite('test.xlsx',txtAd,'Sheet1','C1')
xlswrite('test.xlsx',txtAbc,'Sheet1','D1')
xlswrite('test.xlsx',txtAuc,'Sheet1','E1')
xlswrite('test.xlsx',txtAac,'Sheet1','F1')
xlswrite('test.xlsx',txtAc,'Sheet1','G1')
xlswrite('test.xlsx',txtAcmm,'Sheet1','H1')
% Printing the areas
```

```
for k=1:numFiles;
cellname=[ 'A' num2str(k+1)];
xlswrite('test.xlsx',{pngName{k}},'Sheet1',cellname);
cellname=[ 'B' num2str(k+1)];
xlswrite('test.xlsx',At,'Sheet1',cellname);
cellname=[ 'C' num2str(k+1)];
xlswrite('test.xlsx',Ad{k},'Sheet1',cellname);
cellname=[ 'D' num2str(k+1)];
xlswrite('test.xlsx',Abc{k},'Sheet1',cellname);
cellname=[ 'E' num2str(k+1)];
xlswrite('test.xlsx',Auc{k},'Sheet1',cellname);
cellname=[ 'F' num2str(k+1)];
xlswrite('test.xlsx',Aac{k},'Sheet1',cellname);
cellname=[ 'G' num2str(k+1)];
xlswrite('test.xlsx',Ac{k},'Sheet1',cellname);
cellname=[ 'H' num2str(k+1)];
xlswrite('test.xlsx',Acmm{k},'Sheet1',cellname);
end
```

E Diverging channel inlet velocity boundary condition data

In this Appendix, two sample tables of boundary condition data for the inlet velocity of the diverging channel are given, as discussed in Section 4.6.1, and shown in Figures 4.15 and 4.16. The velocity data were measured by using a Laser Doppler Anemometry (LDA) system on the grid points shown in Figure 3.4, as described in Section 3.1.4. In the following data, v_x, v_y, Tu_x, and Tu_y are axial velocity, vertical velocity, axial velocity fluctuation, and vertical velocity fluctuation, respectively. Points adjacent to the wall with zero velocity are also given to cover completely the inlet section for direct implementation of the tables in CFD simulations. For more details about the LDA system, see Appendix B

Table B.1: Single-phase flow: Re_w= 50,130.

Point	Coordinates			Velocity			Velocity fluctuations	
no.	x (mm)	y (mm)	z (mm)	v_x (m/s)	v_y (m/s)	Velocity Magnitude (m/s)	Tu_x (m/s)	Tu_y (m/s)
1	0	0	0	0	0	0	0	0
2	0	4	0	0	0	0	0	0
3	0	8	0	0	0	0	0	0
4	0	12	0	0	0	0	0	0
5	0	16	0	0	0	0	0	0
6	0	20	0	0	0	0	0	0
7	0	24	0	0	0	0	0	0
8	0	28	0	0	0	0	0	0
9	0	32	0	0	0	0	0	0
10	0	36	0	0	0	0	0	0
11	0	40	0	0	0	0	0	0
12	0	0	5.9806	0	0	0	0	0
13	0	4	5.9806	1.2242	-0.0869	1.2273	0.1178	0.0739
14	0	8	5.9806	1.2164	-0.0726	1.2186	0.1255	0.0850
15	0	12	5.9806	1.1944	-0.0624	1.1960	0.1266	0.0915
16	0	16	5.9806	1.2083	-0.0567	1.2096	0.1317	0.0836
17	0	20	5.9806	1.2409	-0.0425	1.2416	0.1324	0.0916
18	0	24	5.9806	1.2733	-0.0393	1.2739	0.1281	0.0887
19	0	28	5.9806	1.2749	-0.0215	1.2751	0.1173	0.0794
20	0	32	5.9806	1.2666	-0.0004	1.2666	0.1137	0.0710
21	0	36	5.9806	1.1793	0.0152	1.1794	0.1131	0.0737
22	0	40	5.9806	0	0	0	0	0
23	0	0	11.3205	0	0	0	0	0
24	0	4	11.3205	1.3152	-0.0909	1.3183	0.1027	0.0688
25	0	8	11.3205	1.3813	-0.0774	1.3835	0.0943	0.0679

Table B.1 continued from previous page

Point	Coordinates			Velocity			Velocity fluctuations	
no.	x (mm)	y (mm)	z (mm)	v_x (m/s)	v_y (m/s)	Velocity Magnitude (m/s)	Tu_x (m/s)	Tu_y (m/s)
26	0	12	11.3205	1.3907	-0.0718	1.3926	0.0997	0.0701
27	0	16	11.3205	1.3976	-0.0594	1.3989	0.1075	0.0673
28	0	20	11.3205	1.416	-0.0463	1.4168	0.1020	0.0687
29	0	24	11.3205	1.4233	-0.0317	1.4237	0.0988	0.0648
30	0	28	11.3205	1.4207	-0.0178	1.4208	0.0918	0.0437
31	0	32	11.3205	1.3516	-0.0082	1.3516	0.1033	0.0937
32	0	36	11.3205	1.2123	-0.0003	1.2123	0.1292	0.0781
33	0	40	11.3205	0	0	0	0	0
34	0	0	16.6604	0	0	0	0	0
35	0	4	16.6604	1.3279	-0.0824	1.3305	0.1150	0.0689
36	0	8	16.6604	1.4316	-0.0804	1.4339	0.0902	0.0612
37	0	12	16.6604	1.4858	-0.0277	1.4861	0.0798	0.0382
38	0	16	16.6604	1.5138	-0.0397	1.5143	0.0740	0.0485
39	0	20	16.6604	1.5198	-0.0479	1.5206	0.0777	0.0582
40	0	24	16.6604	1.506	-0.0405	1.5065	0.0810	0.0564
41	0	28	16.6604	1.4524	-0.0306	1.4527	0.1017	0.0571
42	0	32	16.6604	1.3564	-0.0225	1.3566	0.1167	0.0627
43	0	36	16.6604	1.2183	-0.0083	1.2183	0.1310	0.0580
44	0	40	16.6604	0	0	0	0	0
45	0	0	22	0	0	0	0	0
46	0	4	22	1.3044	-0.0705	1.3063	0.1197	0.0787
47	0	8	22	1.4073	-0.0607	1.4086	0.1055	0.0644
48	0	12	22	1.4924	-0.0717	1.4941	0.0825	0.0683
49	0	16	22	1.5538	-0.0401	1.5543	0.0649	0.0444
50	0	20	22	1.5633	-0.0229	1.5635	0.0660	0.0278
51	0	24	22	1.5305	-0.0405	1.5310	0.0794	0.0498
52	0	28	22	1.4645	-0.0205	1.4646	0.1053	0.0323
53	0	32	22	1.3694	-0.0179	1.3695	0.1282	0.0400
54	0	36	22	1.2229	-0.0095	1.2229	0.1346	0.0513
55	0	40	22	0	0	0	0	0
56	0	0	27.3401	0	0	0	0	0
57	0	4	27.3401	1.3279	-0.0824	1.3305	0.1150	0.0689
58	0	8	27.3401	1.4316	-0.0804	1.4339	0.0902	0.0612
59	0	12	27.3401	1.4858	-0.0277	1.4861	0.0798	0.0382
60	0	16	27.3401	1.5138	-0.0397	1.5143	0.0740	0.0485
61	0	20	27.3401	1.5198	-0.0479	1.5206	0.0777	0.0582
62	0	24	27.3401	1.506	-0.0405	1.5065	0.0810	0.0564

Table B.1 continued from previous page

Point	Coordinates			Velocity			Velocity fluctuations	
no.	x (mm)	y (mm)	z (mm)	v_x (m/s)	v_y (m/s)	Velocity Magnitude (m/s)	Tu_x (m/s)	Tu_y (m/s)
63	0	28	27.3401	1.4524	-0.0306	1.4527	0.1017	0.0571
64	0	32	27.3401	1.3564	-0.0225	1.3566	0.1167	0.0627
65	0	36	27.3401	1.2183	-0.0083	1.2183	0.1310	0.0580
66	0	40	27.3401	0	0	0	0	0
67	0	0	32.6800	0	0	0	0	0
68	0	4	32.6800	1.3152	-0.0909	1.3183	0.1027	0.0688
69	0	8	32.6800	1.3813	-0.0774	1.3835	0.0943	0.0679
70	0	12	32.6800	1.3907	-0.0718	1.3926	0.0997	0.0701
71	0	16	32.6800	1.3976	-0.0594	1.3989	0.1075	0.0673
72	0	20	32.6800	1.416	-0.0463	1.4168	0.1020	0.0687
73	0	24	32.6800	1.4233	-0.0317	1.4237	0.0988	0.0648
74	0	28	32.6800	1.4207	-0.0178	1.4208	0.0918	0.0437
75	0	32	32.6800	1.3516	-0.0082	1.3516	0.1033	0.0937
76	0	36	32.6800	1.2123	-0.0003	1.2123	0.1292	0.0781
77	0	40	32.6800	0	0	0	0	0
78	0	0	38.0198	0	0	0	0	0
79	0	4	38.0198	1.2242	-0.0869	1.2273	0.1178	0.0739
80	0	8	38.0198	1.2164	-0.0726	1.2186	0.1255	0.0850
81	0	12	38.0198	1.1944	-0.0624	1.1960	0.1266	0.0915
82	0	16	38.0198	1.2083	-0.0567	1.2096	0.1317	0.0836
83	0	20	38.0198	1.2409	-0.0425	1.2416	0.1324	0.0916
84	0	24	38.0198	1.2733	-0.0393	1.2739	0.1281	0.0887
85	0	28	38.0198	1.2749	-0.0215	1.2751	0.1173	0.0794
86	0	32	38.0198	1.2666	-0.0004	1.2666	0.1137	0.0710
87	0	36	38.0198	1.1793	0.0152	1.1794	0.1131	0.0737
88	0	40	38.0198	0	0	0.0000	0.0000	0.0000
89	0	0	44	0	0	0	0	0
90	0	4	44	0	0	0	0	0
91	0	8	44	0	0	0	0	0
92	0	12	44	0	0	0	0	0
93	0	16	44	0	0	0	0	0
94	0	20	44	0	0	0	0	0
95	0	24	44	0	0	0	0	0
96	0	28	44	0	0	0	0	0
97	0	32	44	0	0	0	0	0
98	0	36	44	0	0	0	0	0
99	0	40	44	0	0	0	0	0

Table B.2: Two-phase flow - Case 2: Re_w= 50,130, Re_a = 6.17.

Point	Coordinates			Velocity			Velocity fluctuations	
no.	x (mm)	y (mm)	z (mm)	v_x (m/s)	v_y (m/s)	Velocity Magnitude (m/s)	Tu_x (m/s)	Tu_y (m/s)
1	0	0	0	0	0	0	0	0
2	0	4	0	0	0	0	0	0
3	0	8	0	0	0	0	0	0
4	0	12	0	0	0	0	0	0
5	0	16	0	0	0	0	0	0
6	0	20	0	0	0	0	0	0
7	0	24	0	0	0	0	0	0
8	0	28	0	0	0	0	0	0
9	0	32	0	0	0	0	0	0
10	0	36	0	0	0	0	0	0
11	0	40	0	0	0	0	0	0
12	0	0	5.9806	0	0	0	0	0
13	0	4	5.9806	1.2265	-0.0975	1.2304	0.0720	0.1031
14	0	8	5.9806	1.2477	-0.0805	1.2503	0.0725	0.1147
15	0	12	5.9806	1.2209	-0.0668	1.2227	0.0830	0.1253
16	0	16	5.9806	1.218	-0.0627	1.2196	0.0825	0.1264
17	0	20	5.9806	1.2442	-0.053	1.2453	0.0845	0.1324
18	0	24	5.9806	1.2732	-0.0431	1.2739	0.0813	0.1328
19	0	28	5.9806	1.2929	-0.0296	1.2932	0.0784	0.1161
20	0	32	5.9806	1.2923	-0.0041	1.2923	0.0665	0.1146
21	0	36	5.9806	1.2088	0.0063	1.2088	0.0720	0.1067
22	0	40	5.9806	0	0	0	0	0
23	0	0	11.3205	0	0	0	0	0
24	0	4	11.3205	1.2959	-0.0931	1.2992	0.0663	0.1019
25	0	8	11.3205	1.3797	-0.0911	1.3827	0.0619	0.0895
26	0	12	11.3205	1.3883	-0.0793	1.3906	0.0686	0.0958
27	0	16	11.3205	1.3976	-0.0634	1.3990	0.0700	0.0996
28	0	20	11.3205	1.4133	-0.0447	1.4140	0.0696	0.1006
29	0	24	11.3205	1.4311	-0.0254	1.4313	0.0544	0.0967
30	0	28	11.3205	1.4387	-0.024	1.4389	0.0639	0.0898
31	0	32	11.3205	1.3677	-0.0166	1.3678	0.0629	0.0996
32	0	36	11.3205	1.2117	-0.008	1.2117	0.0727	0.1272
33	0	40	11.3205	0	0	0	0	0
34	0	0	16.6604	0	0	0	0	0
35	0	4	16.6604	1.2964	-0.0846	1.2992	0.0712	0.1181
36	0	8	16.6604	1.4124	-0.0835	1.4149	0.0618	0.0987
37	0	12	16.6604	1.4659	-0.0749	1.4678	0.0569	0.0795

Table B.2 continued from previous page

Point	Coordinates			Velocity			Velocity fluctuations	
no.	x (mm)	y (mm)	z (mm)	v_x (m/s)	v_y (m/s)	Velocity Magnitude (m/s)	Tu_x (m/s)	Tu_y (m/s)
38	0	16	16.6604	1.4966	-0.0658	1.4980	0.0545	0.0796
39	0	20	16.6604	1.519	-0.052	1.5199	0.0554	0.0731
40	0	24	16.6604	1.5121	-0.0401	1.5126	0.0523	0.0735
41	0	28	16.6604	1.4647	-0.0287	1.4650	0.0600	0.0904
42	0	32	16.6604	1.3633	-0.0261	1.3635	0.0654	0.1121
43	0	36	16.6604	1.196	-0.0093	1.1960	0.0763	0.1238
44	0	40	16.6604	0	0	0	0	0
45	0	0	22	0	0	0	0	0
46	0	4	22	1.2728	-0.0788	1.2752	0.0713	0.1222
47	0	8	22	1.3762	-0.0755	1.3783	0.0631	0.1102
48	0	12	22	1.4674	-0.07	1.4691	0.0555	0.0886
49	0	16	22	1.538	-0.0623	1.5393	0.0509	0.0718
50	0	20	22	1.5554	-0.0544	1.5564	0.0479	0.0603
51	0	24	22	1.5315	-0.0456	1.5322	0.0491	0.0758
52	0	28	22	1.4732	-0.0345	1.4736	0.0577	0.0994
53	0	32	22	1.3573	-0.0262	1.3576	0.0676	0.1155
54	0	36	22	1.1929	-0.0051	1.1929	0.0770	0.1349
55	0	40	22	0	0	0	0	0
56	0	0	27.3401	0	0	0	0	0
57	0	4	27.3401	1.2964	-0.0846	1.2992	0.0712	0.1181
58	0	8	27.3401	1.4124	-0.0835	1.4149	0.0618	0.0987
59	0	12	27.3401	1.4659	-0.0749	1.4678	0.0569	0.0795
60	0	16	27.3401	1.4966	-0.0658	1.4980	0.0545	0.0796
61	0	20	27.3401	1.519	-0.052	1.5199	0.0554	0.0731
62	0	24	27.3401	1.5121	-0.0401	1.5126	0.0523	0.0735
63	0	28	27.3401	1.4647	-0.0287	1.4650	0.0600	0.0904
64	0	32	27.3401	1.3633	-0.0261	1.3635	0.0654	0.1121
65	0	36	27.3401	1.196	-0.0093	1.1960	0.0763	0.1238
66	0	40	27.3401	0	0	0	0	0
67	0	0	32.6800	0	0	0	0	0
68	0	4	32.6800	1.2959	-0.0931	1.2992	0.0663	0.1019
69	0	8	32.6800	1.3797	-0.0911	1.3827	0.0619	0.0895
70	0	12	32.6800	1.3883	-0.0793	1.3906	0.0686	0.0958
71	0	16	32.6800	1.3976	-0.0634	1.3990	0.0700	0.0996
72	0	20	32.6800	1.4133	-0.0447	1.4140	0.0696	0.1006
73	0	24	32.6800	1.4311	-0.0254	1.4313	0.0544	0.0967
74	0	28	32.6800	1.4387	-0.024	1.4389	0.0639	0.0898

Table B.2 continued from previous page

Point	Coordinates			Velocity			Velocity fluctuations	
no.	x (mm)	y (mm)	z (mm)	v_x (m/s)	v_y (m/s)	Velocity Magnitude (m/s)	Tu_x (m/s)	Tu_y (m/s)
75	0	32	32.6800	1.3677	-0.0166	1.3678	0.0629	0.0996
76	0	36	32.6800	1.2117	-0.008	1.2117	0.0727	0.1272
77	0	40	32.6800	0	0	0	0	0
78	0	0	38.0198	0	0	0	0	0
79	0	4	38.0198	1.2265	-0.0975	1.2304	0.0720	0.1031
80	0	8	38.0198	1.2477	-0.0805	1.2503	0.0725	0.1147
81	0	12	38.0198	1.2209	-0.0668	1.2227	0.0830	0.1253
82	0	16	38.0198	1.218	-0.0627	1.2196	0.0825	0.1264
83	0	20	38.0198	1.2442	-0.053	1.2453	0.0845	0.1324
84	0	24	38.0198	1.2732	-0.0431	1.2739	0.0813	0.1328
85	0	28	38.0198	1.2929	-0.0296	1.2932	0.0784	0.1161
86	0	32	38.0198	1.2923	-0.0041	1.2923	0.0665	0.1146
87	0	36	38.0198	1.2088	0.0063	1.2088	0.0720	0.1067
88	0	40	38.0198	0	0	0	0	0
89	0	0	44	0	0	0	0	0
90	0	4	44	0	0	0	0	0
91	0	8	44	0	0	0	0	0
92	0	12	44	0	0	0	0	0
93	0	16	44	0	0	0	0	0
94	0	20	44	0	0	0	0	0
95	0	24	44	0	0	0	0	0
96	0	28	44	0	0	0	0	0
97	0	32	44	0	0	0	0	0
98	0	36	44	0	0	0	0	0
99	0	40	44	0	0	0	0	0

F Derivation of the pump specific delivery work for two-phase flows

The specific delivery work of the pump impeller can be obtained by applying the first law of thermodynamics, which can be written as

$$d\dot{W}_t + d\dot{Q} = \dot{m}\ (dh + V\ dV + g\ dz) \tag{F.1}$$

where $d\dot{W}_t$ is the total work given to the system, $d\dot{Q}$ is the heat transfer across the system, $\dot{m}$ is the mass flow rate of the fluid, dh is the change of the specific enthalpy, $V\ dV$ is the change of the specific kinetic energy and $g\ dz$ is the change of the specific potential energy. In real processes, the total work given to the system $d\dot{W}_t$ is equal to the summation of the useful work delivered by the pump $d\dot{W}$ and the dissipation work $d\dot{W}_{diss}$ which is consumed to overcome the friction

$$d\dot{W}_t = d\dot{W} + d\dot{W}_{diss} \tag{F.2}$$

thus

$$d\dot{W} + d\dot{W}_{diss} + d\dot{Q} = \dot{m}\ (dh + V\ dV + g\ dz) \tag{F.3}$$

The dissipation work and the heat transfer occur as the fluid moves from the pump suction side to the pump pressure side, causing an increase in the internal energy together with a volume change of the fluid, where

$$d\dot{W}_{diss} + d\dot{Q} = \dot{m}\ \left(du + p\ d\left(\frac{1}{\rho}\right)\right) \tag{F.4}$$

The change of the specific internal energy can be written as a function of the change in specific enthalpy

$$du = dh - d\left(\frac{p}{\rho}\right) = dh - pd\left(\frac{1}{\rho}\right) - \frac{dp}{\rho} \tag{F.5}$$

$$du + p\ d\left(\frac{1}{\rho}\right) = dh - \frac{dp}{\rho} \tag{F.6}$$

Substituting Equation F.6 into Equation F.4

$$d\dot{W}_{diss} + d\dot{Q} = \dot{m}\,\left(dh - \frac{dp}{\rho}\right) \tag{F.7}$$

Then, substituting Equation F.7 into Equation F.3

$$d\dot{W} + \dot{m}\,\left(dh - \frac{dp}{\rho}\right) = \dot{m}\,\left(dh + V\ dV + g\ dz\right) \tag{F.8}$$

$$d\dot{W} = \dot{m}\,\left(\left(\frac{dp}{\rho}\right) + V\ dV + g\ dz)\right) \tag{F.9}$$

When considering the mixture flow, determining the compression of each phase separately, Equation F.9 can be written as

$$d\dot{W} = \dot{m}_w\,\left(\frac{dp_w}{\rho_w}\right) + \dot{m}_a\,\left(\frac{dp_a}{\rho_a}\right) + \dot{m}_t\ V\ dV + \dot{m}_t\ g\ dz \tag{F.10}$$

By dividing Equation F.10 by the total mass flow rate ($\dot{m}_t$)

$$d\Upsilon = (1 - \dot{\mu})\,\left(\frac{dp_w}{\rho_w}\right) + \dot{\mu}\,\left(\frac{dp_a}{\rho_a}\right) + V\ dV + g\ dz \tag{F.11}$$

$$d\Upsilon = (1 - \dot{\mu})\,\left(\frac{dp_w}{\rho_w}\right) + \dot{\mu}RT\,\left(\frac{dp_a}{p_a}\right) + V\ dV + g\ dz \tag{F.12}$$

Integrating Equation F.12 assuming isontropic compression for the air phase

$$\Upsilon = \frac{1 - \dot{\mu}}{\rho_w}\,(p_D - p_S) + \dot{\mu}RT\ \ln\left(\frac{p_D}{p_S}\right) + \frac{1}{2}\,\left({V_D}^2 - {V_S}^2\right) + g\,(z_D - z_S) \tag{F.13}$$

G Introduction to turbulence modeling

Though turbulence modeling is a very broad topic, a short introduction is given here concerning the basic formulation of the different turbulence models applied in Chapter 6.
In an adiabatic flow system, the average flow properties of a fluid can be obtained by mass conservation (Equation G.14) and momentum equations (Equation G.15); called Reynolds-Averaged Navier-Stokes equation (RANS) [116].

$$\frac{\partial \rho}{\partial t} + \nabla.(\rho\overline{\mathbf{v}}) = 0 \tag{G.14}$$

$$\frac{\partial(\rho\overline{\mathbf{v}})}{\partial t} + \nabla.(\rho\overline{\mathbf{v}} \times \overline{\mathbf{v}}) = -\nabla.\overline{p}\mathbf{I} + \nabla.(\overline{\mathbf{T}} + \mathbf{T}_{RANS}) + \mathbf{f}_b \tag{G.15}$$

where ρ is density, $\overline{\mathbf{v}}$ is mean velocity, $\overline{p}$ is mean pressure, $\mathbf{I}$ is identity tensor, $\overline{\mathbf{T}}$ is mean viscous stress tensor, $\mathbf{T}_{RANS}$ is Reynolds-stress tensor, $\mathbf{f}_b$ is resultant of body forces. The basic function of turbulence models is to appropriately model the Reynolds stresses ($\mathbf{T}_{RANS}$) resulting from Reynolds averaging. Generally, turbulence models can be classified as first-order models including one-equation (Spalart-Allmaras) or two-equation models ($k-\epsilon$ and $k-\omega$), and second-order models (Reynolds stress model; RSM). All first-order models are based on the Boussinesq eddy viscosity hypothesis, which means that the Reynolds stress tensor (τ_{ij}) is proportionally related to the mean strain rate tensor (velocity gradients) through an empirical turbulent viscosity (μ_t). It can be mathematically expressed as given by Equation G.16.

$$\mathbf{T}_{RANS} = 2\,\mu_t\,\mathbf{S} - \frac{2}{3}\rho(\mu_t\nabla.\overline{\mathbf{v}})\mathbf{I} \tag{G.16}$$

where $\mathbf{S}$ is mean rate of the strain tensor.

Spalart-Allamaras model

Spalart-Allamaras model is a simple one-equation model, which was specifically developed for aerospace applications. It solves a transport equation for the turbulence field variable $\tilde{\nu}$ or modified diffusivity [116], as given by Equation (G.17). The eddy viscosity is estimated by Equation (G.18).

$$\frac{\partial(\rho\tilde{\nu})}{\partial t} + \nabla.(\rho\tilde{\nu}\overline{\mathbf{v}}) = \frac{1}{\sigma_{\tilde{\nu}}}\nabla\left[(\mu + \rho\tilde{\nu})\nabla\tilde{\nu}\right] + P_{\tilde{\nu}} + S_{\tilde{\nu}} \tag{G.17}$$

$$\mu_t = \rho f_{\nu 1}\tilde{\nu} \tag{G.18}$$

where $P_{\tilde{\nu}}$ is a production term including diffusion, turbulence production and dissipation, and $S_{\tilde{\nu}}$ is a user-specified source term.

Realizable $k - \epsilon$ model

By definition, two-equation models include two extra transport equations to represent the turbulent properties of the flow. This allows a two-equation model to account for history effects like convection and diffusion of turbulent energy. The realizable $k - \epsilon$ model contains two equations for the turbulent kinetic energy (k) and the turbulence dissipation rate (ϵ), as defined by Equation (G.19) and Equation (G.20), respectively. In these equations, μ is the dynamic viscosity, P is the turbulence production, C and σ are model coefficients, and S is a user-specified source term. The realizable $k-\epsilon$ model is an improved version of the standard $k - \epsilon$ model, since it accounts additionally for certain mathematical constraints concerning Reynolds stresses, in accordance with the turbulence physics [138]. Therefore, the realizable $k - \epsilon$ can more accurately predict jet, separated and recirculating flows compared to the standard $k - \epsilon$ [122], sometimes also better than the $k - \omega$ SST model [123]. The eddy viscosity is modeled using a critical coefficient C_μ, which is expressed as a function of mean flow and turbulence properties, as given by Equation (G.21).

$$\frac{\partial(\rho k)}{\partial t} + \nabla.(\rho k \overline{\mathbf{v}}) = \nabla.\left[(\mu + \frac{\mu_t}{\sigma_k})\nabla k\right] + P_k - \rho(\epsilon - \epsilon_0) + S_k \tag{G.19}$$

$$\frac{\partial(\rho \epsilon)}{\partial t} + \nabla(\rho \epsilon \overline{\mathbf{v}}) = \nabla.\left[(\mu + \frac{\mu_t}{\sigma_\epsilon})\nabla \epsilon\right] + S_\epsilon + \frac{1}{T_e}C_{\epsilon 1}P_\epsilon - C_{\epsilon 2}f_2\rho\left(\frac{\epsilon}{T_e} - \frac{\epsilon_0}{T_0}\right) \tag{G.20}$$

$$\mu_t = \rho C_\mu f_\mu k T \tag{G.21}$$

where T is the turbulent time scale, f_μ is damping function and ϵ_0 is ambient turbulence value.

$k - \omega$ SST model

In contrary to the standard $k - \omega$ model, which is sensitive to inlet free stream turbulence properties, SST model uses $k-\epsilon$ model in the free stream and blends with a $k-\omega$ formulation in the boundary layer [120]. Similarly, this model attempts to predict turbulence by two partial differential equations for the turbulence kinetic energy (k) and the specific rate of dissipation (ω), as given below by Equation (G.22) and Equation (G.23), respectively, where t is turbulent time scale and k_0, ω_0 are ambient turbulence values.

$$\frac{\partial(\rho k)}{\partial t} + \nabla.(\rho k \overline{\mathbf{v}}) = \nabla.[(\mu + \sigma_k \mu_t)\nabla k] + P_k - \rho\beta^* f_{\beta^*}(\omega k - \omega_0 k_0) + S_k \tag{G.22}$$

$$\frac{\partial(\rho \omega)}{\partial t} + \nabla.(\rho \omega \overline{\mathbf{v}}) = \nabla.[(\mu + \sigma_\omega \mu_t)\nabla \omega] + P_\omega - \rho\beta f_\beta(\omega^2 - \omega_0^2) + S_\omega \tag{G.23}$$

where β^*, σ_ω, and σ_k are model coefficients, f_β is a shear modification factor, f_{β^*} is a vortex stretching modification factor, P_ω and P_k are the turbulence production terms, S_ω and S_k are a user-specified source terms, and ω_0 and k_0 are ambient turbulence values that counteract turbulence decay. Finally, the eddy viscosity is determined by Equation (G.24).

$$\mu_t = \rho k T \tag{G.24}$$

Reynolds stress model (RSM)

Reynolds stress model (RSM) is a second-order closure model, which is potentially the most general of all classical turbulence models [138]. Unlike two-equation models, this model solves for 6 additional equations that account for normal and shear stresses in all directions (Equation G.25). The inherent nature of these stress transport equation will automatically accommodate the turbulence anisotropy and streamline curvature. Additionally, one more equation for isotropic turbulent dissipation is solved. This model is assumed to be the most accurate RANS model from which one can accurately describe the physics of all mean flow properties and Reynolds stresses. However, the use of transport equations for all Reynolds stresses makes this model computationally far more expensive and less stable than first-order models.

$$\frac{\partial(\rho \mathbf{R})}{\partial t} + \nabla.(\rho \mathbf{R} \overline{\mathbf{v}}) = \nabla.\mathbf{D} + \mathbf{P} + \mathbf{G} - \frac{2}{3}\rho \mathbf{I} \gamma_M + \phi + \varepsilon + \mathbf{S}_R \tag{G.25}$$

where $textbfR$ is Reynolds stress tensor; $\mathbf{D}$ is Reynolds stress diffusion, ϕ is pressure strain tensor, $\mathbf{P}$ and $\mathbf{G}$ are turbulence and buoyancy production respectively, ε is turbulent dissipation rate tensor, γ_M is dilatation in dissipation, S_R is user specified source. Detailed formulations for each model can be found in Star-CCM+ guide [116].

H Pump simulations from a companion study at Bochum university

In this Appendix, corresponding numerical results of the pump impellers obtained in a companion study at Bochum University are presented and discussed. The 3D CFD simulations of the pump involve single and two-phase flow conditions, considering also the closed impeller and semi-open impeller with the standard gap. The gas accumulations on the impeller blades are obtained by the simulations and are compared to experimental data of some cases of the detailed optical measurements shown in Section 5.9. This section is based on recent publications in 13th the European Conference on Turbomachinery Fluid dynamics & Thermodynamics, and in the 4th International Rotating Equipment Conference [134, 139].

Numerical modeling

All details concerning the numerical set-up can be found in [95, 133, 134]. They are only summarized briefly here. The commercial CFD-solver ANSYS CFX 18.0 was utilized to solve the unsteady Reynolds-averaged Navier-Stokes (URANS) equations. The $k-\omega$ shear stress transport (SST) turbulence model (Menter (1994) [120]) was used to model the turbulence, together with an automatic wall treatment (Menter et al., 2003 [140]). Concerning the gas phase, a monodisperse two-phase model (constant bubble diameter) was employed, considering 3 different values for the bubble diameter. Therefore, in these simulations, the bubble interaction and bubble size distributions are neglected. To stabilize the solver, both the water and air phases were considered as incompressible [95]. Giving that the drag force dominates all other interfacial forces, all non-drag forces were neglected. The drag force was modeled using the Schiller-Naumann drag law [141]. Second-order discretization in space and time is applied. Additionally, two time step sizes were set, i.e. 1° (Coarse) and 0.5° (Fine), with a maximum of 5 inner iterations. The model geometry involves the whole pump, including the suction and discharge pipes, side chambers, 360°-impeller and volute, as can be shown in Figure H.8.

Two hexahedral grids (coarse and fine) were generated using the commercial software ICEM CFD 18.0, with resolutions of 0.7 and 5.6 million cells. Time-averaged values of the pump head H of the last revolution were calculated, after ensuring that the changes of the time-average pump head are lower than 1% over the last three revolutions. The pump head was calculated in the same way as in the measurements, where the static pressure was determined by the arithmetic average of four pressure ports in the suction and pressure pipes, respectively so that the pump head is calculated by:

$$H = \frac{\frac{\sum_{i=1}^{4} p_{D,i}}{4} - \frac{\sum_{i=1}^{4} p_{S,i}}{4}}{g\rho_w} \tag{H.26}$$

The simulation and the experimental results of single-phase flow are compared in Figure H.9, considering the two grid resolutions and the two impellers. As shown, the agreement between the simulations and experiments is overall acceptable. However, the simulations generally underestimate the experiments with an increasing error from part-load to overload, due to

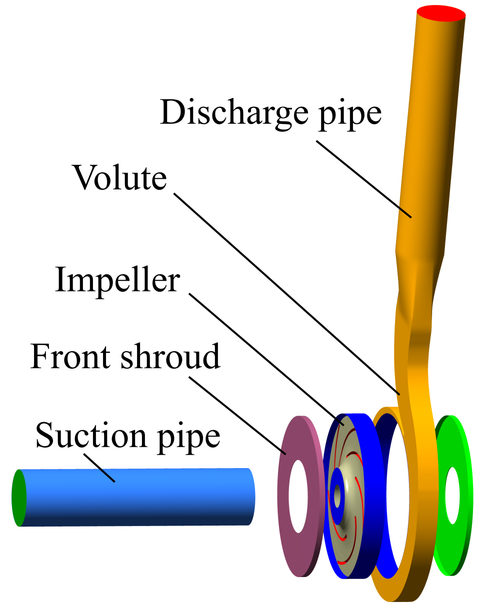

Figure H.8: Illustration of the numerical domain of the pump (adapted from [134]).

Table B.3: Relative errors in dimensionless head between simulations and experiments.

	Relative error in dimensionless single-phase pump head			
	Close Impeller		Semi-open impeller	
	Coarse mesh	Fine mesh	with standard gap	Fine mesh
Part-Load	1.80%	1.63%	4.60%	6.98%
Optimal conditions	4.70%	5.32%	5.95%	8.63%
Overload	12.78%	8.11%	23.34%	14.59%

the increased flow velocity and the associated flow separation at overload conditions. Due to the complex secondary flow that occurs across the tip clearance gap, the simulations of semi-open impeller involve higher errors. The relative errors are shown in details in Table B.3. Further, the numerical results of both grids are comparable with slightly bigger deviations in overload conditions, confirming that the solution of the coarse grid can be considered as grid-independent.

Figure H.10 shows the gas volume fraction of the simulation at midspan of the impellers, considering various bubble diameter, in comparison to the time-averaged detailed optical experiments. As shown, considering the monodisperse model, the bubble diameter has a very significant influence on the simulation results. For $d_B = 0.5$ mm and $d_B = 1.0$ mm, the simulation results of the gas accumulation are to some extent comparable to the experiments. However, the simulations neither can accurately predict the gas accumulation size nor its location for most considered cases. Nevertheless, for the semi-open impeller (last row in Figure H.10), considering a bubble diameter of $d_B = 1.0$ mm and a gas volume fraction of $\varepsilon = 5\%$, the gas accumulation is in a good agreement with the experiments in terms of size and location, where the accumulation appears correctly on the suction side of the blades.

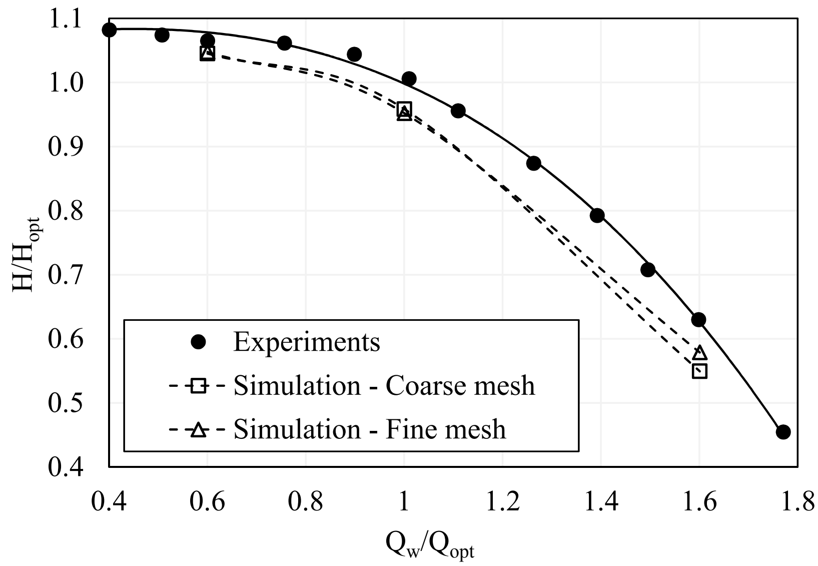

(a) Closed impeller

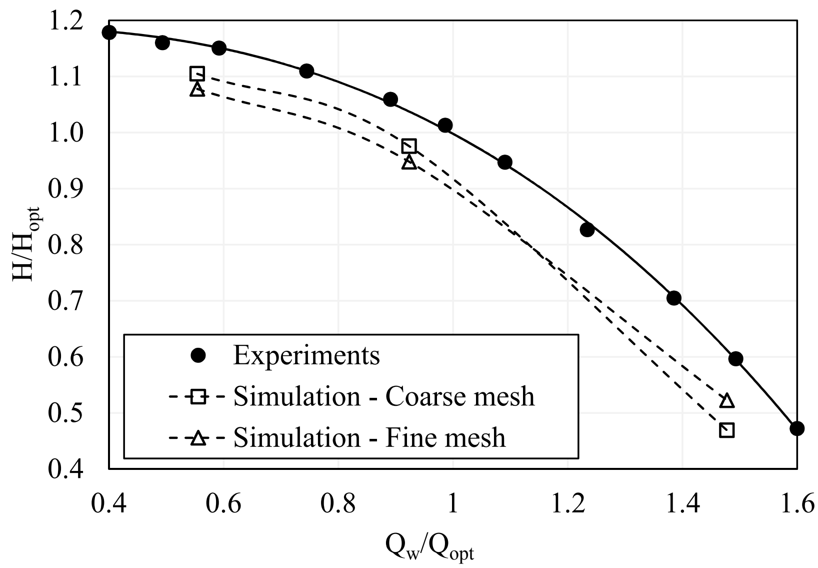

(b) Semi-open impeller with standard gap

Figure H.9: Comparison between experiments and simulations in terms of dimensionless single-phase pump head (adapted from [134]).

Considering now a bubble diameter of $d_B = 2.0$ mm, the simulations evidently overestimate the gas accumulation. Overall, these results confirm that the monodisperse model can only qualitatively capture the two-phase flow behavior. For accurate quantitative predictions, more advanced simulations are needed, considering (1) a polydisperse model for the bubble diameters, (2) corresponding bubble interactions, (3) the compressibility of the gas phase and (4) second-order turbulence models such as Reynolds stress transport model. Additionally, the presented comparisons highlight the importance of the recorded flow images and the averaged two-phase regimes obtained in this thesis.

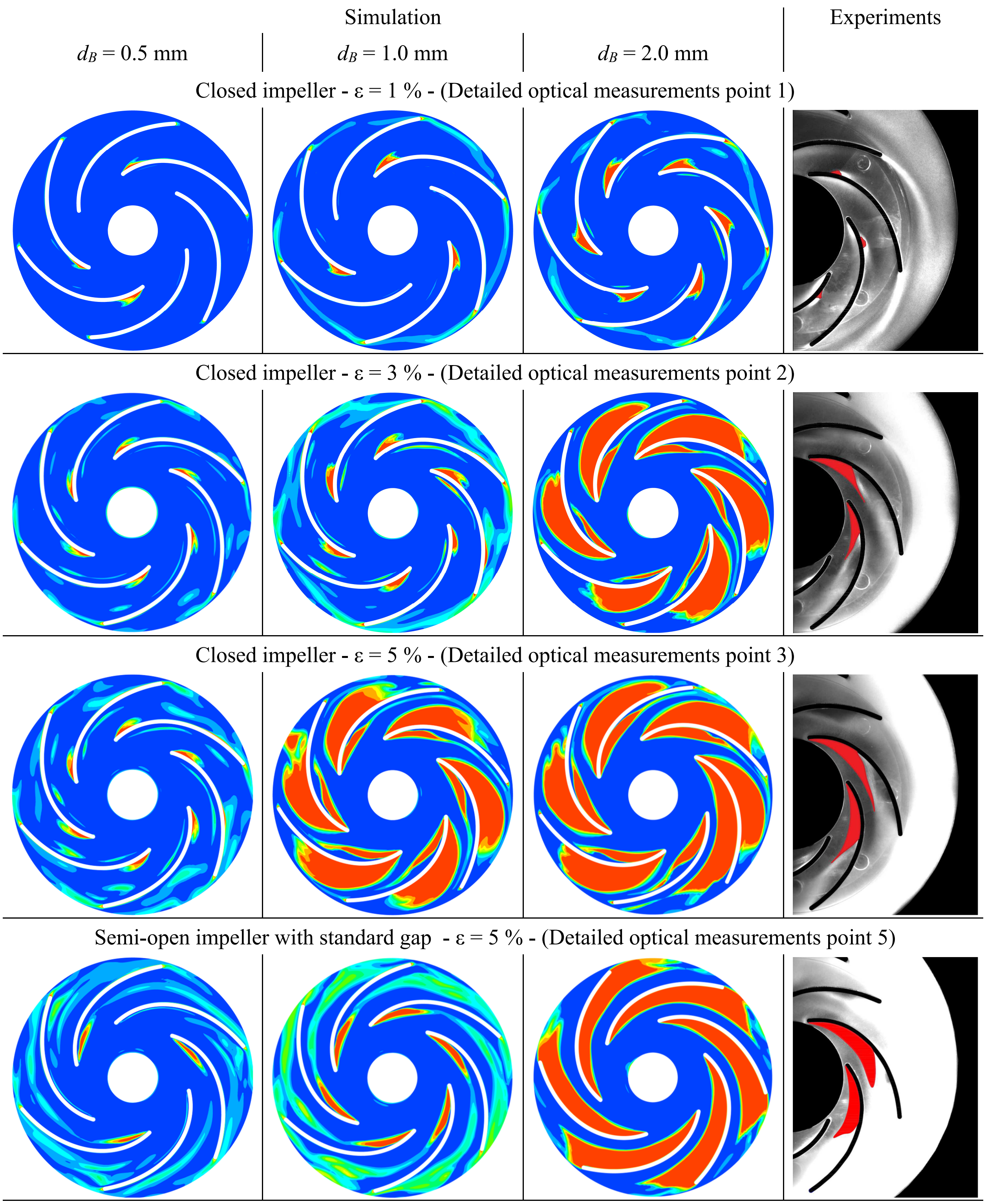

Figure H.10: Gas volume fraction contourplot (blue is continuous water, and red is air accumulation) at midspan of closed impeller and semi-open impeller with standard gap for different bubble diameters compared to detailed optical experiments (adapted from [134]).

Bibliography

[1] M. Ishii and T. Hibiki. *Thermo-fluid dynamics of two-phase flow.* Springer US, Boston, M. A., 2006.

[2] C. E. Brennen. *Fundamentals of multiphase flow.* Cambridge university press, 2005.

[3] L. Cheng, G. Ribatski, and J. R. Thome. Two-phase flow patterns and flow-pattern maps: fundamentals and applications. *Appl. Mech. Rev.*, 61(5):050802, 2008.

[4] R. Kong and S. Kim. Characterization of horizontal air–water two-phase flow. *Nucl. Eng. Des.*, 312:266–276, 2017.

[5] J. Weisman. Two-phase flow patterns. In *Handbook of fluids in motion*, chapter 15, pages 409–425. Butterworth Publishers Woburn, MA, USA, 1983.

[6] M. E. Ewing, J. J. Weinandy, and R. N. Christensen. Observations of two-phase flow patterns in a horizontal circular channel. *Heat Transf. Eng.*, 20(1):9–14, 1999.

[7] Y. Wibisono, E. R. Cornelissen, A. J. B. Kemperman, W. G. J. Van Der Meer, and K. Nijmeijer. Two-phase flow in membrane processes: A technology with a future. *J. Membr. Sci.*, 453:566–602, 2014.

[8] I. Y. Chen, C. Y. Tseng, Y. T. Lin, and C. C. Wang. Two-phase flow pressure change subject to sudden contraction in small rectangular channels. *Int. J. Multiph. Flow*, 35(3):297–306, 2009.

[9] A. Sharma, V. V. Tyagi, C. R. Chen, and D. Buddhi. Review on thermal energy storage with phase change materials and applications. *Renew. Sust. Energy Rev.*, 13(2):318–345, 2009.

[10] J. Caridad, M. Asuaje, F. Kenyery, A. Tremante, and O. Aguillón. Characterization of a centrifugal pump impeller under two-phase flow conditions. *J. Pet. Sci. Eng.*, 63(1-4):18–22, 2008.

[11] Z. Zhu, P. Xie, G. Ou, B. Cui, and Y. Li. Design and experimental analyses of small-flow high-head centrifugal-vortex pump for gas-liquid two-phase mixture. *Chinese J. Chem. Eng.*, 16(4):528–534, 2008.

[12] A. Amoresano, G. Langella, V. Niola, and G. Quaremba. Advanced image analysis of two-phase flow inside a centrifugal pump. *Adv. Mech. Eng.*, 6:1–11, 2014.

[13] A. M. C. Chan, M. Kawaji, H. Nakamura, and Y. Kukita. Experimental study of two-phase pump performance using a full size nuclear reactor pump. *Nucl. Eng. Des.*, 193(1-2):159–172, 1999.

[14] A. Poullikkas. Effects of two-phase liquid-gas flow on the performance of nuclear reactor cooling pumps. *Prog. Nucl. Energy*, 42(1):3–10, 2003.

[15] A. Campo and E. A. Chisely. Experimental characterization of two-phase flow centrifugal pumps. In *ASME 2010 Power Conference*, pages 803–816. American Society of Mechanical Engineers, 2010.

[16] A. Poullikkas. *Two phase flow and cavitation in centrifugal pump: A theoretical and experimental investigation.* PhD thesis, Loughborough University, 1992.

[17] J. J. Manzano-Ruiz. *Experimental and theoretical study of two-phase flow in centrifugal pumps.* PhD thesis, Massachusetts Institute of Technology, 1980.

[18] G. R. Noghrehkar, M. Kawaji, A. M. C. Chan, H. Nakamura, and Y. Kukita. Investigation of centrifugal pump performance under two-phase flow conditions. *J. Fluids Eng.*, 117(1):129–137, 1995.

[19] W. Aziz, S. K. Chaturvedi, and A. Kheireddine. Thermodynamic analysis of two-component, two-phase flow in solar collectors with application to a direct-expansion solar-assisted heat pump. *Energy*, 24(3):247–259, 1999.

[20] M. W. Wambsganss, J. A. Jendrzejczyk, D. M. France, and N. T. Obot. Frictional pressure gradients in two-phase flow in a small horizontal rectangular channel. *Exp. Therm. Fluid Sci.*, 5(1):40–56, 1992.

[21] C. Vallée, T. Höhne, H. Prasser, and T. Sühnel. Experimental investigation and CFD simulation of horizontal stratified two-phase flow phenomena. *Nucl. Eng. Des.*, 238(3):637–646, 2008.

[22] Y. Chen, C. C. Liu, K. H. Chien, and C. C. Wang. Two-phase flow characteristics across sudden expansion in small rectangular channels. *Exp. Therm. Fluid Sci.*, 32(2):696–706, 2007.

[23] F. F. Abdelall, G. Hahn, S. M. Ghiaasiaan, S. I. Abdel-Khalik, S. S. Jeter, M. Yoda, and D. L. Sadowski. Pressure drop caused by abrupt flow area changes in small channels. *Exp. Therm. Fluid Sci.*, 29(4):425–434, 2005.

[24] W. H. Ahmed, C. Y. Ching, and M. Shoukri. Development of two-phase flow downstream of a horizontal sudden expansion. *Int. J. Heat Fluid Flow*, 29(1):194–206, 2008.

[25] S. Anupriya and S. Jayanti. Experimental and modelling studies of gas–liquid vertical annular flow through a diverging section. *Int. J. Multiph. Flow*, 67:180–190, 2014.

[26] J. J. Hwang, F. G. Tseng, and C. Pan. Ethanol-CO_2 two-phase flow in diverging and converging microchannels. *Int. J. Multiph. flow*, 31(5):548–570, 2005.

[27] J. Gamboa and M. Prado. Review of electrical-submersible-pump surging correlation and models. *SPE Prod. Oper.*, 26(04):314–324, 2011.

[28] J. Zhu, X. Guo, F. Liang, and H. Q. Zhang. Experimental study and mechanistic modeling of pressure surging in electrical submersible pump. *J. Nat. Gas Sci. Eng.*, 45:625–636, 2017.

[29] W. M. Verde, J. L. Biazussi, N. A. Sassim, and A. C. Bannwart. Experimental study of gas-liquid two-phase flow patterns within centrifugal pumps impellers. *Exp. Therm. Fluid Sci.*, 85:37–51, 2017.

[30] P. Tillack. *Förderverhalten von Kreiselpumpen bei viskosen, gasbeladenen Flüssigkeiten*. PhD thesis, Technische Universität Kaiserslautern, 1998.

[31] M. Sauer. *Einfluss der Zuströmung auf das Förderverhalten von Kreiselpumpen radialer Bauart bei Flüssigkeits-/Gasförderung*. PhD thesis, Technische Universität Kaiserslautern, 2003.

[32] M. Mansour, B. Wunderlich, and D. Thévenin. Experimental study of two-phase air/water flow in a centrifugal pump working with a closed or a semi-open impeller. In *ASME Turbo Expo 2018: Turbomachinery Technical Conference and Exposition*, page V009T27A012. American Society of Mechanical Engineers, 2018.

[33] Q. Si, G. Bois, Q. Jiang, W. He, A. Ali, and S. Yuan. Investigation on the handling ability of centrifugal pumps under air–water two-phase inflow: model and experimental validation. *Energies*, 11(11):3048, 2018.

[34] Q. Si, G. Bois, K. Zhang, and S. Yuan. Air-water two-phase flow experimental and numerical analysis in a centrifugal pump. In *Proceedings of 12th European Conference on Turbomachinery Fluid Dynamics and Thermodynamics, ETC*, volume 12, 2017.

[35] Sulzer Pumps. *Sulzer centrifugal pump handbook*. Elsevier, 2013.

[36] A. R. Budris and P. A. Mayleben. Effects of entrained air, NPSH margin, and suction piping on cavitation in centrifugal pumps. In *Proceedings of the 15th International Pump Users Symposium*. Texas A&M University. Turbomachinery Laboratories, 1998.

[37] R. Beltur. Experimental investigation of two-phase flow performance of ESP stages. Master's thesis, University of Tulsa, Department of Petroleum Engineering, Tulsa, Oklahoma, USA, 2003.

[38] C. A. Cappellino, D. R. Roll, and G. Wilson. Design considerations and application guidelines for pumping liquids with entrained gas using open impeller centrifugal pumps. In *Proceedings of the 9th International Pump Users Symposium*, pages 262–264. Turbomachinery Laboratories, Department of Mechanical Engineering, Texas A&M University, 1992.

[39] R. Cirilo. *Air-water flow through electric submersible pumps*. PhD thesis, University of Tulsa, Department of Petroleum Engineering, Tulsa, Oklahoma, USA, 1998.

[40] B. Schiavello. *Two-phase flow rotodynamic pumps-experiments and design criteria*. Number 7133. Worthing ton Simson Ltd, 1986.

[41] J. F. Gülich. *Centrifugal pumps*. Springer, 2008.

[42] F. E. Trevisan. *Modeling and visualization of air and viscous liquid in electrical submersible pump*. PhD thesis, University of Tulsa, Department of Petroleum Engineering, Tulsa, Oklahoma, USA, 2009.

[43] F. E. Trevisan and M. Prado. Experimental investigation of the viscous effect on two-phase-flow patterns and hydraulic performance of electrical submersible pumps. *J. Can. Pet. Technol.*, 50(04):45–52, 2011.

[44] H. M. Banjar, J. Gamboa, and H. Q. Zhang. Experimental study of liquid viscosity effect on two-phase stage performance of electrical submersible pumps. In *SPE Annual Technical Conference and Exhibition*. Society of Petroleum Engineers, 2013.

[45] G. M. Paternost, A. C. Bannwart, and V. Estevam. Experimental study of a centrifugal pump handling viscous fluid and two-phase flow. *SPE Prod. Oper.*, 30(02):146–155, 2015.

[46] A. J. Stepanoff. *Pumps and blowers: Two-phase flow*. J. Wiley & sons, 1965.

[47] J. L. Turpin, J. F. Lea, and J. L. Bearden. Gas-liquid flow through centrifugal pumps - correlation of data. In *Proceedings of the 3rd International Pump Symposium*, pages 13–20. Turbomachinery Laboratories, Department of Mechanical Engineering, Texas A&M University, 1986.

[48] J. Gamboa. *Prediction of the transition in two-phase performance of an electrical submersible pump*. PhD thesis, University of Tulsa, Department of Petroleum Engineering, Tulsa, Oklahoma, USA, 2008.

[49] J. Zhu, H. Zhu, J. Zhang, and H. Q. Zhang. An experimental study of surfactant effect on gas tolerance in electrical submersible pump (ESP). In *ASME 2017 International Mechnical Engineering Congress Exposition*, pages V007T09A038–V007T09A038. American Society of Mechanical Engineers, 2017.

[50] L. Barrios. *Visualization and modeling of multiphase performance inside an electrical submersible pump*. PhD thesis, University of Tulsa, Department of Petroleum Engineering, Tulsa, Oklahoma, USA, 2007.

[51] L. Barrios and M. G. Prado. Experimental visualization of two-phase flow inside an electrical submersible pump stage. *J. Energy Resour. Technol.*, 133(4):042901, 2011.

[52] J. Zhang, S. Cai, Y. Li, H. Zhu, and Y. Zhang. Visualization study of gas–liquid two-phase flow patterns inside a three-stage rotodynamic multiphase pump. *Exp. Therm. Fluid Sci.*, 70:125–138, 2016.

[53] C. Shao, C. Li, and J. Zhou. Experimental investigation of flow patterns and external performance of a centrifugal pump that transports gas-liquid two-phase mixtures. *Int. J. Heat Fluid Flow*, 71:460–469, 2018.

[54] T. Schäfer, A. Bieberle, M. Neumann, and U. Hampel. Application of gamma-ray computed tomography for the analysis of gas holdup distributions in centrifugal pumps. *Flow Meas. Instrum.*, 46:262–267, 2015.

[55] M. Neumann, T. Schäfer, A. Bieberle, and U. Hampel. An experimental study on the gas entrainment in horizontally and vertically installed centrifugal pumps. *J. Fluids Eng.*, 138(9):91301, 2016.

[56] M. Murakami, K. Minemura, and M. Takimoto. Effects of entrained air on the performance of centrifugal pumps under cavitating conditions. *Bull. JSME*, 23(183):1435–1442, 1980.

[57] M. Murakami and K. Minemura. Effects of entrained air on the performance of a centrifugal pump: 1st report, performance and flow conditions. *Bull. JSME*, 17(110):1047–1055, 1974.

[58] K. Sekoguchi, S. Takada, and Y. Kanemori. Study of air-water two-phase centrifugal pump by means of electric resistivity probe technique for void fraction measurement: 1st report, measurement of void fraction distribution in a radial flow impeller. *Bull. JSME*, 27(227):931–938, 1984.

[59] S. Sato, A. Furukawa, and Y. Takamatsu. Air-water two-phase flow performance of centrifugal pump impellers with various blade angles. *JSME Int. J. Ser. B Fluids Therm. Eng.*, 39(2):223–229, 1996.

[60] J. Zhu. *Experiments, CFD simulation and modeling of ESP performance under gassy conditions*. PhD thesis, University of Tulsa, Department of Petroleum Engineering, Tulsa, Oklahoma, USA, 2017.

[61] M. Murakami and K. Minemura. Effects of entrained air on the performance of centrifugal pumps: 2nd report, effects of number of blades. *Bull. JSME*, 17(112):1286–1295, 1974.

[62] H. Merry. Effects of two-phase liquid/gas flow on the performance of centrifugal pumps. In *Pumps compressors offshore oil gas, IMechE Conf. C130/76*, page 61, 1976.

[63] A. Furukawa, T. Kuwano, and K. Okuma. Air-water two-phase flow performance of centrifugal pump with tandem circular cascades. In *Proceding of JSME ICFE*, number 97-811, pages 479–484, 1997.

[64] A. Furukawa, S. Shirasu, and S. Sato. Experimental study of gas-liquid two-phase flow pumping action of centrifugal impeller. *ASME-PUBLICATIONS-FED*, 226:89–96, 1995.

[65] A. Serena. *A multiphase pump experimental analysis.* PhD thesis, Norwegian University of Science and Technology, 2016.

[66] M. Romero. An evaluation of an electrical submersible pumping system for high GOR wells. Master's thesis, University of Tulsa, Department of Petroleum Engineering, Tulsa, Oklahoma, USA, 1999.

[67] J. Duran and M. G. Prado. ESP stages air–water two-phase performance—modeling and experimental data. SPE 120628. In *SPE ESP Workshop, Houston, Texas*, pages 28–30, 2004.

[68] S. Zakem. Determination of gas accumulation and two-phase slip velocity ratio in a rotating impeller. In *Polyphase Flow and Transportation Technology, Proceedings of the ASME Century 2 Emerging Technology Conference, San Francisco, New York, NY, USA*, page 167–173. American Society of Mechanical Engineers, 1980.

[69] O. Furuya. An analytical model for prediction of two-phase (noncondensable) flow pump performance. *J. Fluids Eng.*, 107(1):139–147, 1985.

[70] R. Sachdeva. *Two-phase flow through electric submersible pumps.* PhD thesis, University of Tulsa, Department of Petroleum Engineering, Tulsa, Oklahoma, USA, 1988.

[71] R. Sachdeva, D. R. Doty, and Z. Schmidt. Performance of electric submersible pumps in gassy wells. *SPE Prod. Facil.*, 9(01):55–60, 1994.

[72] K. Minemura, T. Uchiyama, S. Shoda, and K. Egashira. Prediction of air-water two-Phase flow performance of a centrifugal pump based on one-dimensional two-fluid model. *J. Fluids Eng.*, 120(2):327–334, 1998.

[73] D. Sun. *Modeling gas-liquid head performance of electrical submersible pumps.* PhD thesis, University of Tulsa, Department of Petroleum Engineering, Tulsa, Oklahoma, USA, 2003.

[74] D. Sun and M. Prado. Modeling gas-liquid head performance of electrical submersible pumps. *J. Pressure Vessel Technol.*, 127(1):31, 2005.

[75] J. Zhu and H. Q. Zhang. Mechanistic modeling and numerical simulation of in-situ gas void fraction inside ESP impeller. *J. Nat. Gas Sci. Eng.*, 36:144–154, 2016.

[76] J. Zhu, J. Zhang, H. Zhu, and H. Q. Zhang. A mechanistic model to predict flow pattern transitions in electrical submersible pump under gassy flow condition. In *SPE Artificial Lift Conference and Exhibition-Americas*. Society of Petroleum Engineers, 2018.

[77] J. Duran. Pressure effects on ESP stages air-water performance. Master's thesis, University of Tulsa, Department of Petroleum Engineering, Tulsa, Oklahoma, USA, 2003.

[78] L. C. Zapata. Rotational speed effects on ESP two-phase performance. Master's thesis, University of Tulsa, Department of Petroleum Engineering, Tulsa, Oklahoma, USA, 2003.

[79] D. Croba and J. L. Kueny. Numerical calculation of 2D, unsteady flow in centrifugal pumps: impeller and volute interaction. *Int. J. Numer. Methods Fluids*, 22(6):467–481, 1996.

[80] J. González, J. Fernández, E. Blanco, and C. Santolaria. Numerical simulation of the dynamic effects due to impeller-volute interaction in a centrifugal pump. *J. Fluids Eng.*, 124(2):348–355, 2002.

[81] M. Jarkowski, M. A. Woodgate, G. N. Barakos, and J. Rokicki. Towards consistent hybrid overset mesh methods for rotorcraft CFD. *Int. J. Numer. Meth. Fl.*, 74(8):543–576, 2014.

[82] H. Ding, F. C. Visser, Y. Jiang, and M. Furmanczyk. Demonstration and validation of a 3D CFD simulation tool predicting pump performance and cavitation for industrial applications. *J. Fluids Eng.*, 133(1):11101–11114, 2011.

[83] J. L. Parrondo-Gayo, J. Gonzalez-Perez, and J. Fernández-Francos. The effect of the operating point on the pressure fluctuations at the blade passage frequency in the volute of a centrifugal pump. *J. Fluids Eng.*, 124(3):784–790, 2002.

[84] F. Gu and M. Cave. A numerical investigation on the volute/diffuser interaction due to the axial distortion at the impeller exit. *J. Fluids Eng.*, 123(3):475–483, 2001.

[85] R. W. Westra, L. Broersma, K. van Andel, and N. P. Kruyt. PIV measurements and CFD computations of secondary flow in a centrifugal pump impeller. *J. Fluids Eng.*, 132(6):061104, 2010.

[86] C. D. P. Maitelli, F. V. M. Bezerra, and W. Mata. Simulation of flow in a centrifugal pump of ESP systems using computational fluid dynamics. *Braz. J. Pet. Gas*, 4(1), 2010.

[87] M. H. Shojaeefard, M. Tahani, M. B. Ehghaghi, M. A. Fallahian, and M. Beglari. Numerical study of the effects of some geometric characteristics of a centrifugal pump impeller that pumps a viscous fluid. *Comput. Fluids*, 60:61–70, 2012.

[88] H. Stel, T. Sirino, F. J. Ponce, S. Chiva, and R. E. M. Morales. Numerical investigation of the flow in a multistage electric submersible pump. *J. Pet. Sci. Eng.*, 136:41–54, 2015.

[89] J. Zhu, H. Banjar, Z. Xia, and H. Q. Zhang. CFD simulation and experimental study of oil viscosity effect on multi-stage electrical submersible pump (ESP) performance. *J. Pet. Sci. Eng.*, 146:735–745, 2016.

[90] J. Zhu, H. Zhu, J. Zhang, and H. Q. Zhang. A numerical study on flow patterns inside an electrical submersible pump (ESP) and comparison with visualization experiments. *J. Petrol. Sci. Eng.*, 173:339–350, 2019.

[91] Z. Y. Yu, B. S. Zhu, S. L. Cao, and G. Y. Wang. Application of two-fluid model in the unsteady flow simulation for a multiphase rotodynamic pump. *IOP Conf. Ser.: Mat. Sci. Eng.*, 52(6):062003, 2013.

[92] Z. Yu, B. Zhu, S. Cao, and Y. Liu. Effect of virtual mass force on the mixed transport process in a multiphase rotodynamic pump. *Adv. Mech. Eng*, 6:958352, 2014.

[93] Z. Yu, B. Zhu, and S. Cao. Interphase force analysis for air-water bubbly flow in a multiphase rotodynamic pump. *Eng. Comput.*, 32(7):2166–2180, 2015.

[94] W. Zhang, Z. Yu, and Y. Li. Application of a non-uniform bubble model in a multiphase rotodynamic pump. *J. Petrol. Sci. and Eng.*, 2018.

[95] T. Müller, P. Limbach, and R. Skoda. Numerical 3D RANS simulation of gas-liquid flow in a centrifugal pump with an Euler-Euler two-phase model and a dispersed phase distribution. In *Proceedings of 11th European Conference on Turbomachinery Fluid Dynamics and Thermodynamics, ETC*, Madrid, 2015.

[96] J. Caridad and F. Kenyery. CFD analysis of electric submersible pumps (ESP) handling two-phase mixtures. *J. Energy Resour. Technol.*, 126(2):99–104, 2004.

[97] R. B. Medvitz, R. F. Kunz, D. A. Boger, J. W. Lindau, A. M. Yocum, and L. L. Pauley. Performance analysis of cavitating flow in centrifugal pumps using multiphase CFD: Pump analysis and design. *J. Fluids Eng.*, 124(2):377–383, 2002.

[98] E. Deniz and N. Eskin. Hydrodynamic characteristics of two-phase flow through horizontal pipe having smooth expansion. *ISI Bilim. Ve Tek. Dergisi-Journal Therm. Sci. Technol.*, 35(1):1–9, 2015.

[99] V. G. Kourakos, P. Rambaud, S. Chabane, D. Pierrat, and J. M. Buchlin. Two-phase flow modelling within expansion and contraction singularities. *Comput. Methods Multiph. Flow V*, 63:27–43, 2009.

[100] E. Deniz and N. Eskin. Experimental and numerical investigation of two-phase flow through enlarging singularity. In *Proceedings of Internatonal Refrigeration and Air Conditioning Conference*, pages 1–9, 2012.

[101] N. Eskin and E. Deniz. Pressure drop of two-phase flow through horizontal channel with smooth expansion. In *Proceedings of Internatonal Refrigeration and Air Conditioning Conference*, pages 1–10, 2012.

[102] A. Ahmadpour, S. N. R. Abadi, and R. Kouhikamali. Numerical simulation of two-phase gas–liquid flow through gradual expansions/contractions. *Int. J. Multiph. Flow*, 79:31–49, 2016.

[103] M. Mansour, M. H. Ali, and R. M. Abdel-Maksoud. Experimental study of expansion and compression effects on the stability of Taylor vortex flow. *Fluid Dyn. Res.*, 48(4):045502, 2016.

[104] R. J. Moffat. Describing the uncertainties in experimental results. *Exp. Therm. Fluid Sci.*, 1(1):3–17, 1988.

[105] M. Mansour, P. Kováts, B. Wunderlich, and D. Thévenin. Experimental investigations of a two-phase gas/liquid flow in a diverging horizontal channel. *Exp. Therm. Fluid Sci*, 93:210–217, 2018.

[106] M. S. Bhatti. Turbulent and transition flow convective heat transfer in ducts. *Handb. Single-Phase Convect. Heat Transf.*, 1987.

[107] W. Zhi-qing. Study on correction coefficients of liminar and turbulent entrance region effect in round pipe. *Appl. Math. Mech.*, 3(3):433–446, 1982.

[108] M. Mansour, B. Wunderlich, and D. Thévenin. Effect of tip clearance gap and inducer on the transport of two-phase air-water flows by centrifugal pumps. *Exp. Therm. Fluid Sci*, 99:487–509, 2018.

[109] P. Stephan, S. Kabelac, M. Kind, H. Martin, D. Mewes, and K. Schaber. VDI heat atlas, 2010.

[110] D. Y. Peng and D. B. Robinson. A new two-constant equation of state. *Ind. Eng. Chem. Fund.*, 15(1):59–64, 1976.

[111] G. Soave. Equilibrium constants from a modified Redlich-Kwong equation of state. *Chem. Eng. Sci.*, 27(6):1197–1203, 1972.

[112] X. M. Guo, Z. C. Zhu, G. P. Shi, and Y. Huang. Effects of rotational speeds on the performance of a centrifugal pump with a variable-pitch inducer. *J. Hydrodyn. Ser. B*, 29(5):854–862, 2017.

[113] J. Moore. A wake and an eddy in a rotating, radial-flow passage – Part 1: Experimental observations. *J. Eng. Power*, 95(3):205–212, 1973.

[114] M. Mansour, T. Parikh, S. Engel, B. Wunderlich, and D. Thévenin. Investigation on the influence of an inducer on the transport of single and two-phase air-flows by centrifugal pumps. In *48th Turbomachinery & 35th Pump Symposia*, 2019.

[115] M. Mansour, T. Parikh, S. Engel, and D. Thévenin. Numerical investigations of gas-liquid two-phase flow in a pump inducer. *J. Fluids Eng.*, 142(4):021302, 2019.

[116] Siemens. STAR-CCM+ version 13.02.013 user guide, 2018.

[117] S. Sarkar and L. Balakrishnan. Application of a Reynolds stress turbulence model to the compressible shear layer. In *21st Fluid Dynamics, Plasma Dynamics and Lasers Conference*, page 1465, 1990.

[118] C. G. Speziale, S. Sarkar, and T. B. Gatski. Modelling the pressure–strain correlation of turbulence: an invariant dynamical systems approach. *J. Fluid Mech.*, 227:245–272, 1991.

[119] T. H. Shih, W. W. Liou, A. Shabbir, Z. Yang, and J. Zhu. A new k-ε eddy viscosity model for high Reynolds number turbulent flows. *Comput. Fluids*, 24(3):227–238, 1995.

[120] F. R. Menter. Two-equation eddy-viscosity turbulence models for engineering applications. *AIAA J.*, 32(8):1598–1605, 1994.

[121] P. Spalart and S. Allmaras. A one-equation turbulence model for aerodynamic flows. In *30th Aerospace Sciences Meeting and Exhibit, AIAA paper 1992-439*, 1992.

[122] M. P. Bulat and P. V. Bulat. Comparison of turbulence models in the calculation of supersonic separated flows. *World App. Sci. J.*, 27(10):1263–1266, 2013.

[123] M. M. Rahman, M. M. Karim, and M. A. Alim. Numerical investigation of unsteady flow past a circular cylinder using 2-D finite volume method. *J. Naval Arch. Mar. Eng*, 4(1):27–42, 2007.

[124] G. Katul. An investigation of higher-order closure models for a forested canopy. *Bound-Lay. Meteorol.*, 89(1):47–74, 1998.

[125] R. S. Amano and P. Goel. Computations of turbulent flow beyond backward-facing steps using Reynolds-stress closure. *AIAA J.*, 23(9):1356–1361, 1985.

[126] H. Pineda, J. Biazussi, F. López, B. Oliveira, R. D. M. Carvalho, A. C. Bannwart, and N. Ratkovich. Phase distribution analysis in an electrical submersible pump (ESP) inlet handling water–air two-phase flow using computational fluid dynamics (CFD). *J. Pet. Sci. Eng.*, 139, 2016.

[127] M. García, Y. Sommerer, T. Schönfeld, and T. Poinsot. Evaluation of Euler-Euler and Euler-Lagrange strategies for large-eddy simulations of turbulent reacting flows. In *ECCOMAS thematic conference on computational combustion*, volume 30. Citeseer, 2005.

[128] J. Jeong and F. Hussain. On the identification of a vortex. *J. Fluid Mech.*, 285:69–94, 1995.

[129] M. Mansour, Z. Liu, G. Janiga, K. D. P. Nigam, K. Sundmacher, D. Thévenin, and K. Zähringer. Numerical study of liquid–liquid mixing in helical pipes. *Chem. Eng. Sci.*, 172:250–261, 2017.

[130] M. Mansour, P. Khot, D. Thévenin, K. D. P. Nigam, and K. Zähringer. Optimal Reynolds number for liquid–liquid mixing in helical pipes. *Chem. Eng. Sci.*, In Press, (2018), 2018.

[131] W. Zhang, Z. Yu, and B. Zhu. Numerical study of pressure fluctuation in a gas-liquid two-phase mixed-flow pump. *Energies*, 10(5):634, 2017.

[132] X. Li, S. Yuan, Z. Pan, Y. Li, and W. Liu. Dynamic characteristics of rotating stall in mixed flow pump. *J. Appl. Math.*, 2013, 2013.

[133] T. Müller, P. Limbach, and R. Skoda. Influence of geometry simplifications and numerical parameters in 3D URANS liquid-gas flow simulations of a radial pump with an Eulerian mono-dispersed two-phase model. In *Proceedings of 16th International Symposium on Transport Phenomena and Dynamics of Rotating Machinery*, 2016.

[134] M. Hundshagen, M. Mansour, D. Thévenin, and R. Skoda. Numerical investigation of two-phase air-water flow in a centrifugal pump with closed or semi-open impeller. In *Proceedings of 13th European Conference on Turbomachinery Fluid Dynamics and Thermodynamics, ETC*, 2019.

[135] T. Frank, P. J. Zwart, E. Krepper, H. M. Prasser, and D. Lucas. Validation of CFD models for mono-and polydisperse air–water two-phase flows in pipes. *Nucl. Eng. Des.*, 238(3):647–659, 2008.

[136] Y. Yeh and H. Z. Cummins. Localized fluid flow measurements with an He–Ne laser spectrometer. *Appl. Phys. Lett.*, 4(10):176–178, 1964.

[137] E. Hecht and A. Zajac. *Optics 4th international edition*. Addison Wesley Publishing Company: Boston, MA, USA, New York, USA, 2003.

[138] H. K. Versteeg and W. Malalasekera. *An Introduction to Computational Fluid Dynamics: the Finite Volume Method*. Pearson Education, 2007.

[139] M. Hundshagen, M. Mansour, D. Thévenin, and R. Skoda. Experimental investigation and 3D-CFD simulation of centrifugal pumps for gas-laden liquids with closed and semi-open impeller. In *4th International Rotating Equipment Conference*, Wiesbaden, Germany, 2019.

[140] F. R. Menter, J. C. Ferreira, T. Esch, B. Konno, and A. C. Germany. The SST turbulence model with improved wall treatment for heat transfer predictions in gas turbines. In *Proceedings of the International Gas Turbine Congress, Tokyo*, 2003.

[141] L. Schiller and A. Z. Naumann. Über die grundlegenden Berechnungen bei der Schwerkraftaufbereitung. *Z. Ver. Deutsch. Inge.*, 77:318–321, 1933.

List of own publications

Journal publications

P. Kováts, F. Martins, **M. Mansour**, D. Thévenin, K. Zähringer. Tomographic PIV measurements and RANS simulations of secondary flows inside a horizontally-positioned helically coiled reactor. *Exp. Fluids*, under review, 2020.

S. Bharadwaj, **M. Mansour**, D. Thévenin. Numerical investigations of turbulent single and two-phase flows in a divergent channel. *Int. J. Multiph. Flow*, under review, 2020.

M. Mansour, D. Thévenin, K. Zähringer. Numerical study of flow mixing and heat transfer in helical pipes, coiled flow inverters and a novel coiled configuration. *Chem. Eng. Sci.*, under review, 2020.

T. Parikh, **M. Mansour**, D. Thévenin. Investigations on the transport of two-phase air-water flows by centrifugal pump with different impeller configurations. *Chem. Eng. Sci.*, In press, 2020.

M. Mansour, T. Parikh, S. Engel, D. Thévenin, Numerical investigations of gas-liquid two-phase flow in a pump inducer. *J. Fluids Eng.*, **146**(4):021302, 2020.

M. Mansour, P. Khot, , P. Kováts, D. Thévenin, K. Zähringer, G. Janiga. Impact of computational domain discretization and gradient limiters on CFD results concerning liquid mixing in a helical pipe. *Chem. Eng. J.*, **383**:123121, 2020.

M. Mansour, A. Landage, P. Khot, K. D. P. Nigam, G. Janiga D. Thévenin, K. Zähringer. Numerical study of gas-liquid two-phase flow regimes for upward flow in a helical pipe. *Ind. Eng. Chem. Res.*, In press, 2019.

M. Mansour, K. Zähringer, D. Thévenin, K. D. P. Nigam, G. Janiga. Multi-objective optimization of liquid-liquid mixing in helical pipes using Genetic Algorithms coupled with Computational Fluid Dynamics. *Chem. Eng. J.*, In press, 2019.

P. Khot, **M. Mansour**, D. Thévenin, K. D. P. Nigam, K. Zähringer. Improving the mixing characteristics of coiled configurations by early flow inversion. *Chem. Eng. Res. Des.*, **146**:324–335, 2019.

M. Mansour, D. Thévenin, K. D. P. Nigam, K. Zähringer. Generally-valid optimal Reynolds and Dean numbers for efficient liquid-liquid mixing in helical pipes. *Chem. Eng. Sci.*, **201**:382–385, 2019.

M. Jokiel, N. M. Kaiser, P. Kováts, **M. Mansour**, K. Zähringer, K. D. P. Nigam, K. Sundmacher. Helically coiled segmented flow tubular reactor for the hydroformylation of long-chain olefins in a thermomorphic multiphase system. *Chem. Eng. J.*, **377**:120060, 2019.

M. Mansour, B. Wunderlich, D. Thévenin. Effect of tip clearance gap and inducer on the transport of two-phase air-water flows by centrifugal pumps. *Exp. Therm. Fluid Sci.*, **99**:487–509, 2018.

M. Mansour, P. Khot, D. Thévenin, K. D. P. Nigam, K. Zähringer. Optimal Reynolds number for liquid-liquid mixing in helical pipes. *Chem. Eng. Sci.*, In press, 2018.

M. Mansour, G. Janiga, K. D. P. Nigam, D. Thévenin, K. Zähringer. Numerical study of heat transfer and thermal homogenization in a helical reactor. *Chem. Eng. Sci.*, **177**:369–379, 2018.

M. Mansour, P. Kováts, B. Wunderlich, D. Thévenin. Experimental investigations of a two-phase gas/liquid flow in a diverging horizontal channel. *Exp. Therm. Fluid Sci.*, **93**:210–217, 2018.

M. Mansour, Z. Liu, G. Janiga, K. D. P. Nigam, K. Sundmacher, D. Thévenin, K. Zähringer. Numerical study of liquid-liquid mixing in helical pipes. *Chem. Eng. Sci.*, **172**:250–261, 2017.

M. Jokiel, L.-M. Wagner, **M. Mansour**, N. M. Kaiser, K. Zähringer, G. Janiga, K. D. Nigam, D. Thévenin, K. Sundmacher. Measurement and simulation of mass transfer and backmixing behavior in a gas-liquid helically coiled tubular reactor. *Chem. Eng. Sci.*, **170**:410–421, 2017.

M. Mansour, M. H. Ali, R.M.A. El-Maksoud. Experimental study of expansion and compression effects on the stability of Taylor vortex flow. *Fluid Dyn. Res.*, **48**(4):045502, 2016.

Proceedings

M. Hundshagen, **M. Mansour**, D. Thévenin, R. Skoda. Experimental investigation and 3D-CFD simulation of centrifugal pumps for gas-laden liquids with closed and semi-open impeller. In: 4th International Rotating Equipment Conference, Wiesbaden, Germany, 24-25 September 2019.

M. Mansour, T. Parikh, S. Engel, B. Wunderlich, D. Thévenin, Investigation on the influence of an inducer on the transport of single and two-phase air flows by centrifugal pumps. In 48th Turbomachinery & 35th Pump Symposia, Houston, TX, USA, 10-12 September 2019.

P. Kováts, **M. Mansour**, C. Velten, D. D. Thévenin, K. Zähringer. Mischungscharakterisierung in Helixreaktoren mittels LIF. In 27. Fachtagung Experimentelle Strömungsmechanik, Deutsche Gesellschaft für Laser-Anemometrie GALA e.V., Erlangen, Germany, 3-5 September 2019.

M. Hundshagen, **M. Mansour**, D. Thévenin, R. Skoda. Numerical investigation of two-phase air-water flow in a centrifugal pump with closed or semi-open impeller. In: 13th European Conference on Turbomachinery Fluid Dynamics and Thermodynamics, Lausanne, Switzerland, 8-12 April 2019.

M. Mansour, B. Wunderlich, D. Thévenin, Experimental study of two-phase air/water flows in a centrifugal pump running with a closed or a semi-open impeller. In: ASME Turbo Expo 2018, Turbomachinery Technical Conference and Exposition, American Society of Mechanical Engineers, Paper number GT2018-75380, Oslo, Norway, 11-15 June 2018.

M. Jokiel, **M. Mansour**, K. Zähringer, G. Janiga, K. D. Nigam, D. Thévenin, K. Sundmacher. Helix reactor for gas-liquid-reactions: Characterization of mass transfer and axial dispersion. In: ADECHEMA Jahrestreffen Reaktionstechnik, Würzburg, Germany, 2017.

M. Mansour, M. H. Ali, R.M.A. El-Maksoud. Some characteristics of Taylor vortex flow. In: Al-Azhar Engineering Twelfth International Conference, Cairo, Egypt, 25-27 December 2012.

Magdeburg,
07.02.2020 Michael Mansour